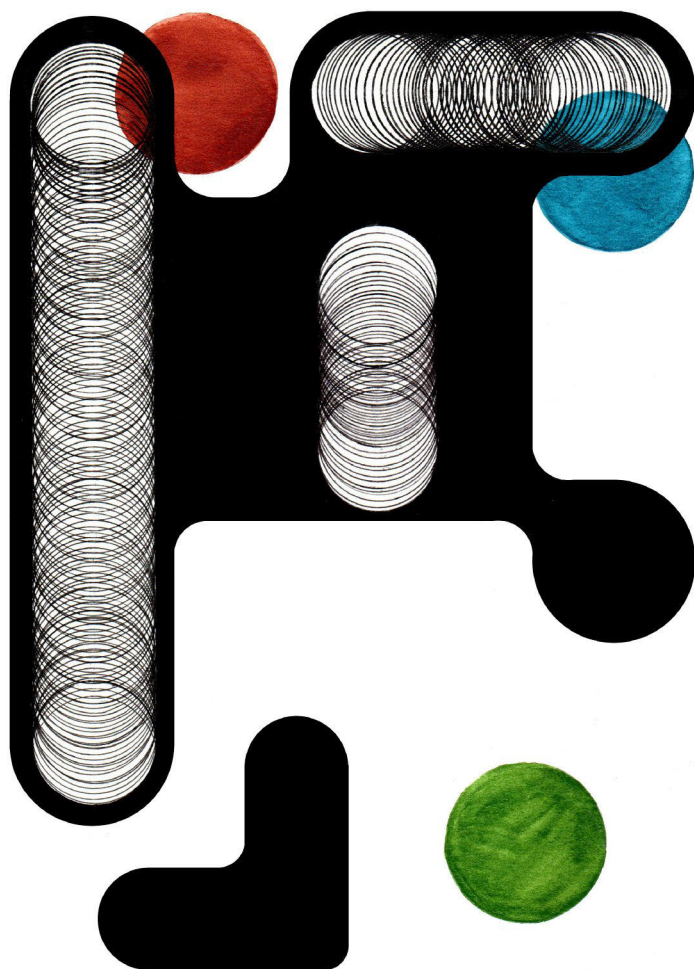


Hydrodeoxygenation of Lignin-Derived Model Compound for Sustainable Aviation Fuel Production Using Bifunctional Catalysts

Mark Eugenii Martínez Klimov



Laboratory of Industrial Chemistry and Reaction Engineering
Johan Gadolin Process Chemistry Centre
Faculty of Science and Engineering / Chemical Engineering
Åbo Akademi University
Åbo/Turku 2023



Mark E. Martinez Klimov

b. 1992 in Mexico City, Mexico

BSc Chemistry, 2016

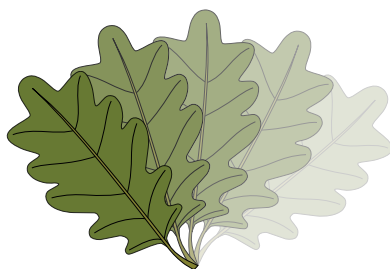
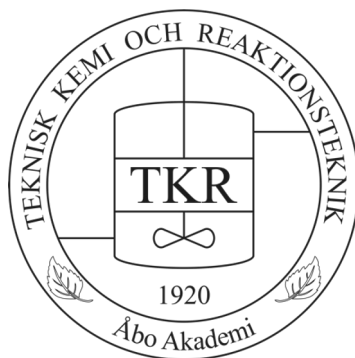
Universidad Nacional Autonoma de Mexico, Mexico City, Mexico

MSc Chemistry, 2018

Universidad Nacional Autonoma de Mexico, Mexico City, Mexico

Hydrodeoxygenation of lignin-derived model compound for sustainable aviation fuel production using bifunctional catalysts

Mark Eugenii Martínez Klimov



Johan Gadolin
Process Chemistry Centre

Laboratory of Industrial Chemistry and Reaction Engineering
Process Chemistry Centre
Faculty of Science and Engineering
Åbo Akademi University
Turku/Åbo 2023

Supervised by

Professor Dmitry Yu. Murzin
Laboratory of Industrial Chemistry and Reaction Engineering
Process Chemistry Centre
Åbo Akademi University, Åbo
Finland

and

Associate Professor Päivi Mäki-Arvela
Laboratory of Industrial Chemistry and Reaction Engineering
Process Chemistry Centre
Åbo Akademi University, Åbo
Finland

Reviewers

Professor David P. Serrano
Director and Head of Unit
IMDEA Energy Institute
Madrid, Spain

Docent Matti Reinikainen
VTT Technical Research Centre of Finland Ltd
Espoo, Finland

Faculty opponent

Professor David P. Serrano
IMDEA Energy Institute
Madrid, Spain

ISBN: 978-952-12-4335-6 (printed version)
ISBN 978-952-12-4336-3 (electronic version)
ISSN 2669-8315 (*Acta technologiae chemicae Aboensia* 2023 A/5)

Painosalama Oy Turku/Åbo 2023

To my family

“Memories and thoughts age, just as people do.
But certain thoughts can never age,
and certain memories can never fade.”

- Haruki Murakami, *The Wind-Up Bird Chronicle*

Preface

The present work was carried out at the Laboratory of Industrial Chemistry and Reaction Engineering, Process Chemistry Centre, Department of Chemical Engineering at Åbo Akademi University between November 2019 and November 2023.

I am profoundly grateful to the Magnus Ehrnrooth Foundation for providing the financial support to complete this project.

I would like to express my sincere gratitude to my supervisors, Professor Dmitry Yu. Murzin and Associate Professor Päivi Mäki-Arvela, for their invaluable support, guidance, and patience throughout this project. Their expertise, encouragement, and belief in my abilities have motivated me. I am truly fortunate to have had the opportunity to work under the supervision of such exceptional researchers.

I am deeply grateful to Professor Dmitry Yu. Murzin for all the opportunities he has given me and for allowing me to come work in this laboratory. His profound knowledge, insightful feedback, and dedication have been instrumental for this work. I am deeply thankful for his countless advice, as well as for all his lessons and guidance in both everyday life and work.

Assistant Professor Päivi Mäki-Arvela, her assistance throughout these years has been indispensable. From showing me how to operate the batch reactor to helping me with articles and characterization, her immense support is greatly appreciated.

To Academy Professor Tapio Salmi, his dedication and enthusiasm to work have been truly inspiring. His stories and eloquence have never failed to entertain, and I am particularly grateful for his assistance with finding and securing funding possibilities.

I would like to acknowledge the Laboratory Manager Dr. Kari Eränen, for always helping with instrumentation, analysis, chemicals, and anything else I could have needed in the laboratory.

Special thanks to Stephanie Weckesser, for designing my thesis cover, I won't forget how friendly and kind she has been to me since my first day at TKR. Additional thanks to my invaluable friends and colleagues, María, Olha, Lu, Adriana, Wilhelm, Jaypee, Laura, Nataliya, Jenni, Andreia, German, Federica, Luca, Ananias, Isa, Noora, Irina, Atte, Charlotta, Pasi T, Pasi V, Johan, Henrik, Narendra, Annika, Rosiina, Veronika, Nemanja, Ole, Christopher, Wander, Tommaso, Marissa, Sara, Mouad, Ekaterina, and everyone else who have made my time here more enjoyable.

I am thankful to my family. To my parents for their endless support, encouragement, and for helping me to develop an interest in science from a young age. To my sister for being understanding and always reassuring, and to my babushka for her wisdom and love.

I have made incredible memories that I will cherish forever.

Abstract

The development for sustainable and renewable fuels is driven by the current reliance on fossil fuels and a need to reduce contaminant gas emissions and adhere to climate-related regulations. The main challenge for the aviation industry in particular is the transition towards cleaner energy sources. A promising solution is manufacturing hydrocarbons from renewable sources, minimizing the environmental impact and high costs required for alternative green technologies.

Lignin is considered as a promising source of materials and biofuels, as it can be transformed through various thermochemical processes to valuable products. To obtain liquid hydrocarbons, lignin needs to undergo pyrolysis, resulting in bio-oil, which requires additional upgrading due to its low heating value, high viscosity, and acidity. Hydrodeoxygenation can be used to remove the oxygen groups, obtaining hydrocarbons compatible with the existing infrastructure.

In this study, hydrodeoxygenation of isoeugenol, a lignin-derived model compound, was investigated using various bifunctional catalysts in both batch and continuous reactors. A series of bimetallic platinum-rhenium catalysts supported on mesoporous and activated carbon were studied, with the purpose of revealing the role of both metals for hydrogenation and deoxygenation. The results indicated that a higher rhenium loading resulted in improved activity, providing the oxygen vacancies required for deoxygenation. Further research performed in a continuous reactor allowed high conversion (100%) and deoxygenation level (90%) at 200 °C.

For the first time studies simulating industrial catalysts and eventual scaling-up were performed for a lignin-derived model compound in batch and continuous reactors using powders and extrudates, respectively, comprising platinum as the active metal, zeolite beta and a binder. The effects of the binder addition, platinum location, and zeolite acidity were evaluated for the powder catalyst, while the effect of platinum location and reaction temperature was evaluated for the extrudates. The addition of binder resulted in a decrease of surface area, total pore volume, and acidity, additionally, the catalysts containing the more acidic zeolite (H-Beta-25) exhibited better catalytic performance (ca. 80% conversion and over 50% yield of the

deoxygenated product) compared to the H-Beta-300. The proximity of platinum to acid sites enhanced considerably catalytic activity, resulting in ca. 20% higher conversion when platinum was deposited on the zeolite rather than only on the binder. The extrudates displayed good stability, with a 10% decrease in catalytic activity after 30 hours of time on stream. Additionally, an effectiveness factor of 0.17 and an apparent activation energy of 14.7 kJ/mol revealed the presence of mass transfer limitations. A high conversion (100%) and a significant yield of deoxygenated products (80%), were obtained at 200 °C.

Referat

Utvecklingen av hållbara och förnybara bränslen drivs av det nuvarande beroendet av fossila bränslen och av ett behov att minska utsläppen av förorenande gaser och följa klimatrelaterade bestämmelser. Den största utmaningen i synnerhet för flygindustrin är övergången till renare energikällor. En hoppningivande lösning är att tillverka kolväten från förnybara källor, vilket minimerar miljöpåverkan och de höga kostnaderna för alternativ grön teknik.

Lignin anses vara en lovande källa till material och biobränslen, eftersom det kan omvandlas till värdefulla produkter genom olika termokemiska processer. För att få flytande kolväten måste lignin genomgå pyrolys, vilket resulterar i bioolja, som i sin tur kräver ytterligare uppgradering på grund av dess låga värmevärde, höga viskositet och surhet. Hydrodeoxygenering kan användas för att avlägsna syregrupperna och erhålla kolväten som är kompatibla med den befintliga infrastrukturen.

I detta arbete undersöktes hydrodeoxygenering av isoeugenol, en ligninbaserad modellförening, med olika bifunktionella katalysatorer i både satsreaktorer och kontinuerliga reaktorer. En serie bimetalliska platina-rhenium-katalysatorer på mesoporöst och aktivt kol studerades, i syfte att undersöka de båda metallernas roll i hydrogenering och i deoxygenering. Det visade sig att en högre rheniumhalt, med större antal syresäten, resulterade i förbättrad deoxygeneringsaktivitet. Det var möjligt att uppnå full omsättningsgrad av isoeugenol med 90% deoxygenering i en kontinuerlig reaktor vid 200 °C.

För första gången utfördes studier med industriellt efterliknande katalysatorer, både i pulverform och i extrudatform med platina som den aktiva metallen, zeolitbeta som bärarmaterial samt ett bindemedel. Studierna innehöll dessutom eventuell uppskalning för en ligninbaserad modellförening i satsreaktorer och kontinuerliga reaktorer. Effekterna av bindemedelstillsatsen, platinaplaceringen och zeolitens surhet utvärderades för pulverkatalysatorn, medan effekterna av platinaplaceringen och reaktionstemperaturen studerades för extrudaten. Tillsatsen av bindemedel resulterade i en förminskad yta, total porvolym och surhet. Det visade sig att katalysatorerna som innehöll den mer sura zeoliten (H-Beta-25) hade bättre katalytisk

prestanda (ca 80% omsättningsgrad och över 50% utbyte av den deoxygenerade produkten) jämfört med andra zeoliter. Placeringen av platina påverkade de katalytiska resultaten. Det påvisades att platina beläget nära surasäten förbättrade aktiviteten med ca 20% jämfört med platina deponerat på bindemedlet. Extrudaten visade god stabilitet, med bara 10% minskning av katalytisk aktivitet efter 30 timmars drift. Massöverföringsbegränsningar påvisades av en effektivitetsfaktor på 0,17 och en aktiveringsenergi på 14,7 kJ/mol. En hög omsättningsgrad (100%) och ett betydande utbyte av deoxygenerade produkter (80%) erhöles vid 200 °C med de industriellt efterliknande katalysatorerna.

List of Publications

The thesis consists of the following publications, which are referred to in the text by their Roman numerals.

- I. **M. E. Martínez-Klimov**, P. Mäki-Arvela, D. Y. Murzin, Catalysis for production of jet fuel from renewable sources by hydrodeoxygenation and hydrocracking, in *Catalysis: Volume 33*, ed. J. Spivey, Y.-F. Han and D. Shekhawat. The Royal Society of Chemistry, UK, 2021, Ch. 6, pp. 181-213.
- II. P. Mäki-Arvela, **M. E. Martínez-Klimov**, D. Y. Murzin, Hydroconversion of fatty acids and vegetable oils for production of jet fuels, *Fuel*, 306 (2021) 121673.
- III. **M. E. Martínez-Klimov**, P. Mäki-Arvela, Z. Vajglová, M. Alda-Onggar, I. Angervo, N. Kumar, K. Eränen, M. Peurla, M. H. Calimli, J. Muller, A. Shchukarev, I. L. Simakova, D. Y. Murzin, Hydrodeoxygenation of isoeugenol over carbon-supported Pt and Pt-Re catalysts for production of renewable jet fuel, *Energy Fuels*, 35 (2021) 17755-17768.
- IV. **M. E. Martínez-Klimov**, P. Mäki-Arvela, A. Çiftçi, N. Kumar, K. Eränen, M. Peurla, E. J. M. Hensen, D. Y. Murzin, Bifunctional Pt-Re catalysts in hydrodeoxygenation of isoeugenol as a model compound for renewable jet fuel production, *ACS Engineering Au*, 5 (2022) 436 – 449.
- V. **M. E. Martínez-Klimov**, P. Mäki-Arvela, Z. Vajglová, C. Schmidt, O. Yevdokimova, M. Peurla, N. Kumar, K. Eränen, D. Y. Murzin, D. Y. Bifunctional Pt catalysts supported on a zeolite-binder matrix for the hydrodeoxygenation of isoeugenol for renewable jet fuel production, *Topics in Catalysis*, 66 (2023) 1296 – 1309.
- VI. **M. E. Martínez Klimov**, O. Yevdokimova, P. Mäki-Arvela, J. Cueto, N. Shcherban, Z. Vajglová, K. Eränen, D. Y. Murzin, Hydrodeoxygenation of isoeugenol in continuous mode using bifunctional Pt-Beta 25-binder catalysts for renewable jet fuel production, *Sustainable Energy and Fuels*, 8 (2023) 90 – 102.

Contribution of the author to the publications I-VI

- I. Wrote the book chapter and contributed to the editing.
- II. Contributed to the editing.
- III. Conducted the experiments, catalyst characterization, and wrote the article.
- IV. Conducted the experiments, catalyst characterization, and wrote the article.
- V. Conducted the experiments, contributed to the catalyst characterization, and wrote the article.
- VI. Conducted the experiments, contributed to the catalyst characterization, and wrote the article.

Conference Presentations Relating to the Topic

1. **M. Martínez-Klimov**, P. Mäki-Arvela, Z. Vajglová, C. Schmidt, O. Yevdokimova, N. Kumar, K. Eränen, D. Y. Murzin, Hydrodeoxygenation of isoeugenol to produce renewable jet fuel using bifunctional catalysts, 15th European Congress on Catalysis (EuropaCat), Prague, Czech Republic, August 27 – September 1, 2023. *Poster presentation.*
2. O. Yevdokimova, N. Shcherban, **M. Martínez-Klimov**, M. Kurmach, O. Shvets, I. L. Simakova, P. Mäki-Arvela, K. Eränen, D. Y. Murzin, Synthesis of jet-fuels from renewable biomass through aldol condensation of cyclopentanone and furfural on different base catalysts, 15th European Congress on Catalysis (EuropaCat), Prague, Czech Republic, August 27 – September 1, 2023. *Poster presentation.*
3. G. Araujo-Barahona, R. Barakov, I. Kopa, **M. Martínez-Klimov**, T. Salmi, N. Shcherban, D. Y. Murzin, Ru, Ni and Pd catalysts deposited onto zeolites and mesoporous molecular sieves for hydrogenation and hydrocracking of biomass-derived compounds, The 28th North American Catalysis Society Meeting (NAM28), Providence, Rhode Island, United States of America, June 18 – 23, 2023. *Oral presentation given by the supervisor.*
4. **M. Martínez-Klimov**, O. Yevdokimova, P. Mäki-Arvela, I. Simakova, Z. Vajglová, N. Kumar, K. Eränen, D. Y. Murzin. Bifunctional catalysts for the production of renewable jet fuel. Finnish Young Scientist Forum for Catalysis, Joensuu, Finland, March 31, 2023. *Poster presentation.*
5. **M. Martínez-Klimov**, P. Mäki-Arvela, A. Çiftçi, N. Kumar, K. Eränen, E. J. M. Hensen, D. Y. Murzin. Synthesis of renewable jet fuel hydrocarbons by hydrodeoxygenation of isoeugenol over bimetallic Pt-Re catalysts. 26th International Congress of Chemical and Process Engineering (CHISA 2022). Prague, Czechia, August 21 – 25, 2022. *Oral presentation.*
6. **M. E. Martínez-Klimov**, P. Mäki-Arvela, I. L. Simakova, D. Y. Murzin. Hydrodeoxygenation over bimetallic Pt-Re catalysts for renewable jet fuel production. 19th Nordic Symposium on Catalysis (NSC 2022). Espoo, Finland, June 6 – 8, 2022. *Oral presentation.*
7. **M. E. Martínez-Klimov**, Z. Vajglová, N. Kumar, K. Eränen, P. Mäki-Arvela, D. Y. Murzin. Hydrodeoxygenation of lignin-derived model compounds to produce renewable jet fuel. 2nd International Conference on Reaction Kinetics, Mechanisms and Catalysis (RKMC 2021). Online in Budapest, Hungary, May 20 – 22, 2021. *Oral presentation.*
8. **M. E. Martínez-Klimov**, P. Mäki-Arvela, N. Kumar, K. Eränen, I. L. Simakova, D. Y. Murzin. Renewable jet fuel production by hydrodeoxygenation of isoeugenol using Pt-Re/Sibunit. Finnish Young Scientist Forum for Catalysis, Turku/Åbo, Finland, April 8, 2022. *Poster presentation.*

List of Other Publications

1. I. Kopa, O. Yevdokimova, **M. E. Martínez-Klimov**, M. Kurmach, D. Y. Murzin, N. Shcherban. Furfural acetalization with ethanol over hierarchical vs. conventional zeolites, *ChemistrySelect*, (2023), submitted.
2. G. Araujo-Barahona, N. Shcherban, K. Eränen, I. Kopa, I. Bezverkhyy, **M. Martínez-Klimov**, Z. Vajglová, A. Aho, J. García-Serna, T. Salmi, D. Y. Murzin, Ruthenium supported on silicate and aluminosilicate mesoporous materials applied to selective sugar hydrogenation: xylose to xylitol, *Chemical Engineering Journal*, (2023), submitted.
3. A. Manabayeva, P. Mäki-Arvela, Z. Vajglová, **M. Martínez-Klimov**, O. Yevdokimova, A. Peuronen, M. Lastusaari, T. Tirri, T. Baizhumanova, K. Kassymkan, G. Kaumenova, A. Brodskiy, R. Sarsenova, K. Shorayeva, S. A. Tungatarova, D. Y. Murzin, Dry reforming of methane over Mn- and Mg-modified Ni-based catalysts, *Applied Catalysis A, General*, (2023), submitted.
4. A. Manabayeva, P. Mäki-Arvela, Z. Vajglová, **M. Martínez-Klimov**, O. Yevdokimova, A. Peuronen, M. Lastusaari, T. Tirri, K. Kassymkan, T. Baizhumanova, M. Zhumabek, R. Sarsenova, Z. Zheksenbaeva, V. Russo, D. Y. Murzin, S. A. Tungatarova, Dry reforming of methane over Ce-, La- and Al-modified Ni-based catalysts, *Industrial & Engineering Chemistry Research*, (2023), submitted.
5. A. M. Manabayeva, P. Mäki-Arvela, Z. Vajglová, **M. Martínez-Klimov**, T. Tirri, T. S. Baizhumanova, V. P. Grigor'eva, M. Zhumabek, Y. A. Aubakirov, I. L. Simakova, D. Y. Murzin, S. A. Tungatarova, Dry reforming of methane over Ni-Fe-Al catalysts prepared by solution combustion synthesis, *Industrial & Engineering Chemistry Research*, 29 (2023) 11439 – 11455.
6. I. L. Simakova, Z. Vajglová, **M. Martínez-Klimov**, K. Eränen, M. Peurla, D. Y. Murzin, One-pot synthesis of menthol from citral over Ni/H-Beta-38 extrudates containing Bentonite clay binder in batch and continuous reactors, *Organic Process Research & Development*, 2 (2022) 295 – 310.
7. I. L. Simakova, P. Mäki-Arvela, **M. Martínez-Klimov**, J. Muller, Z. Vajglová, M. Peurla, K. Eränen, D. Murzin, One-pot synthesis of menthol starting from citral over Ni supported on Attapulgit H-Beta-28 extrudates in a continuous flow: effect of metal location, *Industrial & Engineering Chemistry Research*, 35 (2022) 12998 – 13010.
8. I. Simakova, P. Mäki-Arvela, **M. Martínez-Klimov**, J. Muller, Z. Vajglová, M. Peurla, K. Eränen, D. Y. Murzin, Continuous synthesis of menthol from citronellal and citral over Ni-beta-zeolite-sepiolite composite catalyst, *Applied Catalysis A: General*, 636 (2022) 118586.
9. A. Freites-Aguilera, P. Lindroos, J. Rahkila, **M. E. Martínez-Klimov**, P. Tolvanen, T. Salmi, Lipase catalyzed epoxidation of oleic acid using ultrasound as a process intensification method, *Chemical Engineering and Processing – Process Intensification*, 174 (2021) 108882.

Table of contents

Preface	i
Abstract	iii
Referat	v
List of Publications	vii
Conference Presentations Relating to the Topic	ix
List of Other Publications	xi
1. Introduction	1
1.1. Lignocellulosic biomass and its valorization	1
1.1.1. Lignin valorization	2
1.1.2. Lignin-derived bio-oil	3
1.1.3. Sustainable jet fuel.....	4
1.2. Hydrodeoxygenation	4
1.2.1. Hydrodeoxygenation catalysts and conditions.....	5
1.2.2. Sustainable jet fuel production landscape	6
1.3. Aim and scope of the research	7
2. Experimental	9
2.1. Chemicals and materials	9
2.1.1. PtRe supported on Sibunit carbon (publication III)	9
2.1.2. PtRe supported on activated carbon (publication IV)	9
2.1.3. Pt supported on zeolites and the binder (publications V - VI)	10
2.2. Catalyst synthesis	10
2.2.1. PtRe supported on Sibunit carbon (publication III)	11
2.2.2. PtRe supported on activated carbon (publication IV)	12
2.2.3. Pt supported on zeolite and binder (publications V - VI)	13
2.3. Catalyst characterization	14
2.3.1. Nitrogen physisorption.....	15
2.3.2. Transmission electron microscopy	16
2.3.3. Scanning electron microscopy.....	16
2.3.4. Inductively coupled plasma atomic emission spectroscopy.....	17
2.3.5. X-ray photoelectron spectroscopy	17
2.3.6. Pyridine-coupled Fourier transform infrared spectroscopy	17
2.3.7. Temperature programmed reduction	19
2.3.8. Temperature programmed oxidation	19

2.3.9. X-ray diffraction	20
2.3.10. Surface acidity	20
2.3.11. X-ray absorption spectroscopy	20
2.3.12. Temperature programmed desorption of ammonia	21
2.3.13. Crush test	21
2.4. Reactor systems	21
2.4.1. Batch reactor	21
2.4.2. Continuous trickle-bed reactor	22
2.5. Product analysis	23
3. Results and Discussion	25
3.1. Bimetallic platinum-rhenium catalysts supported on carbon	25
3.1.1. Catalyst characterization	25
3.1.2. Catalytic activity	32
3.1.3. Conclusions – carbon supported catalysts.....	38
3.2. Bifunctional Pt supported on zeolites and the binder	39
3.2.1. Catalyst characterization	39
3.2.2. Catalytic activity	45
3.2.3. Conclusions – zeolite + binder supported catalysts.....	51
3.3. Catalyst comparison.....	53
4. Conclusions and Future Perspectives.....	57
Notations	61
References.....	63
Publications	67

1. Introduction

1.1. Lignocellulosic biomass and its valorization

A drive to develop renewable fuels has increased in the recent years, primarily with the aim to reduce green-house gas emissions, mitigate dependence on the fossil fuels, and meet the climate regulations. A big challenge for the aviation industry is the transition towards cleaner energies, mainly because batteries are not capable of replacing traditional fuels due to their low energy-to-weight ratio.¹ A promising alternative is to obtain hydrocarbons from renewable sources to diminish the environmental impact.^{2,3}

Lignocellulosic biomass is renewable resource that refers to plant-based materials mainly composed of cellulose (40 - 50%), hemicellulose (20 – 35%), and lignin (15 - 35%). These materials make up the structural components of a wide range of plants, including wood and crops.⁴

Lignocellulosic biomass is an attractive, abundant, and versatile resource with promising applications to produce biofuels, materials, and chemicals,⁵ as it can be fragmented into smaller molecules which can then be further converted into valuable products through various chemical processes.⁶

The adequate utilization of biomass is important for the transition towards sustainable energies and materials, while reducing dependence on fossil fuels.

While cellulose and hemicellulose are used extensively in the papermaking, textile, and pharmaceutical industries, lignin is yet to make a commercial breakthrough. Although traditionally considered a waste product, lignin has attracted attention for its potential use as a valuable and sustainable resource in diverse industries.⁷

1.1.1. Lignin valorization

Lignin being a complex biopolymer responsible for providing structural support to plant cells, is composed of phenolic compounds linked together through C-C and C-O bonds, forming complex structures. Its main building blocks are three monomers: namely p-coumaryl, coniferyl, and sinapyl alcohols (Fig. 1).⁸

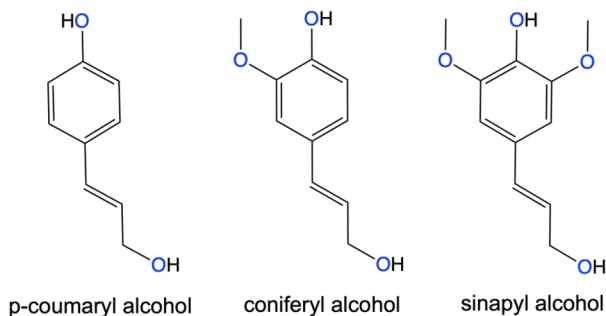


Fig 1. Structure of the three monomers constituting lignin.

Lignin is challenging to valorize, as it is recalcitrant, meaning it is resistant to chemical degradation and its depolymerization through thermochemical processes usually yields a complex mixture of oxygenated molecules, often called lignin-derived bio-oil.

The various potential applications of lignin-derived bio-oil are in chemicals such as adhesives, materials, and biofuels.⁹

Among different thermochemical conversion processes for biomass, pyrolysis has gained importance to produce liquid fuels. It is performed at 300 – 1100 °C in the absence of oxygen, followed by rapid cooling. Pyrolysis generates different fractions of solid, liquid, and gaseous products when operation conditions, such as temperature or heating rate are changed.¹⁰

Bio-oil, comprising the liquid phase produced from pyrolysis, can be used directly as furnace fuel, or can be further processed to obtain hydrocarbons with a higher energy density.¹¹

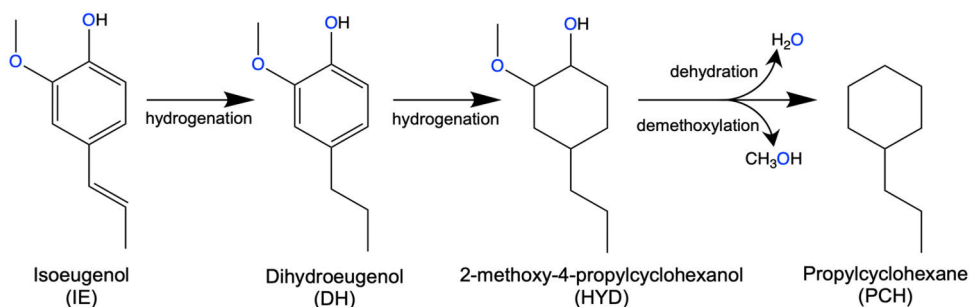
1.1.2. Lignin-derived bio-oil

Lignin-derived bio-oil is a dark liquid obtained from the fragmentation and depolymerization of lignin. It is a complex mixture of hundreds of oxygenated organic compounds such as ketones, esters, ethers, carboxylic acids, and phenols, among others. Its exact composition varies depending on the feedstock.^{12–14}

Bio-oil usually displays low heating value, high viscosity, and corrosiveness, due to its high oxygen content, thereby limiting its use as a fuel.¹⁵ Thus these oxygen moieties need to be removed to obtain hydrocarbons that can be utilized in modern combustion engines, which can be done through hydrodeoxygenation (HDO).

Due to the complexity of bio-oil, model oxygenated mono-phenolic compounds are often studied to understand the HDO reaction network and mechanisms, as phenolic compounds make up a large amount of molecules found in lignin-derived bio-oil.¹⁶ Phenol, guaiacol, isoeugenol, and vanillin are among the most studied model molecules for HDO, representing the phenolic compounds in bio-oil.^{13,17}

Isoeugenol is of particular interest as it resembles the phenylpropane units constituting lignin (Fig. 1), furthermore, its structure contains the hydroxyl, methoxy and allyl groups found in most compounds of lignin-derived bio-oil. An additional benefit is that the HDO product of isoeugenol is propylcyclohexane, which, as discussed in the next section, falls within the hydrocarbon range suitable for jet fuel (Scheme 1).



Scheme 1. A general reaction network for hydrodeoxygenation of isoeugenol.

1.1.3. Sustainable jet fuel

Traditional fossil-derived fuels used for commercial aircrafts consist of a mixture of aliphatic and aromatic hydrocarbons in the C₈ to C₁₆ range. Their main components include alkanes, alkenes, aromatic compounds, and cycloalkane derivatives.^{18,19}

Renewable jet fuel, often called sustainable aviation fuel (SAF), is produced from renewable and sustainable feedstocks, with the main goal of reducing the environmental impact of aviation by lowering emissions of greenhouse gases and promoting sustainability.

Hydrocarbons used in renewable jet fuel can be produced from biomass (such as crop residues and vegetable oils)^{20–22} or by using captured CO₂.²³

An advantage in utilizing the same hydrocarbons from biomass as from fossil fuels is the compatibility with existing equipment, meaning that they can be used in engines and infrastructure currently in use without the need for extensive modifications required for other technologies (drop-in fuels).²⁴ Therefore, if sustainable jet fuels meet fuel standards used in commercial aviation, they could be used as blends with conventional jet fuel, or they could eventually replace fossil-based fuels completely, thereby reducing adoption costs and making them a viable substitute at short-medium term.²⁵

1.2. Hydrodeoxygenation

HDO is a chemical process used in the transformation of biomass-derived feedstocks to remove oxygen moieties from organic compounds to produce oxygen-free hydrocarbons (Fig. 2).

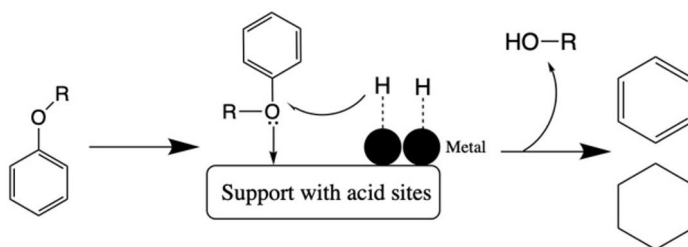


Fig 2. Simplified hydrodeoxygenation reaction.

The two main steps for HDO involve hydrogenation and deoxygenation reactions, therefore, the removal of oxygen requires the use of hydrogen and a bifunctional catalyst with two types of active sites. The hydrogenation sites (usually a metal) are responsible for adsorbing hydrogen onto the catalyst surface while the deoxygenation sites (acid sites or oxygen vacancies) are responsible for facilitating the removal of oxygen from the oxygenated compounds.^{26,27}

Most of the current HDO research is centered on the use of supported noble or transition metals, using either three phase (gas-liquid-solid) or two phase (gas-solid) reactors.

1.2.1. Hydrodeoxygenation catalysts and conditions

HDO catalysts are typically composed of a metal and a support. The most used metals are noble (Pt, Pd, Ru) or other transition metals (Ni, Mo, Co, Fe). The most common supports are Al_2O_3 , SiO_2 , ZrO_2 , various zeolites (H-Y, H-Beta, H-ZSM-5, USY) and different types of carbon.^{28–32} The choice of the metal and the support influences activity and selectivity.

Relatively high reaction conditions are used for HDO, with temperatures ranging from 150 to 400°C, and hydrogen pressures from 1 to 50 bar.²⁶

In recent years shaped catalysts (granules, extrudates) have been developed with the intention to bridge the gap between laboratory-scale research and industrial applications.³³ Continuous systems applied in industry demand the application of shaped catalysts to reduce the pressure drop. For this reason, it is fundamental to

understand shaping processes as well as the interactions between the multiple components that comprise industrial catalysts.³⁴

1.2.2. Sustainable jet fuel production landscape

The commercial aviation fuel market is expected to double from 400 billion liters in 2019 to 870 billion liters by 2050.³⁵ In addition to this growth, more stringent regulations on carbon emissions have made the development of new fuels, obtained from sustainable feedstocks, of utmost importance.

At present, the main alternative jet-fuel pathways certified by the ASTM D7566 to produce synthesized paraffinic kerosene (SPK) are:

FT-SPK – Fischer-Tropsch synthesized paraffinic kerosene involves gasification of feedstock into syngas (H_2 and CO) followed by the Fischer-Tropsch reaction to obtain liquid hydrocarbons.

HEFA – the hydro-processed esters and fatty acids pathway utilizes lipids, vegetable oils, or waste fats, as feedstocks to produce liquid hydrocarbons by deoxygenation followed hydrogenation.

SIP – the synthesized isoparaffins process is based on the fermentation and hydrogenation of sugary feedstocks to obtain farnesane ($C_{15}H_{32}$), which can be blended with traditional jet fuel.

ATJ - Alcohol-to-jet consists of the fermentation of sugars, starches, or hydrolyzed cellulose into isobutanol or ethanol, which are then further upgraded into a mix of hydrocarbons.

CHJ – The catalytic hydrothermolysis jet process uses a supercritical hydrothermal process to convert lipids into paraffins, isoparaffins, cycloparaffins, and aromatic compounds.

HC-HEFA - hydroprocessed hydrocarbons, esters, and fatty acids utilizes the lipids obtained from the *botryococcus braunii* algae, which are subjected to hydrocracking/hydroisomerization to remove the oxygen moieties and saturate double bonds to produce iso-alkanes.

Currently sustainable aviation fuel is produced by few companies, one of the forerunners being Neste, based in Finland. They manufacture ca. 1 million tons per year and are expecting to increase to 1.5 million tons by 2024 by hydrotreating vegetable oils, used cooking oil and animal fat.³⁶

At present, there is no dominant technology for the production of sustainable jet fuel, emphasizing the importance of ongoing research and innovation in the field.

1.3. Aim and scope of the research

The aim of the thesis was to investigate catalytic transformations of isoeugenol, a model compound for lignin-derived monomers, to produce propylcyclohexane, which is an oxygen-free hydrocarbon within the hydrocarbon range of jet fuel. The research was focused on the development of bifunctional catalysts supported on both carbon and zeolites, and its potential for scaling-up from laboratory scale (powders) into continuous processes preferred in industry (granules, extrudates). For this purpose, experiments were conducted in both batch and trickle-bed reactors.

Research on hydrodeoxygenation of biomass-derived compounds is reviewed in [I], while conversion of fatty acids and vegetable oils is covered in [II].

Hydrodeoxygenation of isoeugenol was carried out using bimetallic platinum-rhenium catalysts supported on a mesoporous type of carbon [III] and on microporous activated carbon [IV] with the purpose of understanding the effect of each metal and a variation of their ratios on the reaction.

Further studies on the scaling up were performed using bifunctional catalysts consisting of platinum supported on a zeolite and a binder, where the effect of platinum

location, zeolite acidity and effect of the binder addition were studied. Experiments were carried out in batch [V] and continuous [VI] reactors.

These studies serve as a guide to the research of more complicated mixtures derived from lignin depolymerization. In general, hydrodeoxygenation of lignin-derived compounds, such as isoeugenol, is a step towards the sustainable utilization and valorization of unwanted resources and the development of greener alternatives in the chemical and energy sectors.

2. Experimental

2.1. Chemicals and materials

For hydrodeoxygenation of isoeugenol the following commercially-acquired chemicals were used: isoeugenol (98%, mixture of cis and trans, Aldrich), dihydroeugenol (≥ 99 , Sigma-Aldrich), n-dodecane ($\geq 99\%$, Acros Organics), propylcyclohexane (99%, Aldrich) cyclohexane (99.9+%, Alfa Aesar).

The following gases were used: hydrogen (AGA, 99.999%), argon (AGA, 99.999%) and helium (AGA, 99.996%).

2.1.1. PtRe supported on Sibunit carbon (publication **III**)

The following catalysts were acquired from Degussa: F106XKYF and F1525XKT. Activated carbon Norit was supplied by NORIT (NORIT R3 EXTRA activated carbon) and Sibunit was supplied by the Boreskov Institute of Catalysis, Siberian Branch of the Russian Academy of Sciences.

Tetraammineplatinum(II) nitrate ($\geq 50.0\%$ Pt basis, Aldrich) was used for monometallic and Pt/Norit and Pt/Sibunit. Hexachloroplatinic acid ($\text{H}_2\text{PtCl}_6 \cdot 6\text{H}_2\text{O}$, Kraszvetmet, Krasnoyarsk, Russia) and perrhenic acid. (HReO_4 , 20 wt%, Reachim, Russia) were used as metal precursors for bimetallic PtRe/Sibunit catalysts.

2.1.2. PtRe supported on activated carbon (publication **IV**)

Activated carbon (NORIT RX3 EXTRA) was used as the support for all catalysts in this series.

The metal precursors were chloroplatinic acid hexahydrate ($\text{H}_2\text{PtCl}_6 \cdot 6\text{H}_2\text{O}$) and perrhenic acid (HReO_4 , Aldrich, 65–70 wt% in H_2O , 99.99%).

2.1.3. Pt supported on zeolites and the binder (publications V - VI)

Zeolites NH₄-Beta-25 and H-Beta-300 were obtained from Zeolyst International (SiO₂/Al₂O₃ = 25 and SiO₂/Al₂O₃ = 300, respectively) while the binder Bindzil-50/80 (50% colloidal SiO₂ in H₂O) was supplied by AzkoNobel.

Zeolite NH₄-Beta-25 was transformed into the proton form by calcination at 400 °C.

The organic binder used for extrusion (methylcellulose, viscosity: 4,000 cP) and the platinum precursor ([Pt(NH₃)₄](NO₃)₂, ≥ 50.0% Pt basis) were acquired from Sigma-Aldrich.

2.2. Catalyst synthesis

A summary of all the catalysts used in the present work, including the supported metal and its nominal loading, type of support and the corresponding publication is presented in Table 1. Their synthesis will be described in the following sections.

Table 1. Summary of catalysts used for hydrodeoxygenation of isoeugenol.

Catalyst	Metal	Nominal loading (wt%)	Support	Publication
Pt5/C1	Pt	5	Activated carbon	[III]
Pt5/C2	Pt	5	Activated carbon	[III]
Pt2/Norit	Pt	2	Activated carbon	[III]
Pt4/Sibunit	Pt	4	Sibunit carbon	[III]
Pt4Re4/Sib	Pt, Re	8 (4Pt:4Re)	Sibunit carbon	[III]
Pt6Re2/Sib	Pt, Re	8 (6Pt:2Re)	Sibunit carbon	[III]
Pt2Re6/Sib	Pt, Re	8 (2Pt:6Re)	Sibunit carbon	[III]
Pt4Re4/Sib granules	Pt, Re	8 (4Pt:4Re)	Sibunit carbon	[III]
Pt2.5/AC	Pt	2.5	Activated carbon	[IV]
Re2.5/AC	Re	2.5	Activated carbon	[IV]
Pt2.5Re1.5/AC	Pt, Re	4 (2.5Pt:1.5Re)	Activated carbon	[IV]
Pt2.5Re2.5/AC	Pt, Re	5 (2.5Pt:2.5Re)	Activated carbon	[IV]
Pt2.5Re5/AC	Pt, Re	7.5 (2.5Pt:5Re)	Activated carbon	[IV]
Pt2.5Re12.5/AC	Pt, Re	15 (2.5Pt:12.5Re)	Activated carbon	[IV]
Pt2/B25 ZB	Pt	2	H-Beta-25 + bindzil	[V]

Pt2/B25 Z	Pt	2	H-Beta-25 + bindzil	[V]
Pt2/B25 B	Pt	2	H-Beta-25 + bindzil	[V]
Pt2/B300 ZB	Pt	2	H-Beta 300 + bindzil	[V]
Pt2/B300 Z	Pt	2	H-Beta 300 + bindzil	[V]
Pt2/B300 B	Pt	2	H-Beta 300 + bindzil	[V]
Pt2/ EZB extrudates	Pt	2	H-Beta-25 + bindzil	[VI]
Pt2/ EZ extrudates	Pt	2	H-Beta-25 + bindzil	[VI]
Pt2/ EB extrudates	Pt	2	H-Beta-25 + bindzil	[VI]

2.2.1. PtRe supported on Sibunit carbon (publication III)

Catalysts supported on Sibunit carbon were synthesized in the Boreskov Institute of Catalysis, Novosibirsk, Russia.

For publication III, the catalysts were denoted as PRCXX, where PR represent the supported metals, platinum and rhenium, C represents the Sibunit carbon support and XX the metal ratio (wt%/wt%).

Naming of catalysts has been modified from Publication III to clarify and distinguish them from those presented in Publication IV. The modified notation is as follows: PtXReX/Sib, where X represents the corresponding metal loading in wt%, and Sib represents the Sibunit support. PtRe/Sib will be used to refer to all bimetallic catalysts in this series.

Monometallic Pt catalysts, Pt/Norit and Pt/Sibunit were synthesized by the incipient wetness impregnation of tetraammineplatinum(II) nitrate on Norit or Sibunit, the catalysts were denoted as Pt2/Norit and Pt4/Sibunit respectively.

Bimetallic Pt-Re catalysts with different metal ratios were synthesized by impregnation using an aqueous solution of a mixture of the metal precursors H_2PtCl_6 and HReO_4 .

Three bimetallic catalysts were prepared; Pt4Re4/Sib has a nominal metal loading of each metal of 4 wt%. Pt2Re6/Sib with the nominal metal loading of 2 wt% for Pt and 6 wt% for Re, and Pt6Re2/Sib with the nominal metal loading of 6 wt% for Pt and 2 wt% for Re.

Granulated Pt₄Re₄/Sib catalyst used for the continuous reactor experiments was prepared by the same method as described above only using larger particles of Sibunit (1 mm).

After impregnation the catalysts were dried at 110 °C overnight, reduced in a hydrogen flow with the temperature ramp 2 °C/min until 330 °C and were kept at the final temperature for ca. 6 h.

The catalysts used in the batch reactor were reduced ex-situ under hydrogen flow (40 mL/min) at 350 °C for 3 h (10 °C/min) prior to experiments. The catalysts were flushed with argon after the reduction and the solvent was added to avoid its reoxidation. The catalyst used in the continuous reactor was reduced in-situ under the same conditions as with the catalysts used in the batch reactor.

2.2.2. PtRe supported on activated carbon (publication IV)

Bimetallic and monometallic catalysts were prepared in the Eindhoven University of Technology, The Netherlands. The Pt:Re molar ratio for bimetallic catalysts was set to 1:1, 2:1, 1:2 and 1:5. For publication IV these catalysts were denoted as PRCXX, where PR corresponds to platinum and rhenium, C corresponds to the carbon support, and XX to the molar ratio. The catalyst designation in the thesis has been modified to the following: PtXXReXX/AC, where XX represents the corresponding metal loading in wt%, and AC represents the activated carbon support. PtRe/AC will be used when referring to all bimetallic catalysts supported on activated carbon.

Preparation of Pt and Pt-Re catalysts started with drying the activated carbon overnight at 110 °C, followed by impregnation of the dissolved Pt precursor (H₂PtCl₆) in deionized water. The catalyst was left to dry overnight at 110 °C. For bimetallic Pt-Re catalysts subsequent impregnation of the Re precursor (HReO₄) was done, followed by drying overnight at 110 °C.

Monometallic catalysts Pt_{2.5}/AC and Re_{2.5}/AC were prepared by impregnation using the corresponding precursor.

2.2.3. Pt supported on zeolite and binder (publications **V - VI**)

For publication **V**, the catalysts were denoted as either PtB300ZX or PtB25ZX, depending on the zeolite utilized as a support. Z was used to denote the presence of Bindzil while X corresponds to the location of the metal [A was used for Pt supported on both zeolite and the binder, B for Pt supported only on the zeolite, and C for Pt supported only on the binder]. All catalysts were prepared with the same 70:30 zeolite-to-binder ratio, where 2 wt% of platinum was deposited by the evaporation-impregnation method.

For simplification purposes, the catalysts notation in the thesis has been changed to the following:

- Pt2/BXX**ZB** - Pt located on both zeolite (**Z**) and binder (**B**): A mixture of 70% zeolite and 30% bindzil was stirred for 24 h at room temperature in water (80% water to 20% mixture), followed by the evaporation of water under vacuum, drying at 100 °C for 7 h and calcination at 500 °C. After deposition of platinum from $[\text{Pt}(\text{NH}_3)_4](\text{NO}_3)_2$, the catalyst was reduced in a U-shaped glass reactor under hydrogen flow (40 mL/min) at 350 °C for 3 h with a heating rate of 2 °C/min.
- Pt2/BXX**Z** - Pt located only on zeolite (**Z**): First, platinum was deposited on the zeolite by evaporation-impregnation from $[\text{Pt}(\text{NH}_3)_4](\text{NO}_3)_2$, followed by reduction under hydrogen flow (40 mL/min) at 350 °C for 3 h with a heating ramp of 2 °C/min. Pt/zeolite was mixed afterwards with Bindzil in water for 24 h. The water was evaporated, and the catalyst calcined at 500 °C.
- Pt2/BXX**B** - Pt located on binder (**B**): Bindzil was dried and sieved to a size of 45-63 μm prior to deposition of Pt. After deposition of platinum, Pt/Bindzil was reduced under hydrogen flow (40 mL/min) at 350 °C for 3 h with a heating ramp of 2 °C/min. Thereafter, it was mixed in water with the corresponding amount of the zeolite, followed by calcination of the catalyst at 500 °C.

In the notation above XX represents the Si:Al ratio of the zeolite.

The notation used for extrudates containing 2 wt% of platinum, 69 wt% of zeolite H-Beta-25 and 29 wt% of bindzil (publication **VI**) was as follows; Pt2/EZB when platinum (Pt) was deposited on both zeolite (Z) and the binder (B), Pt2/EZ when platinum was located only on the zeolite, and Pt2/EB when platinum was only on the binder. Pt/E was used when referring to all extrudate catalysts.

Shaping of the previously prepared powders was performed in an extrusion device (TBL-2, Tianjin Tianda Beiyang Chemical Co. Ltd., China). For this, a suspension composed of the catalyst mixture, distilled water and methylcellulose was prepared with a weight ratio of 44.5/54.5/1.0, respectively. The resulting extrudates exhibited a cylindrical shape with a diameter of 1.4 mm and ca. 1 cm of length. After shaping the extrudates were dried at 100 °C and calcined at 400 °C .

2.3. Catalyst characterization

Catalyst characterization was performed to understand the influence of the physical and chemical properties of the catalysts on catalytic activity, with the techniques used summarized in Table 2. The catalysts were characterized by nitrogen physisorption, transmission and scanning electron microscopy (TEM and SEM, respectively), inductively coupled plasma atomic emission spectroscopy (ICP-AES), X-ray photoelectron spectroscopy (XPS), Fourier transform infrared spectroscopy (FTIR) coupled to pyridine as a probe molecule, temperature programmed reduction and oxidation (TPR and TPO, respectively), X-ray diffraction (XRD), surface acidity, X-ray absorption spectroscopy (XAS) and temperature programmed desorption of ammonia (NH₃-TPD) and the crush test.

Catalyst characterization was performed at Åbo Akademi University (nitrogen physisorption, SEM, ICP-AES, pyridine FTIR, TPR, TPO, surface acidity, NH₃-TPD, crush test) as well as in collaboration with the University of Turku (TEM, XPS, XRD), Eindhoven University of Technology, the Netherlands (XAS, HAADF-STEM, ICP-OES) and Umeå University, Sweden (XPS).

Table 2. Summary of catalyst characterization

Catalyst/support	N ₂ Phys	TEM	SEM	ICP	XPS	Py FTIR	TPR	TPO	XRD	Surface acidity	XAS	NH ₃ TPD	Crush test
Carbon Norit	[III]	-	[III]	-	-	-	-	-	-	[III]	-	-	-
Carbon Sibunit	[III]	-	[III]	-	-	-	-	-	-	[III]	-	-	-
Pt5/C1	[III]	[III]	-	-	-	-	-	-	-	[III]	-	-	-
Pt5/C2	[III]	[III]	-	-	-	-	-	-	-	[III]	-	-	-
Pt2/Norit	[III]	[III]	-	-	-	-	-	-	-	[III]	-	-	-
Pt4/Sibunit	[III]	[III]	-	-	-	-	-	-	[III]	[III]	-	-	-
Pt4Re4/Sib	[III]	[III]	-	-	[III]	-	[III]	-	[III]	[III]	-	-	-
Pt6Re2/Sib	[III]	[III]	-	-	[III]	-	[III]	-	[III]	[III]	-	-	-
Pt2Re6/Sib	[III]	[III]	-	-	[III]	-	[III]	-	[III]	[III]	-	-	-
Pt4Re4/Sib granules	[III]	[III]	-	-	-	-	-	-	-	-	-	-	-
Pt2.5/AC	[IV]	[IV]	-	[IV]	-	-	[IV]	-	-	-	[IV]	[IV]	-
Re2.5/AC	[IV]	[IV]	-	[IV]	-	-	[IV]	-	-	-	[IV]	[IV]	-
Pt2.5Re1.5/AC	[IV]	[IV]	-	[IV]	-	-	[IV]	-	-	-	[IV]	-	-
Pt2.5Re2.5/AC	[IV]	[IV]	-	[IV]	-	-	[IV]	-	-	-	[IV]	[IV]	-
Pt2.5Re5/AC	[IV]	[IV]	-	[IV]	-	-	[IV]	-	-	-	[IV]	-	-
Pt2.5Re12.5/AC	[IV]	[IV]	-	[IV]	-	-	[IV]	-	-	-	[IV]	-	-
H-Beta-25	[V]	-	[V]	-	-	[V]	-	-	-	-	-	-	-
H-Beta-300	[V]	-	[V]	-	-	[V]	-	-	-	-	-	-	-
Bindzil	[V]	-	[V]	-	-	[V]	-	-	-	-	-	-	-
Pt2/B25ZB	[V]	[V]	[V]	[V]	-	[V]	-	-	-	-	-	-	-
Pt2/B25Z	[V]	[V]	[V]	[V]	-	[V]	-	-	-	-	-	-	-
Pt2/B25B	[V]	[V]	[V]	[V]	-	[V]	-	-	-	-	-	-	-
Pt2/B300ZB	[V]	[V]	[V]	[V]	-	[V]	-	-	-	-	-	-	-
Pt2/B300Z	[V]	[V]	[V]	[V]	-	[V]	-	-	-	-	-	-	-
Pt2/B300B	[V]	[V]	[V]	[V]	-	[V]	-	-	-	-	-	-	-
Pt2/EZ extrudates	[VI]	[VI]	[VI]	[VI]	-	[VI]	[VI]	[VI]	-	-	-	-	[VI]
Pt2/EZ extrudates	[VI]	[VI]	[VI]	[VI]	-	[VI]	[VI]	[VI]	-	-	-	-	[VI]
Pt2/EB extrudates	[VI]	[VI]	[VI]	[VI]	-	[VI]	[VI]	[VI]	-	-	-	-	[VI]

2.3.1. Nitrogen physisorption

Surface areas and pore-size distribution of the materials were determined by nitrogen physisorption using the Micrometrics 3Flex-3500 equipment. The Dubinin–Radushkevich and Brunauer-Emmett-Teller (BET) methods were used to determine the specific surface area of microporous and other materials, respectively, while pore size distributions were obtained using the Barrett-Joyner-Halenda (BJH) method for the desorption data and nonlocal density functional theory (NL-DFT).

The catalyst pretreatment consisted of two stages of outgassing prior to the measurements. First the catalysts were outgassed ex-situ in a Micromeritics VacPrep 061 Sample Degas System, under vacuum and 180-250 °C for 20-24 hours. Thereafter, they were degassed in-situ for 4-5 hours at 180-250 °C.

2.3.2. Transmission electron microscopy

Transmission electron microscopy was utilized to determine the metal particle size, evaluate the metal dispersion, as well as to study the morphology and porosity of the catalysts. The equipment used for analysis was a JEM-1400Plus (JEOL, Japan) with 120 kV maximal acceleration voltage. The samples were suspended in ethanol and mounted on a copper grid coated with a carbon film and the solvent was evaporated prior to the analysis.

The interpretation of TEM images and determination of particles sizes of the fresh and spent catalysts were done using the ImageJ program. On average 5-10 images per sample and ca. 200 metal-particle measurements were evaluated.

Bimetallic platinum-rhenium catalysts supported on active carbon (publication **IV**) were analyzed using high-angle annular dark-field scanning transmission electron microscopy (HAADF-STEM). Micrographs were obtained at room temperature on a CryoTitan Transmission Electron Microscope equipped with a field emission gun (FEG) and a Cryo-TWIN objective lens. STEM images were acquired with a Fishione HAADF detector.

2.3.3. Scanning electron microscopy

Scanning electron microscopy was utilized to obtain information on the morphology of the neat supports and catalysts. A Zeiss Leo Gemini 1530 microscope combined with secondary electron and backscattered electron detectors was applied. An acceleration voltage of 15 kV was used for the X-ray analyzer.

2.3.4. Inductively coupled plasma atomic emission spectroscopy

Elemental analysis to determine metal loadings of the catalysts was performed with inductively coupled plasma atomic emission spectrometry. Determination of the metal loading of the catalysts was performed on a Goffin Meyvis Spectro Ciruscdd apparatus or on a Perkin Elmer Optima 5300 DV. For this purpose, ca. 50 mg of catalyst were dissolved in a mixture of aqua regia (9 mL HCl 30% + 3 mL HNO₃ 65%) under microwave digestion for 1 hour.

2.3.5. X-ray photoelectron spectroscopy

X-ray photoelectron spectroscopy measurements were performed to determine the chemical state of supported metals. For PtRe/Sib samples it was performed ex situ with an Axis Ultra DLD manufactured by KRATOS Analytical Ltd., using a monochromated Al K α excitation source. For PtRe/AC the measurements were performed ex situ using a Nexsa XPS (ESCA) photoelectron spectrometer manufactured by Thermo Scientific, applying a monochromated Al K α excitation source.

Both series of catalysts were reduced ex situ and then placed on a sample holder for analysis. Deconvolution of peaks was done using the XPSpeak 4.1 program.

2.3.6. Pyridine-coupled Fourier transform infrared spectroscopy

The amount and strength of Brønsted and Lewis acid sites for zeolite-based materials were determined by Fourier transform infrared spectroscopy of adsorbed pyridine using an ATI Mattson FTIR Infinity Series spectrometer.

For this analysis pellets of catalyst of ca. 20 mg in weight and 1.3 cm in diameter were prepared using a hydraulic press. The samples were degassed under vacuum at 450 °C for 1 h, using a 10 °C/min ramp, followed by the adsorption of pyridine for 20

minutes at 100 °C under He flow. Physisorbed pyridine was removed by flowing He through the cell for 15 minutes.

Desorption of pyridine at 250, 350, and 450 °C was done to determine the weak, medium, and strong acid sites, respectively, while measurements were performed at 100 °C.

The Lewis and Brønsted acidity was determined with the absorption bands at 1450 and 1550 cm⁻¹, respectively.

The acid sites were calculated using an average of six measurements, which were taken after each desorption temperature. Concentration of acid sites was determined using the equations 1 and 2, considering molar extinction coefficients reported in the literature.³⁷

For the Brønsted acid sites:

$$C(B) = 1.88 \frac{IA(B)*R^2}{W} \quad (1)$$

and for Lewis acid sites:

$$C(L) = 1.42 \frac{IA(L)*R^2}{W} \quad (2)$$

Where:

C = acid site concentration (mmol/g)

W = pellet mass (g)

IA = integrated area (cm⁻¹)

R = pellet radius (cm)

2.3.7. Temperature programmed reduction

Temperature-programmed reduction was performed to determine the reduction temperature and hydrogen consumption of the fresh catalysts.

For PtRe/Sibunit catalysts TPR was performed in an AutoChem 2910 instrument, where 0.1 g of catalyst was dried at 120 °C for 1 h followed by reduction with 5 vol% hydrogen in argon using the following temperature program: 25–700 °C at 10 °C/min. A thermal conductivity (TC) detector was used, and the cooling system containing liquid nitrogen, a 2-propanol mixture, was applied to dry the gas phase samples before entering the TC detector.

For PtRe/AC the TPR analysis was performed in a tubular quartz reactor and a thermal conductivity detector (TCD). The sample was reduced in 4 vol% H₂ in N₂ at a flow rate of 8 ml/min. The heating was carried out from room temperature until 800 °C with a heating rate of 10 °C/min. The H₂ signal was calibrated using a reference catalyst (CuO/SiO₂).

TPR of zeolite-based catalysts was carried out in a Microtrac Belcat II. For each measurement, around 30 mg of the catalyst was loaded in a quartz reactor and pretreated in-situ at 200°C for 2 h under argon flow. Excess moisture was removed using a trap containing 13X molecular sieves (Sigma-Aldrich). The analysis was performed under a 5 vol% H₂ in Ar flow from 35 °C until 800 °C with a temperature ramp of 10 °C/min.

2.3.8. Temperature programmed oxidation

Temperature-programmed oxidation of the spent catalysts was used to determine the quantity and type of carbonaceous deposits. TPO was performed in a Microtrac Belcat II. The spent catalysts (ca. 30 mg) were loaded in a quartz reactor and pretreated in-situ at 200°C for 2 h under argon flow. The analysis was performed under a 5 vol% of O₂ in Ar flow from 35 °C until 865 °C with a temperature ramp of 10 °C/min.

2.3.9. X-ray diffraction

X-ray diffraction was performed to obtain information on the crystal structure, composition, and phase of the catalytic materials. XRD reflexes of the catalysts were recorded with an X-ray diffractometer D8 (Bruker, Germany) using CuK radiation and a LynxEye detector by scanning with a step of 0.05° and an accumulation time of 3 s at each point with a slit width 0.26° or accumulation time of 1 s at each point with a slit width of 0.52° . The identification of peaks was made by comparison with the literature.

2.3.10. Surface acidity

Surface acidity was determined for PtRe/Sib in accordance with the studies found in the literature.^{38,39} It was determined by measuring the pH of a slurry consisting of 50 mg of the catalyst and 50 mL of distilled water under agitation with a magnetic stirrer. pH of the slurry was determined using a Mettler Toledo pH electrode.

2.3.11. X-ray absorption spectroscopy

XAS was carried out at the European Synchrotron Radiation Facility (ESRF) in Grenoble, France (storage ring 6.0 GeV, ring current 200 mA). The data were collected at transmission mode for Pt LIII and Re LIII edges using a double crystal Si(111) monochromator solid-state detector.

Pt foil was used for calibration. For the Re LIII edge, Re powder and NH_4ReO_4 were used as the reference. The spectra were recorded in a stainless-steel cell under He and H_2 atmosphere.

XANES spectra were recorded while heating the sample to 550°C at a rate of $10^\circ\text{C}/\text{min}$. EXAFS spectra were obtained after the sample was cooled.

2.3.12. Temperature programmed desorption of ammonia

Temperature programmed desorption of ammonia was used to determine the acidity of PtRe/AC catalysts. It was performed in a tubular quartz reactor attached to a heating oven and coupled to a quadrupole mass spectrometer (Balzers TPG-300). The samples were pre-reduced in-situ prior to the analysis. Afterwards the catalyst was exposed to pure NH_3 at room temperature. The temperature ramp used for the analysis was $10\text{ }^\circ\text{C}/\text{min}$ under He flow ($50\text{ ml}/\text{min}$). The signals corresponding to He, NH_3 and H_2O were recorded simultaneously.

2.3.13. Crush test

Mechanical strength of extrudates was determined using a crush tester with two parallel plates (SE 048, Lorentzen & Wettre, Sweden), where the force was applied until the extrudate collapsed. The mechanical strength of the extrudates was determined in both vertical and horizontal positions. An average of 10 extrudates were tested in each position for each type of extrudate.

2.4. Reactor systems

2.4.1. Batch reactor

Batch reactions were carried out in a 300 mL stainless steel autoclave (PARR Instruments) equipped with a heating jacket, mechanical stirrer, gas inlet and outlet lines and a sampling valve. The stirring speed was set to 900 rpm to avoid external mass transfer limitations. The size of the catalyst particles was between $45 - 63\text{ }\mu\text{m}$ to ensure absence of internal mass transfer limitations.

Prior to the experiments, the catalysts were reduced ex-situ in a U-shaped reactor, under hydrogen flow ($40\text{ mL}/\text{min}$) at $350\text{ }^\circ\text{C}$ for 180 min, with a heating ramp of $10\text{ }^\circ\text{C}/\text{min}$.

°C/min. After reduction was finished, the system was flushed with argon and dodecane was added to avoid reoxidation.

The reactor was loaded with 0.05 g of the catalyst, 0.1 g of isoeugenol and 50 mL of dodecane. Argon was used to purge the reactor, followed by pressurizing to 20 bar with hydrogen.

Heating to the desired reaction temperature was done at a rate of 10 °C/min. The pressure was increased to 30 bar when approaching the desired temperature. The liquid samples were taken at regular time intervals and analyzed by GC and GC/MS.

2.4.2. Continuous trickle-bed reactor

Continuous experiments were performed in a fixed-bed reactor equipped with a heating jacket, K-type thermocouple, a pressure controller (Brooks Instrument 5866), high-performance liquid chromatography (HPLC) pump (Knauer Smartline) and 150 mL refrigerated collector vessel. The dimensions of the reactor were the following: 12 cm length, 1.2 mm inner diameter, the catalyst zone of 70 mm and a thermocouple pocket of 3 mm. The reactor was loaded with 0.3 g of the catalyst mixed with 15 g of fine granular quartz (200-800 µm) to have a uniform distribution of the catalyst throughout the catalytic bed, while the remaining space was filled with quartz. The system was purged with an Ar flow of 50 mL/min for 15 minutes prior to the reduction. The in-situ reduction of the catalysts was carried out at 350 °C for 3 hours (temperature ramp 10 °C/min) under hydrogen flow rate of 40 mL/min at atmospheric pressure.

After the catalyst reduction, the system was pressurized to 30 bars with hydrogen and heated to reach the reaction temperature with a ramp of 10 °C/min.

A mixture of isoeugenol in dodecane (0.012M) was used for the catalytic tests.

The reaction mixture was fed downflow via the HPCL pump, under 30 bar of H₂ and the gas flowrate of 0.5 mL/min. The liquid samples taken periodically during 4 h were analyzed using the same procedure as with the batch reactor.

2.5. Product analysis

Gas chromatography analysis of the liquid samples was carried out using an Agilent Technologies 6890N GC system equipped with an Agilent 7683 AutoSampler. The column used was a DB-1 capillary column (Agilent 122-103e) of 30 m length, 250 μ m internal diameter and 0.5 μ m film thickness. Helium was used as a carrier gas with a flow rate of 1.7 mL/min. The temperature program for GC analysis was as follows: 60 °C (5 min), 3 °C/min to 135 °C, and 15 °C/min to 300 °C.

GC-MS analysis was performed using an Agilent Technologies 5973 Mass Selective detector over the same model GC, column and using the same temperature program as used in GC.

3. Results and Discussion

3.1. Bimetallic platinum-rhenium catalysts supported on carbon

3.1.1. Catalyst characterization

Sibunit-supported catalysts (Publication III)

A summary of the textural properties, metal particle sizes and pH of the catalysts and supports slurries is presented in Table 3.

Table 3. Textural properties, metal particle sizes and pH of slurries of the catalysts and supports.

Catalyst	Textural characteristics				Metal particle size (nm)
	SSA (m ² /g)	V _Σ (cm ³ /g)	V _{MP} (cm ³ /g)	D _P (nm)	
Norit	1247	0.58	0.51	0.6	-
Sibunit	330	0.52	0.09	0.9	-
Pt5/C1	450	0.29	0.17	0.6	3.1
Pt5/C2	421	0.28	0.16	0.6	2.9
Pt2/Norit	857	0.39	0.31	0.6	4.2
Pt4/Sibunit	283	0.35	0.08	0.9, > 3.5	3.5
Pt4Re4/Sib	268	0.31	0.07	0.9, > 3.5	1.3
Pt4Re4/Sib spent	222	0.23	0.04	0.9, > 3.5	1.5
Pt6Re2/Sib	277	0.34	0.08	0.9, > 3.5	1.2
Pt2Re6/Sib	275	0.32	0.08	0.9, > 3.5	1.3
Pt4Re4/Sib granulated	234	0.32	0.07	0.9, > 3.5	1.4
Pt4Re4/Sib granulated, spent	176	0.25	0.05	0.9, > 3.5	1.7

Deposition of Pt resulted in a slight decrease of the textural properties for all catalysts, which can be explained by blocking of the pores by the metal. Norit and Pt/Norit gave the highest specific surface area (SSA), total and micropore volume (V_Σ and V_{MP}, respectively), as well as a smaller pore diameter (D_P). The catalysts supported on

mesoporous Sibunit (Pt/Sibunit and PtRe/Sib series) displayed lower SSA, V_{Σ} and V_{MP} .

Commercial catalysts C1 and C2 showed properties similar to those of Norit, all being supported on activated carbon.

Adsorption-desorption isotherms of the three different types of catalysts, as well as for the fresh and spent Pt4Re4/Sib powder and granules are compared in Fig 3.

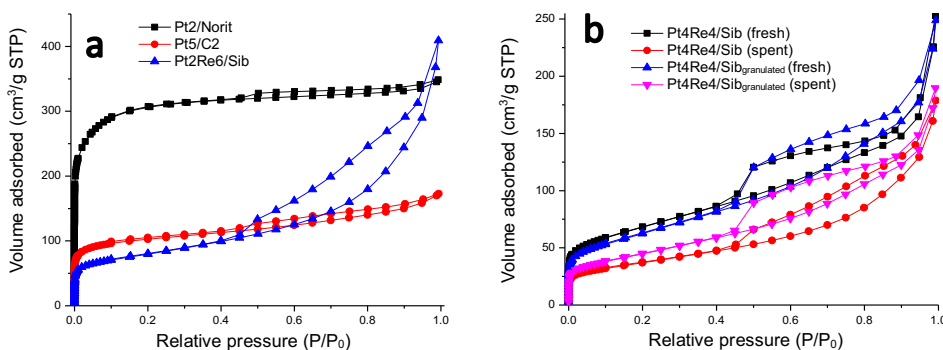


Fig 3. Adsorption-desorption isotherm of a) Pt2/Norit, Pt5/C2, Pt2Re6/Sib and b) Pt4Re4/Sib powder and granules, fresh and spent.

Catalysts supported on activated carbon showed the isotherm of type I and hysteresis type H4, indicating the presence of micropores characteristic activated carbon, while catalysts supported on Sibunit showed a combination of isotherm types I and IV, indicating the presence of both micro- and mesopores, and H3 hysteresis.⁴⁰

NL-DFT pore size distributions exhibited a main pore contribution at around 0.6 nm for catalysts supported on Norit and both Pt5/C1 and Pt5/C2. For PtRe/Sib catalysts, the main peak present in the microporous range was at ca. 0.9 nm, with additional mesoporosity at >3.5 nm.

A decrease in surface area for spent catalysts could be due to formation of carbonaceous species that remained on the surface of the catalysts. A lack of changes in the pore diameter indicated low mechanical degradation.

XRD diffractograms display Pt peaks at around 39.5°, 46°, 67°, and 81°, attributed to (111), (200), (220), and (311) reflections.⁴¹ The presence of these peaks can be attributed to larger metal particles not observed in TEM. The lack of peaks belonging to Re could be caused by high dispersion of Re particles or an overlap with carbon reflections.⁴²

Morphological differences between Sibunit and Norit were observed by SEM (Fig 4). Sibunit consisted of more uniform granules (0.3 – 0.5 µm), while Norit is composed of more heterogeneous and varied particles with the size exceeding 0.5 µm.

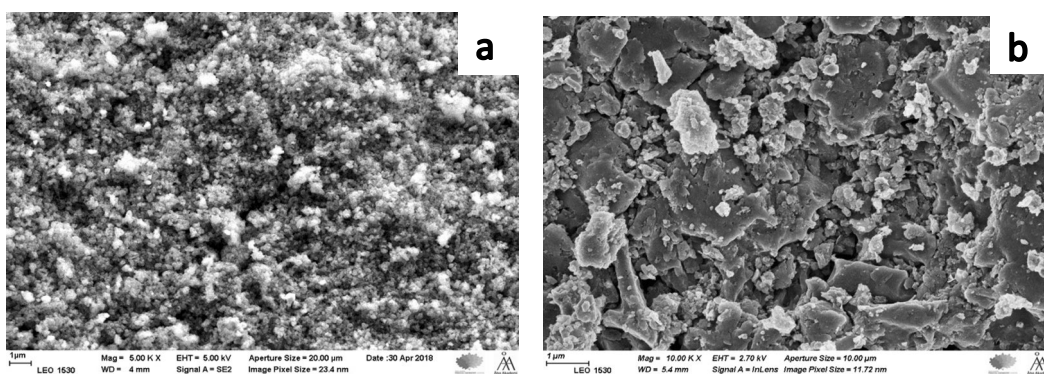


Fig 4. SEM micrographs of (a) Sibunit and (b) Norit.

As observed from TEM micrographs, all catalysts exhibited the metal particle sizes below 5 nm. The smallest metal particles were found in the PtRe/Sib series (<1.4 nm, Table 3) despite higher total metal loadings (Table 1, Table 3). Additionally, PtRe/Sib series showed a smaller metal particle size than monometallic Pt4/Sibunit, indicating that addition of Re helped to stabilize the metal particles on the surface of the support.⁴³

It was not possible to differentiate between Pt and Re nanoparticles in bimetallic catalysts, therefore the combined metal particle size distributions are reported. TEM micrographs for two PtRe/Sib catalysts are presented in Fig 5.

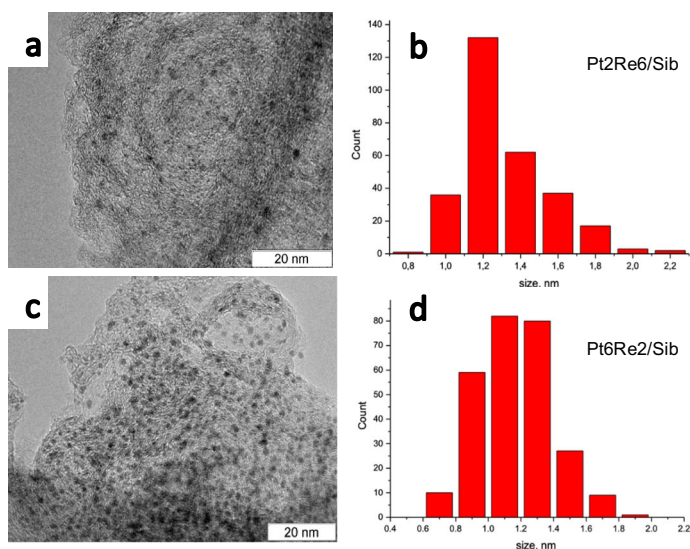


Fig 5. TEM micrographs and the metal particle size distribution of Pt2Re6/Sib (a, b) and Pt6Re2/Sib (c, d).

A comparison of the TEM images (publication III) between the fresh and the spent Pt4Re4/Sib catalysts shows almost no changes in the particle sizes after the reaction (Table 3), indicating good stability of metal particles.

XPS analysis showed that the reduction programme used for PtRe/Sib catalysts resulted in complete reduction of Pt, while Re remains as an oxide. Pt 4f binding energy (BE) of 71.8 eV was assigned to Pt⁰. These results are consistent with the binding BE values of 71.6 eV for zerovalent Pt 4f 7/2.^{44,45} A slight shift after the addition of Re hints at intermetallic interactions. Re 4f binding energy of 44.9 eV was assigned to Re⁴⁺. This species was predominant for all catalysts. The catalyst with the lowest Re content, Pt6Re2/Sib, exhibited an additional signal at 41.2 eV, which was assigned for Re⁰.⁴⁵

Activated carbon supported catalysts (Publication IV)

A summary of the metal loading, textural properties and acidity of the catalysts is presented in Table 4. Catalyst preparation and the following characterization techniques; ICP-IES, HAADF-STEM, TPR, XAS, and TPD-NH₃ have been adapted from a previous publication.⁴⁶

Table 4. Metal loading and textural properties of the catalysts.

Catalyst	Loading (wt%)		Molar ratio Pt:Re	Textural characteristics			
	Pt	Re		SSA (m ² /g)	V _Σ (cm ³ /g)	V _{MP} (cm ³ /g)	D _P (nm)
AC support	-	-	-	1171	0.57	0.47	0.6
Pt2.5/AC	2.44	-	-	1033	0.47	0.37	0.6
Re2.5/AC	-	2.78	-	1030	0.49	0.39	0.6
Pt2.5Re1.5/AC	2.48	1.53	2:1.2	1026	0.49	0.40	0.6
Pt2.5Re2.5/AC	2.53	2.86	1:1.2	1019	0.47	0.38	0.6
Pt2.5Re5/AC	2.51	5.58	1:2.3	1017	0.48	0.37	0.6
Pt2.5Re12.5/AC	2.28	13.41	1:6	1014	0.48	0.36	0.6
Pt2.5Re2.5/AC spent	-	-	-	1002	0.43	0.35	0.6
Pt2.5Re1.5/AC spent	-	-	-	1005	0.43	0.35	0.6
Pt2.5Re12.5/AC spent (270 °C)	-	-	-	992	0.39	0.33	0.6

Metal ratios determined by ICP were close to the theoretical values. Additionally, nitrogen physisorption results showed high specific surface (SSA) area for all catalysts (ca.1000 m²/g). The highest SSA, total pore volume (V_Σ) and the micropore volume (V_{MP}) were obtained for monometallic Pt2.5/AC and Re2.5/AC catalysts, while bimetallic catalysts exhibited a slight decrease of the textural properties, which could be explained by the pore blockage due to increased metal loadings.

Adsorption-desorption isotherms and the pore size distributions of fresh Pt2.5/AC, Re2.5/AC and Pt2.5Re12.5/AC are compared in Figure 6a, while fresh and spent Pt2.5Re1.5/AC and Pt2.5Re2.5/AC are shown in Figure 6b.

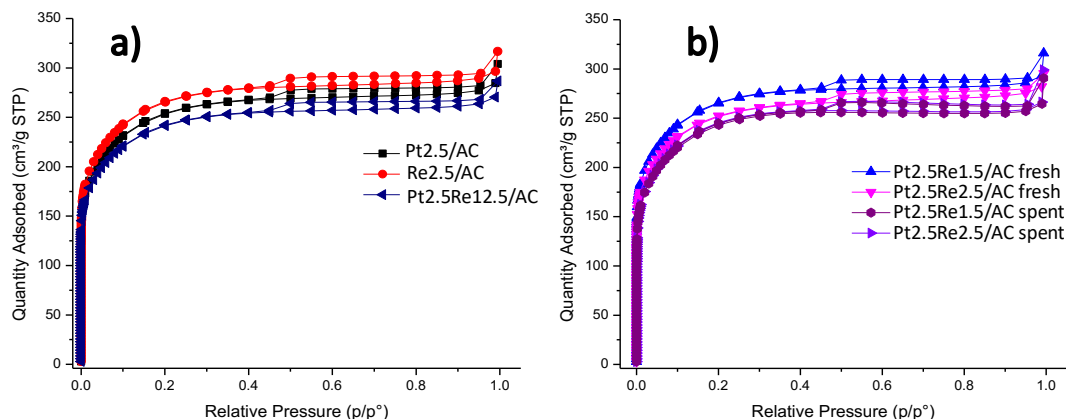


Fig 6. Adsorption-desorption isotherm of a) different types of catalysts and b) fresh and spent Pt_{2.5}Re_{1.5}/AC and Pt_{2.5}Re_{2.5}/AC.

All catalysts displayed isotherms of type I and hysteresis type H4, characteristic of activated carbon, indicating the presence of micropores.⁴⁰ The main pore contribution obtained by NL-DFT was ca. 0.6 nm for all catalysts.

A negligible decrease (<5%) in the surface area and no changes in the pore size distribution were observed for spent catalysts.

Transmission electron micrographs allowed to determine the metal particle sizes of monometallic and bimetallic catalysts (Fig 7). All catalysts exhibited the metal particle sizes in the range of 1-2 nm. Spent catalysts presented almost no changes in the metal particle sizes after the reaction, indicating good stability.

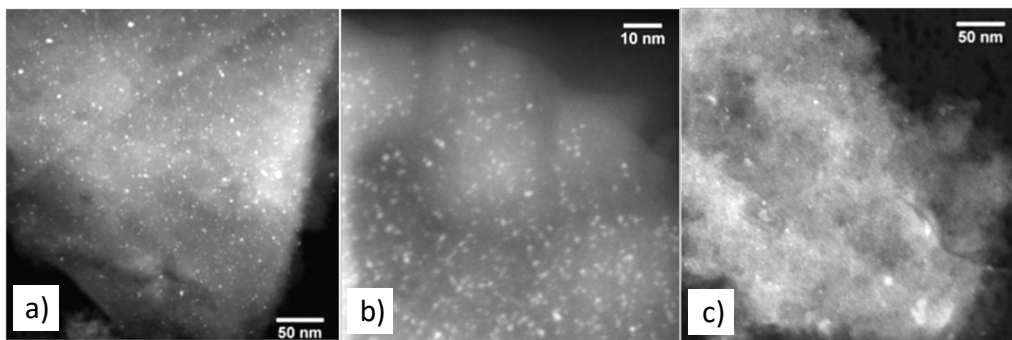


Fig 7. HAADF-STEM micrographs of fresh a) Pt_{2.5}/AC, b) Pt_{2.5}Re_{2.5}/AC and c) Pt_{2.5}Re_{12.5}/AC catalysts.

Reduction profiles determined by TPR display reduction peaks for Pt in the range of 150 - 300 °C,⁴⁷ and between 250 and 450 °C for Re.⁴⁸ Furthermore, shifts in the reduction peaks have been reported due to formation of Pt-Re alloys.⁴⁹

Pt XANES spectra indicated that Pt reduction mainly occurs between 100-200 °C. For Pt2.5Re12.5/AC the edge position shifts to higher energy values than Pt foil and reduced Pt2.5/AC, implying Re influenced the electronic structure of Pt.⁵⁰

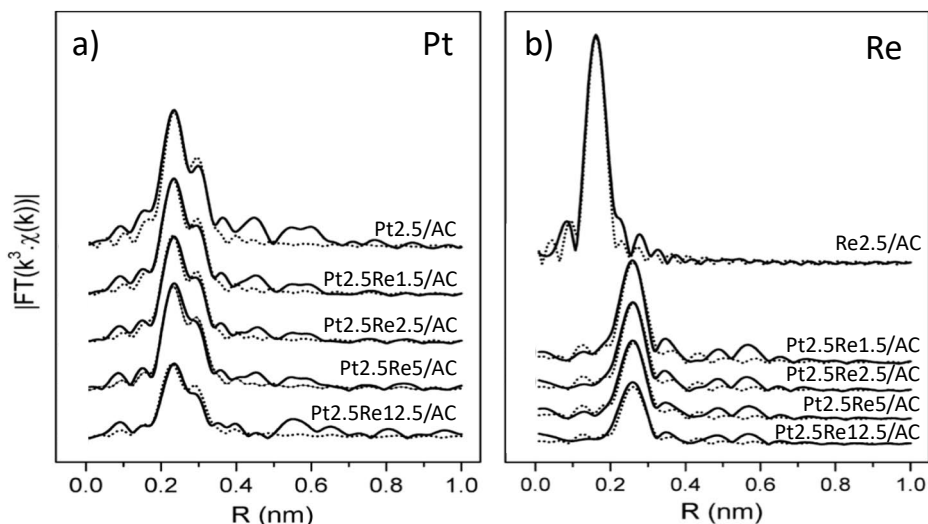


Fig 8. EXAFS spectra Pt L_{III} edge and Re L_{III} edge for monometallic and bimetallic catalysts. Dotted lines represent the fitted spectra.

As determined from EXAFS (Fig 8), the coordination number (CN) of the Pt–M shell decreased as the Pt:Re ratio increased, which could explain the decrease in metal particle sizes with increasing Re content. Furthermore, the Pt–M coordination distance became smaller with increasing Re content.

EXAFS results at the Re L_{III} edge indicated that Re in Re2.5/AC is present mainly as an oxide after reduction at 250 °C, while at 550 °C it is mostly metallic Re and small fraction of ReO_x species. For bimetallic catalysts, it was observed that the (CN) of the Re–M shell increased with the increase of Re loading, which is in accordance with the Pt EXAFS results that explain the decrease in metal particle sizes.

3.1.2. Catalytic activity

Sibunit supported catalysts (Publication III)

All catalysts were highly active for hydrogenation of the side chain double bond of isoeugenol to form dihydroeugenol (DH), resulting in a complete isoeugenol conversion for all tested catalysts, however, the propylcyclohexane yield (PCH Y) was low for monometallic Pt catalysts. On the other hand, as seen from Fig 9, bimetallic catalysts PtRe/Sib showed almost complete dihydroeugenol conversion (DH X, >98%) and a high PCH Y (>66%). Comparison of these results with monometallic Pt4/Sibunit indicates that addition of Re had a noticeable effect on hydrodeoxygenation activity.

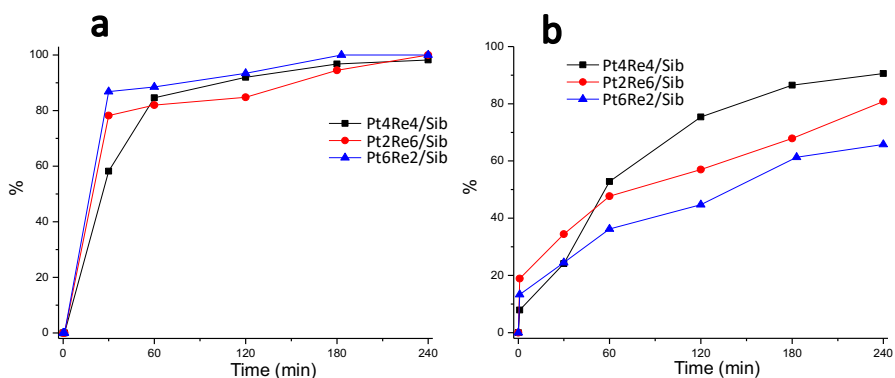


Fig 9. (a) Conversion of dihydroeugenol and (b) yield of propylcyclohexane as a function of time for bimetallic Pt-Re supported on Sibunit.

Varying the Pt:Re ratio resulted in a noticeable effect on activity. While all PtRe/Sib catalysts displayed almost complete conversion at 4 h of the reaction time, the lowest PCH Y (66%) was observed for Pt6Re2/Sib.

The catalysts with a higher amount of Re, Pt4Re4/Sib and Pt2Re6/Sib, exhibited similar activity (PCH Y >84%), with Pt4Re4/Sib displaying the highest PCH Y (84%) at 4h. These results can be explained by the presence of ReOx (XPS results) providing oxygen vacancies required for the deoxygenation to take place.⁵¹

The two best catalysts for HDO were Pt2Re6/Sib and Pt4Re4/Sib, these results are consistent with a higher atomic concentration of Re on the surface of the catalysts and

a predominant ReOx state, as it is necessary for oxygen activation. Moreover, their similar performance indicates that the amount of Pt has a lower effect on activity than the impact of Re, which is especially necessary for an inert support such as carbon.

To explore stability, repeatability and reusability of the catalysts, tests were performed with Pt4Re4/Sib in a batch reactor at 250 °C and 30 bar of H₂ and 4 hours of reaction time.

Table 5. Repeatability and reusability results for Pt4Re4/Sib in a batch reactor at 250 °C.

Catalyst	DH X (%)	GCLPA (%)	PCH Y (%)
Pt4Re4/Sib	98	70	91
Pt4Re4/Sib repeat	100	68	89
Pt4Re4/Sib reuse	100	67	84

The tests demonstrated that the results were reliable (Table 5) and Pt4Re4/Sib displayed consistent performance when the reaction was repeated at the same conditions. The fresh and the spent and washed Pt4Re4/Sib exhibited similar behavior, indicating low catalyst deactivation.

Gas Chromatography Liquid Phase Analysis (GCLPA) was used to determine the mass balance of products remaining in the liquid phase. For this purpose, eq. 3. was used, where ΣC_{all} is the sum of the concentrations of reactants and products at a specific time while C_0 is the initial concentration of dihydroeugenol.

$$GCLPA = \frac{\Sigma C_{all}}{C_0} * 100 \quad (3)$$

GCLPA values remained ca. 70% for all tests, indicating that most products remained in the liquid phase.

The granulated Pt4Re4/Sib was tested in a trickle-bed reactor to investigate scalability, stability, and the product distribution under a continuous flow (0.5 mL/min) of isoeugenol in dodecane at 30 bar H₂ and at 200, 170, 150 and 75 °C. The results are presented in Fig 10.

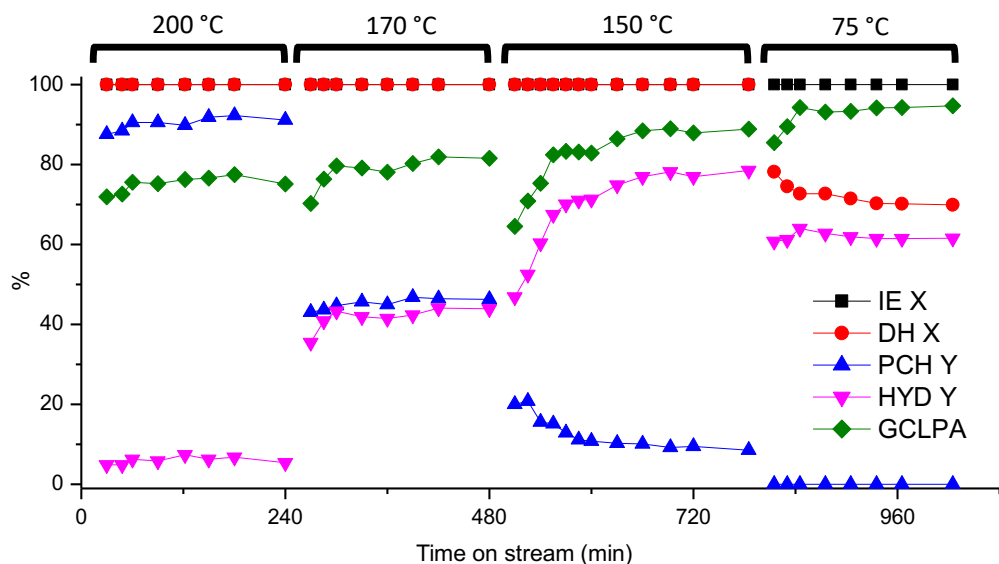


Fig 10. Continuous reactor results for HDO of isoeugenol with catalyst Pt4Re4/Sib, performed at different temperatures, 30 bar H₂ and the liquid flowrate 0.5 mL/min. Isoeugenol conversion (IE X), dihydroeugenol conversion (DH X), propylcyclohexane yield (PCH Y), 2-methoxy-4-propylcyclohexanol yield (HYD Y) and the liquid phase mass balance (GCLPA).

As it can be seen from Fig 10, isoeugenol conversion (IE X) remained at 100% for all temperatures tested. Conversion of dihydroeugenol (DH X) remained at 100 % at temperatures 200 – 150 °C, however, at 75 °C it decreased to ca. 70%. The highest propylcyclohexane yield (PCH Y) was obtained at 200 °C (ca. 90%), concomitant with the lowest mass balance in the liquid phase (ca. 75%).

PCH yield decreased along with the temperature increase, from ca. 10% at 150 °C to ca. 50% at 170 °C. At 75 °C the propylcyclohexane yield was <1%, indicating absence of deoxygenation at this temperature.⁵²

The opposite results were recorded for the formation of 2-methoxy-4-propylcyclohexanol (HYD). At 200 °C very low amounts of HYD were obtained (HYD yield of 5%), while at 75 °C it was the main product (ca. 60%). These results indicate that hydrogenation of the aromatic ring takes place efficiently at low temperatures, which is consistent with thermodynamics.⁵³ Consistent with the literature results, E_a for hydrogenation of the aromatic ring is lower than E_a for deoxygenation.⁵⁴

Deactivation was not observed even after 17 h of time on stream, as conversion and the yield remained constant.

Activated carbon (Publication IV)

The results for all catalysts supported on activated carbon are presented in Fig 11. Monometallic catalysts displayed the lowest dihydroeugenol (DH) conversion and propylcyclohexane (PCH) yields. Such low values are consistent with those reported in the literature for HDO using monometallic catalysts supported on carbon-type materials.⁵⁵

Bimetallic catalysts exhibited considerably higher catalytic activity, achieving complete DH conversion after 4 h of the reaction time and PCH yield exceeding 30%. The lowest PCH yield was obtained with Pt2.5Re1.5/AC (ca. 35%), the catalyst with the highest Pt:Re ratio. On the other hand, Pt2.5Re12.5/AC displayed the highest yield of PCH (ca. 99%) and the maximum mass balance in the liquid phase (GCLPA) value (77%), indicating almost complete conversion of isoeugenol (IE) into PCH at 4 h. GCLPA values for PtRe/AC catalysts indicate that some products were distributed either in the gas phase or in the liquid phase as higher-molecular weight polymers; neither were quantified.

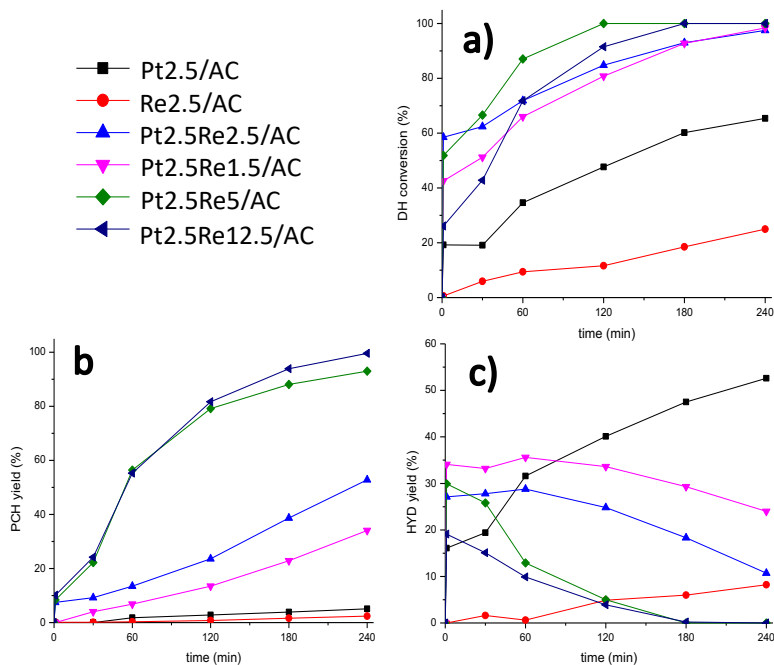


Fig 11. a) Conversion of dihydroeugenol, b) yield of propylcyclohexane, c) yield of hydrogenated intermediate for catalysts supported on activated carbon.

The results indicate that a lower Pt:Re ratio results in higher a HDO activity. Furthermore, selectivity towards propylcyclohexane, normalized at 60% DH conversion, displayed the following trend for PtRe/AC catalysts: Pt2.5Re12.5/AC > Pt2.5Re5/AC > Pt2.5Re2.5/AC > Pt2.5Re1.5/AC, indicating that Re plays an important role for hydrodeoxygenation. These results are consistent with the results from EXAFS and XANES, as the presence and elevation of ReOx species content resulted in a decrease in the metal particle sizes and, therefore, better dispersion and higher HDO activity, in line with literature.^{56,57}

A linear increase in activity can be observed proportional to the total amount of Pt and Re (Fig 12a), with monometallic catalysts displaying the lowest activity, and Pt2.5Re12.5/AC the highest. As expected, an increase in the amount of the active phase allows an increase in activity, however, a lower Pt/Re ratio (Fig 12b) also resulted in higher activity and selectivity, leading to a conclusion that both Pt and Re are indispensable to carry out the reaction.

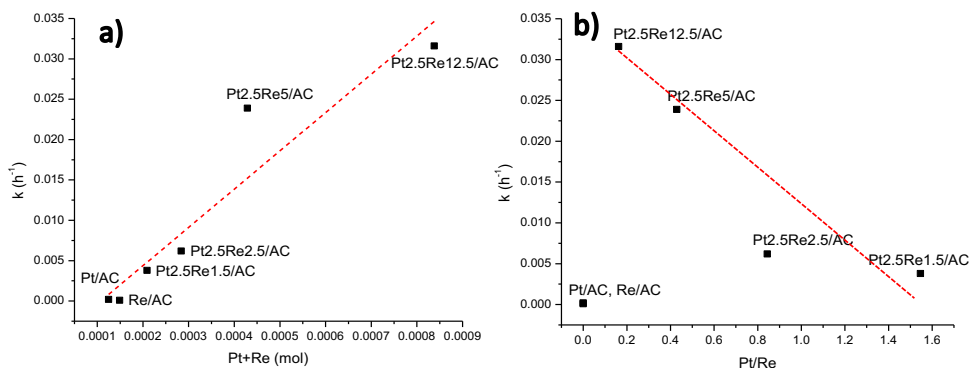


Fig 12. The rate constant as a function of a) the sum of Pt and Re content (mol), b) the Pt/Re molar ratio.

A similar trend as in Fig 12b can be observed in Fig 13, where selectivity towards PCH decreases with an increase of the Pt/Re ratio. For Pt2.5Re12.4/AC and Pt2.5Re5/AC catalysts, activity, and selectivity towards the deoxygenated product increased, indicating that the deoxygenation route was promoted.

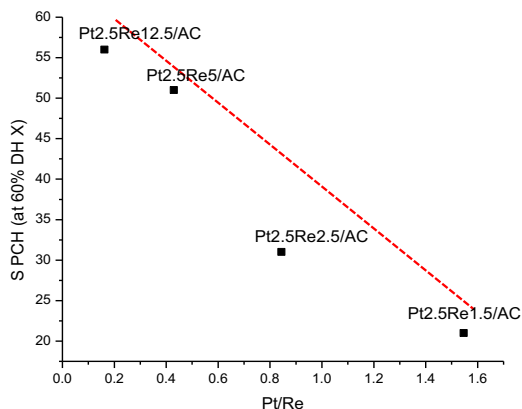


Fig 13. Propylcyclohexane selectivity (at 60% dihydroeugenol conversion) as a function of the Pt/Re molar ratio.

XAS results revealed the presence of ReOx species in catalysts with higher Re loadings. This, in connection to smaller metal particle sizes observed by TEM, could explain the enhanced activity and selectivity towards the deoxygenated product for Pt2.5Re5/AC and Pt2.5Re12.5/AC catalysts. Metallic Pt and ReOx have a bifunctional effect when both are present, promoting deoxygenation or breakage of the C-O bond. Similar findings reported that an oxophilic oxide in close proximity of a metal particle activates the C-O bond, promoting deoxygenation.⁵⁸

3.1.3. Conclusions – carbon supported catalysts

Hydrodeoxygenation of isoeugenol was achieved using two series of bimetallic platinum-rhenium catalysts, at temperatures ranging between 150–270 °C under 30 bar of hydrogen in both batch and continuous reactors.

It was observed that monometallic platinum and rhenium catalysts displayed overall low activity for deoxygenation, however a considerable increase in conversion and yield was obtained when both metals were present.

Bimetallic catalysts containing 4 wt% platinum and 4 wt% of rhenium, supported on mesoporous Sibunit carbon, gave complete conversion, and resulted in high propylcyclohexane yield (84%) at 250 °C. A granulated form of the same catalyst was tested in a continuous trickle-bed reactor, achieving complete conversion (100%) and a high yield of propylcyclohexane (ca. 90%) at 200 °C.

An in-depth study of the effect of the Pt:Re ratio on deoxygenation activity was carried out using bimetallic Pt-Re catalysts supported on microporous activated carbon. The results showed that higher Re loadings resulted in smaller metal particles, and therefore, a higher dispersion. Similarly, as with Sibunit catalysts, the presence of Re oxide species was vital for deoxygenation.

Complete conversion of dihydroeugenol was observed for all catalysts, however, higher yields of propylcyclohexane were obtained when using catalysts with a higher Re content. The catalyst with a Pt/Re atomic ratio of 1/5 was the most active one, achieving 99% propylcyclohexane yield at 4 h and 77% mass balance closure in the liquid phase.

3.2. Bifunctional Pt supported on zeolites and the binder

3.2.1. Catalyst characterization

Powder catalysts

Morphological differences among the zeolites, Bindzil and the mixture of the zeolite and Bindzil can be observed using SEM (Fig 14). H-Beta-25 particles are much smaller (ca. 20-250 nm, Fig 14a) than those of H-Beta-300 (ca. 300-1000 nm, Fig 14b). On the other hand, Bindzil displays mostly spherical particles (ca. 50-200 nm, Fig 14c). For zeolite and Bindzil mixtures (Fig 14d and 14e), it can be observed that the zeolitic particles are surrounded by the spherical Bindzil particles.

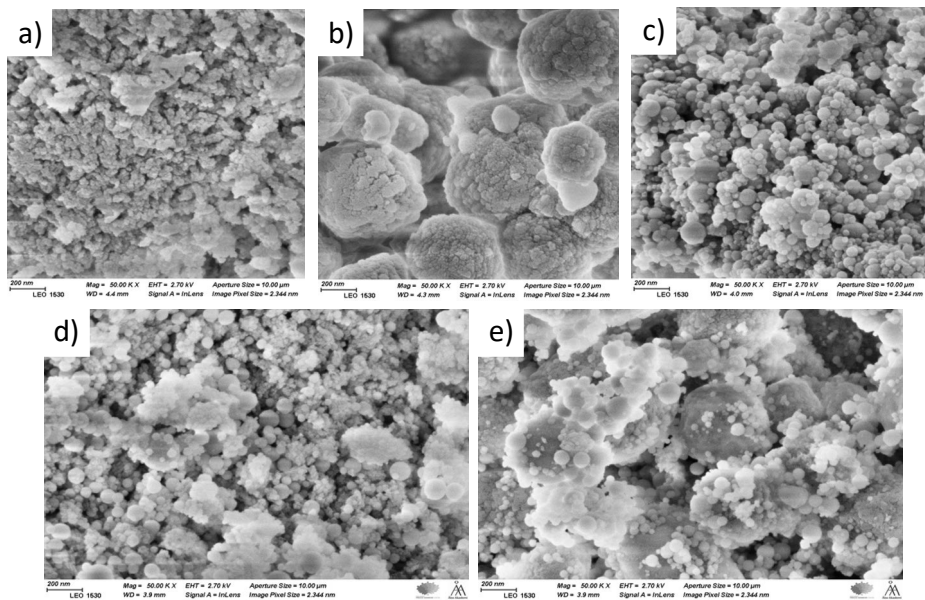


Fig 14. SEM images of a) H-Beta-25, b) H-Beta-300, c) Bindzil, d) H-Beta-25+Bindzil and e) H-Beta-300+Bindzil.

A summary of the metal loadings, metal particle sizes and the textural properties of the catalysts and neat supports is presented in Table 6.

Table 6. Metal loadings, metal particle sizes and textural properties of supports and catalysts.

Catalyst	Pt loading (wt%)	Metal particle size (nm)	Textural characteristics		
			SSA (m ² /g)	V _Σ (cm ³ /g)	V _{MP} (cm ³ /g)
H-Beta-25	-	-	638	0.36	0.31
H-Beta-300	-	-	617	0.29	0.19
Bindzil	-	-	154	0.30	-
Pt2/B25 ZB	1.9	4.2	490	0.31	0.13
Pt2/B25 Z	1.8	4.3	466	0.29	0.11
Pt2/B25 B	1.9	4.7	493	0.32	0.14
Pt2/B300 ZB	1.7	4.4	459	0.23	0.15
Pt2/B300 Z	1.8	4.2	443	0.22	0.14
Pt2/B300 B	1.8	4.6	467	0.26	0.15
Pt2/B300 ZB (spent)	n.d.	4.7	432	0.20	0.12
Pt2/B300 Z (spent)	n.d.	4.8	421	0.18	0.11
Pt2/B300 B (spent)	n.d.	5.3	425	0.21	0.13
Pt2/ EZB (fresh)	2.0	2.9	460	0.64	0.19
Pt2/ EZ (fresh)	2.3	3.9	488	0.67	0.19
Pt2/ EB (fresh)	1.7	5.5	498	0.74	0.20
Pt2/ EZB (spent)	2.0	2.9	317	0.44	0.11
Pt2/ EZ (spent)	2.3	3.9	228	0.28	0.10
Pt2/ EB (spent)	1.7	5.5	323	0.38	0.13

n.d. = not determined

The powder catalysts exhibited specific surface areas in the range 450 - 500 m²/g, as well as total pore volume (V_Σ) of 0.2-0.3 cm³/g and a pore diameter of 0.6 nm.

Extrudate catalysts displayed similar SSA values, in the range of 460 – 498 m²/g, as well as the total pore volume (V_Σ) of ca. 0.7 cm³/g and a micropore volume (V_{MP}) of ca. 0.2 cm³/g. A comparison of the different types of pristine materials, as well as for both series of powder catalysts is presented in Fig 15.

A decrease in the textural properties, specifically noticeable for spent extrudate catalysts, could be caused by blocking of zeolite micropores by coke formed during the reaction, as spent Pt/EZ displayed the lowest surface area (228 m²/g) among the tested catalysts, which correlated with the TPO results.

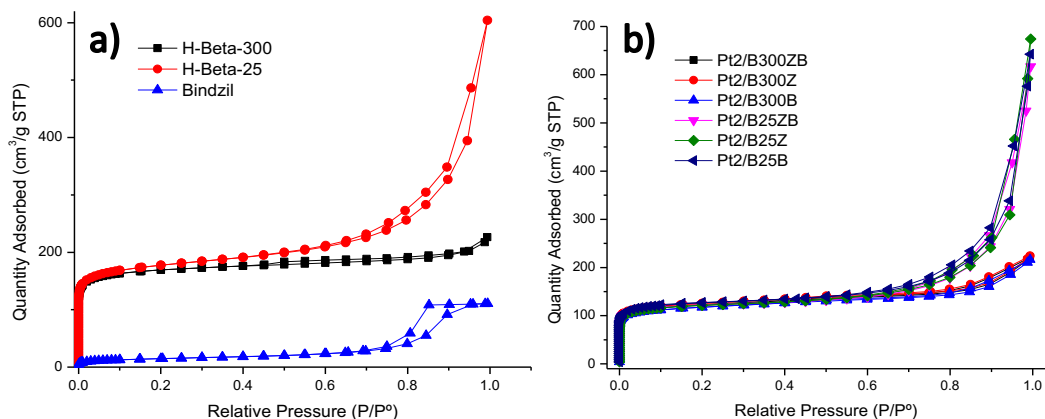


Fig 15. a) Adsorption-desorption isotherms of zeolites H-Beta-300, H-Beta-25 and Bindzil, b) adsorption-desorption isotherm comparison of both series of catalysts.

As presented in Fig 15, both zeolites displayed type I isotherms, characteristic of microporous materials. Zeolite H-Beta-25 exhibits an H3 hysteresis, while Bindzil displays a type IV isotherm and hysteresis H2, due to mesoporosity.⁴⁰

The catalyst metal loadings obtained by ICP were close to the nominal value of 2 wt%. All powder catalysts exhibited an average metal particle size in the range of 4-5 nm, while metal particle sizes for extrudates (Fig 16) were in the range of 2.9 – 5.5 nm.

Metal particle sizes were larger for the catalyst where Pt was deposited only on Bindzil in the case of both powder and extrudates, which could be due to weaker interactions between the non-acidic binder and the Pt particles, leading to agglomeration. Platinum particles were smaller for the catalyst where Pt was deposited on both zeolite and binder, resulting in a better distribution of the metal.

A slight increase in the metal particle size was observed for spent catalysts, indicating that agglomeration occurred during the catalytic reactions.

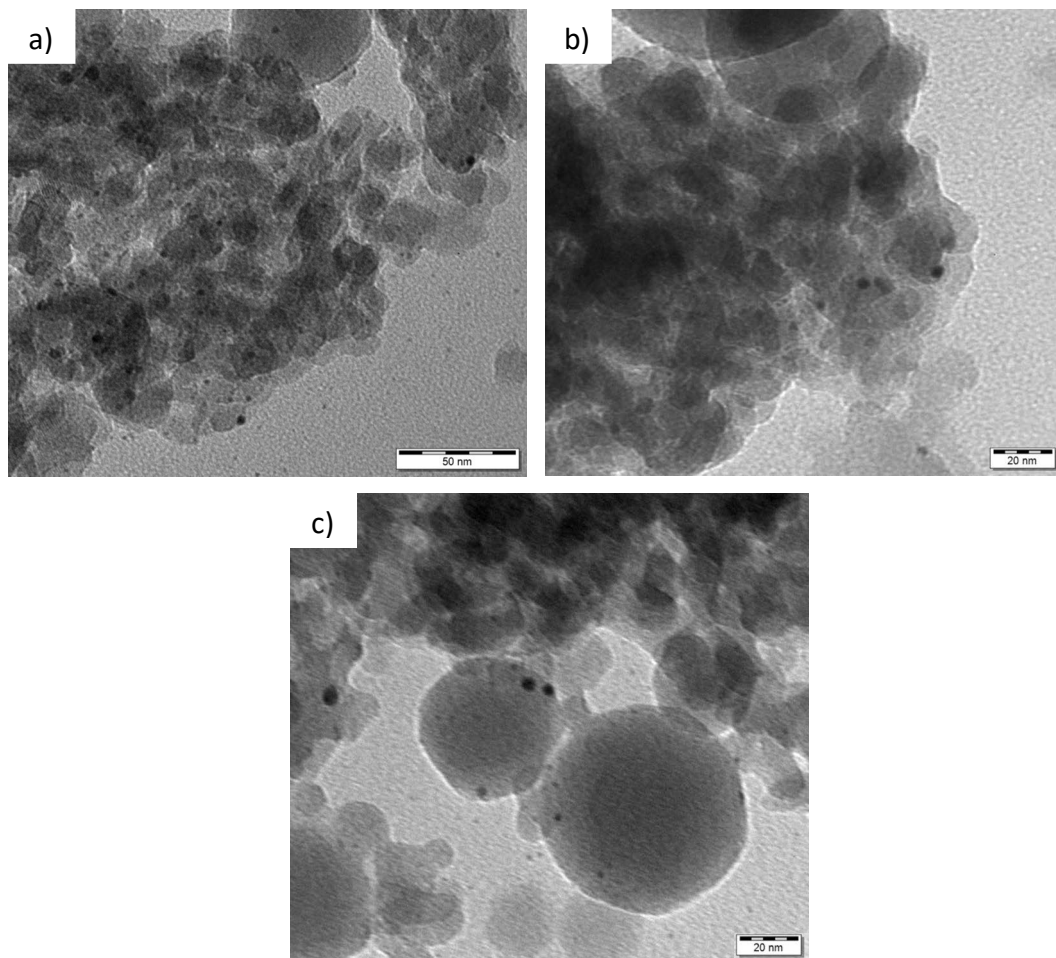


Fig 16. TEM micrographs of fresh a) Pt₂/EZB, b) Pt₂/EZ and c) Pt₂/EB catalysts.

Pyridine FTIR was used to measure the acid site amount and strength of the catalysts and pure supports, with the results presented in Table 7.

Table 7. Support and catalyst acidity determined by pyridine FTIR.

Catalyst	Brønsted acid sites ($\mu\text{mol/g}$)*			Lewis acid sites ($\mu\text{mol/g}$)*			Total acid sites ($\mu\text{mol/g}$)		
	W	M	S	W	M	S	BAS	LAS	Total
H-Beta-25	67	33	129	26	5	6	229	37	266
H-Beta-300	7	29	19	4	1	1	55	6	61
Bindzil	12	0	0	3	0	0	12	3	15
Pt2/B25 ZB	44	10	4	12	4	2	58	18	76
Pt2/B25 Z	51	4	8	7	2	4	63	13	76
Pt2/B25 B	61	4	28	8	1	11	93	20	113
Pt2/B300 ZB	9	2	0	5	3	0	11	8	19
Pt2/B300 Z	6	2	0	6	0	0	8	6	14
Pt2/B300 B	10	8	0	13	2	0	18	15	33
Pt2/ EZB ^a	62	2	3	1	1	0	67	2	69
Pt2/ EZ ^a	42	0	1	3	0	0	43	3	46
Pt2/ EB ^a	49	5	7	1	1	0	61	2	63

* Desorption of pyridine at 250, 350, and 450 °C was done to determine the weak, medium, and strong acid sites, respectively; measurements were taken at 100 °C.

^a values taken from Ref. ⁵⁹

As expected, neat H-Beta-25 displayed the highest acidity, over 4 times higher than H-Beta-300. On the other hand, Bindzil contained the lowest amount of acid sites. Addition of Bindzil to the catalyst mixture resulted in a decrease in the overall acidity.

Likewise, powder catalysts containing H-Beta-25 were more acidic than those with H-Beta-300. For powder catalysts a larger amount of acid sites was obtained when Pt was located only on the binder (Pt/BXX**B**), indicating that deposition of the metal decreased the zeolite acidity, as previously reported in the literature.⁶⁰

For extrudates, catalyst Pt2/EZB displayed the most acid sites, followed by Pt2/EB. Pt2/EZ catalyst where Pt was located only on the zeolite, exhibited the lowest acidity.

Crush tests were performed to determine the mechanical strength of the extrudates. The mechanical strength results, as well as the peak areas for the TPR of the fresh catalysts and TPO of spent ones are given in Table 8.

Table 8. Mechanical strength of extrudates, TPR areas for fresh catalysts and TPO areas of spent catalysts.

Catalyst	Mechanical strength (MPa) ^a		TPR peak area for fresh catalyst (a.u.) ^b	TPO peak area for spent catalyst (a.u.) ^b
	Vertical	Horizontal		
Pt2/EZB	4.4	1.2	753	106
Pt2/EZ	3.8	1.2	324	157
Pt2/EB	2.9	0.7	311	120

^a Values taken from Ref. ⁵⁹

^b Values normalized by mass of the catalyst.

The mechanical strength for the extrudates is within the range for similar types of catalysts reported in the literature.^{61–63}

The catalyst with the highest mechanical strength was Pt2/EZB (4.4 and 1.2 MPa in the vertical and horizontal positions, respectively), where Pt was located on both the zeolite and the binder. The catalyst with the lowest mechanical strength was Pt2/EB (2.9 MPa for the vertical and 0.7 MPa for the horizontal position), which could be caused by a larger intracrystalline void space between the particles.⁶⁴

TPO peak areas presented in Table 8 indicate that Pt2/EZB catalyst had the lowest formation of carbonaceous species after the reaction. On the other hand, Pt2/EZ exhibited larger amounts of carbon deposits, which could negatively impact its catalytic activity, as seen in Fig 19. Additionally, these results were also reflected in a noticeable decrease of the textural properties, as determined by nitrogen physisorption (Table 6).

Different types of carbonaceous deposits on spent extrudate catalysts were observed with TPO. The highest peak intensity for Pt2/EZB and Pt2/EB was obtained at ca. 400 °C, while for Pt2/EZ it was shifted towards 450 °C. A peak at ca. 200 °C is ascribed to reaction intermediates, a second peak at 350 - 400 °C can be associated with side polymeric compounds or active carbon species,⁶⁵ while a peak closer to 600 °C could be assigned to graphite and/or amorphous carbons.⁶⁶

3.2.2. Catalytic activity

Powder catalysts (publication V)

The corresponding graphs for dihydroeugenol (DH) conversion and propylcyclohexane (PCH) yield for both series of powder catalysts are displayed in Fig 17.

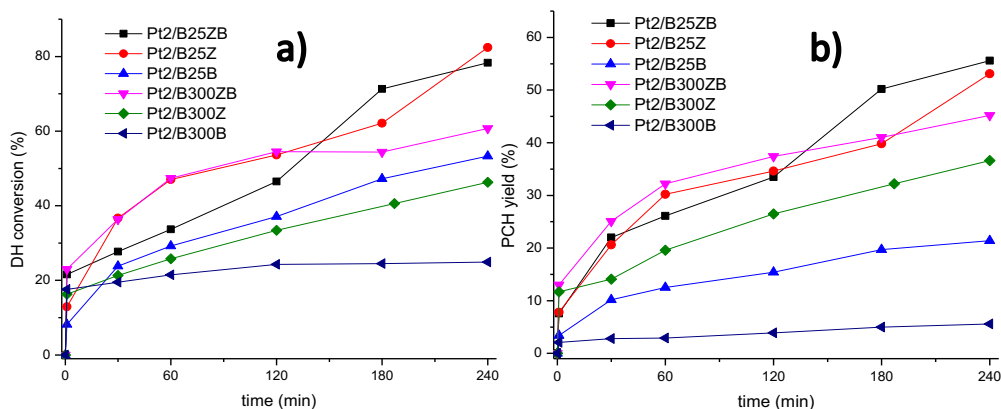


Fig 17. Transformations of isoeugenol at 200 °C and 30 bar of H₂ a) dihydroeugenol conversion and b) propylcyclohexane yield.

DH conversion was higher for the Pt2/B25XX series (78 – 53%) than for Pt2/B300XX (61 – 25%). Deactivation could also be observed for Pt2/B300B catalyst, as DH conversion did not increase considerably after the initial period.

The most active catalysts were those supported only on zeolite or on both zeolite and binder (DH conversion of ca. 80% for Pt2/B25ZB and Pt2/B25Z, and 61% for Pt2/B300ZB). This indicates that proximity between the acid sites and the metal particles is beneficial for the reaction giving improved activity.

The catalysts containing more acidic zeolite H-Beta-25 displayed higher conversion and the yield of propylcyclohexane (ca. 80% conversion and above 50% yield for Pt2/B25ZB and Pt2/B25Z), while the catalysts with H-Beta-300 zeolite exhibited higher selectivity towards propylcyclohexane (over 90% at 40% DH conversion for catalyst Pt2/B300Z). Additionally, the Pt2/B300ZB catalyst afforded a relatively high PCH yield (45%), comparable to that of catalysts containing H-Beta-25.

Propylcyclohexane (PCH) yields were higher in both catalysts of type A (PCH yield of 56% for Pt2/B25**ZB**, and 45% for Pt2/B300**ZB**), which could also be caused by a higher dispersion of the metal particles, as in this type of catalyst, Pt was located on both zeolite and Bindzil.

When comparing rate constants to the total amount of acid sites (Fig 18a) it can be observed that the Pt2/B25XX series displays higher conversion. However, the Pt2/B300XX series displays a similar yield of propylcyclohexane (Fig 18b).

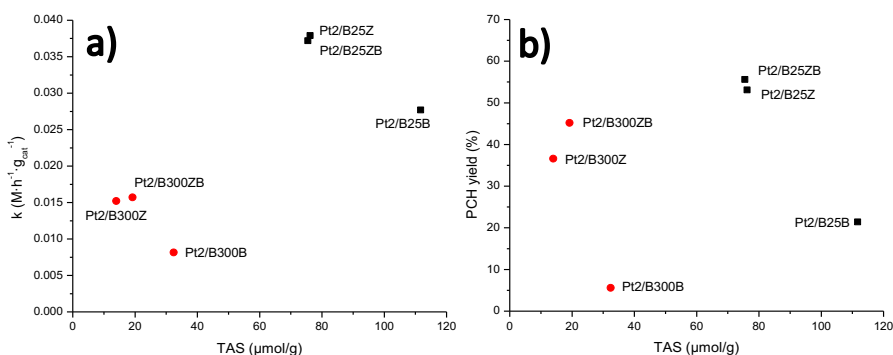


Fig 18. Transformations of dihydroeugenol at 200 °C and 30 bar of H₂: a) rate constants and b) propylcyclohexane yield vs. total acid sites.

Our findings suggest that proximity between two types of active sites is necessary for higher catalytic performance. Additionally, high acidity was not necessary to obtain a similar yield of the desired deoxygenation product.

Extrudates (publication VI)

Time-on-stream behavior for dihydroeugenol (DH) conversion, propylcyclohexane (PCH) yield and GCLPA is displayed in Fig 19. All the extrudate catalysts displayed ca. 50% DH conversion at 150 °C and 30 bar of H₂, under liquid and gas flow of 0.5 mL/min and 40 mL/min, respectively. The catalyst with the highest conversion was Pt2/EZB (53%), while a somewhat lower conversion was recorded for Pt2/EB (49%).

Additional differences between the catalysts can be seen in the propylcyclohexane yield, which was the highest for the former catalyst (39%), while the lowest yield was obtained for Pt2/EB (30%).

A less prominent decline in the catalytic performance for Pt2/EZB could be related to a more stable performance of Pt nanoparticles and their proximity with acid sites.

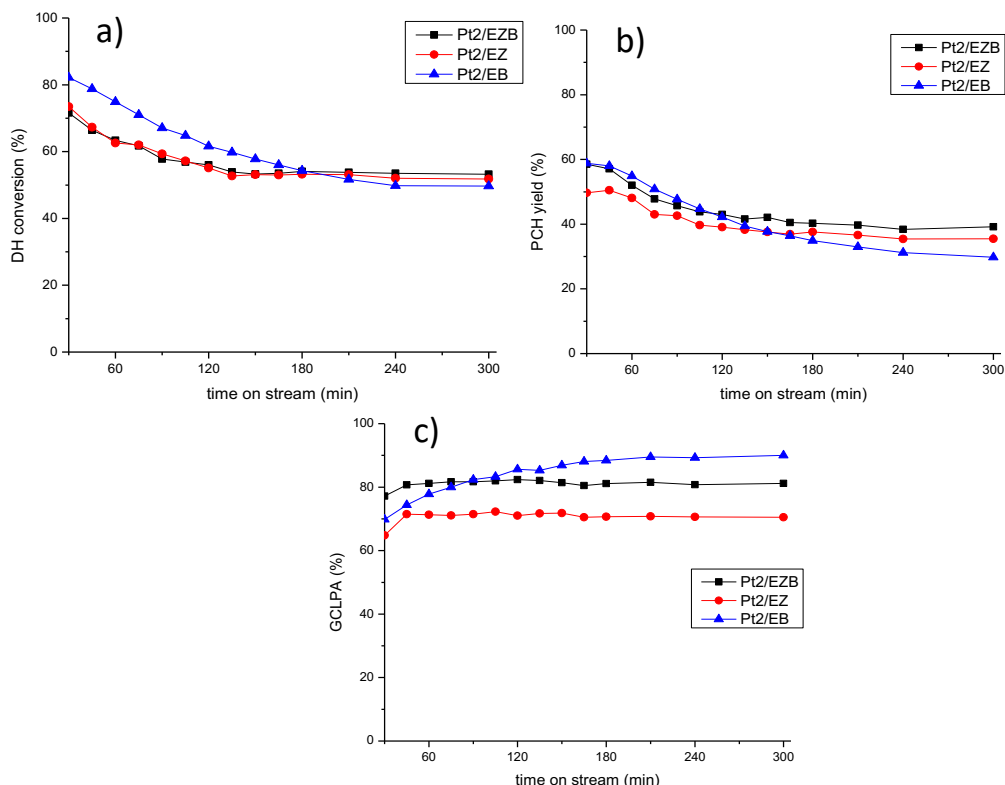


Fig 19. Catalytic activity of Pt/H-Beta-25 and Bindzil extrudates in HDO of isoeugenol at 150 °C and 30 bar of H₂, liquid and gas flows of 0.5 mL/min and 40 mL/min, respectively a) dihydroeugenol conversion, b) propylcyclohexane yield and c) GCLPA as a function of time on stream.

Analogously, as observed for the powder catalysts in batch operation, activity was also improved in continuous reactor when Pt was located on the zeolite, and not on the non-acidic Bindzil. In other words, closer proximity between the acid sites of the zeolite and the platinum particles was beneficial for catalytic performance. In addition,

minimal solvent cracking was observed under the tested reaction, as formation of the cracking-related products for *n*-dodecane was below 0.1%.

Catalyst acidity did not seem to directly influence the yield of propylcyclohexane, as the catalyst with the lowest acidity (Pt2/EZ, total acid sites = 46 $\mu\text{mol/g}$, Table 7) displayed an intermediate PCH yield (35%), however, acidity influenced the side reactions, as the same spent catalyst (Pt2/EZ spent) displayed a larger amount of carbonaceous deposits, as can be seen in TPO (Table 8).

TOF values were calculated considering conversion of dihydroeugenol and platinum dispersion as determined from the Pt particle sizes. A high TOF obtained for Pt2/EB catalyst (21.6 h^{-1}) could be explained by the structure-sensitive nature of the hydrogenolysis reaction, where larger Pt clusters result in a higher activity.⁶⁷

This is further illustrated in Fig 20, where a clear trend between TOF and platinum particle size can be observed. A potential explanation for this effect is related to a larger space available on larger cluster to accommodate a bulky reagent. Analogous dependences have been reported in the literature for transformations of bulky organic compounds.^{68,69}

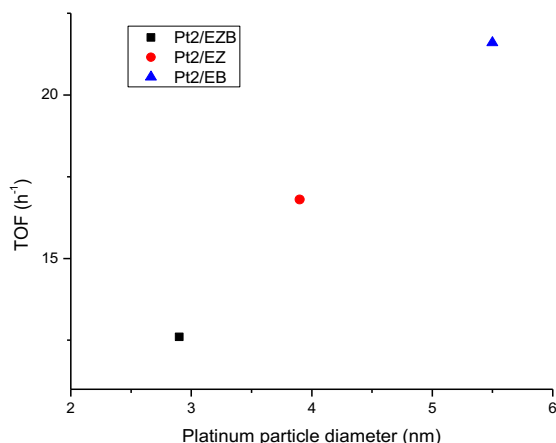


Fig 20. Dependence of TOF on the platinum particle size.

The effect of the reaction temperature on hydrodeoxygenation of isoeugenol was tested using Pt2/EZB catalyst. These reactions were performed in the same trickle-bed reactor, varying the temperature between 65 and 200 $^{\circ}\text{C}$. As presented in Fig 21, DH conversion decreased accordingly with the reaction temperature, GCLPA values decreased between 200 and 150 $^{\circ}\text{C}$ (from 61% to 51%), despite the same conversion,

which could be a first indication of catalyst deactivation. GCLPA increased after lowering further the temperature from 100 °C (58%) to 75 and 65. °C (ca. 71%).

The yield of propylcyclohexane was the highest at 200 °C (80%) decreasing considerably at lower temperature, being at its lowest (5 and 3%) at 75 and 65 °C, indicating that hydrogenation of the aromatic ring was predominant over deoxygenation. This resulted in an increase in the yield of the hydrogenated product, 2-methoxy-4-propylcyclohexanol.

Returning to the initial temperature of 200 °C after testing catalytic activity at lower temperature confirms that deactivation of the catalyst took place during the testing, as both GCLPA and PCH yield decreased ca. 10% each.

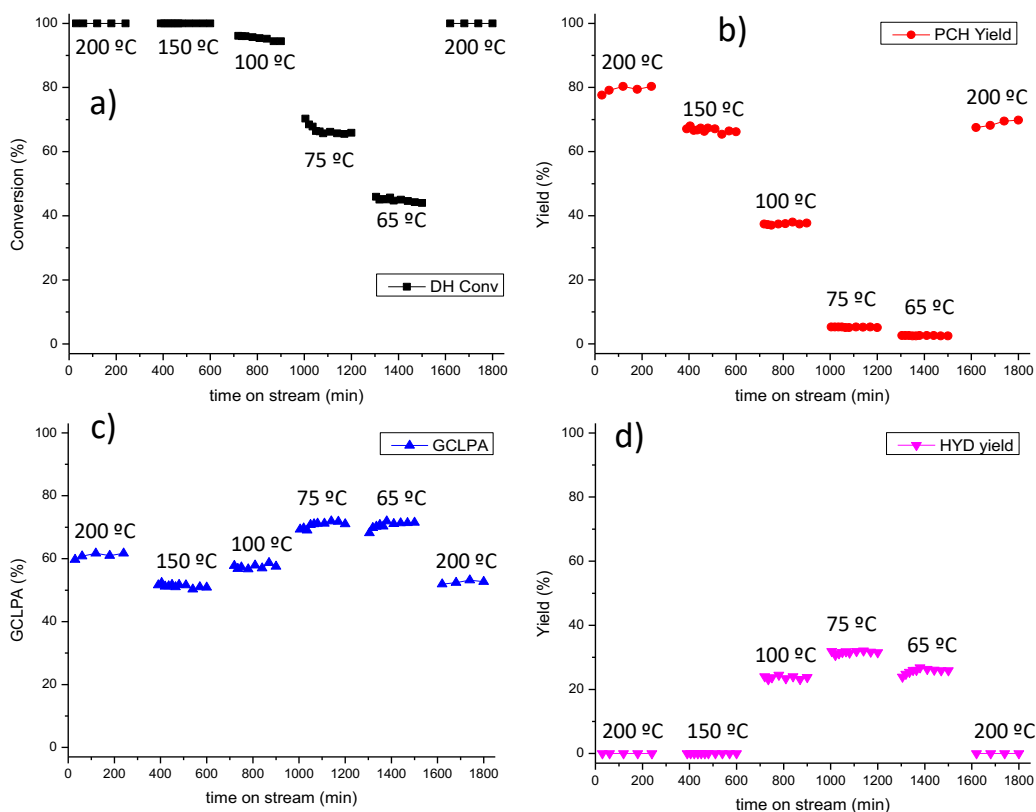


Fig 21. Transformations of isoeugenol using Pt2/EZB in a continuous reactor at different temperatures, 30 bar of H₂ liquid flow of 0.5 mL/min and gas flow of 40 mL/min. a) dihydroeugenol conversion, b) propylcyclohexane yield, c) GCLPA and d) hydrogenated intermediate yield as a function of time on stream.

The catalyst effectiveness factor was calculated to determine the extent of mass transfer limitations when using extrudates, employing the following equation:

$$\eta_{eff} = \frac{r_{extrudates}}{r_{powder}} \quad (4)$$

Where η_{eff} is the catalyst effectiveness factor, and $r_{extrudates}$ and r_{powder} are the rates of formation of propylcyclohexane in the continuous and batch reactors, respectively.

Eq. (4) implicitly assumes, that the batch reactor data were obtained in the kinetic regime, which is justified by efficient stirring and small catalyst particle sizes applied in that study. The rates were determined at 200 °C for Pt2/EZB extrudates and Pt2/B25ZB powder. The catalyst effectiveness factor calculated from Eq. (1) was $\eta_{eff} = 0.17$, indicating that there are significant mass transfer limitations, as expected for shaped catalysts in a trickle bed reactor.

3.2.3. Conclusions – zeolite + binder supported catalysts

Catalysts comprised of 69 wt% of zeolite H-Beta-25 or H-Beta-300, 29 wt% of bindzil as a binder and 2 wt% of platinum displayed high activity in the hydrodeoxygenation of isoeugenol in both batch and continuous trickle-bed reactors under 30 bar of hydrogen at temperatures in the 65 – 200 °C range.

The effects of the binder (bindzil) addition, acidity of the zeolite and the metal location, were studied. Addition of platinum and binder resulted in a decrease of the surface area and the total amount of acid sites when compared to the unmodified zeolite. The location of the platinum was varied depending on its deposition, whether it was on the zeolite, the binder or both. These differences were reflected considerably in the catalytic activity. Overall, the catalysts where Pt was located closer to the acid sites (being deposited on only zeolite or both zeolite and the binder) displayed higher conversion and propylcyclohexane yield, while deposition of platinum on the binder gave the lowest activity.

For powder catalysts tested in a batch reactor, the highest selectivity to propylcyclohexane (92%) and mass balance closure in the liquid phase (85%) was achieved when platinum was located only on H-Beta-300, while the highest conversion of dihydroeugenol of 82% and the yield of propylcyclohexane of 53%, simultaneously with lower GCLPA, were obtained for the catalyst where platinum was located on both zeolite H-Beta-25 and the binder.

Extrudate catalysts comprising 69 wt% of zeolite H-Beta-25, 29 wt% of Bindzil and 2 wt% of platinum displayed similar conversion values among each other (ca. 50%) in a continuous reactor. However, a higher propylcyclohexane yield was obtained when Pt was present on both zeolite and the binder (39%), while deposition of platinum on the non-acidic binder resulted in lower activity (30%). Minimal solvent cracking (<0.1%) was observed under these conditions.

Catalyst stability and the effect of reaction temperature (65 - 200 °C) was studied using the catalyst where platinum was located on both zeolite and the binder with the total time on stream of ca. 30 h. Minor deactivation of ca. 10% was observed when comparing with the initial reaction at 200 °C. At 65 and 75 °C the hydrogenation of the

aromatic ring dominated over deoxygenation. However, complete conversion and high propylcyclohexane yields were achieved at 200 and 150 °C (80 and 66%, respectively). Determination of the catalyst effectiveness factor (0.17) and an apparent activation energy of 14.7 kJ/mol demonstrated significant mass transfer limitations.

3.3. Catalyst comparison

A comparison of the catalytic activity of the main catalysts used in this thesis is presented in Table 9.

Table 9. Comparison of the catalytic activity for all catalysts tested in batch reactor.

Catalyst series	Entry	Catalyst	T (°C)	DH X (%) ^a	PCH Y (%) ^b	HYD Y (%) ^c	GCLPA (%) ^d	Publication
I	1	Pt4/Sibunit	250	<1	<1	<1	99	[III]
	2	Pt4Re4/Sib	250	98	84	0	67	[III]
	3	Pt6Re2/Sib	250	100	66	0	62	[III]
	4	Pt2Re6/Sib	250	100	81	0	62	[III]
II	5	Pt2.5/AC	250	65	5	53	94	[IV]
	6	Re2.5/AC	250	25	2	8	85	[IV]
	7	Pt2.5Re1.5/AC	250	98	34	24	53	[IV]
	8	Pt2.5Re2.5/AC	250	98	53	11	54	[IV]
	9	Pt2.5Re5/AC	250	100	93	0	71	[IV]
	10	Pt2.5Re12.5/AC	250	100	99	0	77	[IV]
III	11	Pt2/B25 ZB	200	78	56	0	68	[V]
	12	Pt2/B25 Z	200	82	53	0	62	[V]
	13	Pt2/B25 B	200	53	21	0	66	[V]
	14	Pt2/B300 ZB	200	61	45	0	78	[V]
	15	Pt2/B300 Z	200	46	37	0	85	[V]
	16	Pt2/B300 B	200	25	6	0	83	[V]

^a Conversion of dihydroeugenol.

^b Yield of propylcyclohexane.

^c Yield of 2-methoxy-4-propylcyclohexanol.

^d Gas Chromatography Liquid Phase Analysis, a mass balance estimation for the liquid phase.

Comparing the results obtained in a batch reactor, it can be initially observed that all bimetallic carbon-supported catalysts (Series I and II, entries 2 - 4, 7 - 10) exhibited dihydroeugenol conversion higher than zeolite-supported ones (Series III, entries 11 - 16), which is obviously related to a higher reaction temperature.

All bimetallic catalysts (entries 2 – 4, 7 – 10) were much more active than monometallic ones (entries 1, 5 and 6) in terms of dihydroeugenol conversion and propylcyclohexane yield, highlighting the importance of both metals for hydrodeoxygenation to take place.

Bimetallic catalysts with a higher Re loading supported on activated carbon (Series II, entries 9, 10) displayed higher yield of propylcyclohexane than all catalysts supported

on mesoporous carbon Sibunit (Series I, ca. 95% vs. ca. 85%), which could be due to a higher total Re loading, as well as a higher surface area in the latter series.

Higher 2-methoxy-4-propylcyclohexanol yields were observed for PtRe/AC catalysts with higher Pt loading, Pt_{2.5}Re_{1.5}/AC and Pt_{2.5}Re_{2.5}/AC (entries 7 and 8), indicating that they were active in hydrogenation of the aromatic ring, but not as active for deoxygenation as catalysts with higher Re loadings.

A considerable benefit of zeolite-based catalysts (Series III) was their high activity at lower temperatures and lower yields of 2-methoxy-4-propylcyclohexanol, indicating that hydrodeoxygenation was more effective for these catalysts. The best performing catalysts for this series, Pt₂/B25ZB (entry 11) displayed similar propylcyclohexane yield as Pt_{2.5}Re_{2.5}/AC (entry 8, 53% vs 56%), despite 50 °C lower reaction temperature. Furthermore, cracking of the solvent was avoided by using these catalysts at 200 °C.

An additional advantage of the zeolite-based catalysts over carbon-supported ones is the ability to regenerate them by burning off carbonaceous deposits through calcination.

Table 10. Comparison of the catalytic activity for catalysts tested in the continuous reactor.

Entry	Catalyst	T (°C)	DH X (%) ^a	PCH Y (%) ^b	HYD Y (%) ^c	GCLPA (%) ^d	Publication
1	Pt4Re4/Sib granules	200	100	90	7	76	[III]
2	Pt4Re4/Sib granules	170	100	46	44	80	[III]
3	Pt4Re4/Sib granules	150	100	10	78	85	[III]
4	Pt4Re4/Sib granules	75	70	0	61	94	[III]
5	Pt2/EZB extrudates	150	53	39	0	81	[VI]
6	Pt2/EZ extrudates	150	51	35	0	70	[VI]
7	Pt2/EB extrudates	150	49	30	0	90	[VI]
8	Pt2/EZB extrudates	200	100	80	0	61	[VI]
9	Pt2/EZB extrudates	150	100	66	0	51	[VI]
10	Pt2/EZB extrudates	100	95	38	24	58	[VI]
11	Pt2/EZB extrudates	75	65	5	32	72	[VI]
12	Pt2/EZB extrudates	65	44	3	26	71	[VI]
13	Pt2/EZB extrudates	200	100	70	0	53	[VI]

^a Conversion of dihydroeugenol.

^b Yield of propylcyclohexane.

^c Yield of 2-methoxy-4-propylcyclohexanol.

^d Gas Chromatography Liquid Phase Analysis, a mass balance estimation for the liquid phase.

Comparing the results obtained in the continuous reactor, between Pt4Re4/Sib granules and Pt/E, it can be concluded that dihydroeugenol conversion is similar at the corresponding temperatures (65% for Pt2/EZB and 70% for Pt4Re4/Sib granules at 75 °C, entries 4 and 11). However, several differences are evident, especially in GCLPA values as well as PCH and HYD yields. GCLPA values were higher when using the carbon-supported catalyst, which could be due to its lower acidity, resulting in less prominent side by-product formation compared to zeolite-based catalysts. In addition, propylcyclohexane yield was higher for Pt4Re4/Sib granules than for Pt2/EZB at 200 °C (90% vs. 80%, entries 1 and 8), however, at 150 °C, all Pt/E catalysts exhibited higher PCH yields (ca. 45% vs 10%, entries 5 – 7 and 3). Formation of the

hydrogenated intermediate is also higher for the bimetallic PtRe catalyst throughout the whole temperature range (7% – 61%), indicating that deoxygenation was not as prevalent at temperatures below 200 °C.

4. Conclusions and Future Perspectives

Hydrodeoxygenation of isoeugenol was investigated using a series of bifunctional catalysts in both batch and continuous reactors under a variety of conditions. Isoeugenol was studied as a model compound for lignin, due to its similarities to lignin's building blocks and the monomers obtained from its depolymerization.

An initial investigation of the effect of metal ratios on hydrodeoxygenation was done for bimetallic platinum-rhenium catalysts supported on mesoporous carbon Sibunit.

The results of experiments performed in a batch reactor revealed the importance of both platinum and rhenium as catalysts for HDO, namely platinum in the reduced state is responsible for hydrogenation, while rhenium as an oxide, acts as an oxophilic metal. Additional tests on repeatability and reusability were performed, resulting in good catalyst stability.

Hydrodeoxygenation of isoeugenol was also done for the first time in a continuous reactor using a catalyst containing 4 wt% of platinum and 4 wt% of rhenium supported on mesoporous Sibunit carbon, where the effect of temperature was tested. High yields for the deoxygenated products (up to 90%) were obtained at 200 °C, while hydrogenation of the aromatic ring was predominant at lower temperatures.

A more in-depth study on the effect of the metal ratio between platinum and rhenium was carried out using bimetallic catalysts supported on activated carbon. The ratios tested ranged from 2:1 to 1:5 of Pt/Re. Higher hydrodeoxygenation activity was obtained when using higher Re loadings, which was attributed to the high hydrogenation capacity of platinum, and the need for oxygen vacancies provided by the rhenium oxide species. As determined from XAS characterization, these ReOx species helped in the dispersion and stability of platinum. On the other hand, the catalyst with a higher Pt:Re ratio (2:1) displayed lower deoxygenation activity, resulting instead only in hydrogenation of the aromatic ring.

A third series of catalysts, a mixture comprised of 2 wt% of platinum on a support comprising 69 wt% of zeolite H-Beta-300 or H-Beta-25, and 29 wt% of bindzil as a

binder, was tested initially in a batch reactor to gain insight on the effect of the use of a non-acidic binder, the metal deposition location, and the zeolite acidity.

The location of platinum was varied systematically when deposition of platinum was done alternatively on the zeolite, on the binder or on both. Furthermore, the addition of Bindzil and platinum resulted in a decrease of the surface area and the total amount of acid sites when compared to the unmodified zeolite

Overall, catalysts containing the more acidic H-Beta-25 zeolite displayed higher activity than those with H-Beta-300. However, the catalyst with Pt on both the binder and H-Beta-300 displayed a similar propylcyclohexane yield, suggesting that an optimum acidity is required for the deoxygenation of isoeugenol.

The location of platinum was also important for hydrodeoxygenation efficiency. The catalysts where Pt was located closer to the acid sites (being deposited on only zeolite or both zeolite and the binder) displayed higher dihydroeugenol conversion and propylcyclohexane yield, while deposition of platinum on the binder gave the lowest activity.

To simulate a scale-up in hydrodeoxygenation of isoeugenol, extrudates comprising 2 wt% of platinum, 69 wt% of zeolite H-Beta-25 and 29 wt% of Bindzil were tested in a continuous trickle-bed reactor.

An initial screening of catalysts in the trickle bed reactor was performed at 150 °C to determine the effect of the platinum location, which was deposited either on the zeolite, on the binder or on both.

Although all catalysts displayed similar dihydroeugenol conversion, a higher propylcyclohexane yield was obtained when Pt was located on both the zeolite and the binder, while deposition of platinum on the non-acidic binder resulted in ca. 10% lower activity. Furthermore, minimal solvent cracking was observed under these conditions being less than 0.1%. The catalyst where platinum was located only on the zeolite exhibited a lower mass balance closure in the liquid phase, which was attributed to a higher formation of carbonaceous species, as confirmed by temperature programmed oxidation and nitrogen physisorption of the spent catalysts.

Based on batch and continuous reactor results, it can be concluded that closer proximity between the metal and acid sites is the key factor determining catalytic performance of zeolite-supported metal nanoparticles in hydrodeoxygenation of isoeugenol.

The effect of reaction temperature was investigated using the catalyst with platinum located on both zeolite and the binder. A loss of 10% in activity was observed when comparing with the initial reaction at 200 °C. Complete dihydroeugenol conversions and high propylcyclohexane yields were achieved at 150 and 200 °C. A catalyst effectiveness factor of 0.17 and an apparent activation energy of 14.7 kJ/mol demonstrated significant mass transfer limitations.

The next step in this research would be to investigate the hydrodeoxygenation of real lignin-depolymerization mixtures. Such studies would provide valuable insights regarding catalyst activity and stability, as these mixtures are much more complex and better represent the feeds that could be used in industry.

Within the framework of the research program in the Laboratory of Industrial Chemistry and Reaction Engineering on sustainable aviation fuels, additional work has been done regarding decarboxylation and hydrocracking of oleic acid as a model lipid feed. Promising results have been obtained using a series of Pd/zeolite catalysts in a batch reactor, with complete conversions at 6 h and the formation of heptadecane, hexadecane and pentadecane as main products.

Furthermore, hydrocracking of hexadecane, a model compound for fatty acid decarboxylation/deoxygenation, has been tested in a temperature range of 150 - 250 °C in a continuous reactor using Ru, Ni and Pd supported on a series of hierarchical zeolites with the goal to optimize the production of hydrocarbons in the jet-fuel range, resulting in a high selectivity towards C8-C12 isomerized products.

Notations

BAS	Brønsted acid sites
DH	dihydroeugenol
EXAFS	Extended X-ray absorption fine structure
FTIR	Fourier transform infrared spectroscopy
GCLPA	gas chromatography liquid phase analysis
HDO	hydrodeoxygenation
HYD	2-methoxy-4-propylcyclohexanol
IE	isoeugenol
LAS	Lewis acid sites
PCH	propylcyclohexane
SEM	scanning electron microscopy
TEM	transmission electron microscopy
TPD	temperature programmed desorption
TOF	turnover frequency
TPO	temperature programmed oxidation
TPR	temperature programmed reduction
X	conversion
XANES	X-ray absorption near edge structure
XAS	X-ray absorption spectroscopy
XPS	X-ray photoelectron spectroscopy
XRD	X-ray diffraction
Y	yield
η_{eff}	effectiveness factor

References

- 1 J. Kammermann, I. Bolvashenkov, K. Tran, H. G. Herzog and I. Frenkel, *Proceedings - ICOECS 2020: 2020 International Conference on Electrotechnical Complexes and Systems*, 2020, 1–6.
- 2 C. B. Field, J. E. Campbell and D. B. Lobell, *Trends Ecol Evol*, 2008, **23**, 65–72.
- 3 H. Wei, W. Liu, X. Chen, Q. Yang, J. Li and H. Chen, *Fuel*, 2019, **254**, 115599.
- 4 N. Sorek, T. H. Yeats, H. Szemenyei, H. Youngs and C. R. Somerville, *Bioscience*, 2014, **64**, 192–201.
- 5 M. S. Singhvi and D. V. Gokhale, *Appl Microbiol Biotechnol*, 2019, **103**, 9305–9320.
- 6 D. P. Serrano, J. A. Melero, G. Morales, J. Iglesias and P. Pizarro, *Catal Rev Sci Eng*, 2018, **60**, 1–70.
- 7 S. Sethupathy, G. Murillo Morales, L. Gao, H. Wang, B. Yang, J. Jiang, J. Sun and D. Zhu, *Bioresour Technol*, 2022, **347**, 126696.
- 8 R. Hatfield and W. Vermerris, *Plant Physiol*, 2001, **126**, 1351–1357.
- 9 S. Sethupathy, G. Murillo Morales, L. Gao, H. Wang, B. Yang, J. Jiang, J. Sun and D. Zhu, *Bioresour Technol*, 2022, **347**, 126696.
- 10 D. Czajczyńska, L. Anguilano, H. Ghazal, R. Krzyżyńska, A. J. Reynolds, N. Spencer and H. Jouhara, *Thermal Science and Engineering Progress*, 2017, **3**, 171–197.
- 11 K. Jacobson, K. C. Maheria and A. Kumar Dalai, *Ren Sust Energy Rev*, 2013, **23**, 91–106.
- 12 G. W. Huber, S. Iborra and A. Corma, *Chem Rev*, 2006, **106**, 4044–4098.
- 13 Q. Bu, H. Lei, A. H. Zacher, L. Wang, S. Ren, J. Liang, Y. Wei, Y. Liu, J. Tang, Q. Zhang and R. Ruan, *Bioresour Technol*, 2012, **124**, 470–477.
- 14 X. Lu, L. Lagerquist, K. Eränen, J. Hemming, P. Eklund, L. Estel, S. Leveneur and H. Grénman, *Ind Eng Chem Res*, 2021, **60**, 16827–16838.
- 15 J. Meng, A. Moore, D. Tilotta, S. Kelley and S. Park, *ACS Sustain Chem Eng*, 2014, **2**, 2011–2018.
- 16 P. J. de Wild, W. J. J. Huijgen, A. Kloekhorst, R. K. Chowdari and H. J. Heeres, *Bioresour Technol*, 2017, **229**, 160–168.
- 17 M. Bertero, G. De La Puente and U. Sedran, *Fuel*, 2012, **95**, 263–271.
- 18 J. I. Hileman and R. W. Stratton, *Transp Policy (Oxf)*, 2014, **34**, 52–62.
- 19 P. Kallio, A. Pásztor, M. K. Akhtar and P. R. Jones, *Curr Opin Biotechnol*, 2014, **26**, 50–55.
- 20 M. C. Vásquez, E. E. Silva and E. F. Castillo, *Biomass Bioenergy*, 2017, **105**, 197–206.
- 21 A. Galadima and O. Muraza, *J Ind Engg Chem*, 2015, **29**, 12–23.
- 22 N. Vela-García, D. Bolonio, M. J. García-Martínez, M. F. Ortega, D. Almeida Streitwieser and L. Canoira, *Energy Convers Manag*, 2021, **244**, 114534.
- 23 L. Zhang, Y. Dang, X. Zhou, P. Gao, A. Petrus van Bavel, H. Wang, S. Li, L. Shi, Y. Yang, E. I. Vovk, Y. Gao and Y. Sun, *Innovation*, 2021, **2**, 100170.
- 24 A. Bauen, N. Bitossi, L. German, A. Harris and K. Leow, *Johnson Matthey Technology Review*, 2020, **64**, 263–278.
- 25 K. S. Ng, D. Farooq and A. Yang, *Ren Sust Energy Rev*, 2021, **150**, 111502.
- 26 X. Wang, M. Arai, Q. Wu, C. Zhang and F. Zhao, *Green Chem*, 2020, **22**, 8140–8168.
- 27 R. Pujro, J. R. García, M. Bertero, M. Falco and U. Sedran, *Energy and Fuels*, 2021, **35**, 16943–16964.

- 28 D. Gao, Y. Xiao and A. Varma, *Ind Eng Chem Res*, 2015, **54**, 10638–10644.
- 29 J. Horáček, G. Št'Ávová, V. Kelbichová and D. Kubička, *Catal Today*, 2013, **204**, 38–45.
- 30 H. Ohta, H. Kobayashi, K. Hara and A. Fukuoka, *Chem Commun*, 2011, **47**, 12209–12211.
- 31 M. Lu, H. Du, B. Wei, J. Zhu, M. Li, Y. Shan and C. Song, *Energy and Fuels*, 2017, **31**, 10858–10865.
- 32 C. A. Teles, R. C. Rabelo-Neto, G. Jacobs, B. H. Davis, D. E. Resasco and F. B. Noronha, *ChemCatChem*, 2017, **9**, 2850–2863.
- 33 S. Mitchell, N. L. Michels and J. Pérez-Ramírez, *Chem Soc Rev*, 2013, **42**, 6094–6112.
- 34 G. T. Whiting, S. H. Chung, D. Stosic, A. D. Chowdhury, L. I. Van Der Wal, D. Fu, J. Zecevic, A. Travert, K. Houben, M. Baldus and B. M. Weckhuysen, *ACS Catal*, 2019, **9**, 4792–4803.
- 35 J. Holladay, Z. Abdullah and J. Heyne, *Sustainable Aviation Fuel: Review of Technical pathways*, United States, 2020, 1–4.
- 36 <https://www.neste.com/products/all-products/saf>, (accessed 2 October 2023).
- 37 C. A. Emeis, *J Catal*, 1993, **141**, 347–354.
- 38 F. Coloma, A. Sepúlveda-Escribano and F. Rodríguez-Reynoso, *J Catal*, 1995, **154**, 299–305.
- 39 H. Markus, P. Mäki-Arvela, N. Kumar, N. V. Kul'kova, P. Eklund, R. Sjöholm, B. Holmbom, T. Salmi and D. Y. Murzin, *Catal Letters*, 2005, **103**, 125–131.
- 40 G. Leofanti, M. Padovan, G. Tozzola and B. Venturelli, *Catal Today*, 1998, **41**, 207–219.
- 41 J. A. Lopez-Ruiz and R. J. Davis, *Green Chemistry*, 2014, **16**, 683–694.
- 42 L. I. Godina, A. V. Kirilin, A. V. Tokarev, I. L. Simakova and D. Y. Murzin, *Ind Eng Chem Res*, 2018, **57**, 2050–2067.
- 43 I. V. Yentekakis, G. Goula, P. Panagiotopoulou, S. Kampouri, M. J. Taylor, G. Kyriakou and R. M. Lambert, *Appl Catal B*, 2016, **192**, 357–364.
- 44 J. Fan, K. Qi, L. Zhang, H. Zhang, S. Yu and X. Cui, *ACS Appl Mater Interfaces*, 2017, **9**, 18008–18014.
- 45 J. F. Moulder, W. F. Stickle, P. E. Sobol and K. D. Bomben, *Handbook of X-ray photoelectron spectroscopy (XPS)*, Perkin-Elmer Corporation, 1992.
- 46 A. Ciftci, D. A. J. M. Ligthart, A. O. Sen, A. J. F. Van Hoof, H. Friedrich and E. J. M. Hensen, *J Catal*, 2014, **311**, 88–101.
- 47 N. Y. Chen, M. C. Liu, S. C. Yang and J. R. Chang, *J Spectrosc*, 2014, **2014**, 1–12.
- 48 H. Iida and A. Igarashi, *Appl Catal A Gen*, 2006, **303**, 192–198.
- 49 X. Di, C. Li, G. Lafaye, C. Especel, F. Epron and C. Liang, *Catal Sci Technol*, 2017, **7**, 5212–5223.
- 50 J. Sá, C. Kartusch, M. Makosch, C. Paun, J. A. Van Bokhoven, E. Kleymenov, J. Szlachetko, M. Nachtegaal, H. G. Manyar and C. Hardacre, *Chem Commun*, 2011, **47**, 6590–6592.
- 51 S. Rong, H. Tan, Z. Pang, Z. Zong, R. Zhao, Z. Li, Z. N. Chen, N. N. Zhang, W. Yi and H. Cui, *Renew Energy*, 2022, **187**, 271–281.
- 52 L. Bomont, M. Alda-Onggar, V. Fedorov, A. Aho, J. Peltonen, K. Eränen, M. Peurla, N. Kumar, J. Wärnå, V. Russo, P. Mäki-Arvela, H. Grénman, M. Lindblad and D. Y. Murzin, *Eur J Inorg Chem*, 2018, **2018**, 2841–2854.
- 53 M. I. Temkin, D. Yu. Murzin and N. V. Kul'kova, *Doklady Acad. Sci. USSR*, 1988, **303**, 659.

- 54 D. Liu, G. Li, F. Yang, H. Wang, J. Han, X. Zhu and Q. Ge, *J Phys Chem C*, 2017, **121**, 12249–12260.
- 55 J. Chang, T. Danuthai, S. Dewiyanti, C. Wang and A. Borgna, *ChemCatChem*, 2013, **5**, 3041–3049.
- 56 K. Baranowska and J. Okal, *Appl Catal A Gen*, 2015, **499**, 158–167.
- 57 S. T. Thompson and H. H. Lamb, *ACS Catal*, 2016, **6**, 7438–7447.
- 58 C. A. Teles, R. C. Rabelo-Neto, N. Duong, J. Quiroz, P. H. C. Camargo, G. Jacobs, D. E. Resasco and F. B. Noronha, *Appl Catal B*, 2020, **277**, 119238.
- 59 Z. Vajglová, N. Kumar, M. Peurla, L. Hupa, K. Semikin, D. A. Sladkovskiy and D. Y. Murzin, *J Chem Tech Biotechnol*, 2021, **96**, 1645–1655.
- 60 D. Kubička, N. Kumar, T. Venäläinen, H. Karhu, I. Kubičková, H. Österholm and D. Y. Murzin, *J Phys Chem B*, 2006, **110**, 4937–4946.
- 61 D. P. Serrano, R. Sanz, P. Pizarro, I. Moreno, P. de Frutos and S. Blázquez, *Catal Today*, 2009, **143**, 151–157.
- 62 Z. Vajglová, N. Kumar, P. Mäki-Arvela, K. Eränen, M. Peurla, L. Hupa, M. Nurmi, M. Toivakka and D. Y. Murzin, *Ind Eng Chem Res*, 2019, **58**, 18084–18096.
- 63 A. M. Najafi, S. Soltanali, F. Khorashe and H. Ghassabzadeh, *Chemosphere*, 2023, **324**, 138275.
- 64 Z. Vajglová, N. Kumar, M. Peurla, L. Hupa, K. Semikin, D. A. Sladkovskiy and D. Y. Murzin, *Ind Eng Chem Res*, 2019, **58**, 10875–10885.
- 65 Z. Alipour, M. Rezaei and F. Meshkani, *J Ind Eng Chem*, 2014, **20**, 2858–2863.
- 66 S. Wang and G. Q. Lu, *J Chem Technol Biotechnol*, 2000, **75**, 589–595.
- 67 R. A. van Santen, *Acc Chem Res*, 2009, **42**, 57–66.
- 68 U. Sanyal, Y. Song, N. Singh, J. L. Fulton, J. Herranz, A. Jentys, O. Y. Gutiérrez and J. A. Lercher, *ChemCatChem*, 2019, **11**, 575–582.
- 69 R. K. Herz, *J Catal*, 1981, **386**, 371–386.

Publications

M. E. Martínez-Klimov, P. Mäki-Arvela, D. Y. Murzin, Catalysis for production of jet fuel from renewable sources by hydrodeoxygenation and hydrocracking, in *Catalysis: Volume 33*, ed. J. Spivey, Y.-F. Han and D. Shekhawat. The Royal Society of Chemistry, UK, 2021, Ch. 6, pp. 181-213.

Reproduced with permission from the Royal Society of Chemistry, the full text is available at: <https://books.rsc.org/books/edited-volume/1533/chapter-abstract/959871/>

Catalysis for production of jet fuel from renewable sources by hydrodeoxygenation and hydrocracking

M. E. Martínez-Klimov, P. Mäki-Arvela and D. Y. Murzin*

DOI: 10.1039/9781839163128-00181

The increase in demand for green fuel sources has led to the development of biomass conversion and upgrading processes. High oxygen content deems bio-oil unsuitable for energy generation due to its corrosiveness and low heating value, hence bio-oil needs upgrading. Hydrodeoxygenation (HDO) and hydrocracking (HDC) are catalytic hydro-treating processes suitable for the production of renewable jet fuel, which is mainly composed of aliphatic and aromatic hydrocarbons (C_8 – C_{16}). This chapter addresses current advances in HDO of model compounds as well as real feeds over a variety of noble and transition metal catalysts. The effects of bifunctional, bimetallic and sulfided catalysts on activity and selectivity are discussed, together with the effect of support type on the reaction. High deoxygenation degree was successfully demonstrated in HDO of fast pyrolysis oil over noble metal catalysts. HDC activity of various vegetable oils is also presented, showing promising results for obtaining hydrocarbons. The industrial application of HDO and HDC of real feedstocks is still rather limited due to fast catalyst deactivation and the complexity of the feedstock itself. Future research will address the challenges of catalyst stability and lowering reaction conditions through new technologies identified based on existing literature, such as electrocatalysis and plasma utilization.

1 Introduction

Nowadays up to 80% of the world's main energy source comes from fossil fuels.¹ As the global population increases, so does the consumption of oil, coal and natural gas. This contributes to the emission of greenhouse gases such as CO_2 and also depletes non-renewable resources.² Biomass, however, is a renewable, sustainable and carbon-rich alternative that could contribute significantly to solve these challenges. Current research efforts in catalysis have focused on the valorization of biomass and the development of sustainable biofuels to substitute or supplement those currently in use in the aviation and automotive industries.³

Biomass refers to all organic matter obtained from plants or animals, including waste.⁴ The main advantage of biomass over other renewable sources of energy is that it can be converted into different types of solid, liquid and gaseous fuels through a series of thermochemical, biochemical and physical processes,⁵ furthermore, liquid fuels for transportation obtained from biomass can even be processed within the current petroleum infrastructure.⁶ Two of the main routes for upgrading biomass-derived oil into liquid fuels are hydrodeoxygenation and selective hydrocracking.⁷

Åbo Akademi University, 20500 Turku/Åbo, Finland.

E-mail: Dmitry.Murzin@abo.fi

1.1 Biomass-derived biofuels

Biomass-derived fuels are classified into generations depending on their origin and production (see Fig. 1).

The first-generation biofuels are derived from sugars, vegetable oils and starch obtained directly from food crops. Corn and sugar cane are the main feedstocks for the production of bioethanol through fermentation, while soybeans are used for the production of biodiesel through transesterification.⁸ The importance of these crops as a food source has limited their application for the production of biofuels, and as a consequence, the interest has turned into non-food feedstocks.⁹

The second-generation biofuels are produced from industrial crops and in some cases from waste obtained from food crops.¹⁰ Also known as advanced biofuels, these are mainly obtained from abundant and inexpensive lignocellulosic biomass or agricultural residue and require additional processing steps and technologies.¹¹ These biofuels are considered to have a neutral or negative carbon emission. The main benefit is the utilization of abundant and lower value feedstock.

The third-generation biofuels are obtained from microalgae. Biofuel yields up to ten times higher¹² make them a good alternative to first- and second-generation biofuels.¹³ Algae can capture high quantities of CO₂ and be used to produce oil,¹⁴ from which hydrogen, butanol, methane, ethanol, jet fuel and biodiesel can be produced.¹⁵ The main disadvantages are the emission of greenhouse gases due to the fertilizer requirements¹⁶ and microalgal lipids are prone to oxidation due to polyunsaturations.¹⁷ These limitations make algae-produced biofuels expensive and not yet suitable for large-scale implementation.

The fourth-generation biofuels are based on bioengineering approaches to modify the metabolism of cyanobacteria, microalgae and fungi (photosynthetic microorganisms¹⁸ maximizing biofuel yields and diminishing costs.¹⁹ A high growth rate and hydrocarbon yields make

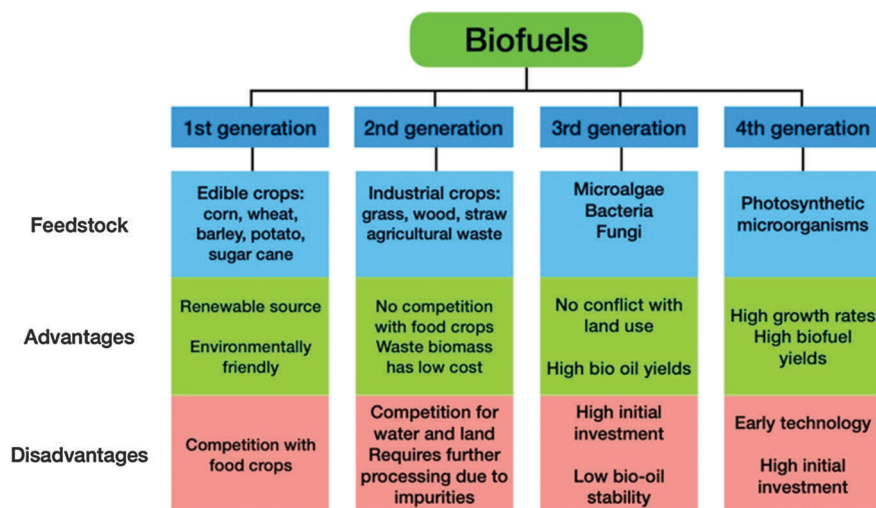


Fig. 1 Biofuel generations, their advantages and disadvantages.

them an attractive alternative,²⁰ however, it still is in early developing stages.²¹

The interest in developing biofuels compatible with current fossil-fuel engines would diminish or even eliminate the need for further engine modifications. The optimal situation would be for biofuels to have similar properties (density, flash point, viscosity and heating value, *etc.*) to fossil-based fuels.²²

1.2 Biomass conversion – pyrolysis overview

Among the different thermochemical conversion processes of organic matter, pyrolysis has gained importance for the production of liquid fuels²³ because of a low initial investment and high energy efficiency, particularly on a small scale.²⁴ The thermal decomposition of biomass is done at temperatures between 300–1100 °C, with a limited supply or even in the absence of oxygen and is followed by rapid cooling.²⁵ It can be divided into slow, fast or flash pyrolysis depending on the conditions used (see Table 1).

Pyrolysis products are separated into solid, liquid and gaseous phases. The solid product is a charcoal-like material that can be used as a solid fuel, in agriculture and for the production of syngas through gasification.³³ Bio-oil comprises the liquid phase, is used directly as a furnace fuel or potentially can be further processed to produce other fuels and chemical products.³⁴ The gaseous phase, called biogas, is composed of CO, CO₂, hydrogen, methane and other light hydrocarbons. Biogas is primarily used for industrial combustion to produce energy.³⁵

The general process of thermal decomposition of biomass starts with the initial evaporation of the water in the feedstock, followed by rapid depolymerization and volatilization.³⁶ Thereafter, there is a period of degradation where secondary reactions occur between the formed products and feedstock components. Finally, the rapid cooling of the pyrolysis vapours results in formation of bio-oil.³⁷

2 Bio-oil composition and properties

Bio-oil is a dark brown liquid obtained from the fragmentation and depolymerization of cellulose, hemicellulose and lignin.³⁸ It is a diverse and complex mixture of several hundreds of organic compounds such as ketones, esters, ethers, carboxylic acids, sugars, furans, phenols, aromatic hydrocarbons and water (see Fig. 2). The exact composition of bio-oil, which varies depending on the feedstock, has been determined as

Table 1 General pyrolysis conditions.^{26–32}

Type	Heating rate (°C/s)	Temperature (°C)	Residence time (s)	Particle size (mm)	Product yield (wt%)		
					Biochar	Bio-oil	Gas
Slow	0.1–0.5	350–600	450–550	5–50	30–65	20–45	20–35
Fast	10–200	400–950	0.5–10	<3	10–15	60–80	10–25
Flash	>1000	700–1300	<0.5	<0.25	10–15	70–75	10–15

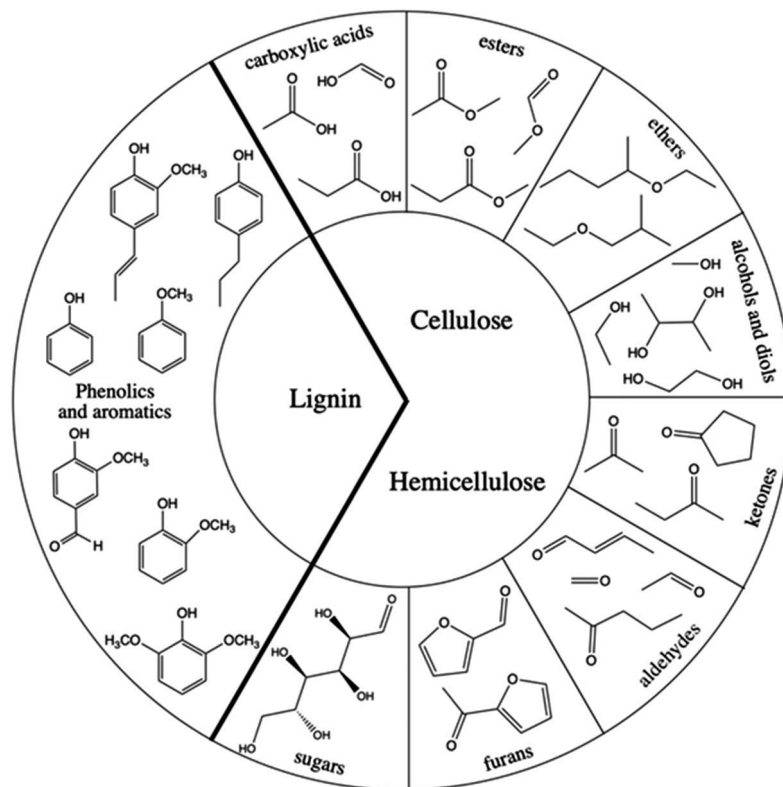


Fig. 2 Oxygen-containing compounds derived from the pyrolysis of lignocellulosic biomass.^{42,43}

follows: 8–26 wt% light oxygenated compounds (C_2 – C_4), 1–7 wt% oxygenated aromatic compounds derived from lignin depolymerization, 7–24 wt% anhydrosugars from cellulose and hemicellulose depolymerization, 3–7 wt% oligomeric products from dehydration and 11–18 wt% oligomeric products from cellulose and lignin.³⁹

Acids, aldehydes, ketones and phenols, account for 50 to 60 wt% of the components in bio-oil.⁴⁰ Aldehydes, ketones, furans, acids, esters, ethers and alcohols are mostly obtained from cellulose and hemicellulose, while phenolic compounds are obtained from the pyrolysis of lignin.⁴¹

Lignin accounts for 15–35 wt% of the dry lignocellulose and it is one of the largest renewable sources of aromatics.⁴⁴ Phenolic compounds are the main fraction found in lignin-derived pyrolysis oil, accounting for 25–40 wt%,⁴⁵ the structure of lignin is built of three monomers: coumaryl, coniferyl, and sinapyl alcohols, which give place to guaiacyl, syringyl and *p*-hydroxyphenyl derivatives.⁴⁶

Knowing the chemical composition and physical properties of bio-oil (see Table 2) is important for determining upgrading pathways and possible applications.

Bio-oil has a higher density and viscosity than the petroleum-based oils.⁴⁷ Viscosity depends on the composition; however, it can also fluctuate due to polymerization within the bio-oil caused by the hydroxyl, carbonyl, and carboxyl groups reacting with each other over time.⁴⁸

Table 2 Physicochemical properties of bio-oil.

Bio-oil properties	
Density at 20 °C (kg l ⁻¹)	1.1–1.4
Viscosity at 40 °C (cP)	30–200
pH	2–4
Heating value (MJ kg ⁻¹)	14–23
Ash content	0.1
Water content (wt%)	20–30
Solid content (wt%)	<1
Solubility in organic solvents	Poor solubility
Flash point (°C)	40–110
Elemental composition (wt%)	
C	50–65
H	5–8
O	35–40
N	<0.5
S	<0.05

The presence of ash and high acidity caused by organic acids make the oil corrosive to materials like steel and aluminum.⁴⁹ Furthermore, the amount of heat produced from the complete combustion of bio-oil is low when compared with petroleum fuels.⁵⁰

Presence of water also lowers the heating value and the combustion rate of bio-oil.⁵¹ Water content in bio-oil comes from the original feed-stock and from the dehydration reactions occurring during pyrolysis.⁴⁰ Water and high oxygen content also mean that bio-oil can't be mixed with regular fossil fuels.⁵²

It becomes clear that the elimination of oxygen-containing groups is of key importance for reducing acidity, viscosity and increasing the heating value of bio-oil so that it can become an additive or replacement for current fuels used in the transportation industry.⁵³

3 Jet fuel composition and specifications

Jet fuel, also known as aviation turbine fuel (ATF) is a type of petroleum-based fuel used for powering turbine engine aircrafts, both military and commercial ones.⁵⁴ Slightly yellow in appearance, it can be commonly found in three types of specifications, Jet A-1 and Jet A for commercial aviation and Jet B for civilian use.⁵⁵

Aromatics account for 8–25% of the jet fuel composition and help to increase the energy density. A lower amount of aromatic compounds can damage the engine and as a consequence reduce its lifetime.⁵⁶

Jet fuel produced from crude oil distillation (205–260 °C)⁵⁷ consists of a mixture of aliphatic and aromatic hydrocarbons (C₈–C₁₆).⁵⁸ The main components include alkanes, alkenes, aromatic compounds and cyclo-alkane derivatives.⁵⁹ The component proportion determines the properties of the fuel. Paraffins and cycloparaffins constitute about 70–85% of jet fuel helping to reduce the freezing point and allowing high-altitude flights.⁶⁰ A high hydrogen-to-carbon ratio ensures the energy density and

Table 3 Jet fuel specifications.

Specification	Unit	Jet A-1 ⁶⁵	Jet A ⁶³	Jet B ⁶⁴
Acidity	mg KOH g ⁻¹	0.1	0.10	0.10
Boiling point	°C	170	170	205
Flash point	°C	38	38	38
Density at 15 °C	kg m ⁻³	775–840	775–840	775–840
Freezing point	°C	– 47	– 40	– 47
Viscosity at –20 to –35.5 °C	cSt	8.0	8.0	8.0
Heat of combustion	MJ kg ⁻¹	42.8	43.28	42.8
Smoke point	mm	25	25	25

cleaner combustion of the fuel. Aromatic compounds enhance lubricity; however, leading to poor combustion which may damage the engine.⁶¹

Commercial jet fuels have strict standards that also consider other characteristics including sulfur content, density, flash point and viscosity to ensure proper engine performance and reliability. The American Society for Testing and Materials (ASTM D1655) defines the types of jet fuels used and their properties such as combustion, volatility, fluidity and thermal stability⁶² (see Table 3).

Jet fuel can be classified based of their performance in Jet A, Jet A-1, JP-5 and JP-8. Jet A and Jet A-1 are used in commercial aircrafts while JP-5 and JP-8 are commonly used for military ones. The only difference between Jet A and Jet A-1 is the freezing point (–40 °C and –47 °C, respectively).⁶⁰

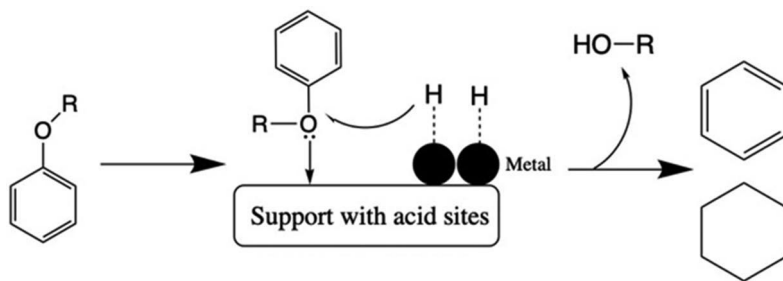
Currently there are five alternative jet-fuels (AJF) approved by ASTM, these are: Direct Sugar to Hydrocarbon (DSHC), Hydroprocessed Esters and Fatty Acids (HEFA), Fischer–Tropsch (FT) and Alcohol to Jet (ATJ). The content of residual oxygenated compounds found in alternative jet fuels has been studied with GC/MS.⁶⁵ It was found that the most common oxygenated compound in AJF are phenols, which even if considered as antioxidants in jet fuel, could cause thermal and oxidative deposits.⁶⁶

4 Bio-oil hydrotreatment

Catalytic hydrotreating is a hydrogenation process used in oil refinery for the removal of sulfur (HDS) and nitrogen (HDN) from hydrocarbons by selectively reacting them with hydrogen.⁶⁷ The importance of removing these elements is to avoid their detrimental effects resulting in catalyst poisoning, to improve the quality of the products and to reduce the emission of harmful gases such as SO_x and NO_x generated during combustion.⁶⁸ The same process can be used to remove oxygen and upgrade bio-oil, producing saturated or aromatic hydrocarbons and thus improving the heating value and chemical stability.⁶⁹

The two primary hydroprocessing methods for removing oxygen from the bio-oil are hydrodeoxygenation (HDO) and hydrocracking (HDC).⁷⁰

HDO is a hydrogenolysis process for removing oxygen from the feed-stock in the form of water, CO₂ or CO, in the presence of catalysts and hydrogen,⁷¹ the resulting products can be saturated or unsaturated hydrocarbons (see Scheme 1). A variety of reactions can take place during



Scheme 1 Simplified HDO reaction.⁸⁶

the HDO process, including hydrogenation, hydrocracking, decarbonylation, dehydration and hydrogenolysis.⁷²

Most of the current HDO research is centered on the use of supported noble or transition metals, using either three phase (gas-liquid-solid) or two phase (gas-solid) reactors. The liquid-phase HDO has an advantage of lower energy consumption due to lower temperatures used, as the reactants do not require vaporization. Lower temperatures are also beneficial for the catalyst stability and effectiveness, as well as for selectivity. The main drawbacks of the liquid-phase HDO compared to the gas-phase counterpart are related to lower reaction rates because of lower temperature and presence of an additional phase boundary leading to potential gas-liquid mass transfer limitations and limited hydrogen solubility.⁷³

Techno-economic analysis of vapor and liquid phase HDO for the commercial scale production is not available in the open literature, however gas phase HDO could potentially be implemented due to similarities with some basic chemicals production processes.⁷⁴

Similarly, HDC is a common process used in oil refineries, it is the scission or breaking of one or more C-C bonds of hydrocarbons derived from petroleum to obtain diesel, jet fuel and gasoline.⁷⁵ This idea has also been applied for upgrading vegetable oils to hydrocarbons for use as liquid fuels.⁷⁶

Hydrocracking typically occurs at high temperature (>350 °C) and under relatively high hydrogen pressures (50–200 bar) generally in the presence of acidic zeolites or bifunctional catalysts,^{77,78} similar to the ones used for HDO. The main benefit of bio-oil HDC is that it is a single step process that consumes less energy than other upgrading processes.⁷⁹

4.1 HDO of lignin-derived phenolic-monomer model compounds

Due to the complexity of bio-oil, model oxygenated mono-phenolic compounds are often studied to understand the HDO reaction network and mechanisms. Phenolic compounds comprise around 20–40 wt% of bio-oil and are mainly obtained from lignin.⁴⁴ Lignin, as mentioned above, is an amorphous biopolymer composed of the three basic phenylpropane monomers⁴⁶ (see Fig. 3a) that are linked to each other through C-C or C-O bonds.⁸⁰ Typically, the most studied model compounds include phenol, guaiacol and eugenol, among others⁸¹ (see Fig. 3b).

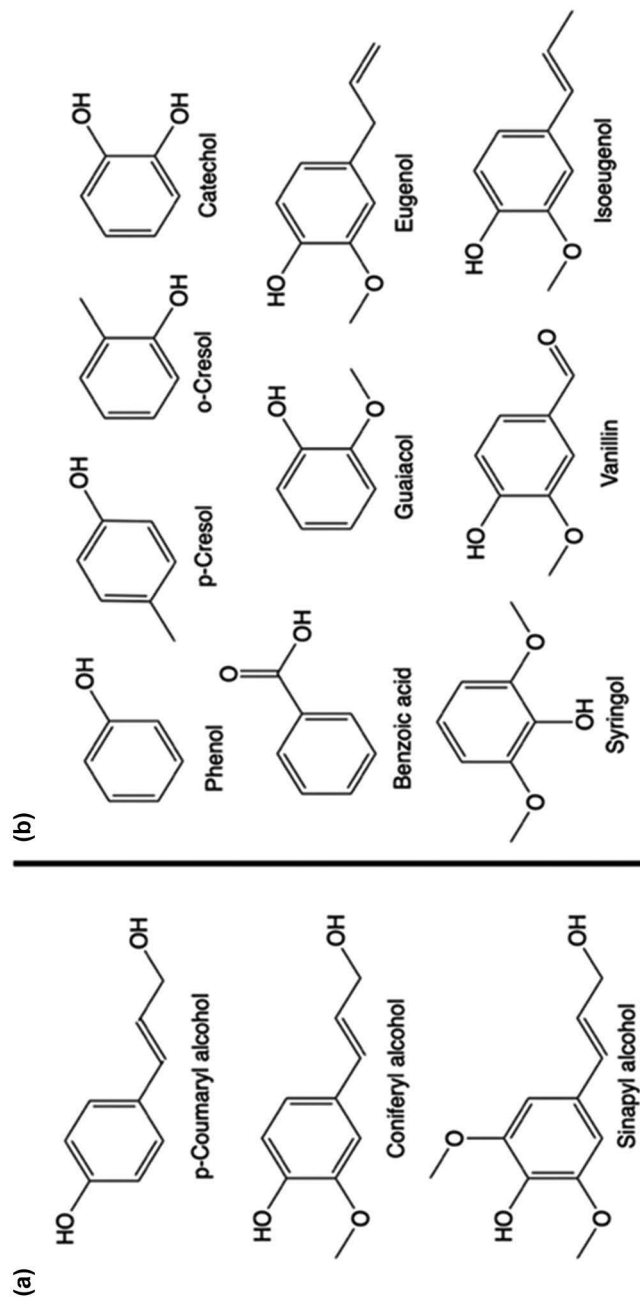
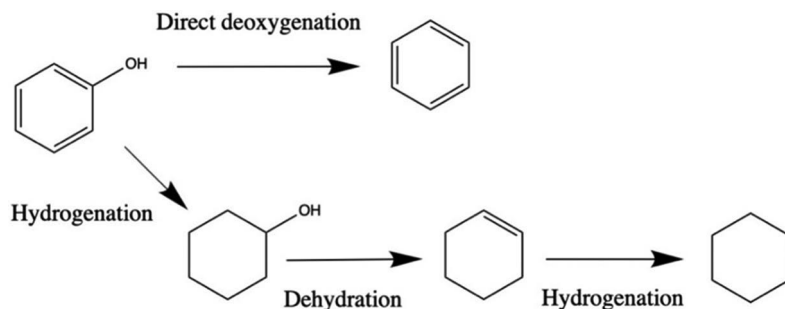


Fig. 3 (a) Phenylpropane monomers present in the lignin structure; (b) Phenolic-monomer model compounds.



Scheme 2 Simplified DDO and HYD routes for the HDO of phenol. Adapted from ref. 72 with permission from John Wiley & Sons, Copyright © 2019 Wiley-VCH Verlag GmbH & Co. KGaA, Weinheim. Adapted from ref. 83 with permission from Elsevier, Copyright 2014.

The main products of the HDO of phenolic compounds are aromatic hydrocarbons and cyclohexanes, which can be obtained through two main routes, direct deoxygenation (DDO pathway) where the phenolic hydroxyl group is directly removed yielding aromatic hydrocarbons⁸² and the hydrogenation–dehydration route (HYD pathway) where the hydrogenation of the aromatic ring occurs first, followed by the deoxygenation, yielding cycloalkanes⁸³ (see Scheme 2).

The C–O bond scission of the DDO pathway is favored by high temperatures and low hydrogen pressure, while the HYD pathway is prevalent at low temperatures and high hydrogen pressures.⁸⁴ It is considered that the DDO pathways are more economical due to the low consumption of hydrogen and the aromatics produced have higher octane ratings, making them more appropriate for mixing with relevant fuel fractions and benefiting the combustion of fuels.⁸⁵

The optimization of reaction parameters (temperature, hydrogen pressure, type of reactor, time on stream, solvent, *etc.*) as well as the catalyst design (selection of metals, particle size and distribution, acidity and textural properties of the support) are the main focus for effective HDO.

4.1.1 Effect of the metal. Catalysts for HDO are usually bifunctional and contain both metal and acid sites in the form of metal particles and a solid acid support,⁸⁶ respectively. Hydrogenation, dehydrogenation, hydrocracking and decarbonylation take place on metal sites,⁸⁷ while dehydration, isomerization and hydrogenolysis occur on the acid sites.⁸⁸ Bimetallic catalysts combine an oxophilic metal and another one that can be reduced.⁸⁹

Metals that are often used in HDO can be either noble metals (Pt, Pd, Rh, Re) or non-noble transition metals (Mo, Ni, Co, Fe). The most common supports are Al₂O₃, SiO₂, ZrO₂, various zeolites (HY, H-Beta, HZSM-5, USY, *etc.*) and carbon (see Table 4).

Sulfided CoMo and NiMo catalysts supported on Al₂O₃ were among the first catalysts used for HDO of bio-oil, as they had been used extensively for HDS and HDN in petroleum processing at an industrial scale.^{99–101} The HDO reactions catalyzed by metal sulfides are summarized in entries 1–10.^{90–92} In these catalysts MoS₂ acts as the active phase and Co or Ni as the promoter, improving the performance.¹⁰²

Table 4 The overview of catalysts for HDO of different model compounds and supported metal catalysts.

Entry	Reactant	Catalyst		Main product	X (%)	Y (%)	Reactor type	Reaction conditions			Ref.
		Metal	Loading (wt%)	Support				T (°C)	P (Mpa)	t (h)	
1	Phenol	CoMo	—	Al ₂ O ₃	27	10	Batch	300	5	4	Dodecane 90
2	Catechol	CoMo	—	Al ₂ O ₃	80	29	Batch	300	5	4	Dodecane
3	Guaiacol	CoMo	—	Al ₂ O ₃	84	29	Batch	300	5	4	Dodecane
4	<i>o</i> -Cresol	CoMo	—	Al ₂ O ₃	23	15	Batch	300	5	4	Dodecane
5	<i>p</i> -Cresol	CoMo	—	Al ₂ O ₃	22	13	Batch	300	5	4	Dodecane
6	Guaiacol	NiMo	3, 14	Al ₂ O ₃	65	25	Batch	300	7	2.5	Hexadecane 91
7	Guaiacol	CoMo	3, 14	Al ₂ O ₃	57	24	Batch	300	7	2.5	Hexadecane 92
8	<i>o</i> -Cresol	CoMo	—	Al ₂ O ₃	87	64	Batch	360	7	1	Hexadecane
9	<i>m</i> -Cresol	CoMo	—	Al ₂ O ₃	92	55	Batch	360	7	1	Hexadecane
10	<i>p</i> -Cresol	CoMo	—	Al ₂ O ₃	95	71	Batch	360	7	1	Hexadecane
11	Guaiacol	Rh	0.39	ZrO ₂	100	—	Batch	300	8	5	Hexadecane 93
12	Guaiacol	Pd	0.25	ZrO ₂	100	—	Batch	300	8	5	Hexadecane
13	Guaiacol	Pt	0.73	ZrO ₂	100	—	Batch	300	8	5	Hexadecane
14	Guaiacol	Rh	0.39	ZrO ₂	98.9	75	Batch	100	8	5	Hexadecane
15	Guaiacol	Pd	0.25	ZrO ₂	13.7	40	Batch	100	8	5	Hexadecane
16	Guaiacol	Pt	0.73	ZrO ₂	10	64	Batch	100	8	5	Hexadecane
17	Guaiacol	Pt	5	C	87	38	Fixed bed	300	0.1	5	— 94
18	Guaiacol	Pd	5	C	70	60	Fixed bed	300	0.1	5	—
19	Guaiacol	Rh	5	C	55	40	Fixed bed	300	0.1	5	—
20	Guaiacol	Ru	5	C	46	35	Fixed bed	300	0.1	5	—
21	Guaiacol	Pd	5	C	99	78	Fixed bed	350	0.1	1	— 95
22	Guaiacol	PdFe	2, 10	C	99	57	Fixed bed	350	0.1	1	—
23	Guaiacol	PdFe	2, 10	C	99	76	Fixed bed	450	0.1	1	—
24	Guaiacol	RuRe	4, 3.6	C	99	57	Batch	240	2	5	2-propanol 96
25	Guaiacol	Pd	0.5	ZSM-5	<5	0.5	Batch	150	4	5	Hexadecane 97
26	Guaiacol	Pd	0.5	ZSM-5	36	8	Batch	200	4	5	Hexadecane
27	Guaiacol	Pd	0.5	ZSM-5	100	63	Batch	250	4	5	Hexadecane
28	Guaiacol	Co	20	SiO ₂	100	98	Batch	300	5	1	Hexadecane 85
29	Guaiacol	Ni	20	SiO ₂	100	49	Batch	300	5	1	Hexadecane
30	Guaiacol	Pd	1	SiO ₂	100	74	Batch	300	5	1	Hexadecane
31	Guaiacol	Pt	1	SiO ₂	98.3	89	Batch	300	5	1	Hexadecane
32	Phenol	Ni	21.4	HZSM-5	98	86	Batch	250	5	2	Water 98
33	Phenol	Co	18.7	HZSM-5	5	3	Batch	250	5	2	Water
34	Phenol	NiCo	9.6, 9.5	HZSM-5	99	98	Batch	250	5	2	Water

In most of these catalysts, sulfur vacancies found at the edges of MoS₂ can act as a Lewis acid that adsorbs atoms with unpaired electrons.¹⁰³ These sites play a crucial role in the breakage of C–O bonds. Ni and Co form Co–Mo–S and Ni–Mo–S stacked slab-like structures,¹⁰⁴ where Mo acts as a noble metal through *d*-electron donation.¹⁰⁵ Ni and Co increase the vacancy activity donating electrons to Mo and thus weakening the Mo–S bond.¹⁰⁶ It has also been found that S–H and Mo–H groups can provide H to saturate C=C double bonds.¹⁰⁷

The activity of a commercial pre-sulfided CoMo/Al₂O₃ catalysts on several model compounds is presented in entries 1–5.⁹⁰ After 4 h HDO of phenol and cresol exhibited low conversion (≈25%). The main products were benzene and toluene, suggesting that these molecules are more stable at such reaction conditions. On the other hand, catechol and guaiacol displayed over 80% conversion and yielded mainly phenol, indicating low deoxygenation. Complete ring hydrogenation products, such as cyclohexane, were present in very low quantities for all reactions, indicating that the hydrogenation pathway was not favourable at these conditions.

Lower liquid phase mass balances for molecules with multiple oxygen groups, such as guaiacol and catechol, indicated the presence of oligomerization products due to intermolecular coupling at high temperatures,¹⁰⁸ these results fall in line with those reported for similar substrates.^{109–111}

A comparison between NiMo and CoMo for the HDO of guaiacol is given in entries 6–7.⁹¹ Although there was low deoxygenation of the reactants at 300 °C (the main product being catechol), it was found that NiMo/Al₂O₃ showed a higher activity, while CoMo/Al₂O₃ displayed a higher selectivity. These results are similar to other studies.^{112,113} Incomplete mass balance closure at the end of the reaction also indicated the formation of heavy products and coke due to polymerization.

Studies on the effect of promoters on Mo/Al₂O₃ catalysts have shown that metals like Co, Rh and Ru exhibit the highest C–O bond hydrogenolysis activity, while catalysts with Ni, Pd and Pt yielded lower hydrogenolysis selectivity, mainly because of high activity for the ring hydrogenation.^{44,114}

The position of substituents in the aromatic ring also influences reactivity (entries 8–10).⁹² A study on the HDO of *o*-, *m*- and *p*-cresol on a CoMo catalyst demonstrated that conversion decreases in the following order: *p*-cresol > *m*-cresol > *o*-cresol, indicating that ortho-substitution results in a lower conversion. Other studies on the effect of the steric hindrance on HDO suggest that molecules can adsorb on the Lewis acid sites in different ways and that the type and position of the functional groups can affect the degree of hydrodeoxygenation.¹¹⁵

There are several disadvantages for the use of sulfided catalysts, one of which is a need of a sulfur source, such as H₂S, to maintain the activity. Sulfur additives are commonly used during the reaction due to the negligible sulfur content of bio-oil.¹¹⁶ However, sulfur leaching can lead to a decreased HDO activity for phenolic compounds.^{117–119} Another major drawback of sulfided catalysts is that high temperatures are required for

hydrodeoxygenation (≈ 400 °C in some cases) and bio-oil can easily polymerize under such conditions, leading to carbon deposition and deactivation.¹²⁰ This has shifted HDO research into reduced transition-metal catalysts.

Noble metals, such as Pt, Pd, Rh and Ru, have also been extensively studied for the HDO of phenolic compounds, however, their exceptional hydrogenation activity usually results in the hydrogenation of the aromatic ring before deoxygenation, and therefore, higher yields of cyclic alkanes such as cyclohexane, instead of aromatic hydrocarbons.¹²¹ Noble metals paired with a moderately acidic support, such as ZrO₂, are effective alternatives to conventional sulfide CoMo catalysts for the production of oxygen-free aromatics.⁹³ Usually Pt exhibits the highest hydrogenation ability, followed by Ru and Pd.¹²²

A comparison of Rh, Pd and Pt supported on ZrO₂ for the HDO of guaiacol at 300 and 100 °C in a batch reactor is shown in entries 11–16.⁹³ The catalysts at 300 °C afforded complete conversion and the main product obtained was benzene, while reactions carried out at 100 °C gave incomplete guaiacol conversions. Rh/ZrO₂ showed higher conversion (99%) than Pt and Pd, this could be due to high metal dispersion in the Rh catalyst and sintering in the case of Pt and Pd. The main products obtained at 100 °C were oxygen-containing compounds, indicating that the saturation of aromatic rings is favored at lower temperatures while deoxygenation products are obtained at higher temperatures. Although Rh has a high potential for the HDO process for bio-oil upgrading, its application is limited due to its rarity and price.¹²³

The HDO of guaiacol using Pd, Pt, Ru and Rh supported on activated carbon in a fixed-bed reactor is shown in entries 17–20.⁹⁴ Pt/C was the most active catalyst with guaiacol conversion of 87% at 5 hour TOS, however, the main product for all catalysts was phenol, indicating that deoxygenation was not achieved. Deactivation of Pd, Rh and Ru catalysts was also observed. In the case of Ru/C, conversion decreased from 75 to 46% during TOS in the fixed bed operation. This effect has also been observed in other studies¹²⁴ and is mainly attributed to coke formation through the deposition of polyaromatics and metallic sintering. A proposed solution to mitigate coke formation is to increase H₂ pressure or lower the reaction temperature. This, however, leads to a higher hydrogen consumption and the hydrogenation of the aromatic ring may occur before the deoxygenation.^{125–127}

Although activated carbon supports are of great interest due to their high specific surface area and thermal stability,^{128,129} their use for HDO is limited in part due to their neutral properties, as seen in entries 17–20, the majority of the products obtained are still oxygenated. Noble metals supported on acidic supports benefit from bifunctional active sites: acid-catalyzed dehydration and metal-catalyzed hydrogenation result in complete deoxygenation¹³⁰ (entries 27–30).^{93,97} However, supports with strong Brønsted acid sites induce a higher rate of coke formation which in turn leads to catalyst deactivation.¹³¹ Bimetallic catalysts, comprising an oxophillic metal (Fe, Re, Mo) as a promoter and a noble or base metal (Ru, Pt, Pd, Ni) supported on carbon are effective

alternatives to metal-acid catalysts, with the main advantage being catalyst stability.^{95,132,133}

Bimetallic catalysts can enhance selectivity towards a particular product by modifying the interactions between the metals to change the geometric and electronic structures of the metal surface.¹³⁴

A comparison of monometallic Pd and bimetallic PdFe catalysts supported on activated carbon (entries 21–23)⁹⁵ show that bimetallic catalysts improved yield towards benzene. The main product for PdFe/C at 350 °C was phenol, with *ca.* 26% yield of benzene as opposed to *ca.* 3% for Pd/C. At 450 °C the main product was benzene with 83% yield and no ring-saturation products were observed. DFT calculations suggested preferential adsorption and activation of phenol on Fe, which likely prevents its hydrogenation on Pd.

Similarly, the promoting effect of Re in a bimetallic RuRe/C catalyst (entry 24)⁹⁶ is observed, where complete deoxygenation of guaiacol into cyclohexane was achieved. It is suggested that the bifunctionality of this catalyst stems from the formation of acid sites which originate from the rhenium oxide species,¹³⁵ while Ru provides metal sites for hydrogenation.¹³⁰

The effect of temperature in the HDO of guaiacol using Pd/ZSM-5 has also been studied (entries 25–27).⁹⁷ Low reaction temperatures and pressures are preferred in industry to minimize energy consumption, and coking formation.⁷² The catalysts exhibited low activity at temperatures below 200 °C. The main products included oxygenated compounds such as cyclohexanone, indicating hydrogenation of the aromatic ring and low deoxygenation efficiency. An increase of temperature to 250 °C shifted the reaction towards the deoxygenation routes, yielding mainly methylated aromatics such as toluene and dimethyl benzene.

Similar results have been found for Ni and Co catalysts.¹³⁶ High temperatures lead to a shift from hydrogenation to deoxygenation, this also results in the formation of coke and catalyst deactivation.¹³⁷

Non-noble transition metal catalysts are also efficient in the HDO for the production of liquid fuels. Typically, non-noble transition metals such as Co, Mo and Fe favor the DDO pathway to produce aromatic hydrocarbons while Ni catalysts usually yield cycloalkanes.⁷²

A comparison between noble and non-noble transition metals (Ni, Co, Pt, Pd) supported on SiO₂ for the HDO of guaiacol (entries 28–31)⁹³ showed that complete guaiacol conversion was obtained for all catalysts except for Pt/SiO₂. Cyclohexane was the main product for all catalysts giving high yields and indicating that Ni and Co can be as active as more expensive noble metals.

Ni and Co are widely studied metals for HDO, either as monometallic or bimetallic.^{138–141,161} Ni is the most common non-noble metal studied for HDO. It has a relatively low electrophilicity,⁷² making the C=O and C–O cleavage less favorable¹⁴² and resulting in formation of cyclic alkanes rather than aromatic compounds. Cobalt, on the other hand, has a higher activity than Ni and usually yields aromatic compounds through the DDO route.^{85,143} Co is mostly used as a promoter to enhance the DDO pathway for other metals, rather than being used by itself.¹⁴⁴

A comparison between Ni, Co and bimetallic NiCo catalysts supported on HZSM-5 shows that the Ni catalyst gave 98% phenol conversion and 88% selectivity towards cyclohexane (entries 32–34),⁹⁸ while a similarly loaded Co catalyst showed very low activity (<10%). Even though the total amount of Ni is less in the bimetallic catalyst, it showed complete phenol conversion and the highest selectivity for deoxygenated products (99.3%). The performance of the NiCo catalyst is the result of increased Ni dispersion through formation of a Ni-Co alloy; Co can form highly dispersed alloys with Ni and stabilize it through formation of a NiCo₂O₄ spinel phase. These small Ni particles accelerate phenol hydrogenation and decrease the coke formation.

4.1.2 Effect of the catalyst support. In HDO the support material is as important as the metal itself. The support is needed not only to stabilize and disperse the metal particles, preventing sintering,¹⁴⁵ but can also provide acid sites, which are important for the HDO reaction.¹⁴⁶ The most common supports are not always acidic. Some examples of frequently used supports for HDO are Al₂O₃, SiO₂, zeolites, TiO₂, ZrO₂, CeO₂ and activated carbon (see Table 5).

Al₂O₃ is one of the most common supports for conventional hydro-treating due to its high surface area, pore structure, thermal stability and mechanical strength.^{147,148} However, water found in bio-oil or formed during the HDO process can convert it into boehmite¹⁴⁹ oxidizing the active metal, and causing catalyst deactivation.^{72,150} This promoted development of alternative supports. Although SiO₂ has weaker interactions with oxygenated compounds than Al₂O₃^{151,152} its low affinity for carbon formation, due to its weak acidity,¹⁵³ makes it a potentially suitable and stable support for HDO. ZrO₂ and TiO₂ have also been of interest due to their amphoteric character, influencing redox properties of the catalysts.¹⁴⁶ They have displayed strong interactions with active species and low coke formation.¹⁵⁴

Mesoporous materials, such as SBA and MCM have large pores and high surface area,¹⁵⁵ which improve diffusion to the active sites.¹⁵⁶ Carbon supports allow for high dispersion of the active species, but weak surface interactions, can lead to metal sintering.¹⁵⁷ An additional advantage of carbon is low cost and a possibility of recovering active metals by burning the catalyst.¹⁴⁷

The HDO of phenol with 5 wt% Ni supported on different supports shows that activity for the cyclohexane production decreased in the following order: Ni/ZrO₂ > Ni/Al₂O₃ > Ni/SiO₂ > Ni/CeO₂ > Ni/C (entries 35–39).¹⁵⁶

The best performing catalyst was Ni/ZrO₂ giving complete conversion of phenol and high deoxygenation activity (83% cyclohexane yield). While Ni/Al₂O₃ also exhibited high activity (100% conversion) both hydrogenation and deoxygenation products were formed, with the cyclohexane yield being 46%. Both of these catalysts showed high carbon balance, indicating that they were less prone to coke deposition. Ni/SiO₂ was slightly less active (80% conversion) and had a lower cyclohexane yield (38%). The Ni/CeO₂ catalyst gave also complete conversion, however the

main product was cyclohexanol, indicating high hydrogenation and low deoxygenation activity. Ni/C was the only catalyst with no activity (2% conversion).

Mortensen *et al.*¹³¹ concluded that activation of phenol takes place on an oxygen vacancy site on the oxide supports, while deoxygenation takes place directly on the surface of Ni nanoparticles. The reaction starts with the heterolytic dissociation of the O–H bond of phenol on the oxide surface of the support. Then the phenoxide interacts with Ni where hydrogen has been adsorbed, leading to hydrogenation of the aromatic ring. Deoxygenation takes place through dehydration, forming cyclohexene, which is finally hydrogenated to form cyclohexane.

Noble metal catalysts, in contrast to nickel, have higher affinity for phenol activation by direct interactions with the aromatic ring.¹³² The effect of the support on the HDO of phenol with Pd in a fixed bed reactor (entries 40–44)¹⁵⁸ shows that Pd/TiO₂ and Pd/ZrO₂ exhibited the highest activity for HDO and a high selectivity to benzene. The product distribution varied depending on support. Cyclohexanone was mainly formed at low conversion for Pd/SiO₂, Pd/Al₂O₃ and Pd/CeO₂ catalysts, however, more prominent formation of benzene still occurred at high conversions.

A correlation between deoxygenation activity and the strength of the interactions of the phenolic oxygen and the oxophilic sites of the support was determined. Stronger interactions (Pd/TiO₂ and Pd/ZrO₂) resulted in hydrogenation of the carbonyl group while weaker ones (Pd/SiO₂ and Pd/CeO₂) lead to the hydrogenation of the aromatic ring, producing cyclohexanol and cyclohexanone at lower WHSV. The Pd/Al₂O₃ catalyst presented enough acidity to promote cyclohexanol dehydration to form cyclohexene.

The reaction pathways start with the dissociative adsorption of phenol on the metal oxide cation sites, followed by formation of a cyclohexadienone as an intermediate. This intermediate is highly unstable and reacts through different pathways. For Pd/ZrO₂ and Pd/TiO₂ catalysts the following step is the hydrogenation of the carbonyl group to 2,4-cyclohexadienol which then dehydrates to benzene. For Pd/SiO₂ and Pd/CeO₂ and Pd/Al₂O₃ the ring hydrogenation leads to the production of 2-cyclohexen-1-one that further hydrogenates to cyclohexanone.

Deactivation of the catalysts was also studied. All catalysts showed significant deactivation during 20 h of time-on-stream, Pd/CeO₂ being the most stable one. Selectivity to benzene decreased and an increase of cyclohexanone formation was observed. Sintering of Pd (with silica as a support) and the loss of acid sites during the reaction for Pd/TiO₂ and Pd/ZrO₂ were determined to be the main causes for deactivation.

HDO with noble metals supported on various zeolites is presented in entries 45–55.^{147,159,160} Zeolites are among the most used catalysts for cracking, isomerization and hydrocarbon synthesis in oil refineries.¹⁶¹ These aluminosilicates are attractive supports for bio-oil hydrotreating not only for their highly ordered structure and uniform pore size but also because their acidity can be tuned to improve activity and selectivity towards a desired product.¹⁶²

Table 5 Overview of different supports for the HDO of different aromatic mono-oxygenated model compounds.

Entry	Reactant	Catalyst		Support	Main product	X (%)	Y (%)	Reactor type	Reaction conditions				Ref.
		Metal	Loading (wt%)						T (°C)	P (Mpa)	t (h)	Solvent	
35	Phenol	Ni	5	ZrO ₂	Cyclohexane	100	83	Batch	275	10	5	—	149
36	Phenol	Ni	5	Al ₂ O ₃	Cyclohexane	100	46	Batch	275	10	5	—	
37	Phenol	Ni	5	SiO ₂	Cyclohexane	80	38	Batch	275	10	5	—	
38	Phenol	Ni	5	CeO ₂	Cyclohexanol	100	88	Batch	275	10	5	—	
39	Phenol	Ni	5	C	—	2	—	Batch	275	10	5	—	
40	Phenol	Pd	1.92	SiO ₂	Benzene	66	39	Fixed bed	300	0.1	0.08	—	158
41	Phenol	Pd	2.28	Al ₂ O ₃	Benzene	58	25	Fixed bed	300	0.1	0.08	—	
42	Phenol	Pd	1.83	TiO ₂	Benzene	72	48	Fixed bed	300	0.1	0.08	—	
43	Phenol	Pd	2.24	ZrO ₂	Benzene	77	51	Fixed bed	300	0.1	0.08	—	
44	Phenol	Pd	2.44	CeO ₂	Benzene	58	29	Fixed bed	300	0.1	0.08	—	
45	Guaiacol	Ni	15.7	Beta (12.5)	Cyclohexane	100	69	Batch	250	4	3.3	—	140
46	Guaiacol	Ni	15.7	Beta (25)	Cyclohexane	95	45	Batch	250	4	3.3	—	
47	Guaiacol	Ni	15.7	Beta (175)	Cyclohexane	66	25	Batch	250	4	3.3	—	
48	Guaiacol	Ni	15.7	Beta (12.5)	Cyclohexane	11	5.4	Fixed bed	230	4	—	—	
49	Guaiacol	Ni	15.7	Beta (25)	Cyclohexane	11	4.4	Fixed bed	230	4	—	—	
50	Guaiacol	Ni	15.7	Beta (175)	Cyclohexane	9	2.4	Fixed bed	230	4	—	—	
51	<i>m</i> -Cresol	Pd	1	HZSM-5 (30)	Methylcyclohexane	100	99	Batch	200	2	6	Dodecane	159
52	<i>m</i> -Cresol	Pd	1	HZSM-5 (100)	Methylcyclohexanone	78	50	Batch	200	2	6	Dodecane	
53	Guaiacol	Pt	0.5	H-Y (2.6)	Cyclohexane	83	48	Batch	250	4	2	Decane	160
54	Guaiacol	Pt	0.5	H-Y (40)	Cyclohexane	72	44	Batch	250	4	2	Decane	
55	Guaiacol	Pt	0.5	H-Y (100)	Cyclohexane	24	18	Batch	250	4	2	Decane	
56	Guaiacol	RuRe	4.0, 3.6	C	Cyclohexane	99	83	Batch	240	2	1	Heptane	130
57	Guaiacol	RuRe	4.0, 3.6	MWCNT	Cyclohexane	99	86	Batch	240	2	1	Heptane	
58	Guaiacol	RuRe	4.0, 3.6	VC	Cyclohexane	93	39	Batch	240	2	1	Heptane	

There are two types of acid sites in zeolites, Brønsted Acid Sites (BAS) donating protons and Lewis Acid Sites (LAS) accepting electrons.¹⁶³ In zeolites BAS are the result of Al substituting Si in the zeolite framework. The cation that compensates the charges is usually H^+ , resulting in a strong Brønsted acid. Structural LAS can be generated in zeolites by high temperature dehydration, which causes dehydroxylation of the Brønsted sites.¹⁶⁴ Other Lewis acid sites can be caused by extra-framework Al species which are not tetrahedrally bound in the framework.¹⁶⁵ In general, the amount of acid sites is proportional to the amount of Al on the framework. Acidic properties depend on the Si/Al ratio, if the ratio increases, the amount of BAS decreases.^{166,167}

The effect of the amount of acid sites on a Ni/Beta zeolite catalyst for the HDO of guaiacol in a batch reactor is presented in entries 45–50.¹⁴⁷ The catalysts were prepared with the same Ni loading (15.7 wt%), but with different Si/Al ratios (12.5, 25 and 175). The rate of cyclohexane formation, which should mainly depend on the catalyst acidity, followed this trend (cyclohexane yields):

Ni/Beta-12.5 (68.9%) > Ni/Beta-25 (45.4%) > Ni/Beta-175 (25.4%).

These results are in agreement with acidity data obtained by NH_3 -TPD and NH_3 -FTIR. The acid sites play a key role in dehydration and demethoxylation reactions.^{167–169} It has also been reported that the acid sites help transalkylation of guaiacol to form catechol, which is more active for HDO.¹⁷⁰

The relationship between catalyst acidity and the formation rate of cyclohexane was evaluated out in a fixed bed reactor with the same catalysts (entries 48–50).¹⁴⁷ The results (at conversion <15%) confirm that the catalyst with a higher amount of acid sites exhibits higher deoxygenation activity and favour cyclohexane formation.

HZSM-5 is a zeolite with strong acidic properties and it has been commonly used for catalytic cracking of bio-oils.¹⁷¹ In entries 51 and 52¹⁵⁹ results for two Pd catalysts supported in HZSM-5 with two different Si:Al ratios tested in HDO of *m*-cresol are reported. Acidity of both catalysts was evaluated through TPD of ammonia. HZSM-5 (30) has a higher acid site density (0.31 mmol g^{-1}) while HZSM-5 (100) had less than half of that (0.12 mmol g^{-1}).

Pd/HZSM-5 (30) showed almost complete conversion at 1 h and a high selectivity for methylcyclohexane (99% at 6 h). On the other hand, Pd/HZSM-5 (100) displayed only 78% conversion and 64% selectivity towards methylcyclohexanone, an oxygenated compound, indicating incomplete deoxygenation at 6 h. The increase of Si resulted in lower acid site density, which in turn gave lower activity.

The HDO of *m*-cresol occurred through tautomerization to a cyclic dienone, followed by hydrogenation of the aromatic ring, giving methylcyclohexanone. Methyl cyclohexane was then obtained *via* C=O hydrogenation and dehydration. It was also observed that selectivity for Pd/HZSM-5 (30) transitioned from favoring C=C hydrogenation to C=O hydrogenation, resulting in high *m*-cresol conversion. A less acidic catalyst, Pd/HZSM-5 (100), favored formation of methylcyclohexanone and

methylcyclohexanol as a consequence of its poorer activity for alcohol dehydration.

The same correlation between the amount of acid sites and HDO activity was found for a series of Pt/HY catalysts with different Si/Al ratios on the HDO of guaiacol (entries 53–55).¹⁶⁰ As the Si/Al molar ratio was increased from 2.6 to 100, the total number of acid sites decreased and guaiacol conversion decreased as well (82.9% to 23.5%). The main product was cyclohexane, indicating high deoxygenation activity.

Studies on the effect of acidity have shown that strong acid sites promote faster coking rate.¹⁷² A higher acid site density also promote more adsorption of oxygenated compounds, which also leads to coke formation.¹⁷³

The use of a bimetallic catalyst comprising Ru and Re supported on activated carbon was discussed in entry 24 and showed a high deoxygenation activity for guaiacol. The use of activated carbon (AC), vulcan carbon (VC) and multiwalled carbon nanotubes (MWCNT) (entries 56–58)¹³⁷ showed high HDO activity for all catalysts. Cyclohexane yields decreased in the following way: RuRe/MWCNT > RuRe/VC > RuRe/AC.

The catalysts RuRe/MWCNT and RuRe/VC exhibited higher activity than RuRe/AC, despite the same metal loading. RuRe/MWCNT and RuRe/VC displayed faster hydrogenolysis rate than RuRe/AC as the complete deoxygenation of guaiacol to cyclohexane occurred within 1 h (>80% yield for both), while it took over 4 h for RuRe/AC to complete the reaction. The pore structure and surface oxygen functionalities of these supports could influence the activity and selectivity of the catalysts. The higher surface oxygen content on the AC support also hindered formation of bimetallic particles, which are necessary for efficient hydrogenolysis of C–OH bonds. The formation of small alkanes (C₃–C₆) was also observed. Propane, butane, pentane, and hexane were formed as cracking side-products.

4.1.3 HDO of real bio-oil. HDO of real lignin, lignin-derived bio-oil and simulated mixtures of oxygenated compounds have been recently studied (see Table 6). Although research of model molecules is important to understand reaction pathways, the HDO of oligomeric compounds can provide better insight for real biorefinery processes. In some cases, depolymerization and HDO are done simultaneously.

HDO of bio-oil with non-noble metals supported on zeolite HZSM-5 showed good degree of deoxygenation (DOD) (entries 59–60).¹⁰⁴ NiCo/HZSM-5 exhibited a higher activity for oxygen removal than the monometallic catalyst (Ni/HZSM-5) as reflected by the deoxygenation degree (DOD). These results were attributed to better dispersed and stabilized Ni particles due to the addition of Co. A higher coke formation was also observed for the monometallic catalyst, which can be related to a higher acid strength.

Bimetallic NiCo/HZSM-5 gave a lower O:C molar ratio for the produced bio-oil and a higher H:C molar ratio (1.91) than with the monometallic catalyst. However, oil obtained with both catalysts showed

Table 6 HDO of real bio-oil.

Entry	Feed	Catalyst	Activity and produced bio-oil properties	Reactor type	Reaction conditions				Ref.
					<i>T</i> (°C)	<i>P</i> (Mpa)	<i>t</i> (h)	Solvent	
59	Bio-oil (PYTEC GmbH) H ₂ O = 33 wt% pH = 3.2 HHV = 21.9 MJ kg ⁻¹	(20 wt%) Ni/HZSM-5	DOD = 25% HHV = 29 MJ kg ⁻¹ Coke deposits = 6.5 wt% O/C = 0.34 H/C = 1.71	Batch	300	6	4	Water	98
60		(10 wt%) Ni (10 wt%) Co/HZSM-5	DOD = 39% HHV = 33 MJ kg ⁻¹ Coke deposits = 4.8 wt% O/C = 0.26 H/C = 1.91						
61	Cork oak bio-oil H ₂ O = 22.4 wt% pH = 2.5 Viscosity = 18.3 cSt HHV = 18.9 MJ kg ⁻¹ O/C = 0.9 H/C = 2.3	(5 wt%) Pt/H-Y (2.6)	pH = 4.6 Viscosity = 18.3 cSt HHV = 24.4 MJ kg ⁻¹ O/C = 0.4 H/C = 1.7	Batch	250	4	2	Decane	160
62	Woody tar H ₂ O = 8.3 wt% pH = 2.3	5 wt% Pt/SiO ₂ 5 wt% Pd/SiO ₂ 20 wt% Co/SiO ₂ 20 wt% Ni/SiO ₂ CoMoS/Al ₂ O ₃	Rate of deoxygenation (%): 37 66 64 72 46	Batch	350	5	3	Hexa-decane	85
63	Fast pyrolysis oil H ₂ O = 30 wt% pH = 2.5 Viscosity = 40 cP	(5 wt%) Pt/C	content (wt%) = 10.2 Oil yield (wt%) = 27 O/C = 0.11 H/C = 1.35	Batch	350	20	4	—	174

Table 6 (Continued)

Entry	Feed	Catalyst	Activity and produced bio-oil properties	Reactor type	Reaction conditions			Ref.
					<i>T</i> (°C)	<i>P</i> (Mpa)	<i>t</i> (h)	
64	HHV = 20.3 MJ kg ⁻¹	(5 wt%) Pd/C	content (wt%) = 6.5 Oil yield (wt%) = 65 O/C = 0.06 H/C = 1.26					
65		(5 wt%) Ru/C	content (wt%) = 5.9 Oil yield (wt%) = 54 O/C = 0.06 H/C = 1.24					
66		(5 wt%) Ru/TiO ₂	content (wt%) = 9.5 Oil yield (wt%) = 67 O/C = 0.09 H/C = 1.31					
67		(5 wt%) Ru/Al ₂ O ₃	content (wt%) = 8.9 Oil yield (wt%) = 35 O/C = 0.04 H/C = 1.09					
68		CoMoS/Al ₂ O ₃	content (wt%) = 7.5 Oil yield (wt%) = 25 O/C = 0.07 H/C = 1.2					
69		NiMoS/Al ₂ O ₃	content (wt%) = 10.6 Oil yield (wt%) = 27 O/C = 0.10 H/C = 1.24					

improvement in O/C and H/C molar ratios when compared to the original bio-oil (O/C \sim 0.51, H/C \sim 1.5).

Molar H/C ratio of the obtained oil with NiCo/HZSM-5 was higher than that of conventional heavy fuel oil and comparable to those of gasoline and diesel. The obtained bio-oil could not be directly used as fuel due to a high O:C ratio, however, it might be suited as a co-feed for a standard refinery unit.⁹⁸

HDO of cork oak-derived bio-oil with Pt/H-Y (entry 61)¹⁶⁷ showed high DOD, the oxygen content was reduced from 49.3% to 28.2% and the carbon content increased from 41.5% to 61.1% simultaneously. pH of the bio-oil increased from 2–3 to 4.6 while viscosity diminished from 18.3 cSt to 2.4 cSt. A heating value (HHV) was also improved, from 18.9 MJ kg⁻¹ of the original bio-oil to 24.4 MJ kg⁻¹ after the reaction.

The HDO of woody tar bio-oil was carried out with different transition metal catalysts (entry 62).⁸⁵ The overall trend of HDO activity was Ni/SiO₂ > Pd/SiO₂, Co/SiO₂ > CoMoS/Al₂O₃ > Pt/SiO₂.

This result showed clearly that the Ni catalyst gave the highest conversion, however, the aromatic selectivity (index of aromatics) decreased in the following order: Co/SiO₂ > CoMoS/Al₂O₃ > Pd/SiO₂ > Pt/SiO₂ > Ni/SiO₂ indicating that the Co catalyst had the highest aromatic hydrocarbon selectivity. This result was explained by the low acidic properties of silica resulting on adsorption of the oxygenated molecules on the weak acid sites of silica by interactions with O atoms, rather than with the aromatic ring.⁸⁵

A screening of catalysts for deep HDO of pyrolysis oil (entries 63–69)¹⁷⁴ showed that the total oil yield was between 25 and 67 wt%. The highest yields were obtained for Pd/C (65% wt%) and Ru/TiO₂ (75 wt%) catalysts. In addition, two liquid phases were obtained, a dense oil phase and a highly acidic aqueous phase (pH 2–3) that contained organic acids, alcohols and esters. The oxygen content of the produced bio-oil varied between 6.5 and 10.6 wt%, the highest being for NiMo/Al₂O₃ and the lowest for Ru/C. Traditional sulfided catalysts exhibited low HDO activity due to the absence of sulfur in the feed.

The effect of the support was determined for Ru catalysts (entries 65–67),¹⁷⁴ for which the bio-oil yield decreased as: TiO₂ > C > Al₂O₃, while for deoxygenation the order was: C > Al₂O₃ > TiO₂.

Low activity of Ru/TiO₂ was attributed to a low surface area and large metal particle sizes. The obtained bio-oil can be used as a replacement or blend of gasoline and diesel, or for co-feeding in oil refineries.¹⁷⁴

4.2 Selective hydrocracking of triglycerides

Triglycerides form all vegetable oils and animal fats.¹⁷⁵ They are composed of three long-chained fatty acid esters and glycerol (see Fig. 4).

Long saturated or unsaturated hydrocarbons chains (C₁₀–C₁₈)¹⁷⁶ make triglycerides attractive for the production of biofuels.

In the recent years research has focused on the upgrading of triglycerides and fatty acids through transesterification and hydrocracking processes.^{177–181}

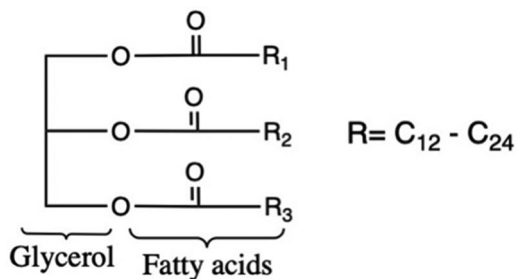


Fig. 4 General triglyceride structure.

Table 7 Summary of the HDC results for several vegetable oils.

Entry	Reactant	Catalyst	Main products and activity	Reactor type	Reaction conditions	Ref.
70	Coconut oil	NiMo/ Al ₂ O ₃	Jet fuel fraction: C ₁₀ –C ₁₆ Y at 260 °C (%) ≈ 10 Y at 340 °C (%) ≈ 55 Y at 380 °C (%) ≈ 55 Main products: saturated hydrocarbons	Fixed bed	T (°C) = 260–380 P (MPa) = 3 LHSV (h ^{−1}) = 1–3	181
71	Sunflower oil	ZSM-5	Hydrocarbon fuels: C ₇ –C ₃₀ Y at 450 °C (%) = 59 Y at 500 °C (%) = 63 Y at 550 °C (%) = 74	Fixed bed	T (°C) = 450, 500 and 550 LHSV (h ^{−1}) = 3	192
72	Palm oil	(1 wt%) Pt/Beta	Light hydrocarbons (<C ₇)	Fixed bed	T (°C) = 295 P (MPa) = 2 LHSV (h ^{−1}) = 2	193

Transesterification is usually used to produce biodiesel (esters) from triglycerides in the presence of a basic catalyst and a short-chain alcohol, such as methanol.¹⁸² Although biodiesel has shown to produce lower emissions and higher burning efficiencies than regular diesel fuel,¹⁸³ its use is limited due to chemical and thermal stability, low compatibility with gas engines, high freezing and cloud points, and low heating values caused by its oxygen content.^{184,185}

Catalytic hydrocracking (HDC) is a process commonly used in petroleum refineries.¹⁸⁶ It is a combination of different reactions (hydrogenation of double bonds, propane split, HDO, decarbonylation and decarboxylation) at high temperatures and pressures used to break down heavy compounds into smaller fragments in the presence of an acidic or bifunctional catalysts¹³¹ (see Table 7), similar to those used for HDO.

The catalytic upgrading of bio-oil to jet fuel range alkanes occurs through two consecutive steps. The first step is the deoxygenation of bio-oil into *n*-alkanes (C₁₅–C₂₀)¹⁸⁷ followed by hydro-isomerization and hydro-cracking of these alkanes to form iso-alkanes (C₈–C₁₆).¹⁸⁸

In general, the hydrocracking reaction can happen through four different mechanisms: Thermal hydrocracking can be achieved without the use of a catalyst. Instead, high temperatures (500–600 °C) and H₂ pressures are used to break carbon bonds through production of free radicals.¹⁸⁹ Acid catalysts can induce cracking through the formation of carbenium (bimolecular cracking) and carbonium ions (monomolecular cracking).¹⁹⁰ Zeolites are the preferred catalysts because of their porosity, which can remove diffusion restrictions, and the optimized amount of acid sites which improves hydro-isomerization and hydrocracking.¹⁸⁸ For bifunctional catalysts composed of a metal and a solid acid, C–C scission and skeletal rearrangement occur *via* carbocations. The reaction goes through dehydrogenation of saturated molecules on the metal sites, followed by hydrogenation of olefinic intermediates desorbed from acid sites.¹⁹¹

The use of conventional sulfided NiMo/Al₂O₃ catalysts (entry 70)¹⁸¹ showed that when increasing temperature and decreasing LHSV the conversion of triglycerides and yield of the jet fuel fraction (C₁₀–C₁₆) increased considerably, from *ca.* 10% yield at 260 °C to 55% yield at temperatures higher than 330 °C. The main drawback of using sulfided NiMo catalysts is that sulfur can be present in the product. The sulfur content in the jet fuel fraction also decreased when increasing temperature and lowering LHSV, it being still present at 340 °C (<10 mg kg⁻¹).

Freezing points of the jet fuel fractions were higher (–11 to +18 °C) than the standard requirements (–47 °C) due to the presence of *n*-paraffins, so the jet fuel fractions had to undergo further isomerization reactions.¹⁸¹

Zeolites without any supported metal have also been used for HDC (entry 71).¹⁹² The effect of temperature was observed in the product distribution, with higher temperatures giving a higher fraction of smaller hydrocarbons (C₇–C₁₁). High temperature (550 °C) gave a higher hydrocarbon yield. Additionally, the gases produced at 550 °C contained high amounts of CO, CO₂, H₂ and light hydrocarbon contents, which could be used as syngas.

Single-step HDC of palm oil with the bifunctional Pt/beta catalyst was carried out to study the catalyst stability (entry 72).¹⁹³ The catalyst showed fast deactivation (within 24 h) and high coke formation (up to 16 wt%). Light hydrocarbons (<C₇) were the main product, with low amounts of isomerized C₈–C₁₆ products, indicating overcracking.

Fast deactivation of Pt/Beta and overcracking were determined to be the result of a lack of hydrogenation and dehydrogenation sites, meaning that Pt was poisoned by generation of CO during carbonylation of fatty acids.¹⁹³

5 Conclusions

The demand for greener and renewable energy sources has grown considerably in recent years. The production of liquid fuels from biomass and its capability to replace at least partially existing fossil fuels or be

added into the current transportation and refining infrastructure have paved the way for the future industrialization.

The design of a bifunctional catalyst for HDO is not a straightforward task, as product selectivity (aromatic or aliphatic compounds), reactor design (batch or continuous) and the mode of operation (two-phase or multiphase) have to be taken into account.

In any case efficient bifunctional catalysts must have a balance between both metal and acid sites. Key features to consider are:

The metal particle size and dispersion. Small well-dispersed metal particles are preferred as they have a higher amount of active surface atoms. On the other hand, stability of metal nanoparticles decreases with size, as smaller particles are more prone to agglomeration.

Selection of the metal. Noble metals (Pt, Pd, Ru, Rh) tend to promote hydrogenation of the aromatic ring before deoxygenation thus giving aliphatic compounds as the main products. Non-noble transition metals (Co, Mo, Fe) with lower hydrogenating activity can shift selectivity towards aromatics. Noble metals also tend to deactivate faster and are more expensive than transition metals. Bimetallic systems can decrease coke formation as the interactions between metals can lead to a weaker adsorption of the intermediates.

Support selection. Supports help to increase the hydrothermal stability of the metal particles, providing also the acid sites needed to carry out the C–O cleavage. Stronger interactions between the phenolic oxygen and oxophilic sites of the support result in hydrogenation of the carbonyl group while weak ones lead to hydrogenation of the aromatic ring. In some instances, the use of certain metal oxides (CoO_x , ReO_x) in combination with a hydrogenating metal has resulted in good aromatic yields.

Zeolites are versatile supports, as the Si:Al ratio can be modified to provide different acid site density or strength, which in turn affects selectivity. Catalysts with a higher amount of acid sites exhibit higher deoxygenation activity, however, too high acidity can also lead to cracking and deactivation through coke formation.

Metal and support interactions. Strong interactions can suppress deactivation caused by metal sintering or leaching. The use of bimetallic catalysts can also help to stabilize certain metals and avoid loss of activity.

6 Future prospects

Overall HDO and HDC processes for the production of biofuels are still at early stages and have much potential. The main challenges in developing efficient catalysts are deactivation by coking and poisoning, catalyst regeneration and decreasing reaction conditions while maintaining activity and selectivity to make these processes attainable at an industrial scale for the production of alternative fuels.

Decreasing costs of the catalysts by taking advantage of promoters or different supports to obtain smaller and stable metal particles is also of industrial importance.^{95,96,137} Obtaining alternate sources of hydrogen,

as most of the H₂ used comes from petroleum refining,¹⁹⁴ has also led to interesting developments.

Avoiding external H₂ supply can be achieved in a number of ways; catalytic transfer hydrogenation/hydrolysis (CTH) allows for the use of hydrogen-donor solvents such as tetralin,^{195,196} decalin¹⁹⁷ and alcohols.^{96,198} Hydrolysis of some metals (Zn, Mg) followed by *in-situ* HDO can be achieved by splitting water on the metallic surface to obtain hydrogen. Recently Zn⁰ was shown to be effective for the production of hydrocarbons from pine sawdust bio-oil.¹⁹⁹ Another study using 2-propanol as a hydrogen donor and a RuRe/C catalyst showed complete guaiacol conversion (99%) at 240 °C for 5 h, giving high cyclohexane yield (>55%).²⁰⁰

Electrocatalytic hydrogenation (ECH) has also attracted attention as an alternative to HDO under very mild conditions. It can be carried out at low temperatures and atmospheric pressure without using molecular H₂ or H donors, relying instead on the reduction of protons from the solution to form atomic hydrogen on the surface of the catalytic electrode, where it can hydrogenate the oxygenated compounds.²⁰¹ A study on the HDO of guaiacol in water using Ru supported on activated carbon cloth as a cathode showed that high conversion (70%) can be achieved at 80 °C, however low deoxygenation activity was obtained.²⁰²

A different ECH study using a dual-catalyst system composed of Pt/C suspended on a soluble polyoxometalate for the HDO of phenol and guaiacol at 35 °C showed conversions over 99% and high hydrogenating activity, yet deoxygenation product yield remained low (19%).²⁰³ These results fall in line with similar studies.^{204,205}

The use non-thermal plasma (NTP) has been recently studied for carrying out HDO under ambient temperature and atmospheric pressure. Interactions between plasma and catalysts have not been completely described, however, it has been hypothesized that electrons generated in a plasma reactor can break certain C–O and C–H bonds with the help of a catalyst.²⁰⁶

The most common technique used is dielectric barrier discharge (DBD) due to its simplicity and efficiency for generating radicals.²⁰⁷ The main parameters to consider are the carrier gas feed, plasma power used (W), voltage (kV) and pulse frequency (kHz). NTP HDO can be carried out in the presence of H₂ flow, studies have shown a high guaiacol conversion (87%) with a Co/SiO₂ catalyst at 80 W plasma power for 3–4 s, however the deoxygenation product yield was low (<2%).²⁰⁸

In-situ hydrogen generation can also be achieved with NTP, a study with different metals on supported Al₂O₃ presented the following guaiacol conversion at 12 kV: PtCl/Al₂O₃ (92%) > PtRe/Al₂O₃ > NiMo/Al₂O₃ > CoMo/Al₂O₃ > Ni/Al₂O₃ > plasma alone (57%). However, deoxygenation was not completely achieved as substituted phenols were the main products obtained.²⁰⁹ These results are in line with other reports in the literature.^{210,211}

Ionic liquids (ILs) have also been tested for HDO. ILs are commonly used for liquid–liquid extraction/separation of azeotropic mixtures due to their solubility properties, which can also be used for the separation of

soluble phenolic compounds and insoluble hydrocarbons in biomass upgrading. ILs, also known as green solvents, are composed of large organic cations coupled with organic and inorganic anions.²¹² They show properties different from conventional solvents, such as low vapor pressures, high viscosities, high ionic conductivity and electrochemical and hydrothermal stability.

The use of ILs for HDO has shown promising results; the use of an IL with Brønsted acidity in combination with noble metal nanoparticles (Rh, Pt, Ru) resulted in high conversion (>95%) for phenol and *p*-cresol into cyclohexane (20% yield) at mild conditions (4 h at 130 °C and 4 MPa of H₂).²¹³ Another study on the use of ILs with Pt supported on HZSM-5 for the HDO of various substituted phenolic compounds demonstrated high deoxygenation activity, namely 94% conversion for 4-propylphenol, giving mainly propylbenzene (70% yield) at even milder reaction conditions (1–2 h at 110 °C and 1 MPa of H₂).²¹⁴ HDO using ILs and metal nanoparticles at lower temperatures (<100 °C) has also been reported,²¹⁵ giving a high deoxygenation degree (>95%) at temperatures as low as 60 °C.²¹⁶

These technologies should be further developed, as they still struggle with selectivity towards complete deoxygenation products or efficiency, which hinders their application for HDO to produce fuels.

References

- 1 K. Nagy and K. Körmendi, *Appl. Energy*, 2012, **96**, 393.
- 2 R. A. Barreto, *Econ. Modell.*, 2018, **75**, 196.
- 3 M. Y. Kim, J.-K. Kim, M.-E. Lee, S. Lee and M. Choi, *ACS Catal.*, 2017, **7**, 6256.
- 4 C.-M. Liu and S.-Y. Wu, *Renewable Energy*, 2016, **96**, 1056.
- 5 A. J. Ragauskas, C. K. Williams, B. H. Davison, G. Britovsek, J. Cairney, C. A. Eckert, W. J. Frederick, J. P. Hallett, D. J. Leak, C. L. Liotta, J. R. Mielenz, R. Murphy, R. Templer and T. Tschaplinski, *Science*, 2006, **311**, 484.
- 6 J. C. Serrano-Ruiz and J. A. Dumesic, *Energy Environ. Sci.*, 2011, **4**, 83.
- 7 Q. Bu, H. Lei, A. H. Zacher, L. Wang, S. Ren, J. Liang, J. Wei, Y. Liu, J. Tang, Q. Zhang and R. Ruan, *Bioresour. Technol.*, 2012, **124**, 470.
- 8 M. Rodionova, R. Poudyal, I. Tiwari, R. Voloshin, S. Zharmukhamedov, H. Nam, B. Zayadan, B. Bruce, H. Hou and S. Allakhverdiev, *Int. J. Hydrogen Energy*, 2017, **42**, 8450.
- 9 A. Kumar and S. Sharma, *Renewable Sustainable Energy Rev.*, 2011, **15**, 1791.
- 10 A. B. H. Trabelsi, K. Zaafour, W. Baghdadi, S. Naoui and A. Ouerghi, *Renewable Energy*, 2018, **126**, 888.
- 11 R. Ravindran and A. K. Jaiswal, *Bioresour. Technol.*, 2016, **199**, 92.
- 12 Y. Chisti, *Biotechnol. Adv.*, 2007, **25**, 294.
- 13 W.-H. Leong, J.-W. Lim, M.-K. Lam, Y. Uemura and Y.-C. Ho, *Renewable Sustainable Energy Rev.*, 2018, **91**, 950.
- 14 A. Demirbas and M. F. Demirbas, *Energy Convers. Manage.*, 2011, **52**, 163.
- 15 N. Pragma, K. K. Pandey and P. Sahoo, *Renewable Sustainable Energy Rev.*, 2013, **24**, 159.
- 16 L. Lardon, A. Hélias, B. Sialve, J.-P. Steyer and O. Bernard, *Environ. Sci. Technol.*, 2009, **43**, 6475.

- 17 P. Schenk, S. Thomas-Hall, E. Stephens, U. Marx, J. Mussnug, C. Posten, O. Kruse and B. Hankamer, *Bioenergy Res.*, 2008, **1**, 20.
- 18 J. Lü, C. Sheahan and P. Fu, *Energy Environ. Sci.*, 2011, **4**, 2451.
- 19 S. V. Vassilev and C. G. Vassileva, *Fuel*, 2016, **181**, 1.
- 20 V. S. Sikarwar, M. Zhao, P. S. Fennell, N. Shah and E. J. Anthony, *Prog. Energy Combust. Sci.*, 2017, **61**, 189.
- 21 K. Dutta, A. Daverey and J.-G. Lin, *Renewable Energy*, 2014, **69**, 114.
- 22 G. R. Timilsina, *Philos. Trans. R. Soc., A*, 2013, **372**, 20120323.
- 23 D. Meier and O. Faix, *Bioresour. Technol.*, 1999, **68**, 71.
- 24 M. I. Jahirul, M. G. Rasul, A. A. Chowdhury and N. Ashwath, *Energies*, 2012, **5**, 4952.
- 25 G.-J. Kwon, D.-Y. Kim, S. Kimura and S. Kuga, *J. Anal. Appl. Pyrolysis*, 2007, **80**, 1.
- 26 S. Ucar and S. Karagoz, *J. Anal. Appl. Pyrolysis*, 2009, **84**, 151.
- 27 H. F. Gercel, *J. Anal. Appl. Pyrolysis*, 2011, **92**, 233.
- 28 S. Grierson, V. Strezov and P. Shah, *Bioresour. Technol.*, 2011, **102**, 8232.
- 29 H. B. Goyal, D. Seal and R. C. Saxena, *Renewable Sustainable Energy Rev.*, 2008, **12**, 504.
- 30 D. Ayhan, *Energy Convers. Manage.*, 2001, **42**, 1357.
- 31 A. Demirbas and G. Arin, *Energy Sources*, 2002, **24**, 471.
- 32 H. F. Gercel, *Bioresour. Technol.*, 2002, **85**, 113.
- 33 F. A. López, T. A. Centeno, I. García-Díaz and F. J. Alguacil, *J. Anal. Appl. Pyrolysis*, 2013, **104**, 551.
- 34 D. Meier, *Adv. Biochem. Eng./Biotechnol.*, 2017, **166**, 1.
- 35 C. E. Efika, C. Wu and P. T. Williams, *J. Anal. Appl. Pyrolysis*, 2012, **95**, 87.
- 36 J. Jae, G. A. Tompsett, Y.-C. Lin, T. R. Carlson, J. Shen, T. Zhang, B. Yang, C. E. Wyman, W. C. Conner and G. W. Huber, *Energy Environ. Sci.*, 2010, **3**, 358.
- 37 E. Ranzi, A. Cuoci, T. Faravelli, A. Frassoldati, G. Migliavacca, S. Pierucci and S. Sommariva, *Energy Fuels*, 2008, **22**, 4292.
- 38 H. Yang, R. Yan, H. Chen, D. H. Lee and C. Zheng, *Fuel*, 2007, **86**, 1781.
- 39 Y. Han, M. Gholizadeh, C.-C. Tran, S. Kaliaguine, C.-Z. Li, M. Olarte and M. Garcia-Perez, *Fuel Process. Technol.*, 2019, **195**, 106140.
- 40 M. Bertero, G. de la Puente and U. Sedran, *Fuel*, 2012, **95**, 263.
- 41 M. García-Pérez, A. Chaale, H. Pakdel, D. Kretschmer and C. Roy, *J. Anal. Appl. Pyrolysis*, 2007, **78**, 104.
- 42 Y. Yu, Y. W. Chua and H. Wu, *Energy Fuels*, 2016, **30**, 4145.
- 43 M. S. Talmadge, R. M. Baldwin, M. J. Biddy, R. L. McCormick, G. T. Beckham, G. A. Ferguson, S. Czernik, K. A. Magrini-Bair, T. D. Foust, P. D. Metelski, C. Hetrick and M. R. Nimlos, *Green Chem.*, 2014, **16**, 407.
- 44 J. Zakzeski, P. C. A. Bruijninx, A. L. Jongerius and B. M. Weckhuysen, *Chem. Rev.*, 2010, **110**, 3552.
- 45 P. J. D. Wild, W. J. J. Huijgen and H. J. Heeres, *J. Anal. Appl. Pyrolysis*, 2012, **92**, 95.
- 46 F. Cheng and C. E. Brewer, *Renewable Sustainable Energy Rev.*, 2017, **72**, 673.
- 47 S. A. Ahmad, G. Ibrahim, K. Slim and A. Karbassi, *Environ. Energy Econ. Res.*, 2019, **3**, 291.
- 48 M. Balat, *Energy Sources, Part A*, 2019, **33**, 674.
- 49 A. V. Bridgwater, *Therm. Sci.*, 2004, **8**, 21.
- 50 J. G. Brammer, M. Lauer and A. V. Bridgwater, *Energy Policy*, 2006, **34**, 2871.

- 51 T. Cornelissen, J. Yperman, G. Reggers, S. Schreurs and R. Carleer, *Fuel*, 2008, **87**, 1031.
- 52 L. Wu, S. Guo, C. Wang and Z. Yang, *Ind. Eng. Chem. Res.*, 2008, **47**, 9248.
- 53 G. W. Huber, S. Iborra and A. Corma, *Chem. Rev.*, 2006, **106**, 4044.
- 54 U. Yildirim and S. Abanteriba, *Procedia Eng.*, 2012, **49**, 310.
- 55 T. Edwards, *J. Eng. Gas Turbines Power*, 2007, **129**, 13.
- 56 B. Gawron and T. Bialecki, *Int. J. Environ. Sci. Technol.*, 2015, **15**, 1501.
- 57 G. Liu, B. Yan and G. Chen, *Renewable Sustainable Energy Rev.*, 2013, **25**, 59.
- 58 P. Kallio, A. Pásztor, M. K. Akhtar and P. R. Jones, *Curr. Opin. Biotechnol.*, 2014, **26**, 50.
- 59 J. I. Hileman and R. W. Stratton, *Transport Policy*, 2014, **34**, 52.
- 60 S. Blakey, L. Rye and C. W. Wilson, *Proc. Combust. Inst.*, 2011, **33**, 2863.
- 61 A. M. Ashraful, H. H. Masjuki, M. A. Kalam, I. M. Rizwanul Fattah, S. Imtenan, S. A. Shahir and H. M. Mobarak, *Energy Convers. Manage.*, 2014, **80**, 202.
- 62 C. Zhang, X. Hui, Y. Lin and C.-J. Sung, *Renewable Sustainable Energy Rev.*, 2016, **54**, 120.
- 63 C. Gutierrez-Antonio, F. I. Gomez Castro, J. A. de Lira-Flores and S. Hernandez, *Renewable Sustainable Energy Rev.*, 2017, **79**, 709.
- 64 M. Rabaev, M. V. Landau, R. Vidruk-Nehemya, V. Koukouliev, R. Zarchin and M. Herskowitz, *Fuel*, 2015, **161**, 287.
- 65 A. P. P. Pires, Y. Han, J. Kramlich and M. Garcia-Perez, *BioResources*, 2018, **13**, 2632.
- 66 P. Aksoy, O. Gül, R. Cetiner, D. A. Fonseca, M. Sobkowiak, S. Falcone-Miller, B. G. Miller and B. Beaver, *Energy Fuels*, 2009, **23**, 2047.
- 67 I. Mochida and K.-H. Choi, *J. Jpn. Pet. Inst.*, 2004, **43**, 145.
- 68 M. E. Pacheco, V. M. M. Salim and J. C. Pinto, *Braz. J. Chem. Eng.*, 2009, **26**, 733.
- 69 L. Zhang, R. Liu, R. Yin and Y. Mei, *Renewable and Sustainable Energy Rev.*, 2013, **24**, 66.
- 70 A. V. Bridgwater, *Biomass Bioenergy*, 2012, **38**, 68.
- 71 A. R. Ardiyanti, S. A. Khromova, R. H. Venderbosch, V. A. Yakovlev and H. J. Heeres, *Appl. Catal., B*, 2012, **117–118**, 105.
- 72 W. Jin, L. Pastor-Perez, D. Shen, A. Sepulveda-Escribano, S. Gu and T. R. Reina, *ChemCatChem*, 2018, **11**, 924.
- 73 D. Murzin and T. Salmi, *Catalytic Kinetics*, Elsevier Science & Technology Books, 2nd edn, 2016.
- 74 B. Donnis, R. G. Egeberg, P. Blom and K. G. Knudsen, *Top. Catal.*, 2009, **52**, 229.
- 75 H. L. Coonradt and W. E. Garwood, *Ind. Eng. Chem. Process Des. Dev.*, 1964, **3**, 38.
- 76 T. J. Benson, R. Hernandez, M. G. White, W. T. French, E. E. Alley, W. E. Holmes and B. Thompson, *Clean: Soil, Air, Water*, 2008, **36**, 652.
- 77 V. Blay, B. Louis, R. Miravalles, T. Yokoi, K. A. Peccatiello, M. Clough and B. Yilmaz, *ACS Catal.*, 2017, **7**, 6542.
- 78 T. Kaka-khel, P. Mäki-Arvela, M. Azkaar, Z. Vajglová, A. Aho, J. Hemming, M. Peurla, K. Ernänen, N. Kumar and D. Y. Murzin, *Mol. Catal.*, 2019, **476**, 110515.
- 79 A. B. M. S. Hossain, A. Salleh, A. N. Boyce, P. Chowdhury and M. Naqiuddin, *Am. J. Biochem. Biotechnol.*, 2008, **4**, 250.
- 80 T. Kotake, H. Kawamoto and S. Saka, *J. Anal. Appl. Pyrolysis*, 2014, **105**, 309.
- 81 A. N. K. Lup, F. Abnisa, M. A. W. D. Wan and M. K. Aroua, *Appl. Catal., A*, 2017, **541**, 87.

-
- 82 Y. Romero, F. Richard, Y. Renéme and S. Brunet, *Appl. Catal., A*, 2009, **353**, 46.
- 83 N. Lei and D. E. Resasco, *J. Catal.*, 2014, **317**, 22.
- 84 V. O. O. Gonçalves, P. M. D. Souza, V. T. D. Silva, F. B. Noronha and F. Richard, *Appl. Catal., B*, 2017, **205**, 357.
- 85 T. Mochizuki, S.-Y. Chen, M. Toba and Y. Yoshimura, *Appl. Catal., B*, 2014, **146**, 237.
- 86 X. Zhang, L. Chen, Q. Zhang, J. Long, T. Wang and L. Ma, *Prog. Chem.*, 2014, **26**, 1997.
- 87 A. Wawrzetz, B. Peng, A. Hrabar, A. Jentys, A. A. Lemonidou and J. A. Lercher, *J. Catal.*, 2010, **269**, 411.
- 88 R. M. West, D. J. Braden and J. A. Dumesic, *J. Catal.*, 2009, **262**, 134.
- 89 Y. Nakagawa, S. Liu, M. Tamura and K. Tomishige, *ChemSusChem*, 2015, **8**, 1114.
- 90 A. L. Jongerius, R. Jastrzebski, P. C. A. Bruijninx and B. M. Weckhuysen, *J. Catal.*, 2012, **285**, 315.
- 91 E. Laurent and B. Delmon, *Appl. Catal., A*, 1994, **109**, 77.
- 92 R. Wandas, J. Surygata and E. Sliwka, *Fuel*, 1996, **75**, 687.
- 93 A. Gutierrez, R. K. Kaila, M. L. Honkela, R. Slioor and A. O. I. Krause, *Catal. Today*, 2009, **147**, 239.
- 94 D. Gao, C. Schweitzer, H. T. Hwang and A. Varma, *Ind. Eng. Chem. Res.*, 2014, **53**, 18658.
- 95 J. Sun, A. M. Karim, H. Zhang, L. Kovarik, X. S. Li, A. J. Hensley, J.-S. McEwen and Y. Wang, *J. Catal.*, 2013, **306**, 47.
- 96 M. Kim, J.-M. Ha, K.-Y. Lee and J. Jae, *Catal. Commun.*, 2016, **86**, 113.
- 97 Y. Wang, H. Huang, N. C. Baxter, Y. Liao, Y. Zhao and S. Wang, *Catal. Today*, 2020, **358**, 60.
- 98 T. M. Huynh, U. Armbruster, M.-M. Pohl, M. Schneider, J. Radnik, D.-L.- Hoang, B. M. Q. Phan, D. A. Nguyen and A. Martin, *ChemCatChem*, 2014, **6**, 1940.
- 99 O. Y. Gutiérrez and T. Klimova, *J. Catal.*, 2011, **281**, 50.
- 100 E. Lecrenay, K. Sakanishi and I. Mochida, *Catal. Today*, 1997, **39**, 13.
- 101 Z. Vít, *Fuel*, 1993, **72**, 105.
- 102 W. Han, S. Wang, X. Li, B. Ma, M. Du, L. Zhou, Y. Yang, Y. Zhang and H. Ge, *RSC Adv.*, 2020, **10**, 8055.
- 103 H. Metiu, S. Chrétien, Z. Hu, B. Li and X. Sun, *J. Phys. Chem. C*, 2012, **116**, 10439.
- 104 M. Brorson, A. Carlsson and H. Topsøe, *Catal. Today*, 2007, **123**, 31.
- 105 R. R. Chianelli, G. Berhault and B. Torres, *Catal. Today*, 2009, **147**, 275.
- 106 Z. He and X. Wang, *Catal. Sustainable Energy*, 2013, **1**, 28.
- 107 Y. Romero, F. Richard and S. Brunet, *Appl. Catal., B*, 2010, **98**, 213.
- 108 E. Laurent and B. Delmon, *Appl. Catal., A*, 1994, **109**, 77.
- 109 J. B. S. Bredenberg, M. Huuska and P. Toropainen, *J. Catal.*, 1989, **120**, 401.
- 110 V. N. Bui, D. Laurenti, P. Afanasiev and C. Geantet, *Appl. Catal., B*, 2011, **101**, 239.
- 111 S. K. Sahoo, S. S. Ray and I. D. Singh, *Appl. Catal., A*, 2004, **278**, 83.
- 112 S. J. Hurff and M. T. Klein, *Ind. Eng. Chem. Fundam.*, 1983, **22**, 426.
- 113 F. P. Petrocelli and M. T. Klein, *Fuel Sci. Technol. Int.*, 1987, **5**, 63.
- 114 J. Shabtai, N. K. Nag and F. E. Massoth, *J. Catal.*, 1987, **104**, 413.
- 115 G. S. Foo, A. K. Rogers, M. M. Yung and C. Sievers, *ACS Catal.*, 2016, **6**, 1292.
- 116 Z. Si, X. Zhang, C. Wang, L. Ma and R. Dong, *Catalysts*, 2017, **7**, 169.
- 117 S. T. Oyama, *Catal. Today*, 1992, **15**, 179.
-

- 118 T. R. Viljava, R. S. Komulainen and A. O. I. Krause, *Catal. Today*, 2000, **60**, 83–92.
- 119 O. I. Senol, E.-M. Ryymin, T.-R. Viljava and A. O. I. Krause, *J. Mol. Catal. A: Chem.*, 2007, **277**, 107.
- 120 W. Luo, W. Cao, P. C. A. Bruijninx, L. Lin, A. Wang and T. Zhang, *Green Chem.*, 2019, **21**, 3744.
- 121 B. Güvenatam, O. Kurşun, E. H. J. Heeres, E. A. Pidko and E. J. M. Hensen, *Catal. Today*, 2004, **233**, 83.
- 122 C. Chen, G. Chen, F. Yang, H. Wang, J. Han, Q. Ge and X. Zhu, *Chem. Eng. Sci.*, 2015, **135**, 145.
- 123 A. N. K. Lup, F. Abnisa, W. M. A. W. Daud and M. K. Aroua, *J. Ind. Eng. Chem.*, 2017, **56**, 1.
- 124 J. Chang, T. Danuthai, S. Dewiyanti, C. Wang and A. Borgna, *ChemCatChem*, 2013, **5**, 3041.
- 125 A. J. Foster, P. T. M. Do and R. F. Lobo, *Top. Catal.*, 2012, **55**, 118.
- 126 R. H. Venderbosch, A. R. Ardiyanti, J. Wildschut, A. Oasmaa and H. J. Heeres, *J. Chem. Technol. Biotechnol.*, 2010, **85**, 674.
- 127 K. C. Kwon, H. Mayfield, T. Marolla, B. Nichols and M. Mashburn, *Renewable Energy*, 2011, **36**, 907.
- 128 N. Kaewtrakulchai, R. Kaewmeesri, Y. Itthibenchapong, A. Eiad-Ua and K. Faungnawakij, *Catalysts*, 2020, **10**, 694.
- 129 A. Centeno, E. Laurent and B. Delmon, *J. Catal.*, 1995, **154**, 288.
- 130 K. B. Jung, J. Lee, J.-M. Ha, H. Lee, D. J. Suh, C.-J. Jun and J. Jae, *Catal. Today*, 2018, **303**, 191.
- 131 P. M. Mortensen, J.-D. Grunwaldt, P. A. Jensen, K. G. Knudsen and A. D. Jensen, *Appl. Catal., A*, 2011, **407**, 1.
- 132 M. Kim, J.-M. Ha, K.-Y. Lee and J. Jae, *Catal. Commun.*, 2016, **86**, 113.
- 133 M. Saidi, F. Samimi, D. Karimipourfard, T. Nimmanwudipong, B. C. Gates and M. R. Rahimpour, *Energy Environ. Sci.*, 2014, **7**, 103.
- 134 S. De, J. Zhang, R. Luque and N. Yan, *Energy Environ. Sci.*, 2015, **9**, 3314.
- 135 S. Liu, S. Dutta, W. Zheng, N. S. Gould, Z. Cheng, B. Xu, B. Saha and D. G. Vlachos, *ChemSusChem*, 2017, **10**, 3225.
- 136 N. T. Tran, Y. Uemura and A. Ramli, *Procedia Eng.*, 2016, **148**, 125.
- 137 N. Arun, R. V. Sharma and A. K. Dalai, *Renewable Sustainable Energy Rev.*, 2015, **48**, 240.
- 138 Y. Yang, C. Ochoa-Hernández, V. A. de la Peña O'Shea, P. Pizarro, J. M. Coronado and D. P. Serrano, *Appl. Catal., B*, 2014, **145**, 91.
- 139 X. Zhang, W. Tang, Q. Zhang, T. Wang and L. Ma, *Energy Procedia*, 2017, **105**, 518.
- 140 P. Yan, M. M.-J. Li, A. A. Adesina, G. Zhao, A. Setiawan, E. M. Kennedy and M. Stockenhuber, *Catal. Sci. Technol.*, 2020, **10**, 810.
- 141 H. Vargas-Villagrán, M. A. Flores-Villeda, I. Puente-Lee, D. A. Solís-Casados, A. Gómez-Cortés, G. Díaz-Guerrero and T. E. Klimova, *Catal. Today*, 2020, **349**, 26.
- 142 H. Shi, J. Chen, Y. Yang and S. Tian, *Fuel Process. Technol.*, 2014, **118**, 161.
- 143 Y. Yang, G. Lv, L. Deng, B. Lu, J. Li, J. Zhang, J. Shi and S. Du, *Microporous Mesoporous Mater.*, 2017, **250**, 47.
- 144 M. Badawi, J.-F. Paul, E. Payen, Y. Romero, F. Richard, S. Brunet, A. Popov, E. Kondratieva, J.-P. Gilson, L. Mariey, A. Travert and F. Maugé, *Oil Gas Sci. Technol.*, 2013, **68**, 829.
- 145 A. Y. Stakheev and L. M. Kustov, *Appl. Catal., A*, 1999, **188**, 3.
- 146 Z. He and X. Wang, *Catal. Sustainable Energy*, 2012, **1**, 28.
- 147 J. Tapia, N. Acelas, D. López and A. Moreno, *Univ. Sci.*, 2017, **22**, 71.

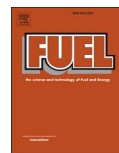
-
- 148 M. Breyse, C. Geantet, P. Afanasiev, J. Blanchard and M. Vrinat, *Catal. Today*, 2008, **130**, 3.
- 149 P. M. Mortensen, J.-D. Grunwaldt, P. A. Jensen and A. D. Jensen, *ACS Catal.*, 2013, **3**, 1774.
- 150 E. Laurent and B. Delmon, *Appl. Catal., A*, 1994, **109**, 97.
- 151 J. S. Yoon, J. W. Choi, D. J. Suh, K. Lee, H. Lee and J. M. Ha, *ChemCatChem*, 2015, **7**, 2669.
- 152 W. Li, C. Pan, L. Sheng, Z. Liu, P. Chen, H. Lou and X. Zheng, *Bioresour. Technol.*, 2011, **102**, 9223.
- 153 K. Yan, Y. Li, X. Zhang, X. Yang, N. Zhang, J. Zheng, B. Chen and K. J. Smith, *Int. J. Hydrogen Energy*, 2015, **40**, 16137.
- 154 V. N. Bui, D. Laurenti, P. Delichère and C. Geantet, *Appl. Catal., B*, 2011, **101**, 246.
- 155 A. Corma, *Chem. Rev.*, 1997, **97**, 2373.
- 156 J. Duan, J. Han, H. Sun, P. Chen, H. Lou and X. Zheng, *Catal. Commun.*, 2012, **17**, 76.
- 157 B. Yan, S. Huang, S. Wang and X. Ma, *ChemCatChem*, 2014, **6**, 2671.
- 158 P. M. De Souza, R. C. Rabelo-Neto, L. E. P. Borges, G. Jacobs, B. H. Davis, D. E. Resasco and F. B. Noronha, *ACS Catal.*, 2017, **7**, 2058.
- 159 J. A. Hunns, M. Arroyo, A. F. Lee, J. M. Escola, D. Serrano and K. Wilson, *Catal. Sci. Technol.*, 2016, **6**, 2560.
- 160 H. Lee, H. Kim, M. J. Yu, C. H. Ko, J.-K. Jeon, J. Jae, S. H. Park, S.-C. Jung and Y.-K. Park, *Sci. Rep.*, 2016, **6**, 28765.
- 161 A. Primo and H. Garcia, *Chem. Soc. Rev.*, 2014, **43**, 7548.
- 162 R. Bai, Y. Song, Y. Li and J. Yu, *Trends Chem.*, 2019, **1**, 601.
- 163 J. F. Haw, *Phys. Chem. Chem. Phys.*, 2002, **4**, 5431.
- 164 E. G. Derouane, J. C. Védrine, R. Ramos Pinto, P. M. Borges, L. Costa, M. A. N. D. A. Lemos, F. Lemos and R. Ribeiro, *Cat. Rev.: Sci. Eng.*, 2013, **55**, 454.
- 165 D. Coster, A. L. Blumenfeld and J. J. Fripiat, *J. Phys. Chem.*, 1994, **98**, 6201.
- 166 G. S. Foo, D. Wei, D. S. Sholl and C. Sievers, *ACS Catal.*, 2014, **4**, 3180.
- 167 W. Song, Y. Liu, E. Barath, C. Zhao and J. A. Lercher, *Green Chem.*, 2015, **17**, 1204.
- 168 M. S. Zanuttini, C. D. Lago, M. S. Gross, M. A. Peralta and C. A. Querini, *Ind. Eng. Chem. Res.*, 2017, **56**, 6419.
- 169 Z. Wang, L. Wang, Y. Jiang, M. Hunger and J. Huang, *ACS Catal.*, 2014, **4**, 1144.
- 170 X. Zhu, L. L. Lobban, R. G. Mallinson and D. E. Resasco, *J. Catal.*, 2011, **281**, 21.
- 171 L. M. López-Renau, L. García-Pina, H. Hernando, G. Gómez-Pozuelo, J. A. Botas and D. P. Serrano, *Biomass Convers. Biorefin.*, 2019, DOI: 10.1007/s13399-019-00455-9.
- 172 Y. Li, C. Zhang, Y. Liu, S. Tang, G. Chen, R. Zhang and X. Tang, *Fuel*, 2017, **189**, 23.
- 173 H. S. Cerqueira, P. Magnoux, D. Martin and M. Guisnet, *Appl. Catal., A*, 2009, **208**, 359.
- 174 J. Wildschut, F. H. Mahfud, R. H. Venderbosch and H. J. Heeres, *Ind. Eng. Chem. Res.*, 2009, **48**, 10324.
- 175 H. Tian, C. Li, C. Yang and H. Shan, *Chin. J. Chem. Eng.*, 2008, **16**, 394.
- 176 J. Orsavova, L. Misurcova, J. Ambrozova, R. Vicha and J. Mlcek, *Int. J. Mol. Sci.*, 2015, **16**, 12871.
- 177 M. E. Martínez-Klimov, P. Ramírez-Vidal, P. Roquero Tejeda and T. E. Klimova, *Catal. Today*, 2020, **353**, 119.
-

-
- 178 S. Lestari, P. Maki-Arvela, J. Beltramini, G. Q. M. Lu and D. Murzin, *ChemSusChem*, 2009, **2**, 1109.
- 179 A. Llamas, M. J. García-Martínez, A. M. Al-lal, L. Canoira and M. Lapuerta, *Fuel*, 2012, **102**, 483.
- 180 X. Zhao, L. Wei, J. Julson, Q. Qiao, A. Dubey and G. Anderson, *New Biotechnol.*, 2015, **32**, 300.
- 181 Z. Eller, Z. Varga and J. Hancsók, *Fuel*, 2016, **182**, 713.
- 182 P. Anand and K. S. Rajendra, *New Biotechnol.*, 2012, **29**, 199.
- 183 A. Demirbas, *Energy Sources, Part A*, 2009, **31**, 602.
- 184 E. Lotero, Y. J. Liu, D. E. Lopez, K. Suwannakarn, D. A. Bruce and J. G. Goodwin, *Ind. Eng. Chem. Res.*, 2005, **44**, 5353.
- 185 O. I. Senol, E. M. Ryymin, T. R. Viljava and A. O. I. Krause, *J. Mol. Catal. A: Chem.*, 2007, **268**, 1.
- 186 J. Weitkamp, *ChemCatChem*, 2012, **4**, 292.
- 187 B. Ma, J. B. Hu, Y. M. Wang and C. Zhao, *Green Chem.*, 2015, **17**, 4610.
- 188 Y. Shi, R. Li, Q. Shen, M. Yang and Y. Wu, *Chem. Commun.*, 2019, **55**, 12096.
- 189 Z. Belohlav, P. Zamostny and T. Herink, *Chem. Eng. Process.*, 2003, **42**, 461.
- 190 S. T. Sie, *Ind. Eng. Chem. Res.*, 1993, **32**, 403.
- 191 J. Weitkamp, *ChemCatChem*, 2012, **4**, 292.
- 192 X. Zhao, L. Wei, J. Julson, W. Qiao, A. Dubey and G. Anderson, *New Biotechnol.*, 2015, **32**, 300.
- 193 M. Y. Kim, J.-K. Kim, M.-E. Lee, S. Lee and M. Choi, *ACS Catal.*, 2017, **7**, 6256.
- 194 S. Kim, E. E. Kwon, Y. T. Kim, S. Jung, H. J. Kim, G. W. Huber and J. Lee, *Green Chem.*, 2019, **21**, 3715.
- 195 E. Churin, R. Maggi, P. Grange and B. Delmon, *Research in Thermochemical Biomass Conversion*, Springer, Berlin, Germany, 1st edn, 1988.
- 196 S. Zhang, Y. Yan, T. Li and Z. Ren, *Bioresour. Technol.*, 2005, **96**, 545.
- 197 X. Zhang, J. Long, W. Kong, Q. Zhang, L. Chen, T. Wang, L. Ma and Y. Li, *Energy Fuels*, 2014, **28**, 2562.
- 198 S. Oh, U.-J. Kim, I.-G. Choi and J. W. Choi, *Energy*, 2016, **113**, 116.
- 199 S. Cheng, L. Wei, J. Julson, K. Muthukumarappan, P. R. Kharel, Y. Cao, E. Boakyec, D. Raynie and Z. Gu, *J. Taiwan Inst. Chem. Eng.*, 2017, **74**, 146.
- 200 M. Kim, J.-M. Ha, K.-Y. Lee and J. Jae, *Catal. Commun.*, 2016, **86**, 113.
- 201 W. Liu, W. You, Y. Gong and Y. Deng, *Energy Environ. Sci.*, 2020, **13**, 917.
- 202 Z. Li, M. Garedew, C. H. Lam, J. E. Jackson, D. J. Miller and C. M. Saffron, *Green Chem.*, 2012, **14**, 2540.
- 203 W. Liu, W. You, Y. Gong and Y. Deng, *Energy Environ. Sci.*, 2020, **13**, 917.
- 204 W. Sauter, O. L. Bergmann and U. Schröder, *ChemSusChem*, 2017, **10**, 3105.
- 205 K. J. Carroll, T. Burger, L. Langenegger, S. Chavez, S. T. Hunt, Y. Román-Leshkov and F. R. Brushett, *ChemSusChem*, 2016, **9**, 1904.
- 206 H. Puliylalil, D. Lašić Jurković, V. D. B. C. Dasireddy and B. Likozar, *B. RSC Adv.*, 2018, **8**, 27481.
- 207 J. Li, C. Ma, S. Zhu, F. Yu, B. Dai and D. Yang, *Nanomaterials*, 2019, **9**, 1428.
- 208 L. T. Duong and A. N. Phan, *Chem. Eng. J.*, 2020, **402**, 125793.
- 209 H. Taghvaei and M. R. Rahimpour, *Process Saf. Environ. Prot.*, 2018, **121**, 221.
- 210 A. Mosallanejad, H. Taghvaei, S. M. Mirsoleimani-azizi, A. Mohammadi and M. R. Rahimpour, *Chem. Eng. Res. Des.*, 2017, **121**, 113.
- 211 H. Taghvaei, M. Kheirollahivash, M. Ghasemi, P. Rostami, B. C. Gates and M. R. Rahimpour, *Energy Fuels*, 2014, **28**, 4545.
-

-
- 212 G. Baskar, G. Kalavathy, R. Aiswarya and I. A. Selvakumari, *Advances in Eco-Fuels for a Sustainable Environment*, Woodhead Publishing, England, 1st edn, 2019.
- 213 N. Yan, Y. Yuan, R. Dykeman, Y. Kou and P. J. Dyson, *Angew. Chem.*, 2010, **122**, 5681.
- 214 H. Ohta, K. Tobayashi, A. Kuroo, M. Nakatsuka, H. Kobayashi, A. Fukuoka, G. Hamasaka, Y. Uozumi, H. Murayama, M. Tokunaga and M. Hayashi, *Chem. - Eur. J.*, 2019, **25**, 14762.
- 215 C. E. J. J. Vriamont, T. Chen, C. Romain, P. Corbett, P. Manageracharath, J. Peet, C. M. Conifer, J. P. Hallett and G. J. P. Britovsek, *ACS Catal.*, 2019, **9**, 2345.
- 216 L. Chen, C. Fink, Z. Fei, P. J. Dyson and G. Laurenczy, *Green Chem.*, 2017, **19**, 5435.

P. Mäki-Arvela, **M. E. Martínez-Klimov**, D. Y. Murzin, Hydroconversion of fatty acids and vegetable oils for production of jet fuels, *Fuel*, 306 (2021) 121673.





Hydroconversion of fatty acids and vegetable oils for production of jet fuels

Päivi Mäki-Arvela, Mark Martínez-Klimov, Dmitry Yu. Murzin *

Laboratory of Industrial Chemistry and Reaction Engineering, Åbo Akademi University, Turku/Åbo, Finland

ARTICLE INFO

Keywords:

Fatty acids
Oil
Hydroconversion
Jet fuels

ABSTRACT

The review covers transformations of vegetable oils and fatty acids to jet fuel intensively studied during the recent years. A special emphasis is put on the liquid product yields and the product distribution with the latter one affecting the fuel properties. In addition, the desired catalyst properties have been summarized. One of the best results was reported for Jatropha oil processing, giving above 80 wt% yield of the liquid phase products over Ni supported on $\text{H}_3\text{PW}_{12}\text{O}_{40}$ /hydroxyapatite at ca. 400 °C under 30 bar hydrogen. Palm oil hydroconversion was performed in a two-step process over Pt/ Al_2O_3 followed by Pt/HY, at 395 °C and 245 °C, respectively giving 54% jet fuel components. Typically also other products such as diesel range hydrocarbons are formed. Fatty acid and ester hydroconversion proceeds at lower temperatures, 255–260 °C over Ni supported catalysts producing above 50% yield of the aviation type fuel components. The desired catalyst contains acid sites with weak and medium strength, small metal particle sizes and mesoporosity, which facilitate diffusion of branched alkanes. Reaction kinetics, mechanism and kinetic modelling are also summarized.

1. Introduction

Production methods for renewable jet fuel has attracted a lot of attention both in industry and in academia during the recent years [1–39]. Jet fuels composed mostly of iso-paraffins, n-paraffins, naphthenes, olefins and aromatic components have strictly regulated properties [40]. Aromatic and cyclic components in jet fuels can be produced via pyrolysis [41] and catalytic liquefaction of wood [42,43] giving biocrude. Phenolic compounds in bio-oil can be hydrodeoxygenated and cracked to corresponding cyclic and aromatic compounds [44,45], while algal and vegetable oils, their esters as well as fatty acids and their esters give diesel [14,15], kerosene (C9–C14) [3,17] and naphtha fractions, >C9 hydrocarbons [14], depending on hydroconversion conditions and the type of catalyst. Fatty acids and oils can also be separately deoxygenated, hydroisomerized and hydrocracked to suitable hydrocarbons in the jet fuel range [15,16,21].

Jet fuel has specific strictly defined properties, such as the heating value, viscosity, aromatic content and the desired ratio between the branched to normal alkanes. Its production in one-step can be demanding and thus also multistep methods with several catalysts in different steps have been developed [15,21,31]. Jet fuel production from renewable sources has been very intensively studied during the recent years [12,13,17,20,38], giving, however, depending on the catalyst properties, also diesel [14], gasoline [14] or aromatic [46] fractions.

The aim of this review is to summarize recent literature on hydro-upgrading of oils, fatty acids and their esters. Hydroupgrading of oils to produce jet fuels means hydrodeoxygenation, in some cases followed by hydroisomerization and hydroconversion. Some reviews on this topic are already available [47–50]. In [49] bio-jet fuel production from different feedstock is summarized rather broadly with especially the catalyst selection for hydroconversion of acids and esters presented very shortly. In [50] hydroconversion using different feedstock is briefly summarized, without providing any details of catalyst properties. The same holds for Ref. [47], even if the effect of the catalyst support has been discussed in a more detailed manner. The main aim in [48] was to summarize reactor modelling. In the current work, the highest yields of jet fuel components from different feedstock are presented and the desired catalyst properties for production of jet fuel components are discussed in detail including the pore size, acidity, metal dispersion and the catalyst morphology. Furthermore, the effect of different reaction parameters, catalyst stability, kinetics, modelling as well as thermodynamics are summarized. Finally, some recommendations for future research are proposed.

2. Properties of oils and jet fuel

Jet fuels have been produced from different oils including algae, [31], Jatropha, [17,31], soybean [14,23] and palm oil [9], free fatty

* Corresponding author.

E-mail address: dmurzin@abo.fi (D.Yu. Murzin).

<https://doi.org/10.1016/j.fuel.2021.121673>

Received 26 May 2021; Received in revised form 3 August 2021; Accepted 7 August 2021

Available online 17 August 2021

0016-2361/© 2021 The Author(s). Published by Elsevier Ltd. This is an open access article under the CC BY license (<http://creativecommons.org/licenses/by/4.0/>).

acids e.g. oleic [12,13] and palmitic [25,27] acids, mixtures of fatty acids [45]. For obvious reasons it is preferable to use non-edible oils as feedstock, e.g. *Jatropha* oil [14]. Typical fatty acid composition in triglycerides and amounts of free fatty acids in different oils are presented in Table 1.

Jet fuels are composed mostly of iso-paraffins, n-paraffins, naphthenes, olefins and aromatic components [40]. In hydroprocessing of oils more aromatics are formed when high amounts of unsaturated acids, e.g. linoleic and linolenic acids, are present [15]. Typically, the aromatic content is low [16,31], however, some aromatics are required to avoid leaks in seals of the fuel system [40], while olefins are undesired. An acceptable lower level of aromatics according to ASTM D7566 is 8% [20], while in [18] it was pointed out that the optimum amount of aromatic compounds in bio jet fuel is 10–15%. On the other hand, the arene content should be lower than 25% according to ASTM regulations [51]. One of the reasons for such restrictions is a desire to diminish the soot formation.

The heating value (HV) of jet fuels is between 44.5 and 47.3 kJ/g [38,40]. When more aromatics are present the energy density of the fuel is low [7]. The heating value can be calculated from the elemental composition of the jet fuel according to the following formula [38]:

$$\text{HHV (MJ/kg)} = 0.095 \cdot S + 1.428 \cdot (\text{H-O}/8) + 0.338 \cdot C \quad (1)$$

in which S, H, O and C denote the weight percentage of elements in the fuel.

Quality of the jet fuel produced from oils, fatty acids and their esters using heterogeneous catalysts has been reported in a few papers and compared with the ASTM standard (Table 2). Details of the corresponding hydroconversion processes are described in Section 3. Hydroconversion of *Jatropha* oil (Table 2, entry 3, 4) in one step gave the desired jet fuel properties [17,31]. Sulfur content in the algal oil derived biofuel was analyzed, being below 20 ppm, when hydroconversion was performed using sulfided Ni-Mo-HZSM-5 as a catalyst [31]. One drawback with such catalyst could be formation of S-containing organic compounds in the product [4]. Furthermore, it was possible to produce good quality jet fuel from soybean oil using a three-step method (Table 2, entry 5) [15]. In this method, hydroconversion of soybean oil was performed with Pt/Al₂O₃/SAPO-11 followed by mild hydroconversion of the heavy fraction of the product from the first step over Ni₂P/HY. In the third step isomerization of light naphtha and the jet fraction from step 1 together with the product of step 2 with Pt/Al₂O₃/SAPO-11 gave suitable jet fuel with the desired properties (Table 2, entry 5) [15]. A two-step method, comprising hydrodeoxygenation with 1 wt% Pt/Al₂O₃ and hydroconversion of the product from the first step with 1 wt% Pt/Beta zeolite for production of jet fuel from palm oil was proposed (Table 2, entry 6) [16]. The composition of Jet-A fuel was analyzed in [20] stating that the ratio between isoalkane to linear alkane, I/N ratio of Jet-A was 1.5. The product in hydroconversion of palm oil over NiAg/SAPO-11 exhibited a suitable flash point and an aromatic content (Table 1, entry 7) [20]. The flash point in palm oil derived jet fuel was 38 °C, however, the flash point should be high

enough to guarantee fire safety [20,40]. Hydroconversion of methyl palmitate over Ni-BTC-MCM-41 gave good quality jet fuel components with an adequate density and the heating value (Table 2, entry 9) [38].

Cold properties of jet fuel can be described by the freezing point, which decreases for paraffins with decreasing the alkane chain length [4]. A high amount of isoparaffins also decreases the freezing point [16]. The position of the methyl group can also affect the freezing point of isoalkanes, e.g. 5-methylparaffins have a lower freezing point than 2-methylparaffins [4]. A high content of C16 to C18 paraffins in the product is not desired, since otherwise the requirement of freezing point is not met [52], as was the case in the products originating from hydroconversion of microalgae biodiesel in [8] and from refined bleached deodorized palm oil (Table 1, entries 8, 11) [9]. The freezing point of the fuel is directly related to its chemical composition. Acidity of the product from hydroconversion of bleached deodorized palm oil was too high (Table 1, entry 8) [9]. One known method to reduce acidity in petroleum oil is to treat the oil under 0.1 MPa of methanol at 220 °C for 1 h [53], which in general can also be done for biobased jet fuels.

In addition, it has been stated in [2] that bio-based kerosene has some benefits in comparison to petroleum-based fuels, such as low SO_x and particulate emissions due to a lower content of aromatics.

3. Production of jet fuels from oils, fatty acids and esters

Several studies has been made for production of jet fuels from fatty acids, [4,12,13,26,27,36] and esters [35,37,38], microalgae biodiesel [8] as well as from oils, e.g. from *Jatropha* [1,2,17,31], camelina [21], sunflower [21], palm [9,16,18,20,21,30], coconut [10], soybean [21,23,32], castor [21] and waste cooking oil [5] via hydroconversion, while some publications are concentrating on production of aromatic compounds [45] and diesel-range alkanes [14,32]. It was challenging to summarize the results as there are just few studies in which the yields of different products are given [1,5,9,14,30,31,38] including the gas- [5,13,14,37] and the solid phase products [15]. In fact, in just few studies the mass balance has been determined [3,12]. In some cases also product distribution by groups, e.g. cycloalkanes, aromatic and alkanes [8,35] or by carbon numbers [31,38] or specific products [36] were provided. Several analytical methods, such as two dimensional GC [3,15], GC-MS, [15,22,26] ¹³C NMR analysis [11] or FTIR [11,22,23] have been utilized for a detailed product analysis. Typically, only the liquid product distribution [20,23,26,27] or selectivity among liquid products [8,13,17,35,37] is reported along with the conversion level, rather than not the absolute yields, as is the case with [6,9,11,12,15,16,22,30,31,32,38]. In Table 3 the most promising results with optimized catalysts and reaction conditions in hydroconversion of oils, acids and ester are given including conversion, yields or selectivity to jet fuel components or alkanes among organic liquid phase products (OLP) and I/N ratio. The proper conditions for producing high-quality jet fuel depend on the feedstock, reaction conditions and selection of the metal and the support. Typically high metal dispersion, large pore sizes or easy accessibility of the reactants to the active sites, e.g. using

Table 1
Chemical composition of different feedstock.

Oil	C20:1	C18:0	C18:1	C18:2	C16:0	C14:0	FFA (%)	Ref.
<i>Jatropha</i> oil	0	7.9	45.4	27.3	19.5	0	1.7	[31]
Palm oil	0.2	3.1	50.1	11.7	24.1	1.6	n.a.	[21]
Soybean oil	5.5	4	29	46	12.5	<3	n.a.	[23]
Sunflower oil	0.3	4.0	24.1	63.7	6.3	0.1	n.a.	[21]
Camelina oil	2.7	2.8	15.0	19.5	5.6	0.1	n.a.	[21]
Castor oil ^a	0	1.0	3.0	5.0	2.0	0	n.a.	[21]
Algal oil		2	39	7	51		1.6	[31]
Maracuja oil	0.2	3.2	11.8	71.4	12.8	0.2	n.a.	[22]
Buriti oil	0	1.3	80.4	0.2	17.1	0.3	n.a.	[22]
Babassu oil	0	3.8	21	1.4	10.8	19.2	n.a.	[22]

^a 89% ricinoleic acid C18:9-cis(11OH).

Table 2
Jet fuel properties.

Entry	Feedstock	Density at 15 °C	Freezing point (°C)	Boiling point (°C)	Flash point (°C)	Viscosity at −20 °C (mm ² /s)	Heating value (MJ/kg)	Aromatic content ASTM D6379	Acid number (mg KOH/g fuel)	Ref.
1	standard	0.775–0.84	Max. −47	n.a.	Min. 38	Max. 8.0	42.8	8–25 vol%	0.1	ASTM D7566 [15]
2	standard	n.a.	−52–−50	n.a.	n.a.	n.a.	57.25	n.a.	n.a.	[40]
3	Jatropha oil	0.78	−55	n.a.	>38	<8.0	>44	<1	n.a.	[31]
4	Jatropha oil	0.814	−50	n.a.	n.a.	3.75	57.25	n.a.	0.010	[17]
5	Soybean oil	0.776	−50	n.a.	48.5	3.3	n.a.	14.3	0.01	[15]
6	Palm oil	0.763	−48	n.a.	51	7.4	47.1	0	n.a.	[16]
7	Palm oil	n.a.	n.a.	n.a.	58	n.a.	n.a.	9	n.a.	[20]
8	Bleached deodorized palm oil	PRO	−32	n.a.	42	n.a.	45.0	n.a.	14	[9]
9	Methyl palmitate	0.7947	n.a.	n.a.	n.a.	n.a.	45.9	n.a.	n.a.	[38]
10	Methyl palmitate	n.a.	n.a.	n.a.	n.a.	n.a.	47.36	n.a.	n.a.	[35]
11	FAME from nannochloropsis	0.794	−35.54	n.a.	n.a.	6.9 at 5 °C	49.01	n.a.	n.a.	[8]

nanosized supports with intraparticle mesopores and a certain acidity are required. Hydroconversion of oils requires typically higher reaction temperatures (360–410 °C) than that of fatty acids and their esters (250–360 °C). Typically hydrogen pressure for hydroconversion of oils is in the range of 20–50 bar) while hydroconversion of fatty acids and esters is performed under 10–40 bar.

Several catalysts were investigated for Jatropha oil hydroconversion including NiO-MoO₃/Al₂O₃, Pt/SAPO-11 and NiO-MoO₃/H-ZSM-5 (Table 3, entry 1) [31]. Rather harsh conditions are required for hydrotreating of this oil due to its high oxygen content [3]. The highest yield of the jet fuel components, 54% was obtained in a one step process over mesoporous 5 wt% NiO-18 wt% MoO₃/H-ZSM-5 at 410 °C under 50 bar hydrogen [31]. This catalyst gave also products with I/N ratio of 2, which is desired for jet fuel. Based on these initial results it was concluded that a balance between acid sites and hydrogenation-dehydrogenation activity for an efficient catalyst is required. Thus, a mesoporous hierarchical ZSM-5 support was loaded with Ni–W resulting in ca. 40% yield of C9–C14 components. The highest yield of C9–C14 hydrocarbons, 77% in Jatropha oil hydroconversion was obtained over an acidic sulfided 4 wt% NiO-24 wt% WO₃/SiO₂-Al₂O₃ catalyst at 420 °C under 80 bar hydrogen under 0.5 h^{−1} space velocity (Table 3, entry 2) [3]. Pilot experiments were also made with this catalyst at the same temperature giving 30% kerosene, 60% diesel and 12% naphtha products comprising 72% paraffins, 21% cyclic hydrocarbons as well as 7% monoaromatics and 0.1% polyaromatics determined by the two-dimensional GC analysis [3]. Furthermore, 29% of carbon was present in the gas phase.

Hydrougrading of soybean oil was studied over different catalysts (Table 3, entries 7–10) [15,21,23,32]. The theoretical liquid phase product yield from soybean oil is 81.5%. A rather high yield, 75%, was obtained over 8 wt% Ni/SAPO-11 in [32] while ca. 16% selectivity among all hydrocarbons was observed for C7–C14 hydrocarbons at 370 °C under 40 bar hydrogen (Table 3, entry 9). In a three step process with separate hydrodeoxygenation, hydroconversion and isomerization catalysts 37% yield of jet fuel was obtained (Table 3, entry 8) [15]. On the other hand, NbOPO₄ gave a high deoxygenation degree, but a low I/N ratio (Table 3, entry 7) [23]. High amounts of aromatic compounds were also formed from soybean oil in its hydroconversion over NbOPO₄ at 350 °C under 10 bar hydrogen [23]. It was, however, stated that a too high amount of aromatic compounds can be diminished by increasing a hydrogen pressure. [23] When the mass of NbOPO₄ catalyst was increased in hydroprocessing of soybean oil at 350 °C under 10 bar hydrogen, the liquid product distribution changed as well (Fig. 4). The highest amount of hydrocarbons among liquid products was obtained with 25 wt% of the catalyst, while with a lower catalyst amount more intermediate oxygenated species were present in the liquid phase [23].

The isomer to normal alkane ratio calculated for the optimized liquid mixture with 25 wt% of the catalyst was only 0.3 [23], being quite far away from the optimum ratio of 2 for jet fuels giving a high heating value [31].

Analogously to soybean hydroprocessing [15], two step processes were developed for transforming palm oil to jet fuel including in the first step hydrodeoxygenation followed by the second step with an acidic hydroconversion/isomerization catalyst (Table 3, entry 11, 12) [15,16]. Especially in two step process using 1 wt% Pt/Al₂O₃ and 0.5 wt% Pt/HY with SiO₂/Al₂O₃ ratio of 30 as catalysts a high jet fuel yield and a high I/N ratio were obtained (Table 3, entry 11) [15]. It was also stated in [15] that at harsh conditions to be used in hydroconversion of palm oil, the HDO catalyst suffered from sintering and can be easily deactivated, thus a two- step process is proposed. The products in [15,16] did not contain aromatics based on two- dimensional GC analysis. Palm oil hydroconversion to jet fuels was also successfully demonstrated in one-step over NiAg and Pd catalysts under high temperatures and hydrogen pressures (Table 3, entries 12–16) [9,15,16,20,30]. The composition of the liquid phase products obtained from palm oil over 30 wt% NiAg/SAPO-11 at 400 °C under 52 bar hydrogen was close to the one for Jet A-1, while over 1 wt% Pt/SAPO-11 at 450 °C under 59 bar hydrogen the products did not contain enough normal alkanes having with a low heating value. Gaseous products formed from palm oil over 30 wt% NiAg/SAPO-11 were CO, CO₂ and propane. The latter can also be dehydrogenated to propene [20]. Furthermore, the carbon yield in [20] determined as a sum of carbon in liquid, gaseous and solid products was 94%.

Hydroconversion of waste cooking oil, methyl palmitate, algal oil and methyl ester of Nannochloropsis was also successfully demonstrated (Table 3, entries 17–21) [6,8,31,33,37,38]. Noteworthy is the low temperature required for 10 wt% Ni/mesoY to catalyze hydroconversion [8], while other Ni catalysts operated at high temperatures [6,38]. Mesopores were created when the support was treated with an optimum NaOH concentration of 0.4 M. In hydroconversion of algal oil over sulfided 5 wt% Ni-18 wt% MoO₃/H-ZSM-5 (Table 3, entry 21) the conversion increased with increasing temperature while an optimum temperature forming hydrocarbons with the yield of 78% was 410 °C under 50 bar hydrogen [31]. A relatively high selectivity to jet fuel hydrocarbons was obtained in continuous hydroprocessing of fatty acid methyl esters from Nannochloropsis over mesoporous 10 wt% Ni/meso Y containing 4 wt% of Keggin type heteropolyacid at 255 °C under 20 bar hydrogen [8]. Under these conditions ca. 11% arenes were generated with the I/N ratio of ca. 0.8 (Table 3, entry 22).

Oleic and palmitic acid hydroconversion was investigated over Ni-, Mo- and Co-zeolites [4,12,13,26–28,36] and over Ni/Al₂O₃ [13] (Table 3, entries 23–30). Fatty acid hydroconversion occurred over Ni

Table 3

Hydroprocessing of oils, fatty acids and their esters. Notation: Y yield, S selectivity, YF yield fraction among liquid phase products, OLP organic liquid product, AFRA aviation fuel range alkanes.

Entry	Feed	Catalyst	Conditions	Conversion (%)	Yield/Selectivity (%)	I/N	Ref.
1	Jatropha oil	Sulfided 5 wt% NiO-18 wt% MoO ₃ /H-ZSM-5 (HSAC)	410 °C, 50 bar H ₂	99	Y = 54	2.6	[31]
3	Jatropha oil	Sulfided 4 wt% NiO-24 wt% WO ₃ /SiO ₂ -Al ₂ O ₃	420 °C, 80 bar, LHSV = 0.5 h ⁻¹	90	YF=C ₉ -C ₁₄ = 77		[3]
4	Jatropha oil	5 wt% Ni-30 wt% H ₃ PW ₁₂ O ₄₀ /nano-hydroxyapatite	360 °C, 30 bar H ₂ , LHSV = 2 h ⁻¹ , H ₂ /oil ratio 600	100	Y _{OLP} = 83.4%	1.64	[11]
5	Jatropha oil	2 wt% Pt/SAPO-11	410 °C, 50 bar H ₂ , LHSV = 1.2 h ⁻¹ , H ₂ /oil ratio 1000 ml/ml	100	S _{C₈-C₁₆} = 59%	0.75	[17]
6	Jatropha oil	Sulfided 3 wt% Co 8 wt% Mo/ mesoporous titanosilicate (MTS)	360 °C, 80 bar H ₂ , LHSV = 2 h ⁻¹ , H ₂ /oil ratio 1500 ml/ml	80	Y _{C₉-C₁₄} = 18%	1.5	[24]
7	Soybean oil	NbOPO ₄	350 °C, 10 bar H ₂ , 5 h	Nearly complete conversion	Deox degree 97%, 97% hydrocarbons in liquid phase Y _{OLP} = 62 Y _{jet fuel} = 37 wt%	0.37	[23]
8	Soybean oil	I. 0.5 wt% Pt/Al ₂ O ₃ /SAPO-11 II. Ni ₂ P/HY III. 0.5 wt% Pt/Al ₂ O ₃ -SAPO-11	I. 370 °C, 30 bar H ₂ , LHSV = 1 h ⁻¹ II. 315 °C, 30 bar H ₂ , 4–7 h ⁻¹ III. 350 °C, 30 bar H ₂ , LHSV = 2–4 h ⁻¹				[21]
9	Soybean oil	8 wt% Ni/SAPO-11	370 °C, 40 bar H ₂ , LHSV = 1 h ⁻¹	100	Y _{OLP} = 75 S _{C₇-C₁₄} = 16 Y _{OLP} = 70.9	85% isomers	[32]
10	Soybean oil	sulfided 2.7 wt% Ni-12.7 wt% Mo/ γ -Al ₂ O ₃	360 °C, 140 bar H ₂ , 8 h				[22]
11	Palm oil	I. 1 wt% Pt/ γ -Al ₂ O ₃ , II: 1 wt% Pt/nano-beta zeolite	360 °C, 20 bar H ₂ , II. 235 °C, 20 bar H ₂ , 5 h III. distillation		Y = 54.8 wt%	7.0	[16]
12	Palm oil	I. 1 wt% Pt/ γ -Al ₂ O ₃ , II: 0.5 wt% Pt/HY (SiO ₂ /Al ₂ O ₃ = 30)	I. 395 °C, 40 bar H ₂ , II. 245 °C, 50 bar H ₂ , WHSV = 2 h ⁻¹		Y _{OLP} = 81.6 wt% S _{C₈-C₁₆} = 66.1 wt%	4.67	[15]
13	Palm oil	30 wt% meso NiAg/SAPO-11	400 °C, 52 bar H ₂ , LHSV = 1 h	100	S _{C₈-C₁₆} = 84%	2.1	[20]
14	Palm oil	10 wt% Ni/SAPO-34	390 °C, 52 bar H ₂ , 8 h	97	Y _{C₈-C₁₆} = 41 ^b		[18]
15	Palm oil	0.5 wt% Pd/Al ₂ O ₃	400 °C, 60 bar H ₂ , 2 h		Y _{kerosene} = 43% Y _{diesel} = 50% ^c Y _{kerosene} = 48% ^c		[30]
16	Bleached deodorized palm oil	0.5 wt% Pd/Al ₂ O ₃	477 °C, 56 bar H ₂ , LHSV = 1.5 h ⁻¹				[9]
17	Waste cooking oil	25 wt% Ni- 0.5 wt% Ag/SAPO-11	380 °C, 40 bar H ₂ , WHSV = 2 h ⁻¹	72	S _{C₈-C₁₆} = 40 ^d	1.23	[6]
18	Waste cooking oil	Presulfided 4 wt% Ni-12 wt% Mo/USY	380 °C, 30 bar H ₂		S = 42%		[33]
19	Methyl palmitate	10 wt% Ni/meso-Y	390 °C, 20 bar H ₂	91	S = 64.8	0.3	[37]
20	Methyl palmitate	2.5 wt% Ni-BTC-MCM-41	390 °C, 20 bar H ₂ , 6 h	n.a.	Y = 53.2%	n.a.	[38]
21	Algae oil	Sulfided 5 wt% NiO-18 wt% MoO ₃ /H-ZSM-5 prepared in the presence of (ODAC) ^e	410 °C, 50 bar H ₂	98	Y _{OLP} = 78.5	2.5	[31]
22	FAME from Nannochloropsis	10 wt% Ni/meso Y-HPW	255 °C, 20 bar H ₂	97.2	Y _{jet biofuel} = 63.1	0.8	[8]
23	Oleic acid	10 wt% Ni-ZSM-5 nanosheet	250 °C, 10 bar H ₂		S _{AFRA} = 51.4	1.7	[12]
24	Oleic acid	4 wt% Ni/Al ₂ O ₃ ALD	360 °C, 30 bar H ₂ , WHSV = 2.4 h ⁻¹ , cyclohexane as a solvent	100	S _{AFRA} = 37.2	2.7	[13]
25	Oleic acid	10 wt% Ni/ZSM-5 nanosheet	250 °C, 10 bar H ₂ , WHSV = 2.4 h ⁻¹ , cyclohexane as a solvent	100	S _{AFRA} = 51.4	1.7	[12]
26	Palmitic acid	4.4 wt% Ni-HMP-49	260 °C, 40 bar H ₂ , 4 h, decalin as a solvent	>99	S _{C₁₂-C₁₄} = 53.5 ^a	0.9	[28]
27	Palmitic acid	4 wt% Ni-H-ZSM-22 (5 wt% NiO)	260 °C, 40 bar H ₂	100	S _{C₁₄-C₁₅} = 73.8 ^a		[4]
28	Palmitic acid	5 wt% CoO over desilicated H-MCM-49	260 °C, 40 bar H ₂ , 4 h, n-decane as a solvent	>99.9	S ₁₂₋₁₄ = 29.3	0.5	[26]
29	Palmitic acid	21 wt% Mo/H-ZSM-22	260 °C, 40 bar H ₂ , 4 h	82	S = 61.7% isoalkanes		[36]
30	Palmitic acid	5 wt% Co-HZM-5	260 °C, 40 bar H ₂ , 4 h, n-decane	100	S _{C₁₃-C₁₆} = 100%	0.51	[27]

^a among liquid phase product, ^b mass based yield.^c determined by volume fraction obtained via distillation, ^d selectivity among C₁-C₁₈ alkanes, except for C₁₅-C₁₈.^e ODAC denotes octadecyldimethyl-(3-trimethoxysilylpropyl)ammonium chloride.

supported zeolites at lower temperatures in comparison to e.g. soybean oil hydroconversion [32]. For oleic acid the yield of the aviation fuel range alkanes (AFRA) was ca. 51% with 97% carbon balance at 250 °C under 10 bar hydrogen over 10 wt% Ni/ZSM-5 nanosheet catalyst (Table 3, entry 23) [12]. Jet fuel range alkanes could be produced from

palmitic acid over 4 wt% Ni-HMP-49 prepared from post-synthesizing H-MCM-49 with tetraethylammonium hydroxide and melt infiltrating nickel on it [28] (Table 3 entry 26, Table S1, entry 26). The reaction conditions were 260 °C and 40 bar hydrogen and after 4 h 100% selectivity to alkanes was obtained. This product contained ca. 49% C₁₂-

C₁₄ cracking compounds with the ratio I/N of 0.9. Analogously mesoporous, post-treated 5 wt% CoO/H-MCM-49, was efficient in hydro-upgrading of palmitic acid (Table 3, entry 28, Fig. 2) [26]. The desired catalyst properties for production of the jet fuels from fatty acids and oils are an appropriate pore size, the presence of strong acid sites facilitating hydroisomerization and hydrocracking [28].

Cycloalkane formation was investigated in hydroconversion of model fatty acids, i.e. stearic, oleic, linoleic and linolenic acids over sulfided 2.7 wt% Ni-12.7 wt% Mo/ γ -Al₂O₃ catalyst at 360 °C under 140 bar hydrogen for 2 h. The main products were n-C₁₇H₃₆ and C₁₈H₃₈, while also large amounts of cycloalkanes were formed, especially when using linolenic acid as a feedstock [22].

In addition to cycloalkanes also alkylbenzenes, such as heptyl benzene, 2-methyloctylbenzene, dodecyl benzene, were formed in ca. 7 wt% from linolenic acid (Fig. 3). Formation of aromatic products in hydroconversion of oils over 1 wt% Pt/Al₂O₃/SAPO-11 depends on the amount of polyunsaturated fatty acids in the feedstock. It can be concluded from Fig. 3 that palm and tallow oils are hydrogenated, while more aromatic compounds are formed from soybean, sunflower and camelina oils [21].

4. Catalyst selection

The product properties in hydroprocessing of oils, fatty acids and their esters over different catalysts depend on the type of feedstock, reaction conditions as well as on the catalyst properties. For production of jet fuels by hydroconversion of fatty acids and oils, bifunctional catalysts with the metal and acid functions are needed, in which the metal facilitates hydrogenation/dehydrogenation and hydroconversion, while acidity is needed for cracking and isomerization. Metal modified zeolites exhibit high acidity, with the disadvantage that, their pores sizes are below 0.7 nm. Triglycerides are large molecules with a cross-section of ca. 0.6 nm [20], therefore configurational diffusion of the reactants and products inside the catalyst pores is also very important. Because a high I/N ratio is a desired property in jet fuels, the sizes of isomers should be considered in relation to the pore sizes. The sizes of n-paraffins, mono-branched, dibranched and tribranched isomers have been approximated as 0.45 nm, 0.58–0.6 nm, 0.61–0.63 nm and 0.65 nm, respectively [54] showing clearly that the zeolites can experience mass transfer limitations. The parameters, which can be fine-tuned for the production of jet

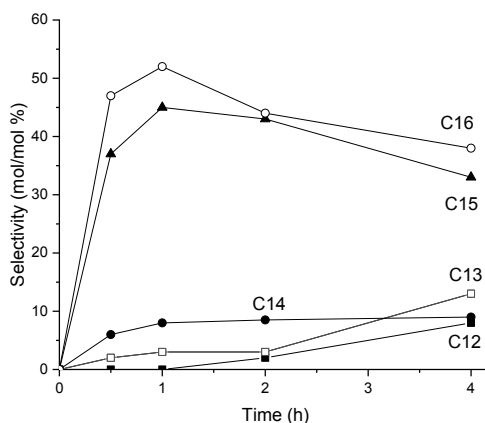


Fig. 2. Selectivity for liquid phase products in hydroconversion of palmitic acid over 5 wt% CoO on desilicated H-MCM-49 at 260 °C under 40 bar hydrogen in n-decane as a solvent, adapted from [26]

fuel are the metal type and particle size, reducibility of the metal, as well as acidity of the catalyst. From the viewpoint of catalyst morphology mesoporosity [15,17,20,23,31,33,38] is beneficial or alternatively nanosized catalyst particles are applied [16,38] (Table 3). Several alternatives exist to create mesoporosity and promote accessibility to the active sites, such as utilization of mesoporous supports (MCM-41), desilication by NaOH treatment [33,37] and dealumination of zeolites [31,33], formation of mesoporous pellets, application of surfactants and different ratios of meso- micropore structural directing agents [31] or utilization of zeolite nanosheets [12,16]. In addition, structured mesoporous catalysts, such as Ni-mesoporous organic framework modified MCM-41, have an opportunity to limit arene formation from methyl palmitate hydroconversion [38].

Supports with suitable properties, such as mesoporosity, as well as appropriate acidity which can be tuned with additives, such as

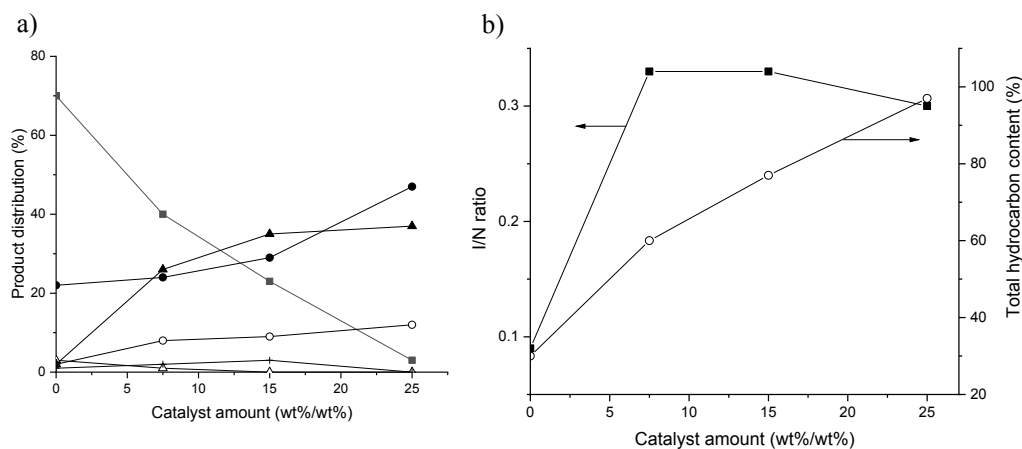


Fig. 1. a) Product distribution in hydroconversion of soybean oil over NbOPO₄ under 10 bar hydrogen at 350 °C in 5 h. Notation: (■) oxygenated products, (▲) aromatics, (●) alkanes, (○) isoalkanes, (+) cycloalkanes and (Δ) olefins, b) (■) I/N ratio and (○) the total content of hydrocarbons . adapted from [23]

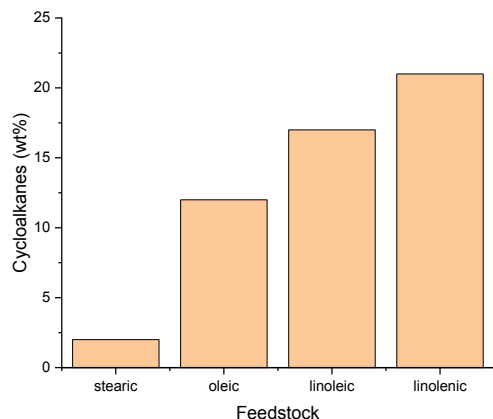


Fig. 3. The amount of formed cycloalkanes in hydroconversion of fatty acid at 360 °C under 140 bar for 2 h over sulfided 2.7 wt% Ni-12.7 wt% Mo/γ-Al₂O₃, adapted from [22]

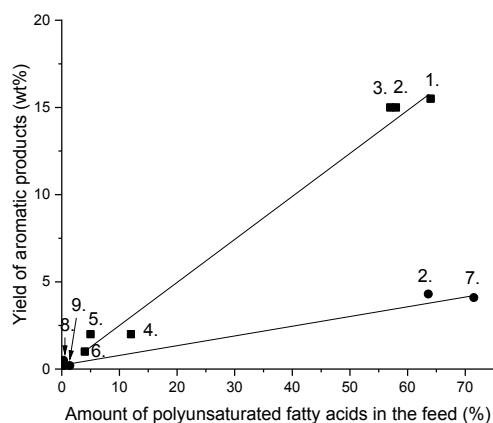


Fig. 4. The yield of aromatic products as a function of the amount of unsaturated fatty acids in the feed in hydroprocessing of different oils over a) 1 wt% Pt/Al₂O₃/SAPO-11 at 370 °C under 30 bar hydrogen adapted from [21] (■) and b) sulfided 2.7 wt% Ni-12.7 wt% Mo/γ-Al₂O₃ at 360 °C under 140 bar hydrogen adapted from [22] (●). Notation: 1. sunflower, 2. soybean, 3. Camellina, 4. palm, 5. castor, 6. tallow, 7. Maracuja, 8. Babassu and 9. Buriti oil.

phosphotungstic acid [8,11] or by adding a second metal, such as silver [5], are beneficial for a proper hydroconversion catalyst. Acidity can also be tuned via the post-synthesis, e.g. dealumination and desilication, which also creates mesopores as mentioned above. In some cases, acidity can also be too high and it can be decreased by the silane treatment [12]. Mesoporosity is often correlated with high acidity [20] and a high metal dispersion [17] as can be seen from Table 4.

Metal selection is also crucial, with noble metal catalysts being more expensive, at the same time facilitating use of milder reaction conditions than with transition metal catalysts. A metal should be highly dispersed on the support and its better reducibility typically enhances catalyst performance. In some cases even the oxidation state of the metal oxide is crucial, for example with Mo/H-ZSM-22, when the ratio Mo⁴⁺/Mo⁰ played an important role [36]. In bimetallic catalysts the electron

Table 4

The properties of the most promising catalysts used in hydroprocessing of oils, fatty acids and their esters.

Entry	catalyst	D pore (nm)	Total acidity (mmol NH ₃ /g)	Dmetal (nm)	Ref.
1	2 wt% Pt-SAPO-11	3.5	n.a.	11.2	[17]
2	I. Pt/γ-Al ₂ O ₃ , II: 1 wt% Pt/nano-beta zeolite	n.a.	^a	1–2	[16]
3	0.95 wt% Pt/Al ₂ O ₃	21–24	0.132 (Lewis acidity)	1.2	[15]
4	1 wt% Pt/Al ₂ O ₃ /SAPO-11	3.7	n.a.	7	[21]
5	4 wt% Ni/Al ₂ O ₃	n.a.	0.604	3.1	[13]
6	4 wt% Ni-H-ZSM-22	n.a.	n.a.	13–66	[4]
7	10 wt% Ni-SAPO-34	n.a.	n.a.	n.s.	[18]
8	8 wt% Ni/SAPO-11	n.a.	1.84	n.a.	[32]
9	10 wt% Ni/meso-Y	2–10	n.a.	14–17	[37]
10	4.4 wt% Ni-HMCM-49 post-treated	n.a.	n.a.	20–40	[28]
11	2.5 wt% Ni-BTC-MCM-41 nanosheets	3.7	n.a.	2–8	[38]
12	10 wt% Ni/ZSM-5 nanosheets	9.8	n.a.	10	[12]
13	5 wt% Ni/H-ZSM-5	n.a.	n.a.	10–60	[27]
14	25 wt% Ni- 0.5 wt% Ag/SAPO-11	n.a.	n.a.	n.a.	[5]
15	30 wt% meso NiAg/SAPO-11	5.8	n.a.	4–6	[20]
16	Sulfided 4 wt% NiO-24 wt % WO ₃ /SiO ₂ -Al ₂ O ₃	4.6	1.1	n.a.	[3]
17	Ni-Mo/H-ZSM-5 (5 wt% NiO, 18 wt% MoO ₃) (high surface area catalyst, HSAC)	3.8	0.42	n.a.	[31]
18	10 wt% Ni/MCM-41 + 20 wt% HPW	3.46	0.73	n.a.	[35]
19	10 wt% Ni/Y – 4 wt% H ₃ PW ₁₂ O ₄₀	2	n.a.	n.a.	[8]
20	5 wt% Ni-30 wt% H ₃ PW ₁₂ O ₄₀ /nano-hydroxyapatite	19.4	n.a.	n.a.	[11]
21	5 wt% CoO in Co-HMCM-49P	^b	^b	<5	[26]
22	21.2 wt% Mo/H-ZSM-22	^c	^c	7–8	[36]
23	3 wt% Co-8 wt% Mo /mesoporous titanosilicate	3.2–3.5	0.5	n.a.	[24]
24	NbOPO ₄	4–6	n.a.	n.a.	[23]

^a Total acidity by pyridine adsorption-desorption FTIR for Pt nano Beta zeolite 401 μmol/g_{cat}, ^b no mesopores, total acidity by pyridine adsorption-desorption FTIR at 250 °C for the support 845 μmol/g_{cat}, ^c micropores, large amount of acid sites with weak and medium strength

transfer effect between the two metals can enhance metal reducibility, for example between Ni and W [11]. Thus Ni-H₃PW₁₂O₄₀/hydroxyapatite was efficient for hydroconversion of Jatropha oil [11]. In addition, the nature of the two metals over the same support, for example mesoporous titanosilicate was studied and a large difference in the performance of Ni-Mo vs Co-Mo supported on mesoporous titanosilicate was observed [24] and will be discussed below.

In this chapter catalyst performance – property relationship will be discussed, especially elucidating the metal particle sizes, catalyst morphology, optimum reaction conditions for specific catalysts and the product quality obtained in hydroconversion of fatty acids, esters and oils.

4.1. Pt catalysts

Several different types of catalysts have been used in hydroconversion of fatty acids and oils, such as noble metal catalysts (Table 4, entries 1–4) as well as less expensive transition metal catalysts (Table 4, entries 5–24).

In hydroconversion of vegetable oils, Pt was supported both on a moderate acidic SAPO-11 [17] as well as on a composite $\text{Al}_2\text{O}_3/\text{SAPO-11}$ [21]. Because the metal dispersion is important to get a high hydroconversion efficiency [17], in the former case of Pt/SAPO-11 dispersion of platinum was boosted via using sodium dodecyl benzene sulfonate as a surfactant. In that case Pt particles of ca. 11 nm were obtained. Furthermore, this support exhibited a larger pore size in comparison to the parent SAPO-11 with such larger pore sizes of 2 wt% Pt/SAPO-11 being important for production of jet fuel components from Jatrophia oil [17]. The catalyst exhibited a higher specific surface area and the pore size, i.e. $206 \text{ m}^2/\text{g}$ and 3.5 nm , respectively, than its counterpart prepared in the absence of a surfactant, namely $195 \text{ m}^2/\text{g}$ and 3.2 nm (Table 4, entry 1, Table S1, entry 1) [17]. For Pt/SAPO-11 with and without the surfactant the jet fuel yields from Jatrophia oil were 59% and 45%, respectively at 400°C under 50 bar hydrogen. Furthermore, more C8-C16 isomers were generated over the former catalyst, e.g. 25% in comparison 21% over Pt/SAPO-11 prepared without the surfactant. Acidity of the catalysts was not determined. In addition, microporous Pt/SAPO-11 gave also a high yield of jet fuel components from Jatrophia oil (54%). It was concluded in [31] that mesoporosity is necessary to obtain a high and stable catalyst performance. In [17] hydrotreating of different vegetable oils was performed using Pt/ $\text{Al}_2\text{O}_3/\text{SAPO-11}$ composite catalyst. Hydrodeoxygenation of soybean oil was successfully performed over this catalysts giving >60% isoparaffinic compounds (See Section 3). This catalyst exhibited also mesopores and relatively small Pt size size (Table 4, entry 4).

Nanosize support particles have also been tested as metal supports for hydroconversion of vegetable oils [16]. They exhibit intercrystalline mesoporosity enhancing thereby mass transfer. Furthermore, it is easier to achieve a better metal dispersion on nanosized support particles and enhance metal reducibility as well as to optimize acidity. Because Pt/ Al_2O_3 is an efficient catalyst for generating long chain hydrocarbons from palm oil [16], not being efficient for producing jet fuel, a two step process was developed in which the long chain hydrocarbons were produced in the first step over Pt/ Al_2O_3 and the product was used as a feedstock for jet fuel generation with bulk and nanosized Pt catalysts supported on ZSM-5 and Beta. A comparative work using both Pt supported on bulk and nano sized particles was performed in hydroconversion of long chain hydrocarbons produced from palm oil in [16]. Nanosized Beta particles exhibited sponge like morphologies with the size of 10 – 50 nm and intercrystalline mesoporosity, while the crystallite size of bulk Beta zeolites was >100 nm. The ratio between the surface Pt to the Brønsted acid sites was demonstrated to influence the yield of jet fuel components and I/N ratio (Fig. 5), showing that Pt supported on both bulk and nano Beta zeolite gave a higher I/N ratio to $Y_{\text{C8}}-Y_{\text{C16}}$ ratio in comparison to Pt-ZSM-5 catalysts. For both Beta and ZSM-5 the nanosize catalysts exhibited a slightly better performance than the corresponding bulk catalysts. At the same time, the latter catalysts exhibited a lower $n_{\text{Pt}}/n_{\text{BA}}$ ratio in comparison to the nano sized catalysts. The lowest ratio of the mesoporous to the microporous volume was also determined for Pt/nano-Beta, which gave the highest yield of jet fuel hydrocarbons.

Diffusion kinetics was investigated in [16] using 2,2,4-trimethylpentane as a model compound at room temperature for different Pt catalysts supported on bulk and nano Beta and ZSM-5 [16]. Diffusion kinetics was analyzed with the Fick second diffusion law

$$\frac{\partial C}{\partial t} = D \left(\frac{\partial^2 C}{\partial x^2} \right) \quad (2)$$

in which C is the concentration, D is diffusivity, t time and x location. The crystal shape was regarded as the slab-like when the normalized uptake $q(t)/q(\infty)$ is defined as

$$A = \frac{q(t)}{q(\infty)} = \frac{2}{\sqrt{\pi}} \sqrt{\frac{D}{L^2}} \sqrt{t} \quad (3)$$

in which L is the characteristic diffusion path length.

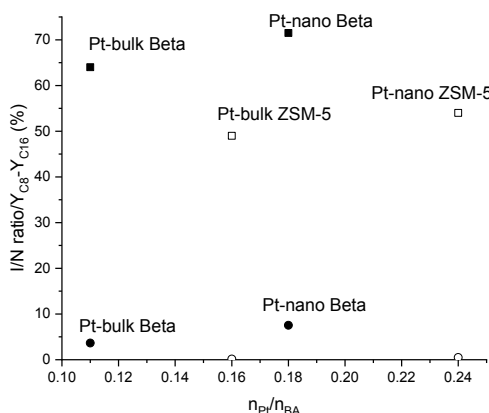


Fig. 5. Correlation between C8-C16 yield to I/N paraffin ratio in hydroconversion of palm oil at 235°C under 20 bar hydrogen with D/L^2 of 2,2,4-trimethylpentane for different catalysts, adapted from [16]. Open symbol denotes Pt-ZSM-5 catalysts and solid one Pt-Beta catalysts.

When diffusivity divided by the characteristic diffusion path length of each catalyst was correlated with the obtained maximum yield of C8-C16 hydrocarbons and the I/N ratio over the same catalysts, it was concluded that both parameters in hydroconversion of palm oil over different Pt catalysts increased with increasing the diffusion rate [16]. In [16] it was also concluded that the highest yield of the desired products was obtained with nanocrystalline Pt/Beta zeolite catalyst with the highest molecular diffusion rate (Fig. 6). Slower diffusion rates result in over-cracking.

Analogously to [16], easy diffusion of reactants and products was facilitated by mesoporosity in 1 wt% Pt/ $\text{Al}_2\text{O}_3/\text{SAPO-11}$ extrudates of unspecified acidity, which were used in hydroconversion of different oils. The suitable mesopore size was 3.7 nm and Pt was uniformly distributed inside the pellets (Table 4, entry 4) [21].

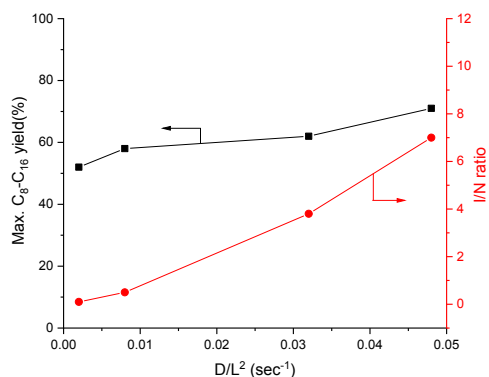


Fig. 6. Yield of C8-C16 hydrocarbons (rectangular) and I/N ratio (ball) in hydroconversion of palm oil at 235°C under 20 bar hydrogen with LHSV of 2 h^{-1} over different Pt catalysts as a function of the ratio between surface Pt to amount of Brønsted acid sites adapted from [16]. Notation: solid symbols: Pt-Beta catalysts and open symbols: Pt-ZSM-5 catalysts. BA - amount of Brønsted acid sites.

4.2. Ni catalysts

Several inexpensive nickel supported catalysts e.g. monometallic [4,12,13,28,35,38] and bimetallic Ni [1,3,20,31,34], have been applied in hydroprocessing of oils and fatty acids to produce aviation fuel range components. In addition, Ni catalysts combined with phosphotungstic acid have been efficient catalysts for production of jet fuels (Table 4, entries 18–20) [8,11,35].

4.2.1. Monometallic Ni catalysts

For monometallic Ni catalysts the jet fuel production was promoted using highly dispersed Ni particles and suitable acidity [4,13]. Specific catalyst preparation methods, such as atomic layer deposition [13] and melt impregnation were used to enhance the desired catalyst properties for production of jet fuel components, e.g. metal dispersion [4] and metal reduction [4] as well as acidity [4] in comparison to the catalysts prepared by incipient wetness method. In such cases Ni/Al₂O₃ was prepared by the atomic layer deposition [13] while 5 wt% NiO/H-ZSM-5 was synthesized by the melt impregnation [4].

Catalyst morphology was also an important parameter [13,38]. For example, mesoporosity in zeolites [33,37] and the mesoporous materials, e.g. MCM-41 as well as nanosizes ZSM-5 [12] and MCM-41 nanosheets [38] was suitable for their application as supports. The desired properties are high metal dispersion [13], suitable acidity [12,38] and a high diffusion rate [37]. In addition, Ni supported on SAPO-34 was efficient producing only a small amount of arenes [18].

The catalyst preparation method can also affect the metal dispersion [4] and the type of metal sites [13]. It is known that, for example, the atomic layer deposition [13] and the melt infiltration method [4,26] increase the metal dispersion. A comparative work in oleic acid hydroconversion was performed with 4 wt% Ni/Al₂O₃ prepared by atomic layer deposition (ALE) and incipient wetness (IW) methods [13]. The former has only Lewis sites and the particle size smaller in comparison to the one prepared by the incipient wetness method, being 3.6 nm and 6.1 nm, respectively. Furthermore, structure sensitivity in oleic acid hydroconversion was confirmed [13]. 4 wt% Ni/Al₂O₃ ALD contained only Lewis acidic sites. A higher alkane selectivity was obtained over 4 wt% Ni/Al₂O₃ ALD in comparison to the catalyst prepared by the incipient wetness method. It was stated that 4 wt% Ni/Al₂O₃ prepared by ALD contained a higher amount of Ni step sites, which was confirmed by CO TPD, showing presence of a peak above 450 °C, ascribed to associative adsorption of CO on Ni step sites [55]. As acidity and porosity of the catalysts were similar, a better performance of Ni/Al₂O₃ ALD in comparison to Ni/Al₂O₃ IW was correlated with the higher amount of Ni step sites facilitating C–C, C–O and H–H cleavage [55].

A higher Ni dispersion was obtained when the melt infiltration method was applied, as in the case of 4 wt% Ni supported on HZSM-22 (Table 4, entry 6) [4]. Three different methods, melt infiltration, incipient wetness and wetness impregnation [4] were used for preparation of 4 wt% Ni supported on HZSM-22. In the melt infiltration method the dried support was in contact with Ni(NO₃)₂·6H₂O at 65 °C for 24 h [56]. This synthesis temperature is above the melting point of the Ni precursor which is impregnated by the capillary forces into the zeolite pores. 4 wt% Ni/HZSM-22 prepared by the infiltration method exhibited also the highest hydrogen consumption in hydrogen TPR and was more active towards formation of isoalkanes in palmitic acid hydroconversion [4]. Strong acid sites promote formation of branched alkanes from palmitic acid [4]. Formation of iso-alkanes was promoted by a higher Ni dispersion on an acidic support, such as on 4 wt% Ni-H-ZSM-22 prepared by the melt infiltration method with Si/Al ratio of 37.5, a high surface area, high crystallinity and a rather high Ni dispersion.

Ni-loading in Ni-BTC/MCM-41 (BTC denotes 1,3,5-benzene-tricarboxylate metal organic framework) catalyst was varied in the range of 2.5 – 20 wt% [38]. Among the studied catalysts, the best one giving a high amount of jet fuels but a low content of aromatic products was 2.5

wt% Ni-BTC/MCM-41 (Table 4, entry 10). These catalysts were prepared as follows: Ni-1,3,5-benzenetricarboxylate metal organic framework (MOF) was synthesized according to [57]. In this method MCM-41 was added into the synthesis solution of MOF and the synthesis was performed at 150 °C for 12 [38]. Thereafter, the catalyst was calcined in air at 550 °C for 4 h. According to EDS mapping Ni-BTC was uniformly loaded inside the pores of MCM-41 [38]. Mesoporous 2.5 wt% Ni in the metal organic framework BTC supported on MCM-41 exhibited a suitable pore diameter of 3.7 nm (Table 4, entry 11), which could partially hinder aromatization, while the pore size of ca. 4 nm nm in 10 wt% Ni in BTC/MCM-41 promoted formation of aromatic compounds in methyl palmitate hydroconversion [38]. Furthermore the best catalyst exhibited more Ni²⁺ than the corresponding 10 wt% Ni catalyst which can be explained by elevation of hydrodeoxygenation ability with a higher content of Ni²⁺ related to more reactive electrons in its unsaturated *d* orbitals [37]. In addition, weak acidity of 2.5 wt% Ni-BTC-MCM-41 based on the peak at 420 °C in ammonia TPD was qualitatively confirmed to be much higher than that for 10 wt% Ni-MCM-41. Besides weak acidity, 2.5 wt% Ni-BTC-MCM-41 exhibited also a small amount of strong acid sites desorbing ammonia at 575 °C [38]. As a comparison 10 wt% Ni-MCM-41 possessed 20 nm Ni particles on MCM-41, when Ni-MOF was not used showing that it was difficult to efficiently disperse nickel on MCM-41. It was also concluded in [38] that the use of Ni containing metal organic framework modified with mesoporous MCM-41 can decrease Ni consumption by 75% still affording a better catalytic performance than 10 wt% Ni/MCM-41 catalyst. These results indicate that such type of novel catalysts has a potential in hydroconversion of fatty acid esters. Furthermore, a low arene content was obtained in the liquid product due to a beneficial catalyst morphology.

Performance of different Ni catalysts supported on MCM-41, HY, SAPO-11 and H-Beta was investigated in palm oil hydroconversion at 390 °C under 30 bar hydrogen [18]. 10 wt% Ni supported catalysts (MCM-41, HY, SAPO-11 and H-Beta) were prepared by wet impregnation in water and dried, calcined and reduced at 500 °C for 4 h. The most important factor determining the yield of the jet fuel components was acidity. In particular 10 wt% Ni/SAPO-34 exhibited the highest alkane and the lowest arene selectivity in hydroconversion of palm oil. Ammonia TPD was qualitatively discussed showing that the best catalyst, Ni-SAPO-34, exhibited the second highest amount of weak acid sites (Table 4, entry 7), while Ni/HY was the most acidic. 10 wt% Ni/H-Beta and Ni/MCM-41 possessed more medium strong acid sites. Among arene products also polycyclic arenes were formed in high amounts over Ni-H-Beta, HY, SAPO-11 and MCM-41 [18].

Desilication with alkali is one method to produce mesopores. 10 wt% Ni supported on mesoporous Y zeolite was prepared by loading nickel with the wet impregnation method (Table 4, entry 9, Table S1, entry 9). For desilication of Y zeolite different amounts of NaOH were used [37] and the highest specific surface area was obtained for Ni/meso-Y catalyst desilicated with an optimum amount of NaOH, namely 0.4 M. This catalyst contained also a large amount of mesopores in the range of 2–10 nm, which was favorable for mass transfer during hydroconversion of methyl palmitate and promoted formation of jet fuel components. With a too high NaOH amount, 0.8 M, the zeolite framework was partially destroyed. When using an optimum NaOH for desilication, some defects emerged and at the same time an increased acid intensity was obtained when some silicon atoms were removed.

In order to enhance mass transfer properties in acidic zeolites, 10 wt% Ni loaded on nanosheet ZSM-5 was also prepared and tested in oleic acid hydroconversion at 250 °C [12]. Since acidity of ZSM-5 is very high, Ni/ZSM-5 nanosheet catalysts were treated with tetraethoxysilane by a chemical liquid deposition method (CLD) to tune the acidity of the catalyst (Table S1, entry 12). The ZSM-5 nanosheets were prepared in one-step hydrothermal process using the Gemini-type quaternary ammonium surfactant (C₂₂H₄₅N⁺(CH₃)₂)-C₆H₁₂-N⁺(CH₃)₂-C₆H₁₃) as a structure-directing agent. By using TEOS modified nanosheet in 10 wt% Ni/ZSM-5 the amount of external Brønsted acid sites decreased with an

increasing Si/Al ratio. When the amount of external Brønsted acid sites, determined from pyridine FTIR with 2,6-di tert butyl pyridine, increased, turnover frequency and the I/N ratio of the product also increased in oleic acid hydroconversion (Table 4, entry 12) [12]. An optimum amount of external Brønsted acid sites was found in 10 wt% Ni/ZSM-5 nanosheets with Si/Al ratio of 200, which was treated once with silane and gave a rather high I/N ratio, but not too high ratio of (C4-C8)/(C10-C14) [12]. It was concluded in [12], that a low amount of external Brønsted acid sites promoted primary cracking, while too high acidity enhanced undesired secondary cracking.

4.2.1.1 Bimetallic Ni catalysts

Several bimetallic Ni catalysts have also been tested in hydroconversion of fatty acids and oils [5,20,24,31]. Another metal can have several roles, such as inhibiting extensive cracking [5] or enhance reducibility of metals [11,35]. For example, a bimetallic 30 wt% NiAg/SAPO-11 catalyst with a relatively high Ni dispersion was an efficient catalyst in palm oil hydroconversion [20]. This catalyst was prepared in the presence of citric acid as a chelating agent (Table 4, entry 15, Table S1, entry 15) [58,59], which can increase Ni dispersion, as was demonstrated in [20]. Furthermore, the role of Ag in 25 wt% Ni- 0.5 wt % Ag/SAPO-11 was to inhibit too extensive cracking [5]. The specific surface area of 30 wt% NiAgSAPO-11, which was prepared in the presence of citric acid was the same for the parent SAPO-11 [20], while acidity of NiAg/SAPO-11, being only qualitatively investigated with pyridine FTIR, was, especially Lewis acidity, ascribed to removal of Al from the framework sites [62]. In palm oil hydroprocessing over Ni-Ag/SAPO higher I/N ratios were obtained with the catalyst prepared in the presence of citric acid than over the counterpart synthesized without citric acid addition. The origin for a better performance of the former catalyst is related to its mesoporosity, a higher Ni dispersion and removal of Al from the framework with the citric acid treatment which increased Lewis acid concentration [60].

Sulfided mesoporous 4 wt% NiO-24 wt% $\text{WO}_3/\text{SiO}_2\text{-Al}_2\text{O}_3$ pellets were efficient in generating $\text{C}_9\text{-C}_{14}$ compounds from Jatropha oil at long residence times and 420 °C (Table 4, entry 16) [3]. Ni was loaded on the pellets by the incipient wetness method. This catalyst was highly acidic, however, out of total acid sites, 71% were weak ones as the desorption peak was found below 330 °C. The ratio between the Lewis to Brønsted sites determined by DRIFTS was 0.56. Furthermore, the large pore size of 4.6 nm promoted formation of the jet fuel components. It was concluded in [2] that if the catalyst has a high hydrogenation ability, less waxy products are formed.

The pore size of hierarchical 5 wt% NiO-18 wt% $\text{MoO}_3/\text{H-ZSM-5}$ was varied using different ratios of micro- to mesoporous structural directing agents (Table 4, entry 17) [31]. 5 wt% NiO 18% $\text{MoO}_3/\text{H-ZSM-5}$ was presulfided with dimethylsulfide to transfer the inactive oxidic catalyst into an activated one [29]. The pore size of 3.6 nm facilitated formation of a lower yield of C9-C15 hydrocarbons from Jatropha oil and from the algae oil than over the corresponding catalyst with the pore size of 3.8 nm (Table 4, entry 17) [31]. The former hierarchical ZSM-5 support was prepared by the hydrothermal synthesis route using a three times higher ratio of micro/mesoporous templating agents, i.e. 7.1 vs 2.4 (Table S1, entry 17). The pore size in this catalyst was varied using organosilane as a template [62]. As a mesopore directing agent, octadecyldimethyl-(3-trimethoxysilylpropyl) ammonium chloride was used and Ni was loaded via wet impregnation followed by drying and calcination of the catalyst. At the same time the HSAC catalyst, in which HSAC indicates high surface area catalyst, exhibited 2.4 fold more strong acid sites in comparison to LSAC [31] due to the presence of extra-framework Al in the former catalyst [61], which was confirmed in HSAC by ^{27}Al -MAS-NMR showing a high peak at 0° [31]. This catalyst gave a higher yield of C9-C15 hydrocarbons in Jatropha oil hydroprocessing and lower isomerization selectivity in comparison to LSAC (low surface area catalyst) (Table 2). In addition, it has been stated that for hierarchical zeolites not only the pore size, but also a higher number of acid sites in the pore mouth are important in enhancing reactivity [12].

The addition of Keggin type phosphotungstic acid to Ni-catalysts has been intensively studied [8,63,64]. For example, mesoporous MCM-41 has typically a mild acidity, which is not sufficient for an effective catalyst. One method to increase acidity of Ni-MCM-41 catalyst is to add a heteropolyacid, e.g. phosphotungstic acid ($\text{H}_3\text{PW}_{12}\text{O}_{40}$), to MCM-41 (Table 4, 18) [8,11]. This heteropolyacid exhibits the Keggin structure, in which P acts as a heteroatom, while polyatoms, such as W are bridged via oxygen in a certain pattern [63]. Addition of phosphotungstic acid to Ni catalysts was demonstrated in [8,11] (Table 4, entry 18–20). In particular 10 wt% Ni-20 wt% HPW-MCM-41 catalyst exhibited a rather large amount of strong acid sites with its pore diameter of ca. 3.5 nm being efficient in hydroconversion of methyl palmitate. Furthermore, HPW is located inside the pores of MCM-41, when the catalyst was prepared by wet impregnation (Table 4, entry 18, Table S1, entry 18) [35]. However, the specific surface area of HPW loaded Ni/MCM-41 catalyst decreased by 25% in comparison with the catalyst without HPW. With loadings higher than 20 wt% of HPW the structure partially collapsed.

In addition, phosphotungstic acid and Ni were loaded on a commercial mesoporous Y zeolite by the wetness impregnation method (Table 4, entry 19) [8]. Acidity of 10 wt% Ni/meso-Y catalysts with different HPW loadings increased with increasing the HPW content [8]. The highest amount of strong acid sites was obtained for 10 wt% Ni/meso-Y containing 4 wt% of HPW. This catalyst contained 1.8 fold more weak acid sites in comparison to strong acid sites determined by ammonia TPD and mesopores above 2 nm, although 80% of the pore volume was present in micropores [8].

When the HPW content increased above 4 wt%, it was agglomerated inside the mesopores of Y-zeolite. The specific surface area also decreased from 630 m^2/g to 480 m^2/g when increasing the HPW loading from 0 to 8 wt% [8]. The highest selectivity to the jet fuel components in microalgae biodiesel hydroconversion was obtained over 10 wt% Ni/meso-Y containing 4 wt% of HPW (Fig. 7) [8].

Co-precipitation was used to prepare 5 wt% Ni-30 wt% $\text{H}_3\text{PW}_{12}\text{O}_{40}$ supported on hydroxyapatite with high acidity and at the same time suitable interactions between Ni and W, promoting reduction of Ni (Table 4, entry 20) [11,64]. The FTIR analysis showed that the Keggin structure was preserved while XRD confirmed the hydroxyapatite structure. According to ammonia TPD acidity increased with increasing HPW loading.

Based on XPS measurements Ni was present both as Ni^0 and Ni^{2+} , while the speciation of W included W^{5+} and W^{6+} . It was additionally

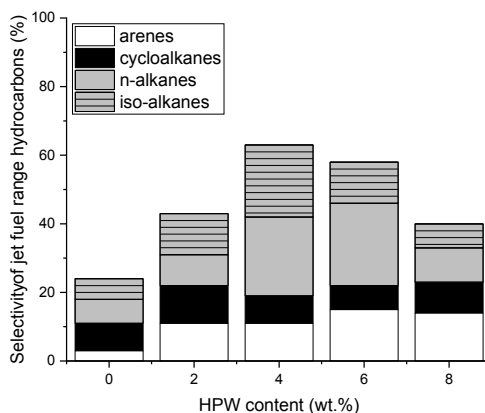


Fig. 7. Selectivity to jet fuel hydrocarbons in hydroconversion of microalgae biodiesel over 10 wt% Ni/meso Y-HPW at 255 °C under 20 bar hydrogen, adapted from [8]

stated that a high amount of acid sites can originate from interactions between Ni and HPW. 30 wt% Ni-HPW/hydroxyapatite exhibited large pores, and according to XPS the amount of Ni^0 was 2.2 fold that found in the corresponding Ni/HA catalyst in the absence of HPW [11]. It was concluded that nickel reduction was promoted due to the electron transfer between Ni and W in the presence of the Keggin type structure and at the same time more W^{6+} was found in the former catalyst than in the latter one. Catalyst acidity can be increased after addition of the Keggin type acid to the metal supported catalysts to promote the jet fuel production [11,35].

4.3. Mono- and bimetallic Co-, and Mo catalysts

Mono- and bimetallic Co, Co-Mo and Ni-Mo catalysts have been studied in hydroconversion of fatty acids [26,27,36]. Monometallic, desilicated cobalt catalyst, Co-H-MCM-49 with 5 wt% CoO, prepared by the solid state ion-exchange combined with the melt infiltration method was used in palmitic acid hydroconversion (Table 4, entry 21, Table S1, entry 26) [26]. Rather strong acid sites in Co supported on post-synthesized H-MCM-49 zeolite are required for production of isomers in palmitic acid hydroconversion [26]. This catalyst exhibited also high crystallinity (95%) compared to the parent material [26]. The support H-MCM-49 was treated with tetraethylammonium hydroxide to tailor its textural properties and acidity [65]. The desilicated H-MCM-49 exhibited 1.3 and 1.7 fold higher amounts of Brønsted and Lewis acid sites, respectively than the corresponding parent zeolite. Furthermore, the ratio between the meso- pore to micropore volume of desilicated 5 wt% CoO/MCM-49 was 2.6, while for the parent Co/MCM-49 it was 2.3 (Table 4, entry 21) [26]. TEOAH was selected due to its lower alkalinity in comparison to NaOH in order to preserve high crystallinity of the support [65]. These properties facilitated a higher cracking activity as well as diffusion of the reactant and products. Strong acidity was present in Co-MCM-49 which was treated with tetraethylammonium hydroxide (TEAOH) (Table 4, entry 21) [26]. At the same time also morphology of the zeolite was changed and the post-synthesized zeolite exhibited more 12 member rings than 10 member rings facilitating better diffusion of the products and a higher cracking activity [26].

In some cases the oxidation state of molybdenum has been a very important parameter [36]. For monometallic 21 wt% Mo/H-ZSM-22 catalyst, calcination and reduction temperatures were optimized to increase metal reducibility (Table 4, entry 22) [36]. The Optimum calcination and reduction temperatures were determined for Mo/H-ZSM-22 catalyst, being 550 °C and 600 °C, respectively, which facilitated a partial reduction of Mo^{4+} to Mo^0 , retaining, however, the zeolite crystallinity opposite to reduction at 700 °C [36]. The catalyst calcined at 550 °C and reduced at 600 °C exhibited also a higher $\text{Mo}^{4+}/\text{Mo}^{6+}$ ratio than after reduction at 700 °C, which was beneficial for the optimal hydrodeoxygenation to hydrodecabonylation ratio and gave the highest I/N ratio. Furthermore, calcination at 650 °C was also too high decreasing the surface area. MoO_x species in Mo/H-ZSM-22 catalyst were uniformly located outside the channels of HZSM-22 being 20 times bigger than the channel size (Table 4, entry 22) [36].

Bimetallic sulfided 3 wt% Co-8 wt% Mo supported on mesoporous titanasilicate (MTS) catalyst exhibited a suitable pore size and 2.9 fold higher oxygen adsorption capacity, being a measure of the metal dispersion, as for the corresponding 3 wt% Co 8 wt% Mo/ Al_2O_3 catalyst (Table 4, entry 23) [24]. Furthermore, its acidity was 5 fold that of $\text{CoMo}/\text{Al}_2\text{O}_3$. The support, mesoporous titanasilicate, exhibited four fold more weak than strong acid sites. A comparative work for hydro-upgrading of Jatropha oil at 300 °C under 80 bar hydrogen using sulfided 3 wt% Ni- 8 wt% Mo supported on mesoporous titanasilicate (MTS) and 3 wt% Co- 8 wt% Mo /MTS, which exhibited similar acidities, showed that the former one was more active giving 85% conversion in comparison to 65% obtained for 3 wt% Co- 8 wt% Mo /MTS. In addition 3 wt% Ni 8 wt% Mo /MTS catalyst promoted formation of oligomeric products lowering thus the yield of C9-C15 products, while less

oligomers were obtained over 3 wt% Co 8 wt% Mo /MTS. Unfortunately reduction of different catalysts was not investigated in [24], although it is well known that Co oxide is more difficult to be reduced than Ni oxide [44]. In addition XPS measurements would have revealed important information about the metal oxidation states.

5. Effect of reaction conditions

The effect of several reaction parameters in hydrougrading of fatty acids and oils has been investigated including temperature, pressure, space velocity and residence time in continuous reactors at different hydrogen to feedstock ratio [1,4,8,9,22,23,31]. The main trends in conversion and selectivity are given below.

5.1. Effect of reaction temperature

The effect of the reaction temperature on hydrougrading of fatty acids and oils has been intensively studied [2,9,12,13,17,18,20,23,25,27,32,45]. One example hydrougrading of Jatropha oil investigated with 2 wt% Pt/SAPO-11 [17], Ni-Mo supported on hierarchical high surface area ZSM-5 [31] or $\text{NiH}_3\text{PW}_{12}\text{O}_{40}/\text{nanohydroxyapatite}$ [11]. In several cases an optimum temperature was reported giving the highest yield of jet fuel components as well as the highest I/N ratio [11,17,31]. For example, in hydrotreatment of Jatropha oil over dodecyl benzene sulfonate modified 2 wt% Pt/SAPO-11 the effect of temperature on selectivity and the deoxygenation degree was studied in the range of 360–440 °C [17]. Deoxygenation degree decreased above 400 °C and at this optimum temperature the highest selectivity to the liquid products was obtained (Fig. 8) [17].

Analogously an optimum temperature of 360 °C was reported in [11] giving the highest I/N ratio in the liquid product in hydroconversion of Jatropha oil under 30 bar hydrogen over 5 wt% Ni- 30 wt% $\text{H}_3\text{PW}_{12}\text{O}_{40}/\text{nanohydroxyapatite}$. At the same time, the total liquid product yield decreased with increasing temperature due to formation of gaseous products. An optimum reaction temperature of 410 °C was also observed in algal oil hydroconversion in a trickle bed reactor operated in a narrow range of LHSV with Ni-Mo supported (5 wt% NiO, 18 wt% MoO_3) on hierarchical high surface area ZSM-5 giving maximally 54% yield of C9-C15 at 96% conversion [31].

The product distribution also changed with increasing temperature

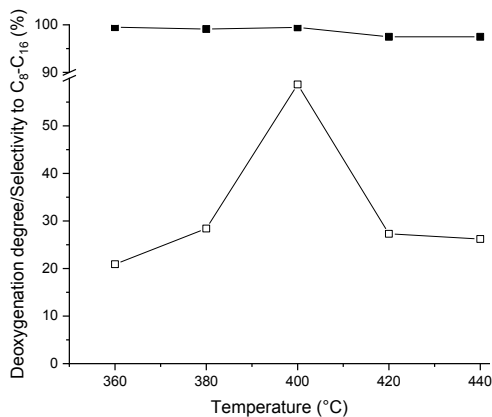


Fig. 8. Deoxygenation degree (■) and selectivity to C₆-C₁₆ hydrocarbons calculated on the mass basis among the liquid products (□) in hydrougrading of Jatropha oil under 50 bar hydrogen using LHSV of 1.2 h⁻¹ over dodecyl benzene sulfonate modified 2 wt% Pt/SAPO-11, adapted from [17]

[22,32]. In soybean oil hydroconversion over 8 wt% Ni/SAPO-11 under 40 bar hydrogen the conversion increased from 90% at 310 °C to complete conversion at 340 °C and at the same time isomer selectivity increased with increasing temperature from 310 °C to 380 °C [32]. In addition, more cycloalkanes and aromatic compounds were formed at higher temperatures over sulfided 2.7 wt% Ni-12.7 wt% Mo/ γ -Al₂O₃ under 140 bar in hydroconversion of highly unsaturated buriti oil (an Amazonian oil) [22] showing that the Diels-Alder reaction is promoted at high temperatures (Fig. 9). In the Diels-Alder reaction unsaturated fatty acids are transformed to cyclopentene (see Section 9).

The temperature effect in hydrougrading of palm oil was studied over 10 wt% Ni/SAPO-34 in [18] and over 30 wt% NiAg/SAPO-11 [20]. In the former case the highest selectivity to the jet fuel components, 65%, was obtained with 10 wt% Ni/SAPO-34 at 390 °C–410 °C under 30 bar hydrogen, while lower temperatures resulted in lower selectivity [18]. Furthermore, NiAg/SAPO-11 gave at 380 °C only 70% selectivity to the jet fuel components (C8–C16) under 52 bar hydrogen from palm oil, while at 400 °C the corresponding selectivity was 84%. At an even higher temperature a slight decrease of selectivity to 80% was observed related to formation of the gas phase products through cracking. At the same time, the I/N ratio increased from 0.5 to 2.5 when increasing temperature from 380 to 420 °C [20].

Hydroconversion of soybean oil was performed over NbOPO₄ in [23,32]. The deoxygenation degree of soybean oil increased with increasing temperature from 300 °C to 350 °C under 10 bar hydrogen being 70 and 77%, respectively [23]. The product distribution changed also in hydrougrading of soybean oil over 8 wt% Ni/SAPO-11 with increasing the reaction temperature from 310 °C to 380 °C. The main products were decarbonylated/decarbonylated products, while the isomer selectivity was 84% at 380 °C. With increasing temperature from 310 °C to 380 °C also selectivity to the cracking products, C7–C14 increased from nearly zero to 25% [32].

In hydroconversion of waste cooking oil over 25 wt% Ni- 0.5 wt% Ag/SAPO-11 selectivity to the jet fuel range alkanes decreased from 75% at 320 °C to 38% at 400 °C under 30 bar hydrogen [5]. Furthermore, catalyst deactivation was also clearly demonstrated through a decreased amount of methane in the gas phase above 380 °C. The main gaseous product was methane, which corresponded to 98% of the total peak area of the gaseous products, ethene, propane and butane.

The temperature effect in palmitic acid hydroconversion has been investigated over 5 wt% Ni and Co supported on H-ZSM-5 [27], 21.2 wt

% Mo/H-ZSM-22 [25], 4 wt% Ni-H-ZSM-22 [4]. The optimum temperature for palmitic acid hydrougrading to jet fuel components was at ca. 260 °C [4,27], much lower than for the feedstock described above. For example, palmitic acid hydroconversion over hierarchical micro- and mesoporous Ni and Co loaded with 5 wt% metal oxide H-ZSM-5 and H-ZSM-5 desilicated with tetraethylammonium hydroxyl was investigated under 40 bar hydrogen in a batch reactor using decane as a solvent [27]. The results showed that more isomers and C14 and C15 hydrocarbons were formed at 260 °C in comparison to 240 °C. A high I/N ratio and high selectivity to iso-C16 were obtained over Co supported on mesoporous H-ZSM-5 at 260 °C under 40 bar hydrogen. Analogously the fraction of isoalkanes increased in hydroconversion of palmitic acid when increasing temperature from 240 to 260 °C over desilicated Ni/HZM-5 catalyst (5 wt% NiO) giving more cracking products [27]. 21.2 wt% Mo/ZSM-22 catalyst promoted formation of the jet fuel components from palmitic acid at 260 °C giving also a high I/N ratio [25]. Analogously the I/N ratio increased in palmitic acid hydroconversion over 4 wt% Ni-H-ZSM-22 in the temperature range of 150 – 260 °C under 40 bar in 4 h [4].

The temperature effect was investigated in oleic acid hydroconversion over tetraoxysilane treated 10 wt% Ni/ZSM-5 nanosheets [12] and 4 wt% Ni/Al₂O₃ prepared by the atomic layer epitaxy (ALE) method [13]. An optimum temperature of 250 °C under 30 bar hydrogen gave the highest yield of the aviation fuel range alkanes (AFRA, C9–C15), ca. 52% with the I/N ratio of 1.7. The organic liquid product yield was slightly higher at 250 °C than either at 240 °C or 260 °C, being ca. 78% at 250 °C. Furthermore, it was observed that the I/N ratio increased with increasing temperature from 240 °C to 260 °C [12]. On the other hand, Ni/Al₂O₃ (ALE) catalyst with a high metal dispersion exhibited an optimum activity under 30 bar hydrogen for hydroconversion oleic acid at 360 °C giving ca. 37% selectivity to AFRA, while at a higher temperature this catalyst was too active for hydroconversion giving ca. 80% selectivity to C4–C8 hydrocarbons [13].

5.1.1. Effect of pressure

The effect of pressure has been investigated in several studies [5,9,12,17,20], typically showing existence of an optimum pressure promoting formation of the jet fuel components [5,20]. For example, an optimum pressure was obtained in hydroconversion of palm oil at 400 °C in the pressure range of 38–59 bar over 30 wt% NiAg/SAPO-11 (Fig. 10) [20]. This was explained by enhanced cracking at a high temperature and pressure and at the same time, reaction of hydrogen with free radicals formed in the cracking reactions suppresses

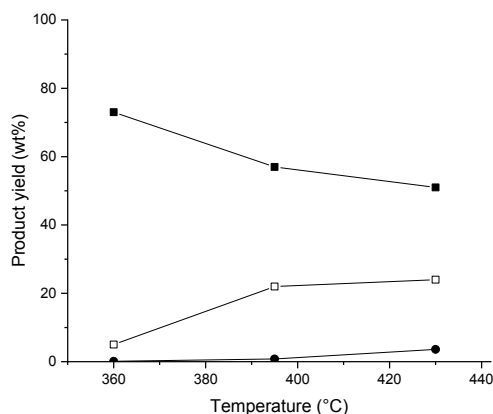


Fig. 9. Effect of temperature on formation of alkanes (■), cycloalkanes (□) and alkylbenzene (●) in hydroconversion of buriti oil at 140 bar for 2 h over sulfided 2.7 wt% Ni-12.7 wt% Mo/ γ -Al₂O₃, adapted from [22]

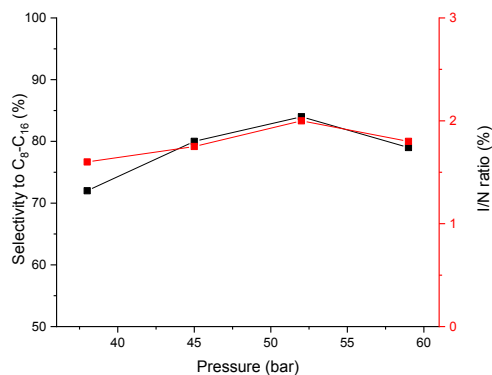


Fig. 10. Selectivity to C8–C16 hydrocarbons (■) and I/N ratio (●) in hydroconversion of palm oil over mesoporous 30 wt% NiAg-SAPO-11, adapted from [20]

isomerization [66].

A high hydrogen pressure increased slightly the yield of C9-C14, while the diesel yield was influenced more, increasing from 18% to 66% when the pressure was increased from 20 to 90 bar in hydroconversion of Jatropha oil over Ni/W/SiO₂-Al₂O₃ catalyst at 420 °C (Fig. 11) [2]. It was concluded in [2] that the pressures above 60 bar promote the C-O cleavage while the C-C cleavage is preferred below 60 bar over 4 wt% Ni- 24 wt% W/SiO₂-Al₂O₃.

On the other hand, above 40 bar in Jatropha oil hydroconversion over sulfided CoMo/Al₂O₃ catalyst at 360 °C the most prominent products were C15-C18 compounds, while the yield of C9-C14 hydrocarbons decreased from 12% to 7% with increasing pressure from 20 to 90 bar [1]. Analogously to [1] the highest I/N ratio, 1.5 was obtained in hydroconversion of Jatropha oil at 400 °C over sodium dodecylbenzene sulfonate (SDBS) modified 2 wt% Pt/SAPO-11 under 40 bar. Above that pressure hydrogenation of the hydrolyzed oil and the subsequent dehydrogenation step, which is catalyzed by the metal, are retarded inhibiting also the following steps, such as isomerization. Pressure changes in hydroconversion of Jatropha oil at 400 °C over dodecylbenzene sulfonate modified SDBS-2 wt% Pt/SAPO-11 did not show any clear influence on C8-C16 selectivity [17].

In hydroconversion of waste cooking oil, it was pointed out that over 25 wt% Ni- 0.5 wt% Ag/SAPO-11 the hydrogen pressure of 20 bar was sufficient to maintain the balance between hydrogenation and dehydrogenation, keeping the methane formation at a low level. On the other hand, at higher hydrogen pressures methane formation increased due to higher cracking [5].

Buriti oil hydroconversion was performed over sulfided 2.7 wt% Ni-12.7 wt% Mo/ γ -Al₂O₃ catalyst under high pressure giving alkanes [22], while formation of cycloalkanes and alkylbenzene was not affected by the increased pressure.

In oleic acid hydroconversion oleic acid at 250 °C conversion increased from 50 to ca. 100% when increasing the hydrogen pressure from 4 to 30 bar [12]. At the same time, the organic liquid product yield increased from 30% to 78%. However, only a minor pressure effect on the I/N ratio, increasing it 1.6 fold, was observed over 10 wt% Ni/ZSM-5 nanosheet catalyst at 250 °C in the pressure range of 4 to 30 bar [12]. A similar result was reported for Jatropha oil hydroconversion over the surfactant modified 2 wt% Pt/SAPO-11 [17]. At the same time, lower hydroisomerization activity is observed at a lower hydrogen pressure.

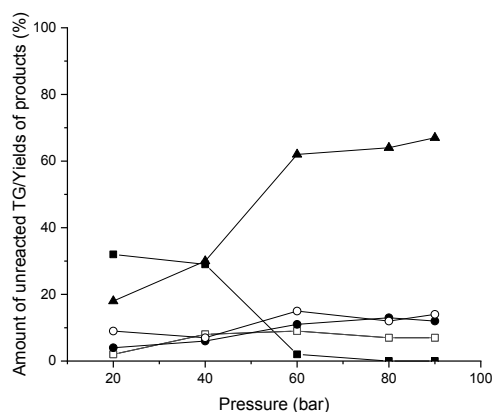


Fig. 11. Effect of pressure in hydroconversion of Jatropha oil at 420 °C in a continuous reactor over sulfided 5 wt% NiO-18 wt% MoO₃/H-ZSM-5 catalyst adapted from [2]. Notation: (■) unconverted triglycerides, (□) < C9, (●) C9-C14, (▲) C15-C18, (○) > C18.

5.1.2. Effect of H₂/feedstock ratio

The effect of hydrogen to feedstock ratio has been investigated in hydroconversion of waste cooking oil [5], Jatropha oil [17] and palm oil [20]. An optimum H₂/feedstock molar ratio of 12.8 was found in the former case with 25 wt% Ni-0.5 wt% Ag/SAPO-11 at 380 °C under 40 bar hydrogen at WHSV of 2 h⁻¹ [5]. Analogously a maximum H₂/feedstock ratio was determined in hydroconversion of Jatropha oil over SDBS-Pt/SAPO-11 giving the highest yield of C₈-C₁₆ [17]. Conversion of Jatropha oil increased with increasing the H₂/feed ratio over Co-Mo/Al₂O₃ [1], lowering at the same time the yield of oligomers, while the yield of heavy C₁₅-C₁₈ hydrocarbons increased and the fractional yield of C₉-C₁₄ was only mildly affected.

5.1.3. Effect of conversion

The effect of conversion was investigated by changing the space velocity and the residence time in hydroconversion of fatty acids and oils [1-3,9,15,17,20]. Typically, as can be anticipated, higher amounts of jet fuel components were obtained with low space velocities [1,5,9]. Examples include Jatropha oil hydroconversion 3.3 wt% CoO-12 wt% MoO₃/Al₂O₃ [67] and Ni-W-SiO₂-Al₂O₃ catalysts [1,2] as well as hydroconversion of waste cooking oil over 25 wt% Ni- 0.5 wt% Ag/SAPO-11 [5]. Conversion of Jatropha oil decreased also with increasing space velocity over sulfided 4 wt% NiO-24 wt% WO₃/SiO₂-Al₂O₃ at 420 °C under 80 bar hydrogen when using H₂/feed ratio of 1500 vol/vol [3]. The highest fractional yield of C₉-C₁₄ hydrocarbons, 72%, in Jatropha oil hydroconversion was obtained over 4 wt% NiO-24 wt% WO₃/SiO₂-Al₂O₃ catalyst in a fixed bed reactor at 420 °C under 80 bar hydrogen with 0.5 h⁻¹ space velocity, while it decreased rapidly with increasing space velocity (Fig. 12) [3]. At the same time, the yield fraction of C₉-C₁₄ hydrocarbons decreased from 12% to 4% and the yield of heavy compounds increased [1]. However, under these conditions, a hot spot corresponding to the temperature of 737 °C was observed in the upper part of the catalyst bed and ca. 340 °C temperature gradient across the bed was observed due to high exothermicity of the reaction [3]. This result clearly showed a need of the liquid/gas quench streams to avoid temperature run-away.

On the other hand, Ni/HZ-1 was more active than Co-HZSM-5 with 5 wt% CoO in [27] in hydroconversion of palmitic acid, because C15 is the main product after 0.5 h in the reaction mixture. This is the third product in the consecutive route, i.e. first hexadecane is formed from palmitic acid, followed by isomerization to methylpentadecane, which is further cracked to pentadecane. In addition, when the space velocity is increased from 1 h⁻¹ to 8 h⁻¹ in Jatropha oil hydroconversion at 360 °C

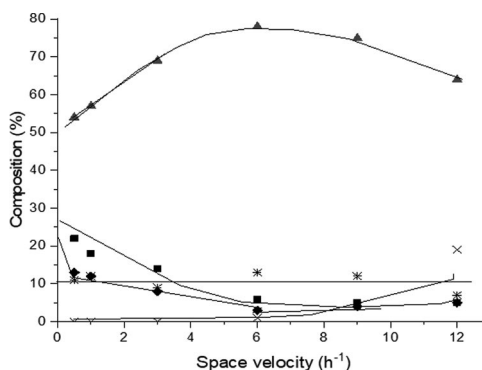


Fig. 12. The product yields in hydroconversion of Jatropha oil over sulfided 4 wt% NiO-24 wt% WO₃/SiO₂-Al₂O₃ at 420 °C under 80 bar hydrogen as a function of space velocity. Symbols: (◆) < C9, (■) C9-C14, (▲) C15-C18, (*) > C18 adapted from [3]. The lines represent modelling results.

under 80 bar over sulfided CoMo/Al₂O₃ complete conversion of oil was obtained [1].

At low space velocities more isomers were formed in soybean oil hydroconversion at 370 °C under 40 bar hydrogen using 300 ml/min flow of hydrogen over 8 wt% Ni/SAPO-11 [32]. It was also demonstrated in [15] that longer residence times gave more aromatic products in hydroconversion of soybean oil over 1 wt% Pt/Al₂O₃/SAPO-11 at 370 °C under 30 bar hydrogen [15]. Furthermore, concentration profiles as a function of residence time indicate parallel hydrogenation and aromatization.

In hydroconversion of refined bleached deodorized palm oil the optimized reaction conditions for production of jet fuel components were 477 °C, 56 bar and 1.5 h over a non acidic Pd/Al₂O₃ catalyst and it was concluded that higher jet fuel yields were obtained with increasing both temperature and LHSV [9].

6. Catalyst stability and long-term performance

Catalyst regeneration and recycling has been intensively studied [8,11,13,16,26,27,31]. In some cases, very stable conversion and selectivity towards different products were obtained, for example in hydroconversion of microalgae based biodiesel over 10 wt%/Ni-4 wt% HPW/meso Y [8], hydroconversion of Jatropha oil over 5 wt% Ni-30 wt% HPW on hydroxyapatite [11], in the two step process to produce jet fuels from palm oil over Pt/γ-Al₂O₃ and in the second step transforming long chain hydrocarbons over Pt/Nano-Beta zeolite [16]. On the other hand, changes in the product distribution in catalyst recycling was observed in hydroconversion of palmitic acid over 21 wt% Mo/ZSM-22 [25], over 4 wt% Ni-H-ZSM-5 [4] and in oleic acid hydroconversion over 4 wt% Ni/Al₂O₃ prepared by ALD [13]. It should, however, be pointed out that in hydroconversion of palmitic acid over desilicated Co/HMCM-49 (5 wt% CoO) only minor changes in the product distribution were observed and conversion, of 99.9% remained the same [26]. This result is important showing suitability of the desilicated bifunctional Co-MCM-49 with large pores and strong acid centers to be used as a catalyst for palmitic acid hydroconversion.

The performance of 5 wt% Ni-30 wt% HPW on hydroxyapatite was very stable in Jatropha oil hydroconversion at 360 °C under 30 bar hydrogen for 196 h time-on-stream [11]. Thermogravimetric analysis of the spent catalyst showed that only 4.3 wt% carbon was accumulated on the catalyst surface. Furthermore, 10 wt% Ni-4 wt% HPW/meso Y exhibited very stable performance in transformations of microalgae based biodiesel giving 61% selectivity of jet biofuel with 97% conversion during 24 h time-on-stream [8]. Sulfided Ni-Mo/ZSM-5 with a high specific surface area (HSAC) containing 5 wt% of NiO and 18 wt% of MoO₃, could be reused in algal oil hydroconversion after regeneration at 450 °C with an air stream and resulfidation [31]. In [31], however, no further details were provided about recycling. When recycling 25 wt% Ni-0.5 wt% Ag/SAPO-11 catalyst in hydroconversion of waste cooking oil [5], some changes in the catalyst properties occurred, such as a change of the Ni particle shape as well as disappearance of acid sites.

A very stable performance of 1 wt% Pt/Al₂O₃ was observed for transforming palm oil to long chain fatty acids under 20 bar hydrogen at 360 °C for 4 days followed by hydroconversion of the obtained product with 1 wt% Pt/nano-Beta zeolite at 235 °C under 20 bar hydrogen [16]. Namely, the C8-C16 yield was 72% after 24 h (71%) after 4 days with the corresponding to I/N ratios of 7.5 and 7.8 [16]. As a comparison the one-step process for palm oil hydroconversion was also investigated over 1 wt% Pt-Nano-Beta at 295 °C under 20 bar hydrogen using WHSV of 2 h⁻¹. The product distribution in that case changed from 2 h time-on-stream with the main product in the hydrocarbon range of 4–8 to mainly C15-C18 at 24 time-on-stream.

Morphology changes of Ni particles were observed in NiAg-SAPO-11 catalyst after its utilization in waste cooking oil hydroconversion [12]. Polyhedral Ni particles found in the fresh catalyst were transformed to the spherical ones after the reaction, when the catalyst was used in hydroconversion of waste cooking oil. XRD patterns from the fresh and spent NiAg/SAPO-11 catalysts were, however, nearly identical showing the metal particle size did not vary. On the other hand, the Ni particle size according to TEM measurements in 10 wt% Ni/ZSM-5 nanosheets was ca. 10 nm and only slight sintering occurred in hydroconversion of oleic acid at 250 °C under 30 bar hydrogen [12]. Furthermore, the MFI structure of the zeolite support remained intact.

7. Reaction kinetics in the batch mode

Hydroconversion of fatty acids and oils has been typically investigated in continuous reactors [1–3,8,10–12,15–17,20,21,24,29,31–33], while batch reactor studies have been scarcely made [18,22,25,28,38]. Among these studies only a few have reported kinetic data as a function of time [4,26,27].

Reaction kinetics in hydroconversion of palmitic acid has been intensively studied [4,27]. The concentrations of different products as a function of reaction time in palmitic acid hydroconversion reveal that deoxygenation is not completed after 30 min because a small amount of hexanoic aldehyde is present in the reaction mixture and conversion of palmitic acid at this point is ca. 95% [27]. The main product is hexadecane with its yield passing through a maximum at 1 h after which methylpentadecane is formed (iso-C16). After prolonged times also small amounts of methyltetradecane as well as lighter cracking products, C13 and C14 are formed (Fig. 13).

The normalized selectivity of different products with carbon numbers ranging from C12 to C16 as a function of time was reported in palmitic acid hydroconversion under similar conditions as above over Co/HMP-49 in [26]. Both selectivity to C16 and C15 passed through a maximum forming C12–C14 hydrocarbons indicating that this catalyst was also very active in hydroconversion in comparison to 4 wt% Ni/HZM-22 (Fig. 14) [4] and Co-H-ZSM-5 (5 wt% CoO) [27].

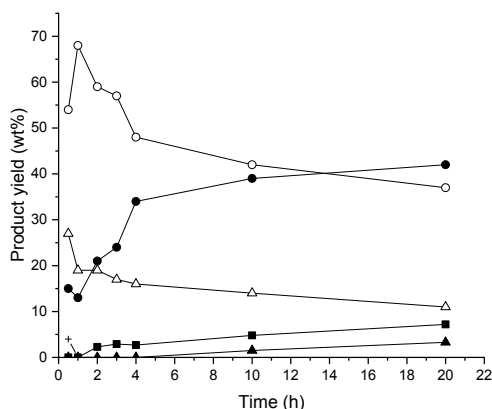


Fig. 13. The fractional product yield as a function of reaction time in hydroconversion of palmitic acid in decane as a solvent at 260 °C under 40 bar hydrogen over post-treated Co/H-ZSM-5 (5 wt% CoO), adapted from [27]. Notation: hexadecanal C15-CHO (○), n-C16 (△), iso-C16 (●), n-C15 (■), iso-C15 (▲) and cracking products (■).

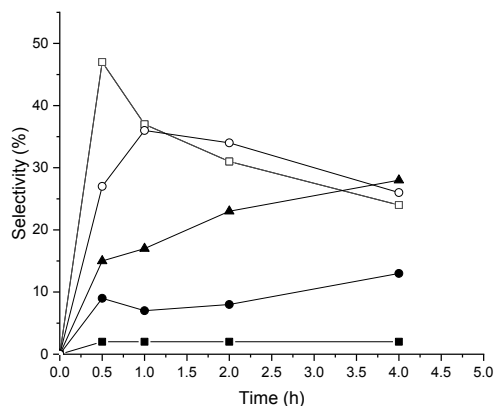


Fig. 14. Selectivity to n-C14 (■), n-C15 (□), iso-C15 (●), n-C16 (○), iso-C16 (▲) in hydroconversion of palmitic acid over 4 wt% Ni-/H-ZSM-22 at 260 °C under 40 bar in a batch reactor, adapted from [4].

8. Kinetic modelling of hydroconversion of oils and fatty acids

Several kinetics models were tested for hydroconversion of Jatropha in a fixed bed reactor over mesoporous sulfided 4 wt% NiO-24 wt% WO₃/SiO₂-Al₂O₃ [3] and for CoMo/Al₂O₃ hydrotreating catalyst, when both temperature and pressure were changed. Furthermore, the H₂/feed ratio and space time were also varied [1,24]. For the former catalyst, which also exhibited acidic properties, more kerosene products were formed, especially at high temperature. Formation of C9-C14 components was the most prominent at 420 °C under 80 bar hydrogen with a low space velocity. The most suitable model contains both parallel formation of oligomers, heavy, middle and naphtha components and a consecutive route from heavy to kerosene and further to naphtha compounds. The model involves several different lumped kinetic constants.

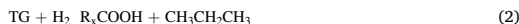
Both diffusivity of different compounds at a given temperature as well as the effectiveness factor, i.e. the ratio between the rate in the presence of mass transfer limitations and the rate in the kinetic regime, were calculated in [3]. The results showed that the effectiveness factor was close to one and the experiments were performed in the diffusion free region. In addition, activation energies were determined for formation of different product groups. The activation energy for transformation of triglycerides is 115 kJ/mol, which it was nearly the same as for formation of diesel, 122 kJ/mol, while higher activation energies were required for formation of naphtha and kerosene, being 130 kJ/mol and 122 kJ/mol, respectively. These results clearly show that a high energy input is required for formation of kerosene and naphtha type compounds. Furthermore, temperature profile along the catalyst bed was calculated. Considering heat of reactions determined separately for different reactions, i.e. depropanation, hydrodeoxygenation, decarboxylation, decarbonylation and hydrocracking. The results showed that exothermicity of hydroconversion of Jatropha oil was very high, 1.34 MJ/kg Jatropha oil, which is nearly 10 fold of the heat released in cracking of vacuum gas oil [68].

It was also observed for hydroconversion of Jatropha oil that for 3 wt% Co-8 wt% Mo/Al₂O₃ the above mentioned model was valid at 360 °C, while another type of parallel-consecutive route was describing better the results below 320 °C [29].

Due to a higher acidity of 3 wt% Co-8 wt% Mo/MTS in comparison to 3 wt% Co-8 wt% Mo/Al₂O₃, the best fitting model for Jatropha oil hydroconversion was based on the parallel direct formation of different fractions at 300 °C [29].

9. Reaction mechanism

The reaction mechanism in hydroconversion of oils [3,16,17,22,23,29,32], fatty acids [4,12,26,25,27,28,45] and their esters [37] has been intensively studied. Hydroconversion of oils starts with hydrogenation of triglycerides (TG) to the corresponding saturated molecules [29], followed by depropanation [15,20]:



Thereafter, fatty acids undergo either hydrodeoxygenation forming water and a hydrocarbon with the same amount of carbon as in the original fatty acid, or alternatively undergoes decarbonylation or decarboxylation forming a hydrocarbon with one carbon less and CO or CO₂, respectively [29]. It was also proposed in [15] that fatty acids formed via hydrolysis of triglycerides can be dehydrogenated forming triene fatty acids, which are transformed to conjugated double bonds [15]. Five-membered hydrocarbon rings are formed by the intermolecular Diels-Alder reaction of the conjugated triene over Lewis acid sites [69]. For example, dodecylbenzene, a product in hydrocracking of soybean oil is formed by a migration of double bonds from C9 to C15 in linoleic and linolenic acids to the terminal position of the hydrocarbon chain before the intermolecular Diels-Alder reaction takes place [15]. It was also reported in [20] that cyclic hydrocarbons are converted to aromatics by ring expansion over Ni and Lewis acid sites. In hydrogenolysis of oils, propane and C6-C8 olefins are formed. Propane can be dehydrogenated to propene and react with C6-C8 olefins. Aromatic compounds can also be formed from e.g. butadiene and ethane, giving first cyclohexene by the Diels-Alder reaction followed by dehydrogenation of cyclohexene [23]. Furthermore, substituted cyclopentane derivatives undergo easily a ring expansion forming for example 1-methylcyclohex-1-ene and toluene [45].

In conjugated trienes the double bond migration towards the end of the carbon chain is followed by hydrodeoxygenation of fatty acids. Diesel range hydrocarbons should be dehydrogenated, isomerized and cracked to form kerosene and gasoline [29], while formation of gaseous products should be avoided. In addition to these products, also oligomers can originate from alkylation reactions [29].

The reaction mechanism in triolein hydroconversion was proposed based on the product distribution. Hexadecane is formed by γ -hydrogen transfer (Fig. 15) [23,70], while oleic acid is generated by β -elimination. Pentadecane formation requires β - γ scission [23].

Different types of β -scission mechanisms for alkylcarbenium ions, proposed in the literature, are shown in Fig. 16 [16]. It has been proposed that mono-, di- and multibranched alkanes are formed in a consecutive manner.

Cracking of tribranched A type (Fig. 16) alkanes produces two branched molecules, while cracking of a dibranched B molecule gives one linear and one branched product. Furthermore, cracking of mono-branched compound C generates only linear products. The relative rates for β -scission as reported in [71] decrease with a decreasing number of branching as follows: $r_A > r_{B1} \approx r_{B2} > r_C \gg r_D$.

The reaction scheme for hydroconversion of palmitic acid was proposed in [29] including palmitic acid hydrogenation to hexadecanal and further to hexadecanol, its dehydration forming hexadecane and further isomerization products by dehydrogenation, and cracking products, e.g. C13 and C13 isomer. In addition, a parallel route was proposed to hydrogenation of palmitic acid, i.e. direct hydroconversion from palmitic acid to C14. Hexadecanal can also decarbonylate and further crack and isomerize forming C12 hydrocarbons.

10. Future research needs and conclusions

Although research on production of jet fuels from fatty acids and oils has been very intensive during recent years, several future research needs could be still identified. Typically, a comprehensive product

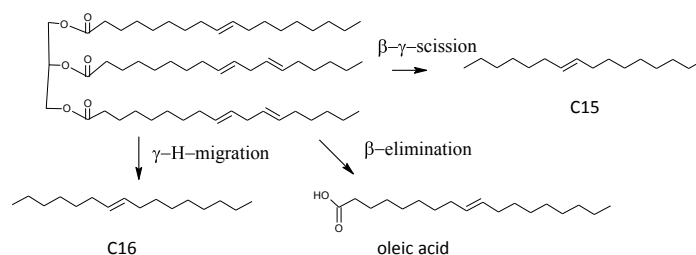


Fig. 15. Hydrotransformations of triglycerides, adapted from [23]

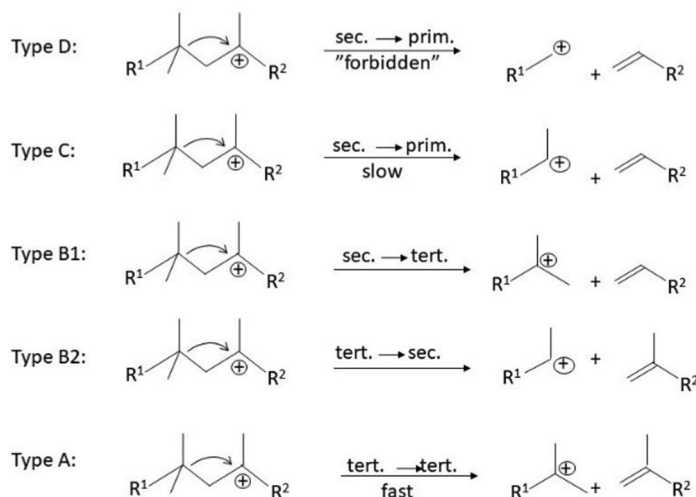


Fig. 16. Proposed β -scission mechanisms for alkylcarbenium ions, adapted from [16]

analysis with a proper mass balance closure, kinetic modelling and thermodynamic analysis have been very scarcely performed [3]. Information of fractional selectivity among liquid phase products is certainly not sufficient for eventual industrial implementation. Thus, future research efforts should be clearly focused on development of suitable analytical approaches for identification as well as quantification of products. Moreover, the broad product distribution adhering to both diesel and jet fuel fraction implies that separation of these products by distillation would be required. In addition if the concentration of aromatics is too high after hydroconversion they should be removed most probably by extraction as typically done in oil refining.

Furthermore, due to harsh reaction conditions, for example in hydroconversion of vegetable oils over Ni-W/SiO₂-Al₂O₃ many carbonaceous species are present in the gas phase (ca. 30 wt%). On the other hand, a two-step process for hydroconversion of palm oil involving hydroisomerisation over Pt/Al₂O₃ in the first step followed by hydrocracking with Pt/Beta zeolite was shown to be more feasible and not suffering extensive catalyst deactivation opposite to the one-step process.

The importance of diffusional limitations for formation of C8-C16 was clearly demonstrated showing a beneficial use of nanosized zeolites as supports. Catalyst acidity is an important parameter and although it has been measured in several publications, many papers

report only qualitative data on acidity, making comparison of the results in different publications challenging.

Finally comprehensive catalyst characterization, such as determination of acidity, metal particle size, reducibility and metal oxidation states, especially using hydrogen temperature programmed reduction [2,3,11,30,32] and XPS [2,3,30,32] would bring more knowledge helping to rationalize the catalyst selection, which at the moment is largely missing [24].

In summary, production of jet fuels by hydroconversion of vegetable oils and fatty acids has been intensively studied during the recent years. The highest yields of organic liquid products, above 80 wt%, have been obtained from *Jatropha* and palm oil using Ni supported on H₃PW₁₂O₄₀/nanosized hydroxyapatite in one step at 360 °C under 30 bar hydrogen [11] and in a two-step process over Pt/Al₂O₃ (hydroisomerization at 395 °C) followed by hydrocracking at 245 °C over Pt on H-Y zeolite [15]. Jet fuel yields are typically maximally ca. 54%, while also other products such as diesel, are formed.

Declaration of Competing Interest

The authors declare that they have no known competing financial interests or personal relationships that could have appeared to influence

the work reported in this paper.

Appendix A. Supplementary data

Supplementary data to this article can be found online at <https://doi.org/10.1016/j.fuel.2021.121673>.

References

- Anand M, Sinha AK. Temperature-dependent reaction pathways for the anomalous hydroconversion of triglycerides in the presence of sulfided Co-Mo-catalyst. *Bioresour Technol* 2012;126:148–55.
- Anand M, Farooqui SA, Kumar R, Joshi R, Kumar R, Sibi MG, et al. Optimizing renewable oil hydroconversion conditions for aviation bio-kerosene production. *Fuel Proc Technol* 2016;151:50–8.
- Anand M, Farooqui SA, Kumar R, Joshi R, Kumar R, Sibi MG, et al. Kinetics, thermodynamics and mechanisms for hydroprocessing of renewable oils. *Appl Catal A Gen* 2016;516:144–52.
- Cao Y, Shi Y, Bi Y, Wu K, Hu S, Wu Y, et al. Hydrodeoxygenation and hydrosomerization of palmitic acid over bi-functional Co/H-ZSM-22 catalysts. *Fuel Proc Technol* 2018;172:29–35.
- Chen Y-K, Hsieh C-H, Wang W-C. The production of renewable aviation fuel from waste cooking oil. Part II: Catalytic hydro-cracking/isomerization of hydro-processed alkanes into jet fuel range products. *Renew Energy* 2020;157:731–40.
- Chen L, Li H, Fu J, Miao C, Lv P, Yuan Z. Catalytic hydroprocessing of fatty acid methyl esters to renewable alkane fuels over Ni/HZSM-5 catalyst. *Catal Today* 2016;259:266–76.
- Cheng J, Li T, Huang R, Zhou J, Cen K. Optimizing catalysis conditions to decrease aromatic hydrocarbons and increase alkanes for improving jet biofuel quality. *Bioresour Technol* 2014;158:378–82.
- Cheng J, Zhang Z, Zhang X, Liu J, Zhou J, Cen K. Hydrodeoxygenation and hydroconversion of microalgae biodiesel to produce jet biofuel over $H_3PW_{12}O_{40}$ -Ni/hierarchical mesoporous zeolite Y catalyst. *Fuel* 2019;245:384–91.
- Duijantut P, Kaewkannetra P. Production of bio-hydrogenated kerosene by catalytic hydroconversion from refined bleached deodorised palm/palm kernel oils. *Renew Energy* 2020;147:464–72.
- Eller Z, Varga Z, Hancsók J. Advanced production process of jet fuel components from technical grade coconut oil with special hydroconversion. *Fuel* 2016;182:713–20.
- Fan K, Liu J, Yang X, Rong L. Hydroconversion of Jatropha oil over $Ni-H_3PW_{12}O_{40}$ /nano-hydroxyapatite catalyst. *Int J Hydrogen Energy* 2014;39(8):3690–7.
- Feng F, Niu X, Wang Li, Zhang X, Wang Q. TEOS-modified Ni/ZSM-5 nanosheet catalysts for hydroconversion of oleic acid to high-performance aviation fuel: effect of acid spatial distribution. *Micropor Mesop Mater* 2020;291:109705. <https://doi.org/10.1016/j.micromeso.2019.109705>.
- Feng F, Shang Z, Wang Li, Zhang X, Liang X, Wang Q. Structure-sensitive hydro-conversion of oleic acid to aviation-fuel-range-alkanes over alumina-supported nickel catalyst. *Catal Commun* 2020;134:105842. <https://doi.org/10.1016/j.cattcom.2019.105842>.
- Ishihara A, Fukui N, Nasu H, Hashimoto T. Hydroconversion of soybean oil using zeolite–alumina composite supported NiMo catalysts. *Fuel* 2014;134:611–7.
- Jeong H, Bathula HB, Kim TW, Han GB, Jang JH, Jeong B, et al. Superior long-Term Stability of a mesoporous alumina-supported Pt catalyst in the hydrodeoxygenation of palm oil. *ACS Sustain Chem Eng* 2021;9(3):1193–202.
- Kim MY, Kim JK, Lee ME, Lee S, Choi M. Maximizing biojet fuel production from triglyceride: importance of the hydroconversion catalyst and separate deoxygenation/hydroconversion steps. *ACS Catal* 2017;7(9):6256–7.
- Li X, Chen Y, Hao Y, Zhang Xu, Du J, Zhang A. Optimization of aviation kerosene from one-step hydrotreatment of catalytic Jatropha oil over SDBS-Pt/SAPO-11 by response surface methodology. *Renew Energy* 2019;139:551–9.
- Li T, Cheng J, Huang R, Yang W, Zhou J, Cen K. Hydroconversion of palm oil to jet biofuel over different zeolites. *Int J Hydrogen Energy* 2016;41(47):21883–7.
- Li T, Cheng J, Huang R, Zhou J, Cen K. Conversion of waste cooking oil to jet biofuel with nickel-based mesoporous zeolite Y catalyst. *Bioresour Technol* 2015;197:289–94.
- Lin C-H, Wang W-C. Direct conversion of glyceride-based oil into renewable jet fuels. *Renew Sustain Energy Rev* 2020;132:110109. <https://doi.org/10.1016/j.rser.2020.110109>.
- Rabaev M, Landau MV, Vidruk-Nehemya R, Koukouliev V, Zarchin R, Herskowitz M. Conversion of vegetable oils on Pt/Al_2O_3 /SAPO-11 to diesel and jet fuels containing aromatics. *Fuel* 2015;161:287–94.
- da Rocha Filho GN, Brodzki D, Djéga-Mariadassou G. Formation of alkanes, alkylcycloalkanes and alkylbenzenes during the catalytic hydroconversion of vegetable oils. *Fuel* 1993;72(4):543–9.
- Scalaferrri CA, Pasa VMD. Production of jet fuel and green diesel range biohydrocarbons by hydroprocessing of soybean oil over niobium phosphate catalyst. *Fuel* 2019;245:458–66.
- Sharma RK, Anand M, Rana BS, Kumar R, Farooqui SA, Sibi MG, et al. Jatropha-oil conversion to liquid hydrocarbon fuels using mesoporous titanasilicate supported sulfide catalysts. *Catal Today* 2012;198(1):314–20.
- Shi Y, Cao Y, Duan Y, Chen H, Chen Yu, Yang M, et al. Upgrading of palmitic acid to iso-alkanes over bi-functional Mo/ZSM-22 catalysts. *Green Chem* 2016;18(17):4633–48.
- Shi Y, Li R, Shen Q, Yang M, Wu Y. The selective production of jet fuel range alkanes via the catalytic upgrading of palmitic acid over Co/HMCM-49 catalysts. *Chem Commun* 2019;55(80):12096–9.
- Shi Y, Xing E, Cao Y, Liu M, Wu K, Yang M, et al. Tailoring product distribution during upgrading of palmitic acid over bi-functional metal/zeolite catalysts. *Chem Eng Sci* 2017;166:262–73.
- Shi Y, Zhang J, Xing E, Xie Y, Cao H. Selective production of jet-fuel-range alkanes from palmitic acid over Ni/H-MCM-49 with two independent pore systems. *Ind Eng Chem Res* 2019;58(47):21341–9.
- Sinha AK, Anand M, Rana BS, Kumar R, Farooqui SA, Sibi MG, et al. Development of hydroprocessing route to transportation fuels from non-edible plant-oils. *Catal Surveys Asia* 2013;17(1):1–13.
- Srihanun N, Duijantut P, Muanruksa P, Kaewkannetra P. Biofuels of green diesel–kerosene–gasoline production from palm oil: effect of palladium cooperated with second metal on hydroconversion reaction. *Catalysts* 2020;10(2):241.
- Verma D, Kumar R, Rana BS, Sinha AK. Aviation fuel production from lipids by a single-step route using hierarchical mesoporous zeolites. *Energy Environ Sci* 2011;4(5):1667–71.
- Wang C, Liu Q, Song J, Li W, Li P, Xu R, et al. High quality diesel-range alkanes production via a single-step hydrotreatment of vegetable oil over Ni/zeolite catalyst. *Catal Today* 2014;234:153–60.
- Zhang Z, Wang Q, Chen H, Zhang X. Hydroconversion of waste cooking oil into green biofuel over hierarchical USY-supported NiMo catalyst: a comparative study of desilication and dealumination. *Catalysts* 2017;7(10):281. <https://doi.org/10.3390/catal7100281>.
- Zhang Z, Wang Q, Chen H, Zhang X. Hydroconversion of waste cooking oil into bio-jet fuel over a hierarchical NiMo/USY or Al-SBA-15 zeolite. *Chem Eng Technol* 2018;41(3):590–7.
- Zhang Z, Cheng J, Zhu Y, Guo H, Yang W. Jet fuel range hydrocarbons production through competitive pathways of hydroconversion and isomerization over HPW-Ni/MCM-41 catalyst. *Fuel* 2020;269:117465.
- Zhang J, Shi Y, Cao H, Wu Y, Yang M. Conversion of palmitic acid to jet fuel components over Mo/H-ZSM-22 bi-functional catalysts with high carbon reservation. *Appl Catal A Gen* 2020;608:117847. <https://doi.org/10.1016/j.apcata.2020.117847>.
- Zhang Ze, Cheng J, Qiu Yi, Zhang Xi, Zhou J, Cen K. Competitive conversion pathways of methyl palmitate to produce jet biofuel over Ni/desilicated meso-Y zeolite catalyst. *Fuel* 2019;244:472–8.
- Zhu Y, Zhang Y, Cheng Z, Guo J, Yang H. Ni-BTC metal-organic framework loaded on MCM-41 to promote hydrodeoxygenation and hydroconversion in jet biofuel production. *Int J Hydrogen Energy* 2021;46(5):3898–908.
- Zanata M, Tri Wulan Amelia S, Mumtazy MR, Kurniawansyah F, Roesyadi A. Synthesis of bio jet fuel from crude palm oil by HEFA (Hydroprocessed Esters and Fatty Acids) using Ni-Mo catalyst supported by rice husk Ash-based SiO_2 . In *Materials Science Forum* 2019; 964:193-8. Trans Tech Publications Ltd.
- Pires AP, Han Y, Kramlich J, Garcia-Perez M. Chemical composition and fuel properties of alternative jet fuels. *Bio Res* 2018;13(2):2632–57.
- Mullen CA, Boateng AA, Mihalick DJ, Goldberg NM. Catalytic fast pyrolysis of white oak wood in a bubbling fluidized bed. *Energy Fuels* 2011;25(11):5444–51.
- Van den Bosch S, Schutyser W, Koelewijn S-F, Renders T, Courtin CM, Sels BF. Tuning the lignin oil Off-content with Ru and Pd catalysts during lignin hydrolysis on birch wood. *Chem Commun* 2015;51(67):13158–61.
- Jogi R, Mäki-Arvela P, Virtanen P, Kumar R, Kumar N, Hemming J, Smeds A, et al. Biocrude production through hydro-liquefaction of wood biomass in supercritical ethanol using iron silica and iron beta zeolite catalysts. *J Chem Technol Biotechnol* 2019; 94(11):3736–44.
- Lindfors C, Mäki-Arvela P, Paturi P, Aho A, Eränen K, Hemming J, et al. Hydrodeoxygenation of isoeugenol over Ni- and Co-supported catalysts. *ACS Sustain Chem Eng* 2019;7(17):14545–60.
- Bomont L, Alda-Ongarr M, Fedorov V, Aho A, Peltonen J, Eränen K, et al. Production of cycloalkanes in hydrodeoxygenation of isoeugenol over Pt- and Ir-modified bifunctional catalysts. *Eur J Inorg Chem* 2018;2018(24):2841–54.
- Xing S, Lv P, Wang J, Fu J, Fan P, Yang L, et al. One-step hydroprocessing of fatty acids into renewable aromatic hydrocarbons over Ni/HZSM-5: insights into the major reaction pathways. *Phys Chem Phys* 2017;19(4):2961–73.
- Sonthalia A, Kumar N. Hydroprocessed vegetable oil as a fuel for transportation sector: a review. *J Energy Inst* 2019;92(1):1–17.
- Tirado A, Ancheyta J, Trejo F. Kinetic and reactor modeling of catalytic hydrotreatment of vegetable oils. *Energy Fuels* 2018;32(7):7245–61.
- Wei H, Liu W, Chen X, Yang Q, Li J, Chen H. Renewable bio-jet fuel production for aviation: a review. *Fuel* 2019;254:115599. <https://doi.org/10.1016/j.fuel.2019.06.007>.
- Vásquez MC, Silva EE, Castillo EF. Hydrotreatment of vegetable oils: a review of the technologies and its developments for jet biofuel production. *Biomass Bioenergy* 2017;105:197–206.
- ASTM. Standard specification for aviation turbine fuels. D1655–19a. West Conshohocken, PA: ASTM International; 2019.
- Braun-Unkoff M, Kathrotia T, Rauch B, Riedel U. CEAS Aeron J 2016;7(1):83–94.
- Mandal PC, Abdullah AB, Rahman MM. Total acid number reduction of 2,6-naphthalenedicarboxylic acid using subcritical methanol for reducing acidity of heavy oil: a kinetic study. *Proc Eng* 2016;148:1213–9.
- Jiménez-Cruz F, Laredo GC. Molecular size evaluation of linear and branched paraffins from the gasoline pool by DFT quantum chemical calculations. *Fuel* 2004; 83(16):2183–8.

- [55] Gould TD, Lubers AM, Neltner BT, Carrier JV, Weimer AW, Falconer JL, et al. Synthesis of supported Ni catalysts by atomic layer deposition. *J Catal* 2013;303: 9–15.
- [56] Li X, Quek X-Y, Michel Ligthart DAJ, Guo M, Zhang Yi, Li C, et al. CO-PROX reactions on copper cerium oxide catalysts prepared by melt infiltration. *Appl Catal B Environ* 2012;123-124:424–32.
- [57] Gan Q, He H, Zhao K, He Z, Liu S. Morphology-dependent electrochemical performance of Ni-1, 3, 5-benzenetricarboxylate metal-organic frameworks as an anode material for Li-ion batteries. *J Coll Int Sci* 2018;530:127–36.
- [58] Yang L, Xing S, Sun H, Miao C, Li M, Lv P, et al. Citric-acid-induced mesoporous SAPO-11 loaded with highly dispersed nickel for enhanced hydroisomerization of oleic acid to iso-alkanes. *Fuel Proc Technol* 2019;187:52–62.
- [59] Zhang Q, Long K, Wang J, Zhang T, Song Z, Lin Q. A novel promoting effect of chelating ligand on the dispersion of Ni species over Ni/SBA-15 catalyst for dry reforming of methane. *Int J Hydrogen Energy* 2017;42(20):14103–14.
- [60] Pu X, Liu N-W, Shi Li. Acid properties and catalysis of USY zeolite with different extra-framework aluminum concentration. *Microp Mesop Mat* 2015;201:17–23.
- [61] Li S, Zheng A, Su Y, Zhang H, Chen L, Yang J, et al. Brønsted/Lewis acid synergy in dealuminated HY zeolite: a combined solid-state NMR and theoretical calculation study. *J Am Chem Soc* 2007;129(36):11161–71.
- [62] Choi M, Cho HS, Srivastava R, Venkatesan C, Choi D-H, Ryoo R. Amphiphilic organosilane-directed synthesis of crystalline zeolite with tunable mesoporosity. *Nat Mater* 2006;5(9):718–23.
- [63] Qiu B, Yi X, Lin L, Fang W, Wan H. The hydroconversion of n-decane over bifunctional Ni-H3PW12O40/SiO2 catalysts. *Catal Today* 2008;131(1–4):464–71.
- [64] Chakraborty R, Das SK. Optimization of biodiesel synthesis from waste frying soybean oil using fish scale-supported Ni catalyst. *Ind Eng Chem Res* 2012;51(25): 8404–14.
- [65] Shi Y, Xing E, Xie W, Zhang F, Mu X, Shu X. Enhancing activity without loss of selectivity–Liquid-phase alkylation of benzene with ethylene over MCM-49 zeolites by TEOAH post-synthesis. *Appl Catal A Gen* 2015;497:135–44.
- [66] Du H, Liu D, Li M, Wu P, Yang Y. Effects of the temperature and initial hydrogen pressure on the isomerization reaction in heavy oil slurry-phase hydroconversion. *Energy Fuels* 2015;29(2):626–33.
- [67] Kumar R, Rana BS, Tiwari R, Verma D, Kumar R, Joshi RK, et al. Hydroprocessing of jatropha oil and its mixtures with gas oil. *Green Chem* 2010;12(12):2232. <https://doi.org/10.1039/c0gc00204f>.
- [68] Moghadassi A, Amini N, Fadaei O, Bahmani M. Kinetics, thermodynamics and mechanisms for hydroprocessing of renewable oils. *Petrol Sci Technol* 2011;1: 31–7.
- [69] Davis BH. Alkane dehydrocyclization mechanism. *Catal Today* 1999;53(3): 443–516.
- [70] Morgan T, Grubb D, Santillan-Jimenez E, Crocker M. Conversion of triglycerides to hydrocarbons over supported metal catalysts. *Topics Catal* 2010;53(11–12):820–9.
- [71] Weitkamp J. Catalytic hydroconversion—mechanisms and versatility of the process. *ChemCatChem* 2012;4(3):292–306.

M. E. Martínez-Klimov, P. Mäki-Arvela, Z. Vajglová, M. Alda-Onggar, I. Angervo, N. Kumar, K. Eränen, M. Peurla, M. H. Calimli, J. Muller, A. Shchukarev, I. L. Simakova, D. Y. Murzin, Hydrodeoxygenation of isoeugenol over carbon-supported Pt and Pt-Re catalysts for production of renewable jet fuel, *Energy Fuels*, 35 (2021) 17755-17768.



Hydrodeoxygenation of Isoeugenol over Carbon-Supported Pt and Pt–Re Catalysts for Production of Renewable Jet Fuel

Mark E. Martínez-Klimov, Päivi Mäki-Arvela, Zuzana Vajglova, Moldir Alda-Onggar, Ilari Angervo, Narendra Kumar, Kari Eränen, Markus Peurla, Mehmet Harbi Calimli, Joseph Muller, Andrey Shchukarev, Irina L. Simakova, and Dmitry Yu. Murzin*



Cite This: *Energy Fuels* 2021, 35, 17755–17768

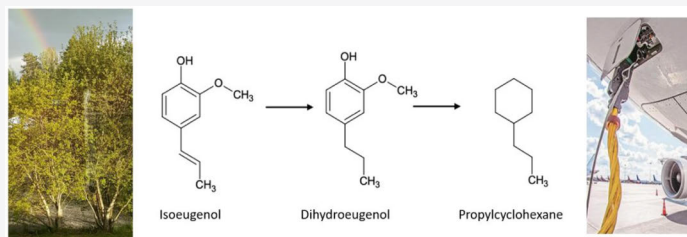


Read Online

ACCESS |

Metrics & More

Article Recommendations



ABSTRACT: A series of monometallic platinum and bimetallic platinum–rhenium catalysts supported on mesoporous carbon Sibunit, which is a type of mesoporous, microcrystalline carbon, were investigated for hydrodeoxygenation (HDO) of isoeugenol (IE) at 200–300 °C and 30 bar of H₂, using dodecane as a solvent. Catalytic activity was tested in a batch reactor to screen the catalysts and, for comparison, also in the continuous mode. For batch experiments, complete conversion, and a high yield of the desired product, propylcyclohexane (PCH), were obtained for all bimetallic PtRe/Sibunit in 240 min, with the highest yield of PCH when Pt:Re ratio was 1:1 or 1:3. The results for Pt–Re (1:1) were reproducible, in terms of catalytic activity and reusability of catalysts, which showed no deactivation. Monometallic Pt catalysts displayed low activity. Continuous experiments were performed with PtRe(1:1)/Sibunit at 30 bar H₂, 0.5 mL/min of the liquid flow, and temperatures between 75 °C and 200 °C. The distribution of products showed deoxygenation at higher temperatures, while at lower temperatures, mainly oxygenated products were formed. XPS results confirmed the presence of ReOx species, where an increase in the platinum loading resulted in a decrease in the fraction of ReOx species and subsequently lower PCH yield.

INTRODUCTION

Fossil-derived fuels still provide most of the energy used worldwide, with its consumption still increasing yearly.¹ This constant increase of greenhouse gases emissions, depletion of nonrenewable resources, and alternative-fuel regulations have promoted the development of new technologies and processes to solve these challenges.²

While the use of electric and hybrid vehicles has increased considerably in recent years, these technologies are not appropriate for their use on commercial airplanes, mainly because of insufficient electrical storage as well as the weight of batteries and electric propulsion systems.³ Therefore, biomass, being a renewable and sustainable feedstock alternative to such fossil feedstock as crude oil, has attracted much attention as a source for production of fuels and chemicals.⁴

One of the main conversion processes to obtain bio-oil is the pyrolysis of lignocellulosic biomass. The obtained bio-oil is rich in oxygenated compounds, making it unsuitable as a fuel,

because of, for example, high viscosity, a low heating value, high acidity, and chemical instability.⁵ Bio-oil requires additional steps to be able to obtain biofuels⁶ that could substitute or supplement those currently in use.⁷ One of the main routes for upgrading biomass-derived oil into liquid fuels is through hydrodeoxygenation (HDO).⁸ In HDO, oxygen is removed from organic molecules as water, CO₂, or CO, in the presence of a catalyst and hydrogen.

Bifunctional catalysts with two types of active sites are required for HDO: one site to activate hydrogen (metal), and another one to activate oxygen (oxophilic metal or acid

Received: August 3, 2021

Revised: September 20, 2021

Published: October 18, 2021



support). Hydrogenation, dehydrogenation, hydrocracking, and decarbonylation occur on metal sites, while dehydration, isomerization, and hydrogenolysis occur on the acid sites.⁹ Monometallic catalysts deposited on oxide supports and carbon have been extensively studied for the HDO of various model compounds.¹⁰ The most common catalysts are noble¹¹ (such as Pt, Rh, Pd), or transition metals¹² (such as Ni, Co, Mo) supported on zeolites,¹³ or oxides (e.g., Al_2O_3 ¹⁴ and SiO_2 ¹⁵). Bimetallic catalysts mainly studied for HDO include Mo in combination with Ni and Co,¹⁶ which have been traditionally used for HDO processes in petroleum refining. Bimetallic catalysts containing noble metals and rhenium (RuRe/C ,¹⁷ IrRe/SiO_2 ,^{18,19} RePd/CeO_2 ,²⁰ $\text{IrRe/Al}_2\text{O}_3$ ¹⁴) have shown that the presence ReOx resulted in activity elevation. While Re has been mainly studied in the context of catalytic reforming and aqueous phase reforming, the interest in rhenium has expanded to other reactions, where the oxophilic nature of the metal could improve catalytic activity.

Studies have found that oxides of Mg, Mo, W, and Fe can enhance HDO by improving the reducibility of Pt species through an electron transfer.²¹ DFT calculations have also proved a synergistic effect between Pt and MOx species in adsorbing/activating C–O bonds, making metal–metal oxide catalysts interesting and promising for HDO.²²

The use of new supports such as nanotubes,²³ ordered-mesoporous silica,^{24,25} and different types of carbon,²⁶ has attracted the attention of researchers, because of their properties, such as high surface area, porosity, acidity, or basicity, etc. Among such supports, Sibunit, which is a type of mesoporous, microcrystalline carbon, is considered as an attractive material, because of its high mechanical strength,²⁷ reasonably large surface area, high purity, and chemical stability,²⁸ combining the properties of graphite and activated carbon. Additional benefits of Sibunit-based catalysts are that they can be produced in large scale and in different shapes, such as whole and hollow cylinders, rings, etc., allowing for a wide range of applications.²⁹ This material is synthesized via the deposition of pyrolytic carbon from C_1 – C_3 hydrocarbons on granulated carbon black, followed by condensation and steam activation.³⁰ Temperature-programmed desorption (TPD) studies of Sibunit have reported that CO and CO_2 evolutions resemble those for other various carbonaceous materials, with a high amount of carboxylic groups on the surface.³¹

Currently, most HDO is performed on a laboratory scale, using three-phase systems (gas–liquid–solid) in batch reactors. While this approach gives information regarding kinetics, industrial interest focuses on continuous flow processes, which allow for scalability, higher and constant throughput, and improved automation.³²

Studies on HDO in continuous reactors have mostly centered on guaiaicol;^{19,33,34} however, isoeugenol has not been studied previously in this type of systems. Isoeugenol is a model compound of interest, as its structure is representative of the three phenylpropane units that constitute lignin.³⁵ Its molecular structure also contains the main oxygenated groups, more specifically, the hydroxyl, methoxy, and allyl groups found in the compounds of lignin-derived bio-oil.

Research focused on the HDO of isoeugenol using bimetallic catalysts—in particular, bimetallic Pt–Re—in both batch and continuous reactors has been scarce. Our previous research on isoeugenol HDO was focused on Ir, Pt, and Re catalysts supported on alumina, highlighting the importance of

an oxophilic metal for the reaction.¹³ Another investigation of Ir and Ni catalysts supported on ZrO_2 resulted in the formation of large amounts of gas-phase products, therefore giving a low mass balance closure in the liquid phase.³⁶

The purpose of this work was to study HDO of isoeugenol using monometallic Pt and bimetallic Pt–Re supported on carbon as catalysts in a batch reactor. Furthermore, HDO of isoeugenol was investigated for the first time in a continuous reactor.

EXPERIMENTAL SECTION

Chemicals. The following chemicals were acquired commercially: isoeugenol (98%, mixture of *cis* and *trans*, Aldrich), dihydroeugenol (≥ 99 , Sigma–Aldrich), *n*-dodecane ($\geq 99\%$, Acros Organics), benzene ($\geq 99\%$, Sigma–Aldrich), propylcyclohexane (99%, Aldrich) cyclohexane (99.9%, Alfa Aesar), hexane ($> 97\%$, Sigma–Aldrich), tetraammineplatinum(II) nitrate ($\geq 50.0\%$ Pt basis, Aldrich), H_2PtCl_6 (Krasvmetmet, Krasnoyarsk, Russia) and HReO_4 (20 wt %, Reachim, Russia).

The following gases were used: hydrogen (AGA, 99.999%), argon (AGA, 99.999%), and helium (AGA, 99.996%).

Preparation of Catalysts. The following catalysts were acquired from Degussa: F106XXKYF and F1525XKT. The notation given to these catalysts was Pt/C1 and Pt/C2, respectively, both containing up to 5 wt % Pt on activated carbon.

Activated carbon Norit was supplied by NORIT (NORIT R 3 EXTRA activated carbon) and Sibunit was supplied by the Borekov Institute of Catalysis, Siberian Branch of the Russian Academy of Sciences.

Monometallic Pt catalysts, Pt/Norit, and Pt/Sibunit were synthesized by the incipient wetness impregnation of tetraammineplatinum(II) nitrate ($\geq 50.0\%$ Pt basis, Aldrich) on Norit or Sibunit, the catalysts were denoted as Pt/Norit and Pt/Sibunit, respectively.

Bimetallic Pt–Re catalysts (PRC series; PRC11, PRC31, and PRC13) were synthesized by impregnation. Sibunit ($< 63 \mu\text{m}$) was impregnated with an aqueous solution of a mixture of the metal precursors H_2PtCl_6 (OAO Aurat, Russia) and HReO_4 (20 wt %, Reachim, Russia). Three bimetallic catalysts with different metal ratios were prepared: 1:1 with the nominal metal loading of each metal of 4 wt %, 1:3 with the nominal metal loading of 2 wt % for Pt and 6 wt % for Re, and 3:1 with the nominal metal loading of 6 wt % for Pt and 2 wt % for Re. The catalysts were named PRC11, PRC13, and PRC31, respectively.

Granulated PRC11 catalyst used for the continuous reactor experiments was prepared by the same method as described above, only using larger particles of Sibunit (1 mm).

After impregnation, the catalysts were calcined at 110 °C overnight, reduced in a hydrogen flow with a temperature ramp of 2 K/min until 330 °C, and kept at the final temperature for ca. 6 h.

The catalysts used in the batch reactor were reduced *ex situ* under hydrogen flow (40 mL/min) at 350 °C for 3 h (10 °C/min) prior to experiments. After reduction, the catalyst was flushed with argon and the solvent was added to avoid reoxidation of the catalyst. The catalyst used in the continuous reactor was reduced *in situ* under the same conditions as with the catalysts used in the batch reactor.

A summary of the catalysts used in the current work is presented in Table 1.

Reactor Setup and Analysis. HDO of isoeugenol was performed as a model reaction to determine the activity of Pt and Pt–Re catalysts supported on carbon. The reactions were performed in a 300 mL stainless steel batch reactor (PARR Instruments) equipped with a mechanical stirrer. The samples were taken at regular time intervals. The stirring speed was set to 900 rpm to avoid external mass-transfer limitations. The size of the catalyst particles was $< 63 \mu\text{m}$, to ensure the absence of internal mass-transfer limitations. For HDO of isoeugenol, 0.05 g of the catalyst, 0.1 g of the reactant, and 50 mL of dodecane were used. The liquid samples were analyzed by gas

Table 1. Summary of Catalysts Used for HDO of Isoeugenol

denomination	Catalyst			
	metal	loading (wt %)	support	type
Pt/C1	platinum	5	activated carbon	commercial (Degussa)
Pt/C2	platinum	5	activated carbon	commercial (Degussa)
Pt/Norit	platinum	2	activated carbon	self-synthesized
Pt/Sibunit	platinum	4	mesoporous carbon	self-synthesized
PRC11	platinum, rhenium	4 and 4	mesoporous carbon	self-synthesized
PRC31	platinum, rhenium	6 and 2	mesoporous carbon	self-synthesized
PRC13	platinum, rhenium	2 and 6	mesoporous carbon	self-synthesized
PRC11 granulated	platinum, rhenium	4 and 4	mesoporous carbon	self-synthesized

chromatography (GC) and gas chromatography/mass spectroscopy (GC/MS). In GC analysis, a DB-1 capillary column (Agilent, Model 122-103e) of 30 m length, 250 μ m internal diameter and 0.5 μ m film thickness was utilized. Helium was applied as a carrier gas with the flow rate of 1.7 mL/min. The temperature program for GC analysis was as follows: 60 °C (5 min), 3 °C/min to 135 °C, and 15 °C/min to 300 °C. GC-MS analysis was performed over the same column and using the same temperature program as used in GC.

Continuous experiments were performed in a laboratory-scale fixed-bed reactor with the following dimensions: 12 cm length, 1.2 mm inner diameter, 70-mm catalyst zone, 3-mm thermocouple pocket. The reactor was loaded with 0.3 g of the catalyst mixed with 15 g of fine granular quartz (200–800 μ m) to have a uniform distribution of the catalyst throughout the catalytic bed; the remaining space was filled with quartz. The reaction mixture was fed downflow via a high-performance liquid chromatography (HPLC) pump (Knauer Smartline). The reaction conditions were as follows: 30 bar H₂, gas flow rate of 0.5 mL/min, liquid flow rate of 0.5 mL/min, temperatures between 75 and 200 °C. The catalyst was reduced in situ at 350 °C for 3 h (temperature ramp = 10 °C/min) under a hydrogen flow rate of 40 mL/min at atmospheric pressure. The liquid samples taken periodically during 4 h were analyzed using the same procedure as that used with the batch reactor.

Catalyst Characterization. Textural properties of the catalysts were determined using nitrogen physisorption (Micrometrics, Model 3Flex-3500). The Dubinin–Radushkevich method was used to

determine the specific surface area while the pore size distributions were obtained with the Barrett–Joyner–Halenda (BJH) approach, using desorption data and density functional theory (DFT) method. Prior to the measurements the catalysts were outgassed ex-situ under vacuum and 180 °C for 20–24 h in a Micromeritics VacPrep 061 Sample Degas System. Thereafter, they were degassed in situ for 4 h at 180 °C.

Surface acidity was determined in accordance with the studies found in the literature focusing on carbon-supported catalysts.^{37–41} It was determined by measuring the pH of a slurry consisting of 50 mg of the catalyst and 50 mL of distilled water under agitation with a magnetic stirrer. The pH of the slurry was determined using a Mettler Toledo pH electrode.⁴²

X-ray diffraction (XRD) reflexes of catalysts were recorded with an X-ray diffractometer (Model D8, Bruker, Germany) using Cu K radiation and a LynxEye detector by scanning with a step of 0.05° and an accumulation time of 3 s at each point with a slit width of 0.26° or accumulation time of 1 s at each point with a slit width of 0.52°.

Scanning electron microscopy (SEM) was utilized to obtain information on the morphology of supports and catalysts. A Zeiss Leo Gemini 1530 microscope, combined with secondary electron and backscattered electron detectors, was applied. An acceleration voltage of 15 kV was used for the X-ray analyzer.

Transmission electron microscopy (TEM) was utilized to determine the metal particle size and study the morphology and porosity. The equipment used for analysis was a Model JEM-1400Plus system (JEOL, Japan) with a maximal acceleration voltage of 120 kV. The interpretation of TEM images and determination of particle sizes of the fresh and spent catalysts were done using the ImageJ program.

Prior to the TEM analysis, the samples were ground and suspended in ethanol. A drop of suspension was mounted on a copper grid coated with a carbon film and the solvent evaporated. The particle size distribution of metal particles was determined by measuring the diameter (*d*) of more than 300 particles visible in TEM micrographs.

Temperature-programmed reduction with H₂ (TPR) was performed in an AutoChem 2910 instrument. An amount of 0.1 g of catalyst was dried at 120 °C for 1 h, followed by reduction with 5 vol % hydrogen in argon, using the following temperature program: 25–700 °C at 10 °C/min. A thermal conductivity (TC) detector was used, and the cooling system, containing liquid nitrogen and a 2-propanol mixture, was applied to dry the gas-phase samples before entering the TC detector.

X-ray photoelectron spectroscopy (XPS) measurements were performed ex situ with an Axis Ultra DLD electron spectrometer manufactured by KRATOS Analytical, Ltd., using monochromated Al K α excitation source.

Table 2. Textural Properties, Metal Particle Sizes, and pH of Slurries of Catalysts and Supports

catalyst	Textural Characteristics					metal particle size (nm)	pH of slurry
	SSA ^a (m ² /g)	V _Σ (cm ³ /g)	V _{MP} (cm ³ /g)	D _p (nm)			
				BJH	DFT		
Norit	1247	0.58	0.51	4	0.6–0.7	—	7.5
Sibunit	330	0.52	0.09	4	0.9, >3.5	—	6.5
Pt/C1	450	0.29	0.17	4	0.6–0.7	3.1	5.7
Pt/C2	421	0.28	0.16	4	0.6–0.7	2.9	4.9
Pt/Norit	857	0.39	0.31	4	0.6–0.7	4.2	7.1
Pt/Sibunit	283	0.35	0.08	4	0.9, >3.5	3.5	6.6
PRC11	268	0.31	0.07	4	0.9, >3.5	1.3	6.0
PRC11 (used)	222	0.23	0.04	4	0.9, >3.5	1.5	—
PRC31	277	0.34	0.08	4	0.9, >3.5	1.2	6.1
PRC13	275	0.32	0.08	4	0.9, >3.5	1.3	6.0
PRC11 granulated	234	0.32	0.07	4	0.9, >3.5	1.4	6.0
PRC11 granulated (used)	176	0.25	0.05	4	0.9, >3.5	1.7	—

^aSpecific surface area.

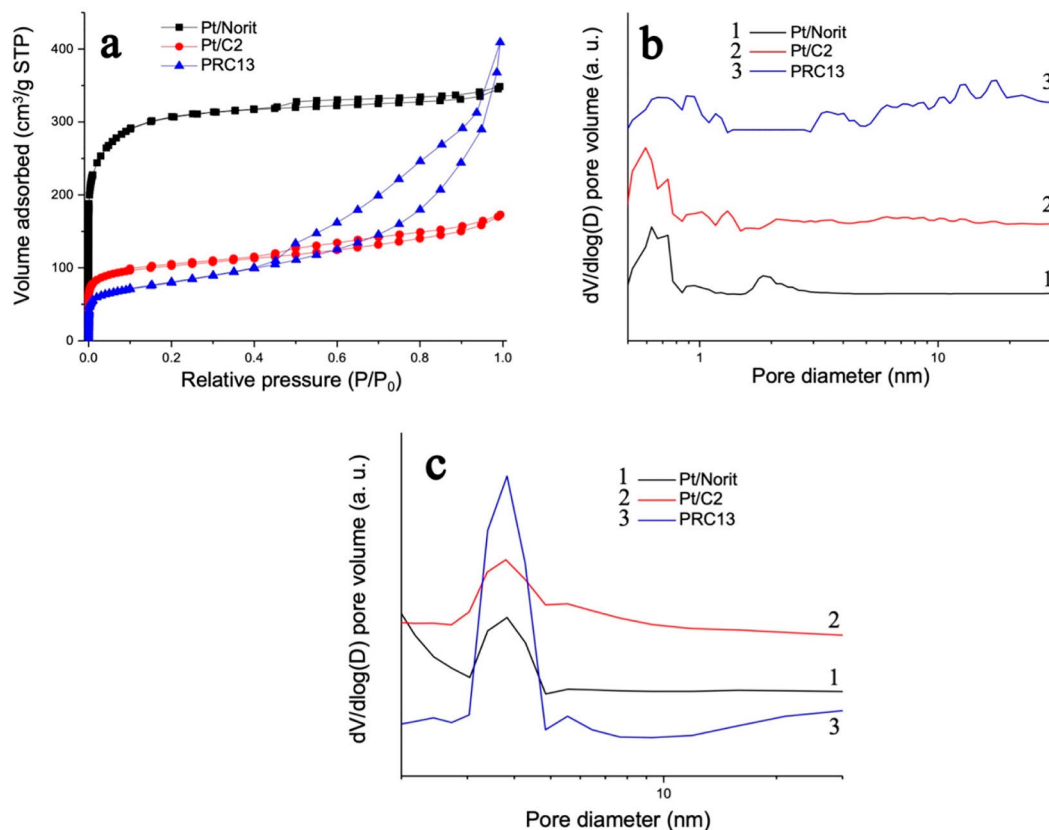


Figure 1. (a) Adsorption–desorption isotherm, (b) DFT pore size distribution, and (c) BJH pore size distribution of Pt/Norit, Pt/C2, and PRC13 catalysts.

RESULTS AND DISCUSSION

Catalyst Characterization. A summary of the textural properties, metal particle sizes, and pH of the catalysts and supports slurries is presented in Table 2. Results will be discussed in the following sections.

Nitrogen physisorption results (Table 2) show that deposition of Pt resulted in a slight decrease of the textural properties for all catalysts, which can be explained by blocking of the pores by the metal. The highest specific surface area (SSA), total pore volume (V_{Σ}) and the micropore volume (V_{MP}) were recorded for C_{NORIT} and the corresponding catalyst Pt/Norit. On the other hand, the catalysts supported on mesoporous Sibunit (Pt/Sibunit and PRC series) showed lower SSA, V_{Σ} , and V_{MP} .⁴³ The addition of Re had a very low effect on the textural properties of PRC catalysts. Commercial catalysts Pt/C1 and Pt/C2 showed properties similar to those of Norit, all being supported on activated carbon.

Catalysts supported on Sibunit had much lower V_{MP} values (<1 cm³/g), when compared to catalysts supported on activated carbon (>0.15 cm³/g), and the adsorption isotherms and the pore size distribution indicated its mesoporous characteristics.

Three different types of catalysts are compared in Figure 1, including adsorption–desorption isotherms (Figure 1a) and the pore size distributions obtained by DFT (Figure 1b) and BJH (Figure 1c).

Catalysts supported on activated carbon showed the isotherm of type I and hysteresis type H4, indicating the presence of micropores characteristic activated carbons, according to the IUPAC classification.⁴⁴

On the other hand, all catalysts supported on Sibunit showed a combination of isotherm types I and IV, indicating the presence of both micropores and mesopores, and H3 hysteresis. Pore size distribution obtained by DFT (Figure 1b) exhibited a main pore contribution between 0.6 and 0.7 nm for catalysts supported on Norit and both Pt/C1 and Pt/C2. Pore size distribution obtained by BJH (Figure 1c) exhibits a narrow main pore contribution for all samples at ca. 4 nm.

For PRC catalysts, the main peak present in the microporous range was between 0.9 nm and 1.1 nm; however, more porosity was present at >3.5 nm, indicating mesoporosity.²⁷

The spent PRC11 catalysts used in batch and continuous reactors were characterized by nitrogen physisorption. The results (Table 2, Figure 2) show that surface area decreased after the reaction for both cases. This could be due to

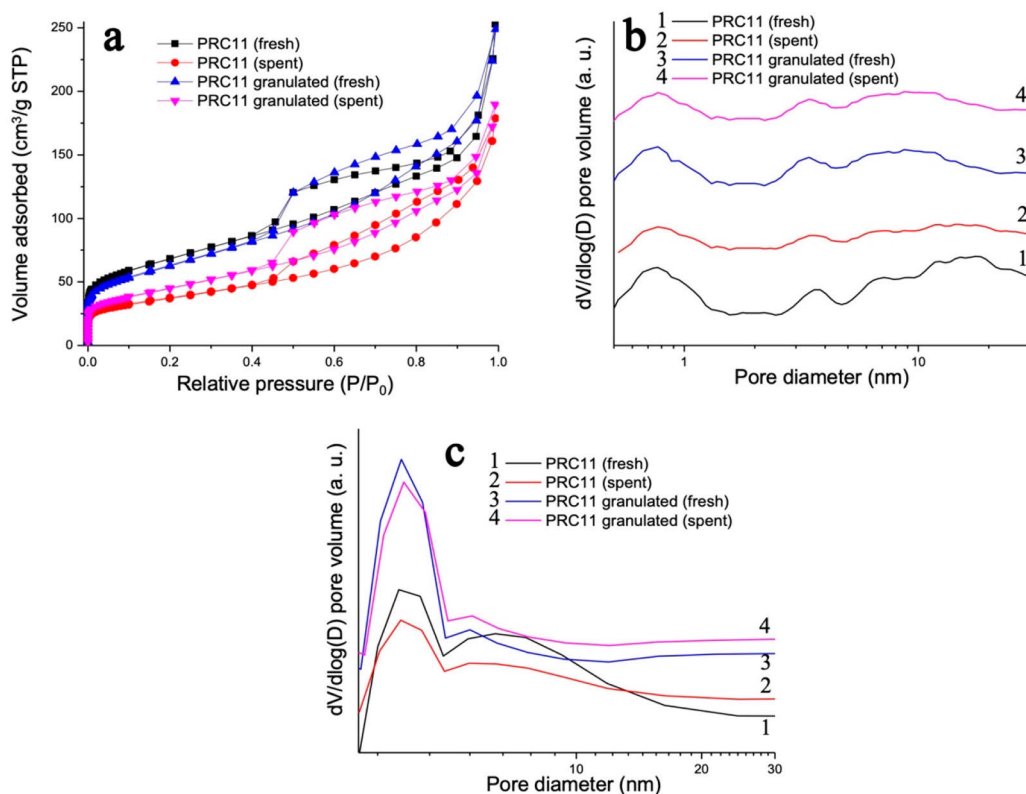


Figure 2. (a) Nitrogen adsorption–desorption isotherms, (b) DFT pore size distribution, and (c) BJH pore size distributions for the fresh, spent, and granulated PRC11.

formation of carbonaceous species that remained on the surface of the catalysts. Pore size distribution (Figures 2b and 2c) showed no changes in pore diameter, indicating low mechanical degradation.

The relative acidity of different catalysts shown in Table 2 indicates that both commercial catalysts exhibited high acidity when compared to the rest, with Pt/C2 being the most acidic catalyst of all (pH 4.9). The pH of the slurry was also measured for the pure supports Norit and Sibunit, where Sibunit displayed the lower pH value (pH 6.5). A slight decrease in pH was observed after deposition of Pt. All bimetallic PRC catalysts showed very similar pH values (pH ~6), indicating that the addition of Re did not affect acidity considerably.

Pt peaks at $\sim 39.5^\circ$, 46° , 67° , and 81° (Figure 3) are attributed to the (111), (200), (220), and (311) reflections.⁴⁵ The presence of these peaks can be attributed to larger metal particles not considered or observed in TEM. Peaks at 26° and 42° belong to the carbon support, indicating presence of the microcrystalline structures.^{46,47} The lack of peaks belonging to Re could be caused by high dispersion of Re particles or an overlap with carbon reflections.⁴⁸

The lack of Pt peaks in PRC11 shows that the addition of Re improved Pt dispersion. As Figure 3 shows, the best Pt–Re

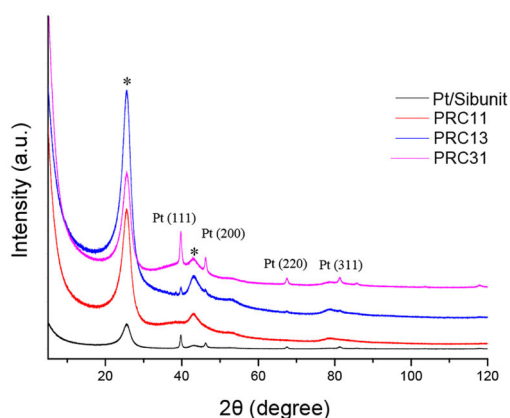


Figure 3. XRD diffractogram comparison of monometallic Pt/Sibunit and bimetallic PRC catalysts. Asterisk symbol (*) denotes signals for the Sibunit support.

ratio is 1:1, since Pt peaks are present for both PRC13 and PRC31.

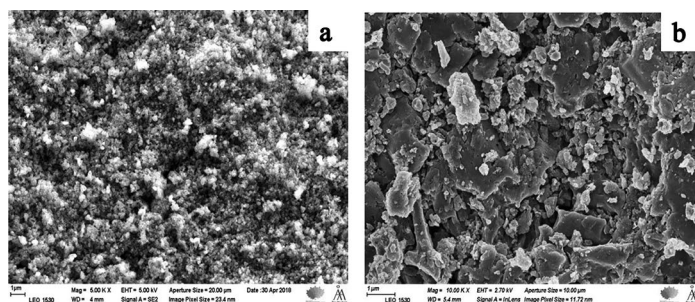


Figure 4. SEM micrographs of (a) Sibunit and (b) Norit.

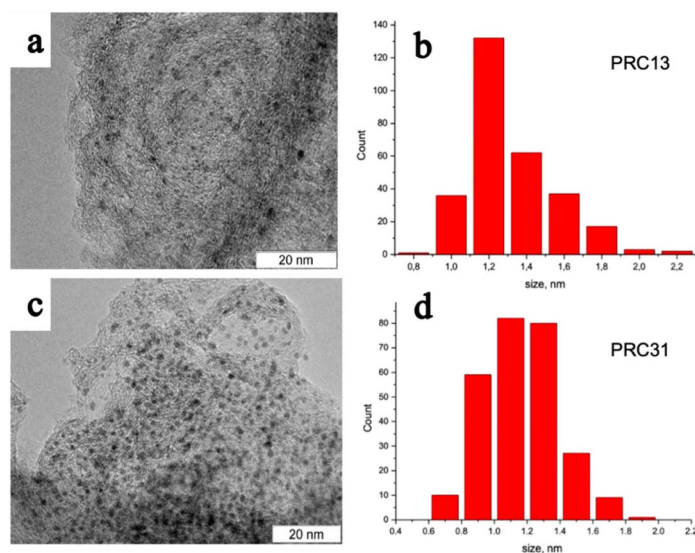


Figure 5. TEM micrographs and the metal particle size distribution of (a, b) PRC13 and (c, d) PRC31.

SEM analysis allows one to observe the morphological differences between Sibunit and Norit (Figure 4). It is possible to see that the structure of Sibunit consists of more-uniform granules ($0.3\text{--}0.5\text{ }\mu\text{m}$), while Norit is composed of more-heterogeneous and varied particles with sizes exceeding $0.5\text{ }\mu\text{m}$.

TEM images of the reduced catalysts allow one to determine the metal particle size and the morphology of the catalysts with the results given in Table 2.

As can be seen from this table, all catalysts exhibited the metal particle sizes of $<5\text{ nm}$. The smallest metal particles and the highest metal dispersion were found in the PRC series ($<1.4\text{ nm}$), despite higher total metal loadings. In addition, PRC series showed a smaller metal particle size than monometallic Pt/Sibunit, indicating that the addition of Re helped to stabilize the metal particles on the surface of the support.⁴⁹

Commercial catalysts presented similar particle sizes, $\sim 3\text{ nm}$ in size, while synthesized monometallic catalysts, Pt/Norit, and Pt/Sibunit exhibited the largest metal particle sizes.

For bimetallic PRC series, it was not possible to differentiate between Pt and Re nanoparticles; therefore, the combined metal particle size distributions and TEM micrographs for two PRC catalysts are presented in Figure 5.

A comparison of the TEM images (Figure 6) between the fresh and the spent PRC11 catalysts shows almost no changes in the particle sizes after the reaction, indicating good stability of metal particles.

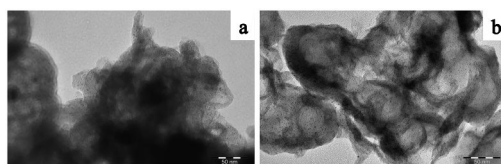


Figure 6. TEM micrographs of (a) fresh PRC11 and (b) spent PRC11.

Reduction profiles for the PRC series of catalysts (Figure 7, Table 3) display two main peaks, namely, the first one at low temperatures (85–150 °C) and the second at higher temperatures (440–550 °C).

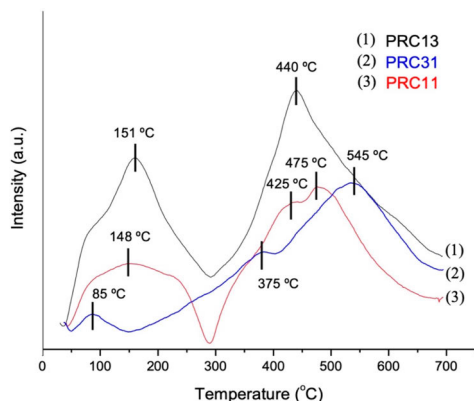


Figure 7. TPR profiles of bimetallic PRC11, PRC13, and PRC31 catalysts.

Table 3. Results from Hydrogen TPR

catalyst	$T_{\text{max}1}$ (°C)	$T_{\text{max}2}$ (°C)	total area (a.u.)
PRC11	148	475	96.6
PRC31	85	545	94.7
PRC13	151	440	165.6

Reduction peaks of monometallic platinum supported on carbon have been reported in the range of 150–300 °C,⁵⁰ whereas, for Re reduction, temperatures are higher, between

250 °C and 450 °C.⁵¹ The peaks observed at 85–150 °C correspond to complete reduction of Pt, while those at 375 °C for PRC31 and at 425 °C for PRC11 are consistent with the results reported for the reduction of Re species supported on carbon.⁵¹ However, broad peaks at higher temperatures (500–800 °C) attributed to methane formation, coming from the reaction of the carbon support with hydrogen, overlap with those of Re, making analysis challenging.

Shifts in the reduction temperatures have also been reported due to formation of Pt–Re alloy.^{39–42} Migration of ReOx species toward reduced Pt has also been found, because of weak interactions between the metal and the carbon support.⁵²

The first reduction peak can be attributed to the coreduction of Pt and Re, indicating that Re is in close interaction with Pt. This promotion of the Re reduction can be caused by hydrogen spillover from the reduced Pt, which has been reported in the literature.^{50,53–55}

The catalysts with the higher amount of Pt show both the lowest and the highest reduction peaks, indicating weak interactions between the metals. On the other hand, higher reduction temperatures for PRC11 and PRC13 could be due to strong Re–Pt interactions.⁴⁰ The intensity of the peaks increases as the Re content increases.

As observed from XRD and XPS results, reduction temperatures used for PRC catalysts result in complete reduction of Pt, while Re remains as an oxide. In the case of PRC31 with low Re loading, a certain amount of Re was reduced.

XPS analysis was performed for reduced PRC series catalysts to investigate the electronic state of platinum and rhenium on the surface.

Results (Figure 8, Table 4) showed mixed oxidation states for metals in all catalysts. A Pt 4f_{7/2} binding energy (BE) of 71.8 eV was assigned to Pt⁰. These results are consistent with the BE values of 71.6 and 74.9 eV reported for a Pt 4f doublet

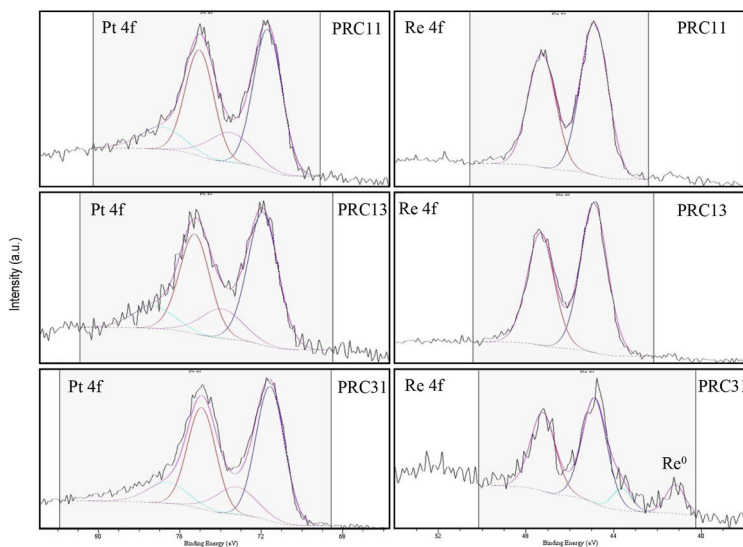


Figure 8. Pt 4f and Re 4f XPS spectra for PRC11, PRC13, and PRC31.

Table 4. XPS Results for PRC Series Catalysts

line	PRC13			PRC11			PRC31			
	BE (eV)	fwhm (eV)	AC (at. %)	BE (eV)	fwhm (eV)	AC (at. %)	BE (eV)	fwhm (eV)	AC (at. %)	
C 1s	284.23	0.85	96.62	284.22	0.9	96.96	285.24	0.85	97.51 ^a	C–C, sp ₂
O 1s	530.2	1.45	1.39	530.3	1.45	1.38	530.7	1.9	0.96	Re=O
	531.4	1.5	0.39	531.6	1.5	0.56				Re–OH
	532.7	2.55	1.12	533.1	1.9	0.53	533.0	2.2	0.95	C–OH
Pt 4f 7/2	72.0	1.7	0.14	71.8	1.55	0.22	536.3	2.9	0.18	π – π^* excitation
Re 4f 7/2							71.7	1.55	0.33	Pt (0)
							41.2	1	0.01	Re metal
	44.9	1.4	0.35	44.9	1.4	0.32	44.9	1.3	0.05	ReO ₂
Re/Pt	2.5	1.45	0.46							

^aTotal carbon atomic concentration, including C–OH, vibrational structure, and π – π^* excitation.

Scheme 1. General Reaction Scheme of Hydrodeoxygenation of Isoeugenol Using Pt and Pt–Re as Catalysts Supported on Carbon

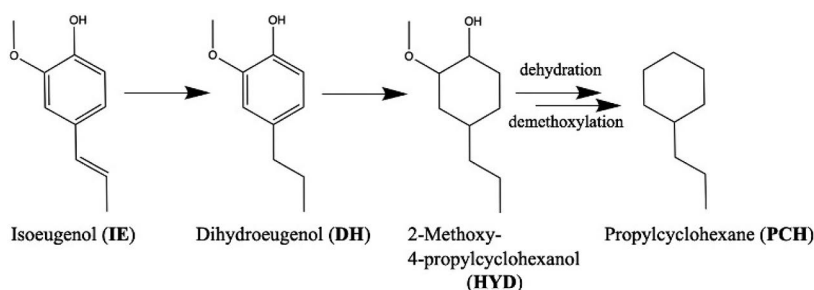


Table 5. Catalytic Activity of Pt and Pt–Re Catalysts Supported on Carbon in the Hydrodeoxygenation of Isoeugenol, Performed in a Batch Reactor

entry	catalyst	temperature, T (°C)	IE conversion after 4 h (%) ^a	liquid-phase mass balance (%)	PCH Y (%)	initial rate (mol/L h g _{in})
1	Pt/C1	200	100 (36)	82	<1	2.9
2	Pt/C1	300	100 (100)	32	31	4.7
3	Pt/C2	250	100 (71)	92	12	4.1
4	Pt/Norit	250	100 (23)	99	<1	
5	Pt/Sibunit	250	100 (<1)	99	<1	
6	PRC11	250	100 (98)	67	84	7.4
7	PRC31	250	100 (100)	62	66	15.4
8	PRC13	250	100 (100)	62	81	6.3

^aConversion of dihydroeugenol (DH) is shown in parentheses (DH X).

in metallic Pt.⁵⁶ The slight increase in BE after the addition of Re may indicate intermetallic interactions.

An Re 4f binding energy of 44.9 eV was assigned to Re⁴⁺. This species was predominant for all catalysts. The catalyst with the lowest Re content, PRC 31, exhibited an additional signal at 41.2 eV, which was assigned for Re⁰.⁵⁷ However, note that, since the measurements were done ex situ, the rhenium oxidation state can be influenced by exposure of highly oxophilic rhenium to ambient conditions.

The highest Re/Pt ratio was observed for PRC13 followed by PRC11 and thereafter PRC31.

Catalytic Activity. Monometallic Pt and bimetallic Pt–Re catalysts supported on carbon were tested in hydrodeoxygenation (HDO) of isoeugenol (IE). A general reaction scheme based on the reactants and products determined by GC and GC–MS is presented in Scheme 1.

Hydrogenation of the double bond located in the propene group of IE occurred almost immediately (after 1 min reaction

time);⁵⁸ therefore, transformations of dihydroeugenol (DH) were followed.

Catalytic results and reaction conditions used for batch experiments with monometallic and bimetallic catalysts are summarized in Table 5. Two main products were found by GC and GC–MS: 2-methoxy-4-propylcyclohexanol, resulting from hydrogenation of the aromatic ring, and propylcyclohexane, the desired product of the aromatic ring hydrogenation and complete deoxygenation.

All catalysts were highly active for hydrogenation of the side-chain double bond of isoeugenol to form dihydroeugenol (DH), resulting in a complete isoeugenol conversion for all tested catalysts, however, propylcyclohexane yield (PCH Y) was low for monometallic Pt catalysts. On the other hand, bimetallic catalysts exhibited higher PCH Y values (80%–85%). Results will be discussed in more detail in the following sections.

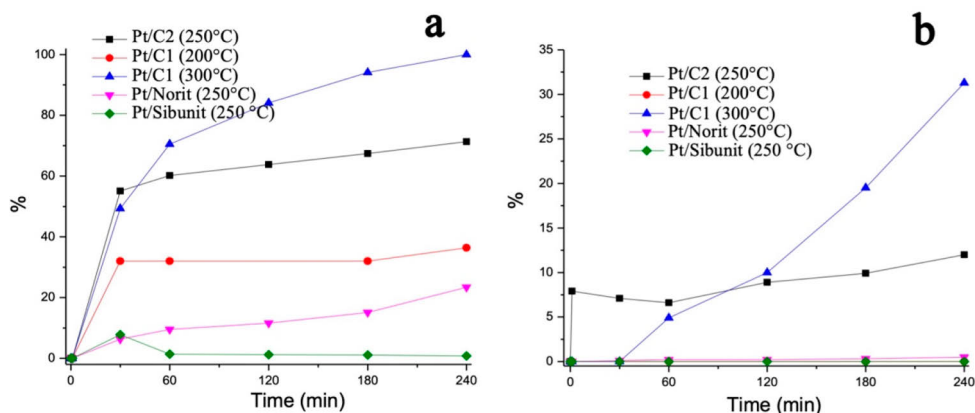


Figure 9. (a) Conversion of dihydroeugenol, as a function of time, and (b) yield of propylcyclohexane, as a function of time for monometallic Pt catalysts.

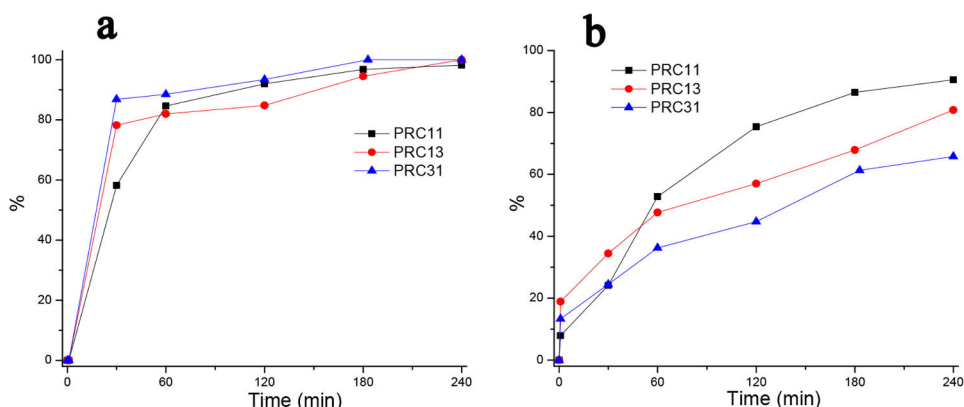


Figure 10. (a) Conversion of dihydroeugenol and (b) yield of propylcyclohexane, as a function of time for bimetallic Pt–Re catalysts.

All monometallic Pt catalysts displayed high hydrogenating activity of IE, being, however, poorly active in deoxygenation activity, as follows from Figure 9.

The lowest activity was obtained for the commercial catalyst Pt/C1 at 200 °C (Table S, entry 1, at 4 h reaction time; DH X = 36%, PCH Y < 1%). The same catalyst was tested at 300 °C (Table S, entry 2), resulting in the highest PCH Y (32%); however, the mass balance in the liquid phase at 4 h for reaction time was the lowest (32%), indicating that most products were distributed either in the gas phase, due to cracking, or as higher-molecular-weight polymers; neither of which was quantified.

The rest of the catalysts were tested at an intermediate temperature, 250 °C, to get better insight regarding their performance.

At 250 °C, the commercial catalyst Pt/C2 (Table S, entry 3) exhibited a higher activity than Pt/Norit and Pt/Sibunit (Table S, entries 4 and 5, respectively). This can be a result of catalyst acidity (Table 2), given that Pt/C2 has the highest acidity of all catalysts (pH of slurry 4.9). Both Pt/Norit and Pt/Sibunit displayed low deoxygenation activity, resulting in PCH Y < 1%.

As a comparison, monometallic Pt/C with pH 5.6 was not efficient in the HDO of guaiacol, giving mainly oxygenated products at 300 °C under 30 bar H₂.⁵⁹

Bimetallic catalysts Pt–Re supported on Sibunit showed almost complete DH X (>98%) and a high PCH Y (>66%) (entries 6–8, Figure 10). Comparison of these results with monometallic Pt/Sibunit indicates that addition of Re had a noticeable effect on HDO activity, even if the slurry pH was not too acidic (Table 2).

Varying Pt:Re ratio also showed an effect on activity. While all PRC catalysts displayed almost complete conversion at 4 h of the reaction time, the lowest PCH Y (66%) was observed for PRC31.

Catalysts with a higher amount of Re, PRC11 and PRC13, had similar activity (PCH Y > 84%), with PRC11 displaying the highest PCH Y (84%) at 4 h. These results can be explained by the presence of ReOx (XPS results; see Figure 8) providing oxygen vacancies required for the deoxygenation to occur.⁶⁰

The two best catalysts for HDO were PRC13 and PRC11; these results are consistent with a higher atomic concentration

(AC) of Re on the surface of the catalysts and a predominant ReOx state, since it is necessary for oxygen activation. Moreover, their similar performance indicates that the amount of Pt has a lower effect on activity than the impact of Re, which is especially necessary for an inert support such as carbon.

For comparison, in a previous work¹³ bimetallic PtRe/Al₂O₃ catalysts tested for HDO of isoeugenol under the same reaction conditions showed a lower PCH Y (54%) at 240 min. These results suggest that the choice of support plays a very important role. The use of Sibunit was not only beneficial for the metal dispersion and the particle size (6.5 nm for PtRe/Al₂O₃), but also had a positive effect on the activity of PtRe catalysts.

To explore the stability of the catalyst, repeatability and reusability tests were performed with PRC11 in a batch reactor at 250 °C and 30 bar of H₂. The obtained results are presented in Table 6 and Figure 11.

Table 6. Repeatability and Reusability Results for PRC11 in a Batch Reactor

catalyst	temperature, T (°C)	IE X after 4 h (%) ^a	liquid-phase mass balance (%)	PCH Y (%)
PRC11	250	100 (98)	70	91
PRC11 repeat	250	100 (100)	68	89
PRC11 reuse	250	100 (100)	67	84

^aconversion of DH in parentheses (DH X).

From these tests, it can be seen that PRC11 displays consistent results when the reaction is repeated under the same conditions. Reusability tests were performed with the spent PRC11, which was washed with acetone and dried in air. The results show similar performance as with the fresh catalyst, indicating low catalyst deactivation.

A comparison of the results obtained in this work and those reported in the previous research is presented in Table 7. It can be observed that PCH yields and the mass balance in the liquid phase are higher for PRC11 and PRC13 catalysts under the same reaction conditions (250 °C, 30 bar H₂, and 4 h of reaction time).

Table 7. Comparison of Isoeugenol HDO under 250 °C, 30 bar H₂ and 4 h of Reaction Time with the Literature

catalyst	IE conversion after 4 h (%) ^a	liquid-phase mass balance (%)	PCH Y (%)	ref
PRC11	100 (98)	67	84	—
PRC31	100 (100)	62	66	—
PRC13	100 (100)	62	81	—
3, 1 wt % IrRe/Al ₂ O ₃	100 (24)	53	69	13
10 wt % Ni/ZrO ₂	100 (95)	15	16	31
3 wt % Ir/ZrO ₂	100 (0)	37	33	31
10 wt % Ni/SBA-15	100 (100)	51	53	61

^aconversion of DH in parentheses (DH X).

Granulated PRC11 was tested in a trickle-bed reactor to investigate scalability, stability, and the product distribution under a continuous flow (0.5 mL/min) of isoeugenol in dodecane at 30 bar H₂ and at 200, 170, 150, and 75 °C. The results are presented in Figure 12.

As it can be seen from Figure 12, IE X remained at 100% for all temperatures tested. DH X remained at 100% at temperatures of 200–150 °C; however, at 75 °C, it decreased to ca. 70%. The highest PCH Y was obtained at 200 °C (ca. 90%), concomitant with lowest mass balance in the liquid phase (ca. 75%).

PCH Y decreased as the temperature increased, from ca. 10% at 150 °C to ca. 50% at 170 °C. At 75 °C, PCH Y was <1%, indicating absence of deoxygenation at this temperature. This result is in accordance with the thermodynamics of IE HDO.⁶²

The opposite results were recorded for HYD. At 200 °C, very low amounts of 2-methoxy-4-propylcyclohexanol were obtained (HYD Y ≈ 5%), whereas at 75 °C, it was the main product (ca. 60%). These results indicate that hydrogenation of the aromatic ring occurs efficiently at low temperatures, which is consistent with thermodynamics.⁶³ Consistent with the literature results, the activation energy (*E*_a) for hydrogenation of the aromatic ring is lower than the *E*_a value for deoxygenation.⁴⁷

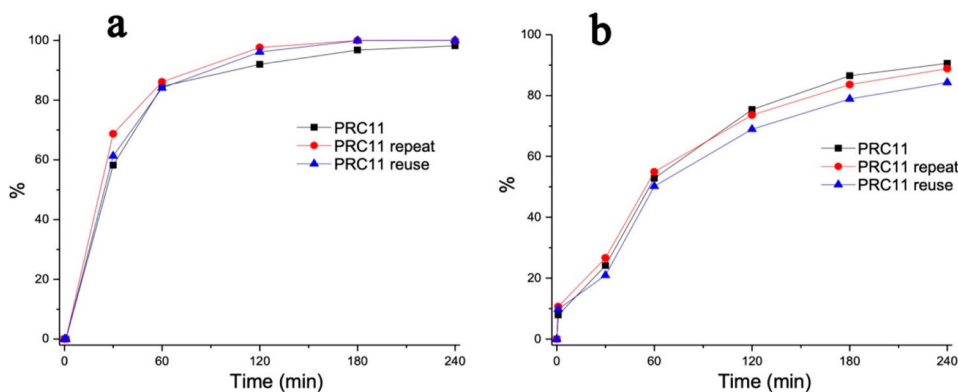


Figure 11. (a) Conversion of dihydroeugenol and (b) the yield of propylcyclohexane, as a function of time for PRC11 catalyst, repeatability, and reusability of the spent catalyst.

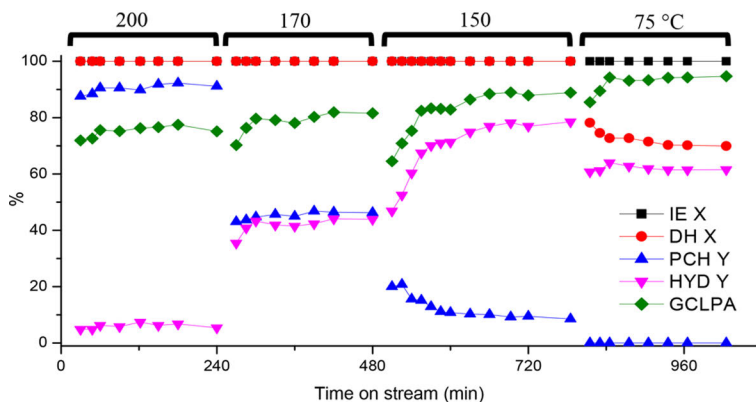


Figure 12. Continuous reactor results for HDO of isoeugenol performed at different temperatures, 30 bar H_2 , and the liquid flow rate of 0.5 mL/min. Isoeugenol conversion (IE X), dihydroeugenol conversion (DH X), propylcyclohexane yield (PCH Y), 2-methoxy-4-propylcyclohexanol yield (HYD Y) and the liquid-phase mass balance (GCLPA).

Deactivation was not observed even after 17 h of time on stream, as conversion and yield remained constant.

A comparison between the batch and continuous results for PRC11 show that high conversion was achieved for both isoeugenol and dihydroeugenol, the mass balance in the liquid phase remained >60% and propylcyclohexane yield remained between 85% and 90%.

Apparent activation energy was calculated for isoeugenol HDO using the results at 60 min for experiments at different temperatures performed in the continuous reactor. From the Arrhenius plot presented in Figure 13, the apparent activation

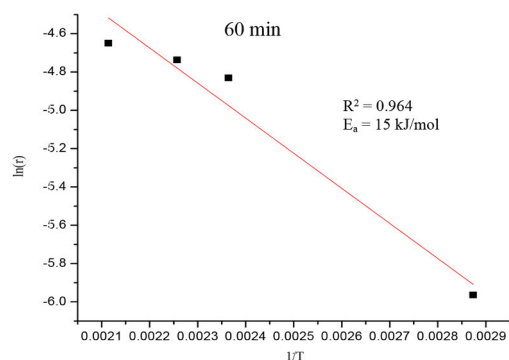


Figure 13. Arrhenius plot for the hydrodeoxygenation (HDO) of isoeugenol on granulated PtRe(1:1)/Sibunit. The slope gives the apparent activation energy of the reaction: $E_a = 15$ kJ/mol.

energy for HDO of IE using granulated PRC11 was determined to be 15 kJ/mol. This, along with visible changes in the slope upon temperature elevation, indicates that the presence of mass-transfer limitations in a continuous reactor with the catalyst particles exhibits a larger size than the counterparts applied in the batch reactor.

CONCLUSIONS

Hydrodeoxygenation (HDO) of isoeugenol was investigated at 200–300 °C under 30 bar of hydrogen pressure for the first time using monometallic commercial and synthesized catalysts, as well as bimetallic Pt–Re catalysts supported on mesoporous carbon.

For monometallic catalysts, commercial 5% Pt on active carbon catalyst showed the highest propylcyclohexane yield (31%) but the lowest mass balance in the liquid phase (32%) at 300 °C. At 250 °C, a similar catalyst exhibited higher propylcyclohexane yield and dihydroeugenol conversion, compared to less-acidic Pt/Norit and Pt/Sibunit.

Compared to monometallic Pt catalysts, bimetallic ones displayed higher activity for deoxygenation, giving complete conversion of isoeugenol and dihydroeugenol and resulting in high PCH Y at 250 °C and 30 bar H_2 . PRC11 catalyst was the most active (isoeugenol conversion = 100%, dihydroeugenol conversion = 98%, propylcyclohexane yield = 84%) under the tested reaction conditions.

The best bimetallic catalysts were PRC11 and PRC13, which according to XPS contained ReOx species.

Granulated PRC11 was tested in a continuous trickle-bed reactor at 75–200 °C, 30 bar H_2 , and 0.5 mL/min of liquid flow. This is the first study where the HDO of isoeugenol has been reported in the open literature in a continuous reactor. At low temperatures, the main product obtained was 2-methoxy-4-propylcyclohexanol, which indicated that deoxygenation was not occurring, however, complete conversion (100%) and a high yield of propylcyclohexane (ca. 90%) was obtained at 200 °C.

AUTHOR INFORMATION

Corresponding Author

Dmitry Yu. Murzin — *Johan Gadolin Process Chemistry Centre, Åbo Akademi University, Turku/Åbo FI-20500, Finland*; orcid.org/0000-0003-0788-2643;
Email: dmurzin@abo.fi

Authors

Mark E. Martinez-Klimov – Johan Gadolin Process Chemistry Centre, Åbo Akademi University, Turku/Åbo FI-20500, Finland

Päivi Mäki-Arvela – Johan Gadolin Process Chemistry Centre, Åbo Akademi University, Turku/Åbo FI-20500, Finland; orcid.org/0000-0002-7055-9358

Zuzana Vajglova – Johan Gadolin Process Chemistry Centre, Åbo Akademi University, Turku/Åbo FI-20500, Finland

Moldir Alda-Onggar – Johan Gadolin Process Chemistry Centre, Åbo Akademi University, Turku/Åbo FI-20500, Finland

Ilari Angervo – Wihuri Physical Laboratory, Department of Physics and Astronomy, University of Turku, FI-20014 Turku, Finland

Narendra Kumar – Johan Gadolin Process Chemistry Centre, Åbo Akademi University, Turku/Åbo FI-20500, Finland

Kari Eränen – Johan Gadolin Process Chemistry Centre, Åbo Akademi University, Turku/Åbo FI-20500, Finland

Markus Peurla – Institute of Biomedicine, University of Turku, FI-20520 Turku, Finland

Mehmet Harbi Calimli – Johan Gadolin Process Chemistry Centre, Åbo Akademi University, Turku/Åbo FI-20500, Finland; Department of Medical Services and Techniques, Tuzluca Vocational School, University of Iğdır, Iğdır 76000, Turkey

Joseph Muller – Johan Gadolin Process Chemistry Centre, Åbo Akademi University, Turku/Åbo FI-20500, Finland

Andrey Shchukarev – Department of Chemistry, Umeå University, 901 87 Umeå, Sweden

Irina L. Simakova – Boreskov Institute of Catalysis, Novosibirsk 630090, Russia; orcid.org/0000-0002-5138-4847

Complete contact information is available at:

<https://pubs.acs.org/10.1021/acs.energyfuels.1c02656>

Notes

The authors declare no competing financial interest.

ACKNOWLEDGMENTS

Electron microscopy samples were processed and analyzed in the Electron Microscopy Laboratory, Institute of Biomedicine, University of Turku, which receives financial support from Biocenter Finland. I.S. is grateful for the support from the Ministry of Science and Higher Education of the Russian Federation, under the governmental order for Boreskov Institute of Catalysis (Project No. AAAA21-121011390055-8). M.E.M.K. acknowledges the financial support received from the Magnus Ehrnrooth Foundation.

REFERENCES

- (1) Ritchie, H.; Roser, M. *Energy*; 2020. Published online at OurWorldInData.org. Available via the Internet at: <https://ourworldindata.org/energy> (accessed June 2, 2019).
- (2) Markard, J. The Next Phase of the Energy Transition and its Implications for Research and Policy. *Nat. Energy*. **2018**, *3* (8), 628–633.
- (3) Kammermann, J.; Bolvashenkov, I.; Tran, K.; Herzog, H. -G.; Frenkel, I. Feasibility Study for a Full-Electric Aircraft Considering Weight, Volume, and Reliability Requirements. In *2020 International Conference on Electrotechnical Complexes and Systems (ICOECS)*, 2020; pp 1–6, DOI: 10.1109/ICOECS50468.2020.9278461.

- (4) Zhou, C.-H.; Xia, X.; Lin, C.-X.; Tong, D.-S.; Beltrami, J. Catalytic Conversion of Lignocellulosic Biomass to Fine Chemicals and Fuels. *Chem. Soc. Rev.* **2011**, *40* (11), 5588–5617.

- (5) Meng, J.; Moore, A.; Tilotta, D.; Kelley, S.; Park, S. Toward Understanding of Bio-Oil Aging: Accelerated Aging of Bio-oil Fractions. *ACS Sustainable Chem. Eng.* **2014**, *2* (8), 2011–2018.

- (6) Xiu, S.; Shabbazi, A. Bio-oil Production and Upgrading Research: A Review. *Renewable Sustainable Energy Rev.* **2012**, *16* (7), 4406–4414.

- (7) Hu, X.; Gholizadeh, M. Progress of the Applications of Bio-Oil. *Renewable Sustainable Energy Rev.* **2020**, *134*, 110124.

- (8) Mortensen, P. M.; Grunwaldt, J.-D.; Jensen, P. A.; Knudsen, K. G.; Jensen, A. D. A Review of Catalytic Upgrading of Bio-oil to Engine Fuels. *Appl. Catal., A* **2011**, *407* (1–2), 1–19.

- (9) Mäki-Arvela, P.; Murzin, D. Y. Hydrodeoxygenation of Lignin-Derived Phenols: from Fundamental Studies Towards Industrial Applications. *Catalysts* **2017**, *7* (9), 265.

- (10) He, Z.; Wang, X. Hydrodeoxygenation of Model Compounds and Catalytic Systems for Pyrolysis Bio-oils Upgrading. *Catal. Sustainable Energy* **2012**, *1*, 28–52.

- (11) Laskar, D. D.; Tucker, M. P.; Chen, X.; Helms, G. L.; Yang, B. Noble-metal Catalyzed Cydrodeoxygenation of Biomass-Derived Lignin to Aromatic Hydrocarbons. *Green Chem.* **2014**, *16* (2), 897.

- (12) Jin, W.; Pastor-Perez, L.; Shen, D.; Sepulveda-Escribano, A.; Gu, S.; Ramirez Reina, T. Catalytic Upgrading of Biomass Model Compounds: Novel Approaches and Lessons Learnt from Traditional Hydrodeoxygenation - a Review. *ChemCatChem* **2019**, *11* (3), 924–960.

- (13) Luo, W.; Cao, W.; Bruijninx, P. C. A.; Lin, L.; Wang, A.; Zhang, T. Zeolite-Supported Metal Catalysts for Selective Hydrodeoxygenation of Biomass-Derived Platform Molecules. *Green Chem.* **2019**, *21* (14), 3744–3768.

- (14) Alda-Onggar, M.; Mäki-Arvela, P.; Eränen, K.; Aho, A.; Hemming, J.; Paturi, P.; Peurla, M.; Lindblad, M.; Simakova, I. L.; Murzin, D. Y. Hydrodeoxygenation of Isoeugenol Over Alumina Supported Ir-, Pt- and Re Catalysts. *ACS Sustainable Chem. Eng.* **2018**, *6* (12), 16205–16218.

- (15) Teles, C. A.; Rabelo-Neto, R. C.; de Lima, J. R.; Mattos, L. V.; Resasco, D. E.; Noronha, F. B. The Effect of Metal Type on Hydrodeoxygenation of Phenol Over Silica Supported Catalysts. *Catal. Lett.* **2016**, *146* (10), 1848–1857.

- (16) Horáček, J.; Kubička, D. Bio-Oil Hydrotreating Over Conventional CoMo and NiMo Catalysts: The role of Reaction Conditions and Additives. *Fuel* **2017**, *198*, 49–57.

- (17) Jung, K. B.; Lee, J.; Ha, J.-M.; Lee, H.; Suh, D. J.; Jun, C.-H.; Jae, J. Effective Hydrodeoxygenation of Lignin-Derived Phenols Using Bimetallic RuRe catalysts: Effect of Carbon Supports. *Catal. Today* **2018**, *303*, 191–199.

- (18) Liu, S.; Simonetti, T.; Zheng, W.; Saha, B. Selective Hydrodeoxygenation of Vegetable Oils and Waste Cooking Oils to Green Diesel Using a Silica-Supported Ir-ReO_x Bimetallic Catalyst. *ChemSusChem* **2018**, *11* (9), 1446–1454.

- (19) Liu, S.; Dutta, S.; Zheng, W.; Gould, N. S.; Cheng, Z.; Xu, B.; Saha, B.; Vlachos, D. G. Catalytic Hydrodeoxygenation of High Carbon Furfurylmethanes to Renewable Jet-fuel Ranged Alkanes over a Rhenium-Modified Iridium Catalyst. *ChemSusChem* **2017**, *10* (16), 3225–3234.

- (20) Ota, N.; Tamura, M.; Nakagawa, Y.; Okumura, K.; Tomishige, K. Hydrodeoxygenation of Vicinal OH Groups over Heterogeneous Rhenium Catalyst Promoted by Palladium and Ceria Support. *Angew. Chem.* **2015**, *127* (6), 1917–1920.

- (21) Zhang, J.; Zhao, C.; Li, C.; Li, S.; Tsang, C.-W.; Liang, C. The Role of Oxophilic Mo Species in Pt/MgO Catalyst as Extremely Active Sites for Enhanced Hydrodeoxygenation of Dibenzofuran. *Catal. Sci. Technol.* **2020**, *10*, 2948–2960.

- (22) Goulas, K. A.; Mironenko, A. V.; Jenness, G. R.; Mazal, T.; Vlachos, D. G. Fundamentals of C–O Bond Activation on Metal Oxide Catalysts. *Nat. Catal.* **2019**, *2*, 269–276.

- (23) Fang, H.; Zheng, J.; Luo, X.; Du, J.; Roldan, A.; Leoni, S.; Yuan, Y. Product Tunable Behavior of Carbon Nanotubes-Supported Ni–Fe catalysts for Guaiacol Hydrodeoxygenation. *Appl. Catal., A* **2017**, 529, 20–31.
- (24) Tran, N. T. T.; Uemura, Y.; Ramli, A. Hydrodeoxygenation of Guaiacol over Al-MCM-41 Supported Metal Catalysts: A Comparative Study of Co and Ni. *Procedia Eng.* **2016**, 148, 1252–1258.
- (25) Vargas-Villagrán, H.; Flores-Villeda, M. A.; Puente-Lee, I.; Solís-Casados, D. A.; Gómez-Cortés, A.; Díaz-Guerrero, G.; Klimova, T. E. Supported Nickel Catalysts for Anisole Hydrodeoxygenation: Increase in the Selectivity to Cyclohexane. *Catal. Today* **2020**, 349, 26–41.
- (26) Jung, K. B.; Lee, J.; Ha, J.-M.; Lee, H.; Suh, D. J.; Jun, C.-H.; Jae, J. Effective Hydrodeoxygenation of Lignin-Derived Phenols Using Bimetallic RuRe Catalysts: Effect of Carbon Supports. *Catal. Today* **2018**, 303, 191–199.
- (27) Plaksin, G. V.; Baklanova, O. N.; Lavrenov, A. V.; Likholobov, V. A. Carbon Materials from the Sibunit Family and Methods for Controlling Their Properties. *Solid Fuel Chem.* **2014**, 48 (6), 349–355.
- (28) Lokteva, E. S.; Lunin, V. L.; Golubina, E. V.; Simagina, V. I.; Egorova, M.; Stoyanova, I. V. C-C Bond Formation During Hydrodechlorination of CCl₄ on Pd-Containing Catalysts. *Stud. Surf. Sci. Catal.* **2000**, 130, 1997–2002.
- (29) Baklanova, O. N.; Likholobov, V. A.; Tsekanovich, M. S.; Davydova, V. Y.; Chirkova, O. A.; Drozdov, V. A.; Surovikin, Y. V. Effect of the Particle Size of Globular Nanodisperse Carbon on the Texture and Strength of Molded Sibunit-Type Materials. *Catal. Ind.* **2009**, 1 (2), 153–156.
- (30) Fenelonov, V. B.; Likholobov, V. A.; Derevyankin, A. Y.; Mel'gunov, M. S. Porous Carbon Materials Prepared from C1-C3 Hydrocarbons. *Catal. Today* **1998**, 42, 341.
- (31) Gaillard, F.; Hachimi, A. E.; Descorme, C.; Besson, M.; Joly, J.-P.; Polyanskaya, E. M.; Taran, O. P.; Parmon, V. N. Study of oxygen groups at a porous carbon surface by a new fast intermittent thermodesorption technique. *Carbon* **2011**, 49 (6), 2062–2073.
- (32) Costandy, J. G.; Edgar, T. F.; Baldea, M. Switching from Batch to Continuous Reactors is a Trajectory Optimization Problem. *Ind. Eng. Chem. Res.* **2019**, 58 (30), 13718–13736.
- (33) Roberts, E. J.; Habas, S. E.; Wang, L.; Ruddy, D. A.; White, E. A.; Baddour, F. G.; Griffin, M. B.; Schaidle, J. A.; Malmstadt, N.; Brutchey, R. L. High-Throughput Continuous Flow Synthesis of Nickel Nanoparticles for the Catalytic Hydrodeoxygenation of Guaiacol. *ACS Sustainable Chem. Eng.* **2017**, 5 (1), 632–639.
- (34) Yan, P.; Li, M. M.-J.; Adesina, A. A.; Zhao, G.; Setiawan, A.; Kennedy, E. M.; Stockenhuber, M. The Role of Acid and Metal Sites in Hydrodeoxygenation of Guaiacol over Ni/Beta Catalysts. *Catal. Sci. Technol.* **2020**, 10, 810–825.
- (35) Duval, A.; Lawoko, M. A Review on Lignin-Based Polymeric, Micro- and Nano-structured Materials. *React. Funct. Polym.* **2014**, 85, 78–96.
- (36) Alda-Onggar, M.; Mäki-Arvela, P.; Aho, A.; Simakova, I. L.; Murzin, D. Y. Hydrodeoxygenation of Phenolic Model Compounds over Zirconia Supported Ir and Ni-Catalysts. *React. Kinet., Mech. Catal.* **2019**, 126, 737–759.
- (37) Coloma, F.; Sepúlveda-Escribano, A.; Rodríguez-Reinoso, F. Heat-Treated Carbon-Blacks as Supports for Platinum Catalysts. *J. Catal.* **1995**, 154 (2), 299–305.
- (38) Sepúlveda-Escribano, A.; Coloma, F.; Rodríguez-Reinoso, F. Platinum Catalysts Supported on Carbon Blacks with Different Surface Chemical Properties. *Appl. Catal., A* **1998**, 173 (2), 247–257.
- (39) Moreno-Castilla, C.; Carrasco-Marín, F.; Parejo-Pérez, C.; López Raman, M. Dehydration of Methanol to Dimethyl Ether Catalyzed by Oxidized Activated Carbons with Varying Surface Acidic Character. *Carbon* **2001**, 39 (6), 869–875.
- (40) Wang, S.; Lu, G. Q. Effects of Acidic Treatments on the Pore and Surface Properties of Ni Catalyst Supported on Activated Carbon. *Carbon* **1998**, 36 (3), 283–292.
- (41) Zazo, J. A.; Fraile, A. F.; Rey, A.; Bahamonde, A.; Casas, J. A.; Rodríguez, J. J. Optimizing Calcination Temperature of Fe/Activated Carbon Catalysts for CWPO. *Catal. Today* **2009**, 143 (3–4), 341–346.
- (42) Markus, H.; Mäki-Arvela, P.; Kumar, N.; Kul'kova, N. V.; Eklund, P.; Sjöholm, R.; Holmbom, B.; Salmi, T.; Murzin, D. Y. Hydrogenolysis of Hydroxymatairesinol over Carbon-Supported Palladium Catalysts. *Catal. Lett.* **2005**, 103 (1–2), 125–131.
- (43) Kovalenko, G. A.; Rudina, N. A.; Perminova, L. V.; Chuenko, T. V.; Skrypnik, O. V. Preparation and Characterization of Nanoporous Carbon Supports on a Nickel/Sibunit Catalyst. *Kinet. Catal.* **2009**, 50 (4), 597–605.
- (44) Leofanti, G.; Padovan, M.; Tozzola, G.; Venturelli, B. Surface Area and Pore Texture of Catalysts. *Catal. Today* **1998**, 41 (1–3), 207–219.
- (45) Lopez-Ruiz, J. A.; Davis, R. J. Decarbonylation of Heptanoic Acid over Carbon-Supported Platinum Nanoparticles. *Green Chem.* **2014**, 16 (2), 683–694.
- (46) Qiu, T.; Yang, J.-G.; Bai, X.-J.; Wang, Y.-L. The Preparation of Synthetic Graphite Materials with Hierarchical Pores from Lignite by One-Step Impregnation and Their Characterization as Dye Absorbents. *RSC Adv.* **2019**, 9 (22), 12737–12746.
- (47) Borisov, V. A.; Iost, K. N.; Temerev, V. L.; Surovikin, Y. V.; Smorokov, A. A.; Fedotova, P. A.; Shlyapin, D. A. High-Temperature Modification of Sibunit for its Application as a Support for Ruthenium Catalysts in Ammonia Synthesis. *AIP Conf. Proc.* **2018**, 2141, 020017.
- (48) Godina, L. I.; Kirilin, A. V.; Tokarev, A. V.; Simakova, I. L.; Murzin, D. Y. Sibunit-Supported Mono- and Bimetallic Catalysts Used in Aqueous-Phase Reforming of Xylitol. *Ind. Eng. Chem. Res.* **2018**, 57, 2050–2067.
- (49) Yentekakis, I. V.; Goula, G.; Panagiotopoulou, P.; Kampouri, S.; Taylor, M. J.; Kyriakou, G.; Lambert, R. M. Stabilization of Catalyst Particles Against Sintering on Oxide Supports with High Oxygen Ion Lability Exemplified by Ir-Catalyzed Decomposition of N₂O. *Appl. Catal., B* **2016**, 192, 357–364.
- (50) Chen, N.-Y.; Liu, M.-C.; Yang, S.-C.; Chang, J.-R. EXAFS Peaks and TPR Characterizing Bimetallic Interactions: Effects of Impregnation Methods on the Structure of Pt-Ru/C Catalysts. *J. Spectrosc.* **2014**, 2014, 1–12.
- (51) Di, X.; Li, C.; Lafaye, G.; Especel, C.; Epron, F.; Liang, C. Influence of Re–M Interactions in Re–M/C Bimetallic Catalysts Prepared by a Microwave-Assisted Thermolytic Method on Aqueous-Phase Hydrogenation of Succinic Acid. *Catal. Sci. Technol.* **2017**, 7 (22), 5212–5223.
- (52) Simonetti, D.; Kunkes, E.; Dumesic, J. Gas-Phase Conversion of Glycerol to Synthesis Gas over Carbon-Supported Platinum and Platinum–Rhenium Catalysts. *J. Catal.* **2007**, 247 (2), 298–306.
- (53) Conner, W. C.; Falconer, J. L. Spillover in Heterogeneous Catalysis. *Chem. Rev.* **1995**, 95 (3), 759–788.
- (54) Prins, R. Hydrogen Spillover. Facts and Fiction. *Chem. Rev.* **2012**, 112 (5), 2714–2738.
- (55) Nakagawa, Y.; Tazawa, S.; Wang, T.; Tamura, M.; Hiyoshi, N.; Okumura, K.; Tomishige, K. Mechanistic Study of Hydrogen-Driven Deoxydehydration over Ceria-Supported Rhenium Catalyst Promoted by Au Nanoparticles. *ACS Catal.* **2018**, 8 (1), 584–595.
- (56) Fan, J.; Qi, K.; Zhang, L.; Zhang, H.; Yu, S.; Cui, X. Engineering Pt/Pd Interfacial Electronic Structures for Highly Efficient Hydrogen Evolution and Alcohol Oxidation. *ACS Appl. Mater. Interfaces* **2017**, 9 (21), 18008–18014.
- (57) *Handbook of X-ray Photoelectron Spectroscopy*; Chastain, J., King, R. C., Jr., Eds.; Physical Electronics, Inc., 1995; 261 pp.
- (58) Lindfors, C.; Mäki-Arvela, P.; Paturi, P.; Aho, A.; Eränen, K.; Hemming, J.; Peurla, M.; Kubická, D.; Simakova, I. L.; Murzin, D. Y. Hydrodeoxygenation of Iseugenol over Ni- and Co-Supported Catalysts. *ACS Sustainable Chem. Eng.* **2019**, 7 (17), 14545–14560.
- (59) Sulman, A.; Mäki-Arvela, P.; Bomont, L.; Alda-Onggar, M.; Fedorov, V.; Russo, V.; Eränen, K.; Peurla, M.; Akhmetzyanova, U.; Skuhrovcová, L.; Tišler, Z.; Grénman, H.; Wärmä, J.; Murzin, D. Y.

Kinetic and Thermodynamic Analysis of Guaiacol Hydrodeoxygenation. *Catal. Lett.* **2019**, *149* (9), 2453–2467.

(60) Alvarez, C.; Cruces, K.; Garcia, R.; Sepulveda, C.; Fierro, J. L. G.; Ghampson, I. T.; Escalona, N. Conversion of Guaiacol over Different Re Active Phases Supported on CeO₂-Al₂O₃. *Appl. Catal., A* **2017**, *547*, 256–264.

(61) Tieuli, S.; Mäki-Arvela, P.; Peurla, M.; Eränen, K.; Wärnå, J.; Cruciani, G.; Menegazzo, F.; Murzin, D. Y.; Signoretto, M. Hydrodeoxygenation of Isoeugenol over Ni-SBA-15: Kinetics and Modelling. *Appl. Catal., A* **2019**, *580*, 1–10.

(62) Bomont, L.; Alda-Onggar, M.; Fedorov, V.; Aho, A.; Peltonen, J.; Eränen, K.; Peurla, M.; Kumar, N.; Wärnå, J.; Russo, V.; et al. Production of Cycloalkanes in Hydrodeoxygenation of Isoeugenol over Pt- and Ir-Modified Bifunctional Catalysts. *Eur. J. Inorg. Chem.* **2018**, *2018*, 2841–2854.

(63) Temkin, M. I.; Murzin, D. Y.; Kul'kova, N. V. Kinetics and Mechanism of Liquid-Phase Hydrogenation. *Doklady Acad. Sci. USSR* **1988**, *303*, 659.

M. E. Martínez-Klimov, P. Mäki-Arvela, A. Çiftçi, N. Kumar, K. Eränen, M. Peurla, E. J. M. Hensen, D. Y. Murzin, Bifunctional Pt-Re catalysts in hydrodeoxygenation of isoeugenol as a model compound for renewable jet fuel production, *ACS Engineering Au*, 5 (2022) 436 – 449.

Bifunctional Pt–Re Catalysts in Hydrodeoxygenation of Isoeugenol as a Model Compound for Renewable Jet Fuel Production

Mark Martinez-Klimov, Päivi Mäki-Arvela, Ayşegül Çiftçi, Narendra Kumar, Kari Eränen, Markus Peurla, Emiel J. M. Hensen, and Dmitry Yu. Murzin*



Cite This: *ACS Eng. Au* 2022, 2, 436–449



Read Online

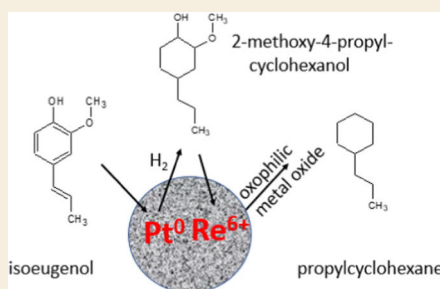
ACCESS |

Metrics & More

Article Recommendations

ABSTRACT: Bimetallic platinum–rhenium catalysts supported on activated carbon were tested for the hydrodeoxygenation (HDO) of isoeugenol at 250 °C and 30 bar of H₂ in a batch reactor. The catalysts were characterized by inductively coupled plasma atomic emission spectrometry (ICP-IES), N₂ physisorption, electron microscopy (high-angle annular dark-field scanning transmission electron microscopy (HAADF-STEM), transmission electron microscopy (TEM)), temperature-programmed reduction, X-ray absorption spectroscopy (X-ray absorption near-edge structure (XANES) and extended X-ray absorption fine structure (EXAFS)), and temperature-programmed desorption of ammonia. Bimetallic catalysts containing Pt and Re were much more active than monometallic Pt/C and Re/C. Complete isoeugenol conversion, high propylcyclohexane yield (99%), and a high liquid-phase mass balance (77%) were obtained for the catalyst with the highest Re loading, Pt–Re(1:5)/C. Such high activity is attributed to a synergistic effect between the reduced Pt and the Re-oxide species, as both metal active sites and oxygen vacancies are required for HDO. The apparent activation energy for the HDO of isoeugenol with Pt–Re(1:5)/C was 44 kJ/mol.

KEYWORDS: hydrodeoxygenation, bimetallic catalyst, platinum, rhenium, activated carbon, jet fuel



INTRODUCTION

Depleting fossil resources and increased greenhouse gas emissions have accelerated the development of alternative processes and technologies assisting the transition to the use of renewable fuels.¹ These can for instance be obtained from biomass, an abundant resource comprised of cellulose, commonly used in the pulp and paper industry,² hemicellulose, already employed to produce platform chemicals like xylitol³ and furfural,⁴ and lignin, which can be upgraded to produce fine chemicals and biofuels.^{5,6}

Lignin is of particular interest, as it is one of the main natural sources containing aromatic rings.⁷ Obtained as an undesired residue from industries like paper making, it can be utilized to obtain valuable products.⁸ Lignin is a complex biopolymer, which can be depolymerized through thermochemical processes into a mixture of oxygenated molecules.⁹ Lignin-derived mixtures need to be further upgraded, as they exhibit a low heating value, and are also viscous and corrosive because of their oxygen content.¹⁰

A common way to remove oxygen-containing functionalities from these molecules is hydrodeoxygenation (HDO). Catalysts used for HDO of biogenic compounds are often bifunctional, as they require a metal for hydrogenation and a solid acid support or a metal oxide with O-vacancies.^{11,12} Studies on

HDO catalysts were initially performed with sulfided NiMo and CoMo supported on Al₂O₃ and SiO₂ used for hydrodesulfurization (HDS) due to obvious similarities between HDO and HDS.¹³ Recently, attention has shifted to non-sulfided monometallic and bimetallic catalysts on a variety of supports, such as different types of carbon (activated carbon,¹⁴ carbon black,¹⁵ Vulcan carbon),¹⁶ Sibunit,¹⁷ metal oxides (TiO₂,¹⁸ ZrO₂,¹⁹ CeO₂),^{20,21} and nanostructured materials (carbon nanotubes,²¹ SBA-15,²² and MCM-41).²³ The most studied metals for HDO include Ni, Mo, Co, Pt, Ru, and Pd.²⁴

Bimetallic Pt–Re catalysts have been widely used in reforming processes²⁵ because Re has a promoting effect on such catalysts, improving activity and stability.²⁶ The use of Re is not only limited to reforming, as it is also used in fuel cells and other sustainable processes.²⁷ This combination of metals, however, has been scarcely used for HDO of isoeugenol. Our previous study on bimetallic Pt–Re catalysts supported on a

Received: March 16, 2022

Revised: May 11, 2022

Accepted: May 12, 2022

Published: June 2, 2022



mesoporous carbon (Sibunit) demonstrated an increased activity when compared to typical catalysts reported in the literature and used under similar reaction conditions.¹⁷ The previous investigation was limited regarding the effect of Re on isoeugenol HDO, as only three bimetallic catalysts with less variations of Pt and Re loadings were tested.

Activated carbon is the most common carbon support used in catalysis. It is attractive due to its large surface area and porosity, allowing for better dispersion of the active phase.²⁸ Due to its hydrophobicity, activated carbon shows a particular affinity to nonpolar solvents, such as hydrocarbons.²⁹ Other advantages include the easier reducibility of supported metals and the recovery of these metals by burning away the support.³⁰

HDO of model molecules representing lignin phenolics is often studied to obtain an insight into catalytic activity and stability. Phenol,³¹ guaiacol,^{32,33} anisole,²² and vanillin³⁴ are the most common model molecules studied due to their availability and simplicity, although they are not the most representative of real lignin feedstock.³⁵ Isoeugenol is an attractive lignin-derived model compound, as it closely resembles the monomeric phenylpropane building blocks found in lignin. It contains methoxy, hydroxyl, and allyl groups, which are functional groups commonly found in most lignin-derived compounds.³⁶ The main HDO product of isoeugenol is propylcyclohexane, a molecule that can be representative of the hydrocarbons found in jet fuel.

Renewable jet fuel must exhibit similar properties as conventional jet fuel to be used with current technologies. Fossil-derived jet fuel consists mainly of aliphatic and aromatic hydrocarbons in the range of C₈–C₁₆, with alkanes, alkenes, cycloalkanes, and aromatics being the main components.^{37,38}

The need for renewable jet fuel arises as new regulations aim to boost sustainable fuels and meet climate targets.³⁹ More importantly, hydrocarbons used for commercial aircrafts cannot be replaced by batteries, i.e., the direction the automobile industry seems to be taking, as batteries with enough energy density to propel a plane would be too heavy.⁴⁰

However, a transition toward renewable and sustainable fuels could be done with the utilization of biomass and oxygen removal processes such as HDO. Hydrocarbons obtained from HDO of lignocellulosic biomass could potentially be mixed with fossil-derived hydrocarbons or even replace them, helping to lower the carbon footprint.⁴¹

In the present work, hydrodeoxygenation of isoeugenol over bimetallic Pt–Re catalysts supported on activated carbon was studied and compared to monometallic Pt and Re catalysts. To study the effect of Re on the bimetallic catalytic systems and their activity in HDO, a series of catalysts with a fixed amount of Pt and varied Re loading were investigated.

EXPERIMENTAL SECTION

Catalyst preparation and the following characterization techniques; inductively coupled plasma atomic emission spectrometry (ICP-AES), high-angle annular dark-field scanning transmission electron microscopy (HAADF-STEM), temperature-programmed reduction (TPR), X-ray absorption spectroscopy (XAS), and temperature-programmed desorption of ammonia (TPD-NH₃) have been reported in a previous publication.²⁶

Catalyst Preparation

The catalysts were prepared by incipient wetness impregnation of the dissolved metal precursors chloroplatinic acid hexahydrate (H₂PtCl₆·6H₂O) and perhenic acid (HReO₄, Aldrich, 65–70 wt % in H₂O,

99.99%) onto activated carbon (NORIT RX3 EXTRA). Bimetallic catalysts supported on carbon were denoted as PRCXX, where PR corresponds to platinum and rhenium, C corresponds to the carbon support, and XX to the molar ratio. For bimetallic catalysts, the molar ratios of Pt/Re were set to 1:1, 2:1, 1:2, and 1:5 by maintaining Pt loading to 2.5 wt % and varying the Re loading accordingly.

Monometallic catalysts Pt/C and Re/C were also studied, their respective nominal loading was 2.5 wt % for both Pt and Re.

Preparation of Pt and Pt–Re catalysts supported on carbon was as follows: activated carbon was first dried overnight at 110 °C, followed by impregnation of the dissolved Pt precursor (H₂PtCl₆·6H₂O) in deionized water. The catalyst was left to dry overnight at 110 °C. For bimetallic Pt–Re catalysts, subsequent impregnation of the Re precursor (HReO₄) was performed, followed by drying overnight at 110 °C.

Monometallic Re/C was prepared by the same method, only using the Re precursor.²⁶

A summary of the catalysts used in the current work is presented in Table 1.

Table 1. Summary of Catalysts Supported on Activated Carbon Used for HDO of Isoeugenol

catalyst denomination	metal	nominal metal loading (wt %)		metal molar ratio
		Pt	Re	
Pt/C	platinum	2.5		
Re/C	rhenium		2.4	
PRC21	platinum, rhenium	2.5	1.2	2:1
PRC11	platinum, rhenium	2.5	2.4	1:1
PRC12	platinum, rhenium	2.5	4.8	1:2
PRC15	platinum, rhenium	2.5	11.9	1:5

Catalytic Tests

Prior to the experiments, the catalysts were reduced *ex situ* in a U-shaped reactor, under a hydrogen flow (40 mL/min) at 350 °C for 180 min, with a heating ramp of 10 °C/min. After reduction was finished, the system was flushed with argon, and dodecane was added to avoid reoxidation.

HDO reactions were carried out in a 300 mL stainless steel batch reactor (PARR) equipped with a heating jacket and mechanical stirring. A heating rate of the reactor was 10 °C/min. To avoid external mass-transfer limitations, the stirring speed was set to 900 rpm. To avoid internal mass-transfer limitations, the size of the catalyst particles was below 63 μm. The following quantities were used for the reaction: 0.1 g of the reactant, 0.05 g of the catalyst, and 50 mL of dodecane.

The reactor was initially purged with 7 bar of argon (AGA, 99.999%) for 10 min, followed by purging with 10 bar of hydrogen (AGA, 99.999%) for 10 min. The reactor was then pressurized to 20 bar with hydrogen. After heating to the reaction temperature, hydrogen was added to the reactor to reach 30 bar of total pressure if needed.

Reaction time started after the reaction temperature and stirring speed were reached. Samples were taken at regular time intervals and analyzed by GC and GC/MS. A DB-1 capillary column (Agilent 122-103e) of 30 m length, 250 μm internal diameter, and 0.5 μm film thickness was utilized for GC analysis. The carrier gas employed was He (flow rate of 1.7 mL/min). The temperature program was 60 °C (5 min), 3 °C/min to 135 °C, and 15 °C/min to 300 °C. GC–MS analysis was performed using the same temperature program and type of column as used in GC.

Catalyst Characterization

Inductively Coupled Plasma Atomic Emission Spectrometry (ICP-AES). Elemental analysis was performed with inductively coupled plasma atomic emission spectrometry (ICP-AES). Determination of

Table 2. Metal Loading and Textural Properties of the Catalysts

catalyst	metal loading (wt %) ²⁶			textural characteristics			
	Pt	Re	molar ratio Pt/Re	SSA (m ² /g)	V _Σ (cm ³ /g)	V _{MP} (cm ³ /g)	D _p (nm)
C support				1096	0.57	0.47	0.59, 0.67
Pt/C	2.44			1033	0.47	0.37	0.59, 0.67
Re/C		2.78		1030	0.49	0.39	0.59, 0.67
PRC21	2.48	1.53	2:1.2	1026	0.49	0.40	0.59, 0.68
PRC11	2.53	2.86	1:1.2	1019	0.47	0.38	0.59, 0.67
PRC12	2.51	5.58	1:2.3	1017	0.48	0.37	0.59, 0.67
PRC15	2.28	13.41	1:6	1014	0.48	0.36	0.59, 0.68
PRC11 spent				1002	0.43	0.35	0.59, 0.68
PRC21 spent				1005	0.43	0.35	0.59, 0.68
PRC15 spent (270 °C)				992	0.39	0.33	0.59, 0.68

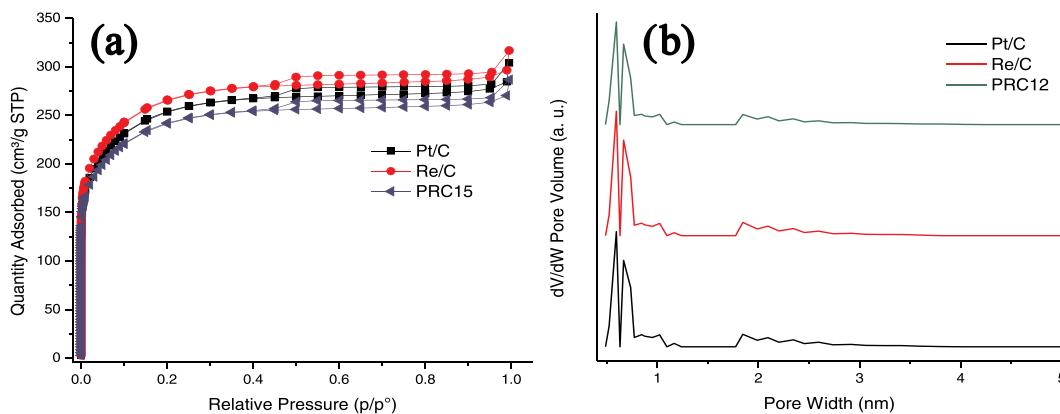


Figure 1. (a) Adsorption–desorption isotherm and (b) pore-size distribution of Pt/C, Re/C, and PRC12.

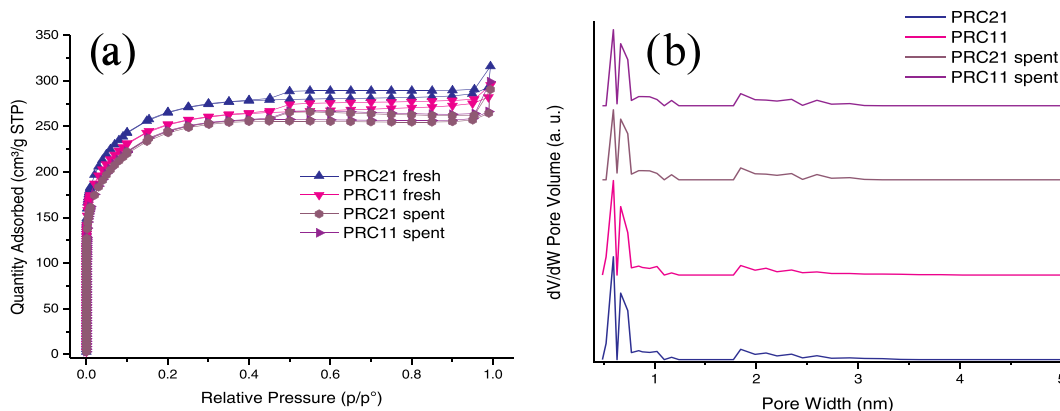


Figure 2. (a) Nitrogen adsorption–desorption isotherms and (b) pore-size distribution comparison of fresh and spent catalysts.

the metal loading of the catalysts was performed on a Goffin Meyvis Spectro Cirusccd apparatus.²⁶

Nitrogen Physisorption. Textural properties of the fresh and spent catalysts were determined by nitrogen physisorption (Micromeritics 3Flex-3500). The specific surface area was determined by the Dubinin–Radushkevich method and pore-size distributions were calculated with the density functional theory (DFT) method. The catalyst pretreatment consisted of two stages of outgassing. First, they

were outgassed *ex situ* in a Micromeritics VacPrep 061 Sample Degas system under vacuum at 200 °C for 20–24 h, followed by *in situ* degassing for 5 h at 250 °C.

Electron Microscopy (HAADF-STEM, TEM). Electron microscopy was utilized to determine the metal particle sizes and evaluate the metal dispersion. High-angle annular dark-field scanning transmission electron microscopy (HAADF-STEM) micrographs were obtained at room temperature on a CryoTitan transmission electron

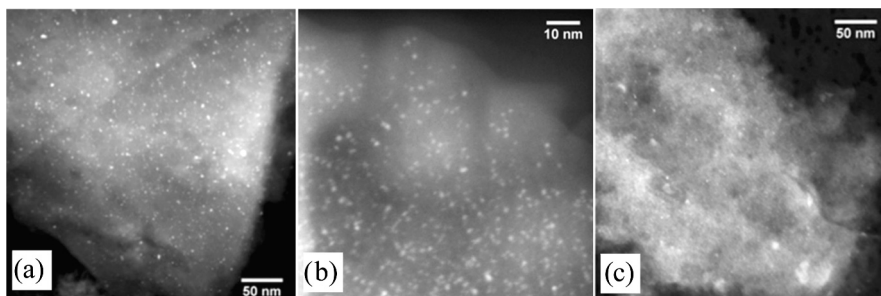


Figure 3. HAADF-STEM micrographs of fresh (a) Pt/C, (b) PRC11, and (c) PRC15 catalysts. Reprinted with permission from ref 26. Copyright 2014 Elsevier.

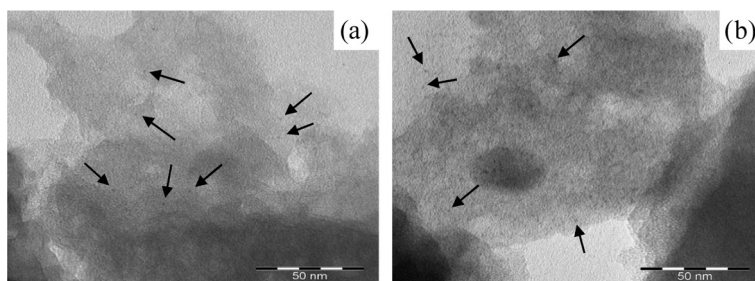


Figure 4. TEM micrographs of the spent (a) PRC11 and (b) PRC15 (270 °C) with arrows pointing at metallic particles.

microscope equipped with a field emission gun (FEG) and a Cryo-TWIN objective lens. STEM images were acquired with a Fishione HAADF detector.²⁶ The spent catalysts were characterized with a JEM-1400Plus (JEOL, Japan) transmission electron microscope at 120 kV maximal acceleration voltage. The samples were reduced, ground, and suspended in ethanol and then mounted on a copper grid prior to the analysis. The average particle size was determined by measuring the diameter of more than 300 particles.

Temperature-Programmed Reduction (TPR). TPR analysis was performed using a tubular quartz reactor and a thermal conductivity detector (TCD). The sample was reduced in 4 vol % H₂ in N₂ at a flow rate of 8 mL/min. The heating was carried out from room temperature until 800 °C with a heating rate of 10 °C/min. The H₂ signal was calibrated using a reference catalyst (CuO/SiO₂).²⁶

X-Ray Photoelectron Spectroscopy (XPS). X-ray photoelectron spectroscopy (XPS) measurements were performed *ex situ* with a Nexsa XPS (ESCA) photoelectron spectrometer manufactured by Thermo Scientific, using a monochromated Al K α excitation source. The catalysts were reduced *ex situ* and then placed on a sample holder for analysis.

X-Ray Absorption Spectroscopy (XAS). XAS was carried out at the European Synchrotron Radiation Facility (ESRF) in Grenoble, France (storage ring 6.0 GeV, ring current 200 mA). Data were collected in transmission mode for Pt LIII and Re LIII edges using a double crystal Si(111) monochromator solid-state detector. EXAFS was performed with an EXCURVE931 using curved wave theory. Pt foil was used for calibration. For the Re LIII edge, Re powder, and NH₄ReO₄ were used as the reference. The spectra were recorded in a stainless steel cell under a He and H₂ atmosphere. XANES spectra were recorded while heating the sample to 550 °C at a rate of 10 °C/min. EXAFS spectra were obtained after the sample was cooled.²⁶

Temperature-Programmed Desorption of Ammonia (TPD-NH₃). Temperature-programmed desorption (TPD) of ammonia was performed in a tubular quartz reactor attached to a heating oven and coupled to a quadrupole mass spectrometer (Balzers TPG-300). The

samples were pre-reduced *in situ* prior to the analysis. Afterward, the catalyst was exposed to pure NH₃ at room temperature. The temperature ramp used for the analysis was 10 °C/min under He flow (50 mL/min). Signals corresponding to He, NH₃, and H₂O were recorded simultaneously.²⁶

RESULTS AND DISCUSSION

Catalyst Characterization

A summary of the metal loading and textural properties of the catalysts is presented in Table 2.

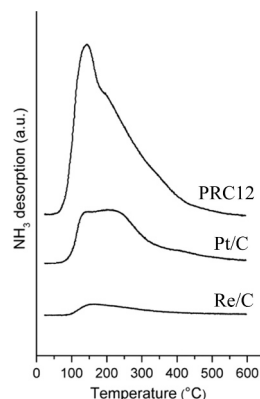


Figure 5. NH₃-TPD profiles of Pt/C, Re/C, and PRC12. Reprinted with permission from ref 26. Copyright 2014 Elsevier.

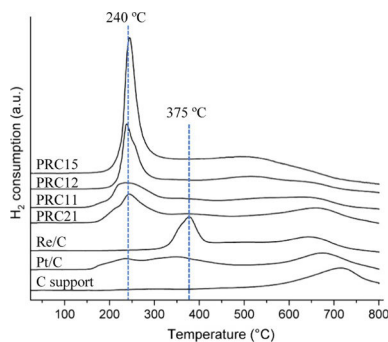


Figure 6. TPR profiles of the activated carbon support, monometallic Pt/C and (c) Re/C and bimetallic PRC21, PRC11, PRC12 and PRC15 catalysts. Reprinted with permission from ref 26. Copyright 2014 Elsevier.

Table 3. Temperature-Programmed Reduction (TPR) Results for Mono- and Bimetallic Catalysts

catalyst	T_{max} (°C)	H ₂ /M ratio ²⁶
Pt/C	240	4.84
Re/C	375	9.59
PRC21	240	6.40
PRC11	240	4.70
PRC12	240	3.62
PRC15	240	3.55

The catalysts displayed attractive characteristics; metal atomic ratios (Table 2) calculated by the metal loadings obtained by ICP were close to the nominal values, indicating good deposition. Additionally, nitrogen physisorption results (Table 2) showed a high specific surface (SSA) area for all

catalysts (ca. 1000 m²/g). Catalysts displayed a slight decrease in textural properties when compared to the pure carbon support, which could be caused by metal deposition. The highest SSA, total pore volume (V_{Σ}), and the micropore volume (V_{MP}) were obtained for monometallic Pt/C and Re/C catalysts, while bimetallic catalysts exhibited a slight decrease in the textural properties, which could be explained by pore blockage due to increased metal loadings.

Adsorption–desorption isotherms and the pore-size distributions of fresh Pt/C, Re/C, and PRC12 are compared in Figure 1.

All catalysts displayed isotherms of type I and hysteresis type H4, characteristic of activated carbon, indicating the presence of micropores.⁴² The main pore contribution obtained by NL-DFT (Figure 1b) was ca. 0.6 nm for all catalysts.

The decrease in the surface area for spent catalysts was not significant (Figure 2a). Pore-size distribution (Figure 2b) showed no changes in the pore diameter between the fresh and spent catalysts.

Transmission electron micrographs allowed to determine the metal particle sizes of monometallic and bimetallic catalysts (Figure 3, Figure 4). All catalysts exhibited metal particle sizes in the range of 1–2 nm.

The average number-weighted particle sizes for the catalyst were as follows: 2 nm for Pt/C, 1–2 nm for Re/C, 1.9 for PRC21, and 1.5 nm for PRC11. For PRC15 it was not possible to determine the particle sizes, which could be due to smaller not detectable nanoparticles.⁴³ Moreover, it has been reported that the addition of Re helps in stabilizing other metals in a highly dispersed form on the surface of the support.⁴⁴

TEM micrographs of the spent catalysts (Figure 4) show that there were almost no changes in the metal particle sizes during the reaction. Even after operation at 270 °C (Figure 4b), the particle sizes remained under 2 nm, indicating good stability of metal particles.

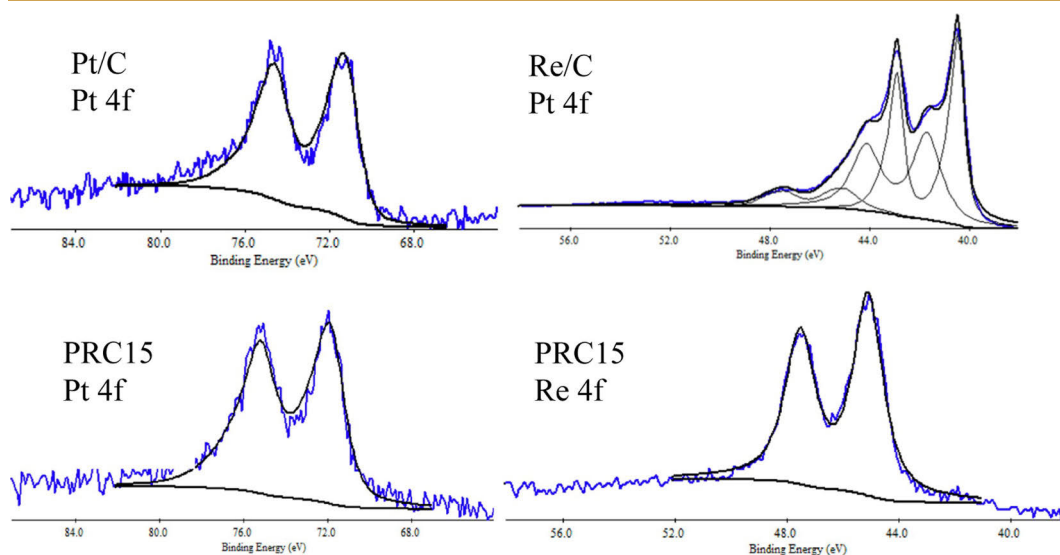


Figure 7. Pt 4f and Re 4f XPS spectra for monometallic Pt/C, Re/C, and bimetallic PRC15 catalysts.

Table 4. XPS Results for Monometallic Pt/C, Re/C, and Bimetallic PRC15 Catalysts

line	Pt/C		Re/C		PRC15		
	BE ^a (eV)	FWHM (eV)	BE ^a (eV)	FWHM (eV)	BE ^a (eV)	FWHM (eV)	
Pt 4f _{7/2}	70.99	1.55			71.99	1.66	Pt ⁰
Re 4f _{7/2}			40.60	0.96			Re ⁰
			41.60	0.96			Re ³⁺
			45.08	1	45.11	1.28	Re ⁶⁺

^aShifts in BE values have been normalized with C 1s for these catalysts.

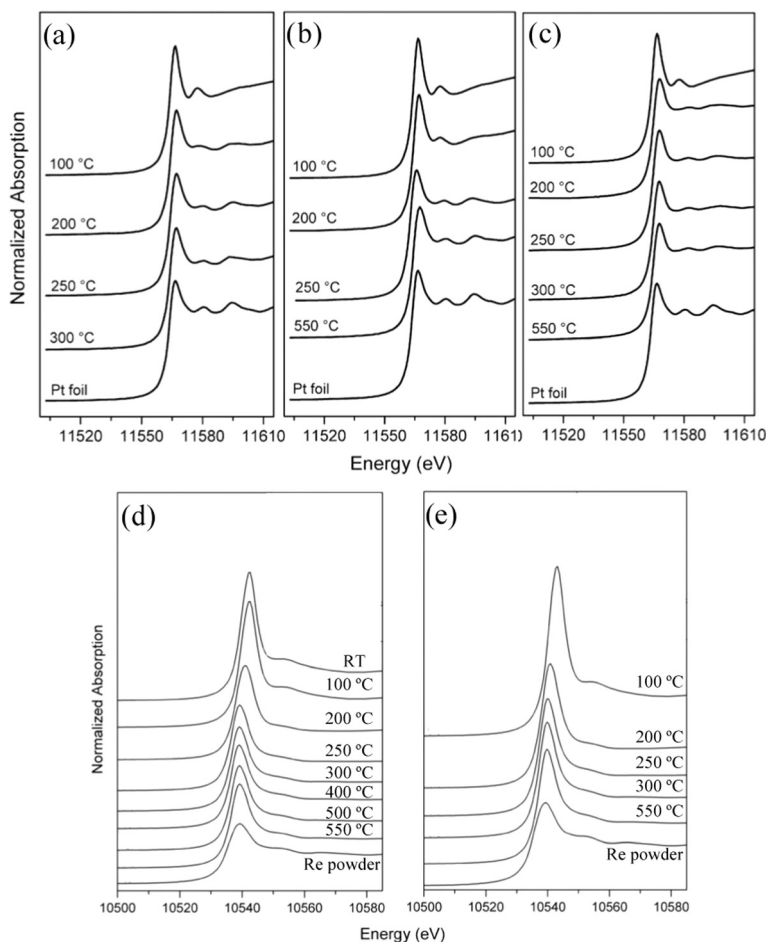


Figure 8. XANES Pt L_{III} edge near-edge spectra of (a) PRC21, (b) PRC11, and (c) PRC15 and Re L_{III} edge near-edge spectra of (d) PRC12 and (e) PRC15 after reduction at different temperatures. Reprinted with permission from ref 26. Copyright 2014 Elsevier.

NH₃-TPD was performed to obtain information on the acid sites of the catalysts. Pt/C and PRC12 were reduced at 300 °C, while Re/C was reduced at 550 °C. The NH₃-TPD profiles are presented in Figure 5. It should be noted that TPD and ammonia TPD of the bare support resulted in peaks at ca. 150 °C of inferior intensity assigned to CO₂ release due to the decomposition of the surface carboxylic groups. Subsequently, desorbed ammonia from the catalysts can be assigned to NH₃

released from the metal phase rather than from the active carbon support.

The higher intensity for the peak observed for PRC12 could be caused by higher dispersion of the metal phase, resulting in more available acid sites, and therefore, more desorbed ammonia. These results are in accordance with microscopy and EXAFS results. The increase of acid sites for bimetallic

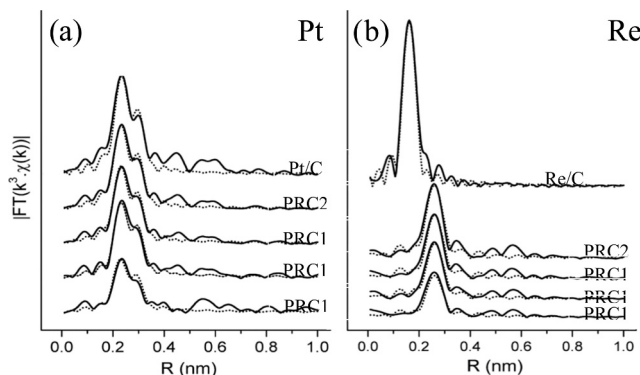


Figure 9. EXAFS spectra Pt L_{III} edge and Re L_{III} edge for monometallic and bimetallic catalysts. Dotted lines represent the fitted spectra. Reprinted with permission from ref 26. Copyright 2014 Elsevier.

Scheme 1. General Reaction Scheme of Hydrodeoxygenation of Isoeugenol

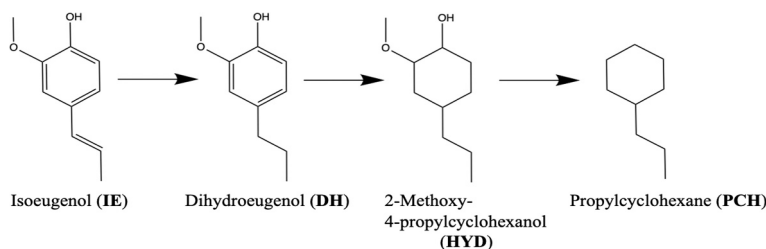


Table 5. Catalytic Activity of Monometallic Pt/C, Re/C, and PRC Catalysts in the Hydrodeoxygenation of Isoeugenol, Performed in a Batch Reactor at 250 °C

entry	catalyst	IE conversion at 4 h (%) ^a	GCLPA (%) ^b	PCH yield (%)	PCH selectivity (%) ^c	HYD yield (%)
1	Pt/C	100 (65)	94	5	4	53
2	Re/C	100 (25)	85	2		8
3	PRC21	100 (98)	53	34	21	24
4	PRC11	100 (98)	54	53	31	11
5	PRC12	100 (100)	71	93	51	0
6	PRC15	100 (100)	77	99	56	0

^aConversion of DH in parenthesis (DH X). ^bGCLPA (gas chromatography liquid-phase analysis) is an approximation for the mass balance in the liquid phase. ^cSelectivity at 60% DH conversion.

catalysts can also help explain the presence of ReOx, which has been found to be important for deoxygenation.¹⁷

Reduction profiles for monometallic and bimetallic catalysts were determined by TPR (Figure 6 and Table 3). Reduction peaks for Pt supported on activated carbon have been reported in the 150–300 °C range,⁴⁵ for Re it was between 250 and 450 °C.⁴⁶ Furthermore, shifts in the reduction peaks have been reported due to the formation of the Pt–Re alloy.^{47,48} Additionally, migration of ReOx species toward Pt⁰ has also been reported, which can be a result of weak interactions between the metal and the carbon support.⁴⁹

The TPR profile of the activated carbon support displays a peak at ca. 725 °C, observed also for all other samples. This peak has been attributed to the reduction of functional groups

on the surface and formation of methane due to interactions between the support and hydrogen.^{49,50}

For monometallic catalysts, the reduction profile of Pt/C shows two broad signals below 400 °C (Pt⁴⁺ to Pt⁰), while Re/C reduction displays a pronounced peak at ca. 375 °C (Re⁷⁺ to Re⁰).⁴⁹ All PRC catalysts presented a single reduction peak at around 240 °C.

From the TPR profiles, it can be observed that the total amount of consumed H₂ is the lowest for Pt/C. Lower reduction temperatures for bimetallic PRC, when compared to Re/C, indicate that Pt facilitates the reduction of Re,⁴⁹ which could be due to hydrogen spillover from Pt⁰ to ReOx,^{46,51–53} however, a clear signal for Re reduction could not be observed.

The H₂/M ratio was determined by the amount of H₂ consumed per total moles of Pt and Re. The H₂/M ratio (Table 3) is higher than 2 for Pt/C, which could be caused by the reduction of surface oxygen groups of the support. The H₂/M ratio decreases as the Re/Pt ratio increases. High H₂/M values indicate that more H₂ is needed to reduce Re.

X-ray photoelectron spectroscopy (XPS) was performed to determine the electronic states of Pt and Re on the surface of reduced monometallic Pt/C, Re/C, and PRC15 catalysts (Figure 7 and Table 4). The binding energy (BE) values have been normalized to that of C 1s (284.5 eV) for all catalysts. XPS spectra for monometallic Pt/C showed a doublet for Pt 4f_{7/2} with the binding energy (BE) of 70.99 eV assigned to Pt⁰, which is consistent with the BE values reported in the literature.⁵⁴ The same Pt 4f_{7/2} doublet assigned to Pt⁰ could be observed at the BE of 70.90 eV for the PRC15 catalyst.

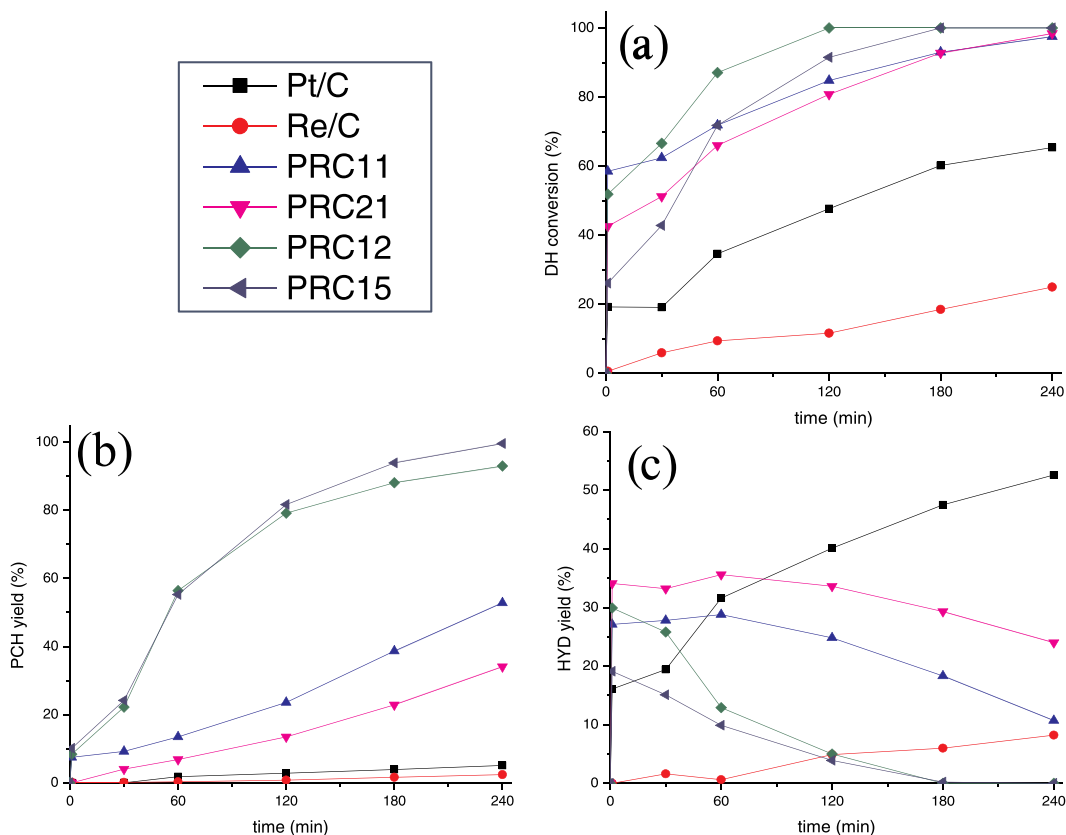


Figure 10. (a) Conversion of dihydroeugenol, (b) yield of propylcyclohexane, and (c) yield of hydrogenated intermediate as a function of time. Conditions: 250 °C and 30 bar of H_2 .

XPS spectra for monometallic Re/C showed mixed oxidation states; namely, Re $4f_{7/2}$ binding energy of 40.6 eV was assigned to Re^0 , a binding energy of 41.6 eV was assigned to Re^{3+} , while the binding energy of 45.07 eV corresponds to Re^{6+} . Bimetallic PRC15 spectra displayed a doublet signal for Re 4f with a binding energy of 45.02 eV, indicating that Re^{6+} was the predominant species. These values are also consistent with the literature.^{54,55} It's important to note that the measurements were performed *ex situ*, and as rhenium is highly oxophilic;⁶³ its oxidation state could be influenced by exposure to air.

XANES provided a better understanding of the reduction behavior of the catalysts. Figure 8 displays the XANES Pt L_{III} edge near-edge spectra of PRC21, PRC11, and PRC15 and Re L_{III} near-edge spectra of PRC12 and PRC15 after reduction at different temperatures.

Changes between 200 and 550 °C are small for Pt L_{III} spectra, indicating that Pt reduction mainly occurs between 100 and 200 °C. For PRC15 (Figure 8c), the edge position shifts to higher energy values than Pt foil and reduced Pt/C, implying that Re influenced the electronic structure of Pt.⁵⁶

A shift to lower energies is observed in Re L_{III} XANES spectra of PRC12 and PRC15 (Figure 8d,e). A comparison of

the spectra from 100 to 550 °C reveals that Re reduction occurs at higher temperatures, as the spectra display only a minor shift toward lower energy between 250 and 550 °C, which could indicate a partial reduction at these temperatures.⁵⁷ XANES spectra of PRC15 are consistent with those of XPS and TPR, showing that a significant amount of Re is found as oxide species when reduced at 350 °C.^{43,58,59}

Fourier transform (FT) EXAFS spectra for the catalysts at the Pt L_{III} edge after reduction at 300 °C are presented in Figure 9a. The backscattering functions of Pt and Re were very similar, making the determination between Pt bound to Re or Pt challenging.⁶⁰ For bimetallic catalysts, the absence of a Pt–O shell indicates that Pt is reduced at 300 °C. The coordination number (CN) of the Pt–M shell increases with increasing reduction temperature due to the increase in the size or ordering of particles. An increase in the Pt/Re ratio resulted in a decrease of the CN for the Pt–M shell. These results explain the decrease in metal particle sizes with increasing Re content. Furthermore, the Pt–M coordination distance becomes smaller with increasing Re content.

EXAFS results at the Re L_{III} edge (Figure 9b) indicate that Re in Re/C is present mainly as an oxide after reduction at 250 °C, while at 550 °C it is mostly metallic Re and a small portion

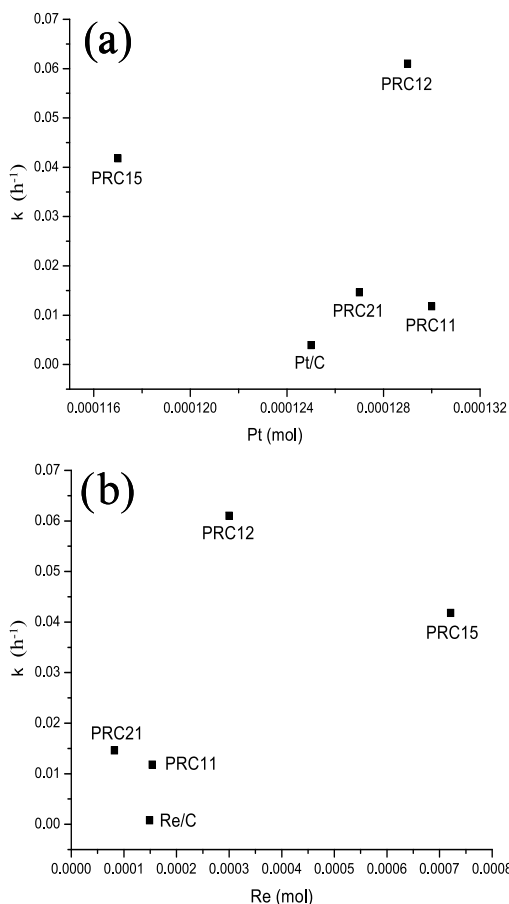


Figure 11. (a) Activity as a function of the amount of Pt (mol) and (b) activity as a function of the amount of Re (mol).

of ReOx species, which is consistent with the reduction temperature observed for Re/C in TPR (375 °C). For bimetallic catalysts, it was observed that the CN of the Re–M shell increased with the increase of Re loading, this is in accordance with the Pt EXAFS results that explain the decrease in metal particle sizes.

Catalytic Activity

The catalysts were tested for the hydrodeoxygenation (HDO) of isoeugenol (IE) in a batch reactor at temperatures between 230 and 270 °C. The simplified reaction network is presented in Scheme 1.

As reported previously, hydrogenation of the propene group occurs immediately,⁶¹ converting isoeugenol (IE) into dihydroeugenol (DH) in less than 1 min. This is followed by hydrogenation of the aromatic ring, forming 2-methoxy-4-propylcyclohexanol (HYD), which is a hydrogenated intermediate still containing hydroxy and methoxy groups. Their elimination through deoxygenation results in the desired product propylcyclohexane (PCH).

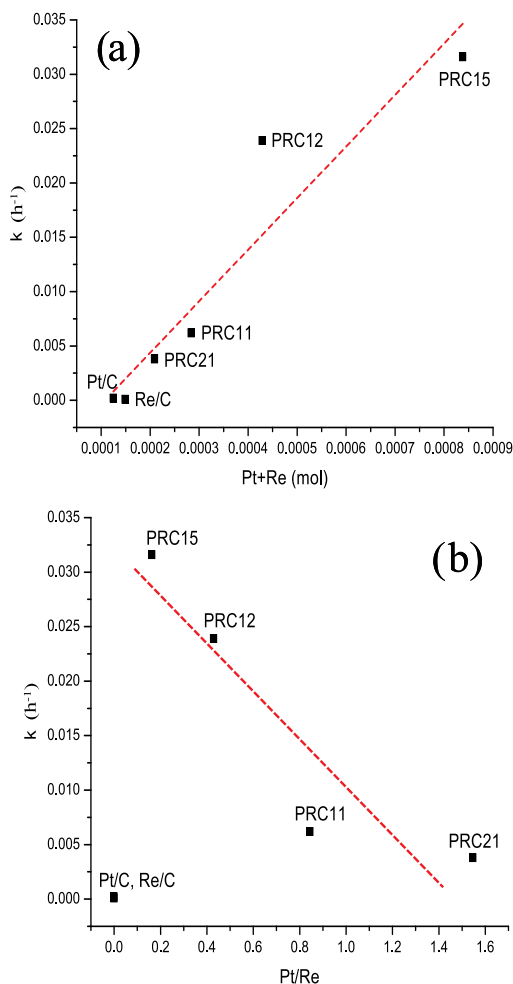


Figure 12. Rate constant as a function of (a) the sum of the Pt and Re content (mol) and (b) the Pt/Re molar ratio.

The catalytic results for monometallic and bimetallic catalysts at 250 °C are summarized in Table 5. The main products were 2-methoxy-4-propylcyclohexanol and propylcyclohexane. Time-dependent yields of these compounds are presented in Figure 10.

All catalysts displayed complete isoeugenol conversion (IE X) in less than 1 min, therefore, dihydroeugenol conversion (DH X) was followed. Data in Figure 10 also illustrate that further transformations of DH started during heating of the reactor or within the 1st min of the reaction, before the first sample is taken, as a substantial conversion of DH is achieved at time zero.

Monometallic catalysts displayed the lowest conversion of DH, 65% for Pt/C (entry 1) and 25% for Re/C (entry 2). Such low values are consistent with those reported in the literature for HDO using monometallic catalysts supported on carbon-type materials.¹⁷ Propylcyclohexane yields (PCH Y)

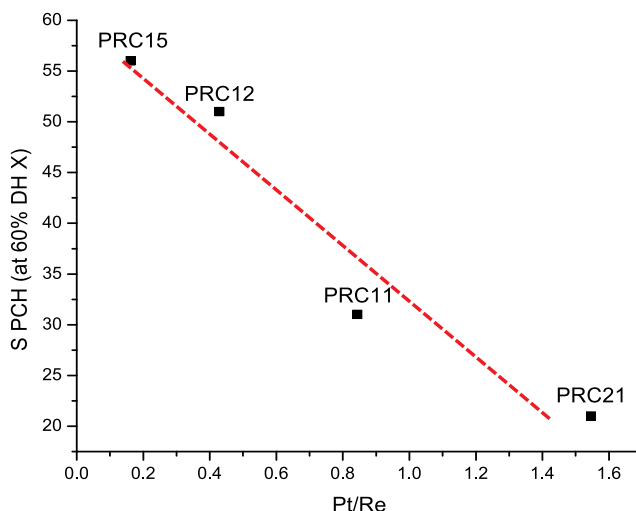


Figure 13. Propylcyclohexane selectivity (at 60% dihydroeugenol conversion) as a function of the Pt/Re molar ratio.

Table 6. Catalytic Activity of PRC15 Catalysts in the Hydrodeoxygenation of Isoeugenol, Performed at 230, 250, and 270 °C

catalyst	temperature (°C)	IE conversion at 4 h (%) ^a	GCLPA (%) ^b	PCH yield (%)	PCH selectivity (%) ^c
PRC15	230	100 (100)	68	88	74.5
PRC15	250	100 (100)	77	99	64.3
PRC15	270	100 (100)	71	92	76.9

^aConversion of DH in parenthesis (DH X). ^bGCLPA (gas chromatography liquid-phase analysis) is an approximation for the mass balance in the liquid phase. ^cSelectivity at 80% DH conversion.

were also the lowest for these catalysts, while Pt/C displayed the highest yield of the hydrogenated intermediate (HYD) among all catalysts (Figure 10c). High GCLPA values indicate that most of the products remained in the liquid phase and that deoxygenation/hydrogenolysis was minimal, reflecting relatively low catalytic activity. While gas-phase products were not analyzed, the formation of methanol and H₂O is expected.⁶² Subsequently Pt/C and Re/C exhibited mediocre conversion along with high GCLPA.

From these results it can be inferred that while Pt is active in hydrogenating the double bonds from the propenyl group and the aromatic ring, it is not effective in deoxygenation, giving only 5% yield of PCH. Low HYD yields for Re/C (ca. 2%) indicate that rhenium *per se* is not as effective for hydrogenation as Pt/C.

However, for bimetallic catalysts, there was a clear synergetic effect, as all of them exhibited higher catalytic activity than the monometallic catalysts individually, achieving complete DH conversion after 4 h of the reaction time and PCH Y >30%. The lowest PCH Y was obtained with PRC21 (entry 3, ca. 35%), the catalyst with the highest Pt/Re ratio. On the other hand, PRC15 displayed the highest PCH Y (entry 6, ca. 99%) and the maximum GCLPA value (77%), indicating almost complete conversion of IE into PCH at 4 h. GCLPA values for PRC catalysts indicate that volatile products were distributed

either in the gas phase or in the liquid phase as higher-molecular weight polymers; neither were quantified.

These values seem to indicate that a lower Pt/Re ratio results in higher HDO activity. Furthermore, selectivity toward PCH (normalized at 60% DH conversion) displays the following trend for PRC catalysts: PRC15 > PRC12 > PRC11 > PRC21, indicating that Re plays an important role in hydrodeoxygenation. These results are consistent with the results from XPS, EXAFS, and XANES, as the presence and increase of the ReO_x species content resulted in a decrease in the metal particle sizes, and therefore, better dispersion and higher HDO activity. This promotion effect can be explained by the complementarity between the high hydrogenating ability of Pt and the oxophilicity of Re, visible in Figure 11a,b, illustrating that the rate does not depend on the molar content of Pt or Re separately, as no clear trend can be observed.

For these calculations, the reaction was considered to be first-order in DH, while as the pressure was constant and an excess of H₂ of used, the apparent rate constant contains the hydrogen pressure dependence. The rate constant was obtained considering the formation of PCH within 60–240 min time interval. The values for the constant (*k*) were obtained by linear regression.

On the other hand, when considering both metals, a clear trend of the Pt/Re molar ratio on the rate constant could be identified (Figure 12). A linear increase in activity can be observed proportional to the total amount of Pt and Re (Figure 12a), with monometallic catalysts displaying the lowest activity, and PRC15 the highest. As expected, an increase in the amount of the active phase allows an increase in activity, however, a lower Pt/Re ratio (Figure 12b) also resulted in higher activity and selectivity, leading to a conclusion that both Pt and Re are indispensable to carry out the reaction.

A similar trend as in Figure 12b can be observed in Figure 13, where selectivity toward PCH, the deoxygenated product, is plotted vs the Pt/Re molar ratio. As apparently clear from Figure 13 selectivity is decreasing with an increase of the Pt/Re ratio, highlighting the importance of Re in this catalytic system.

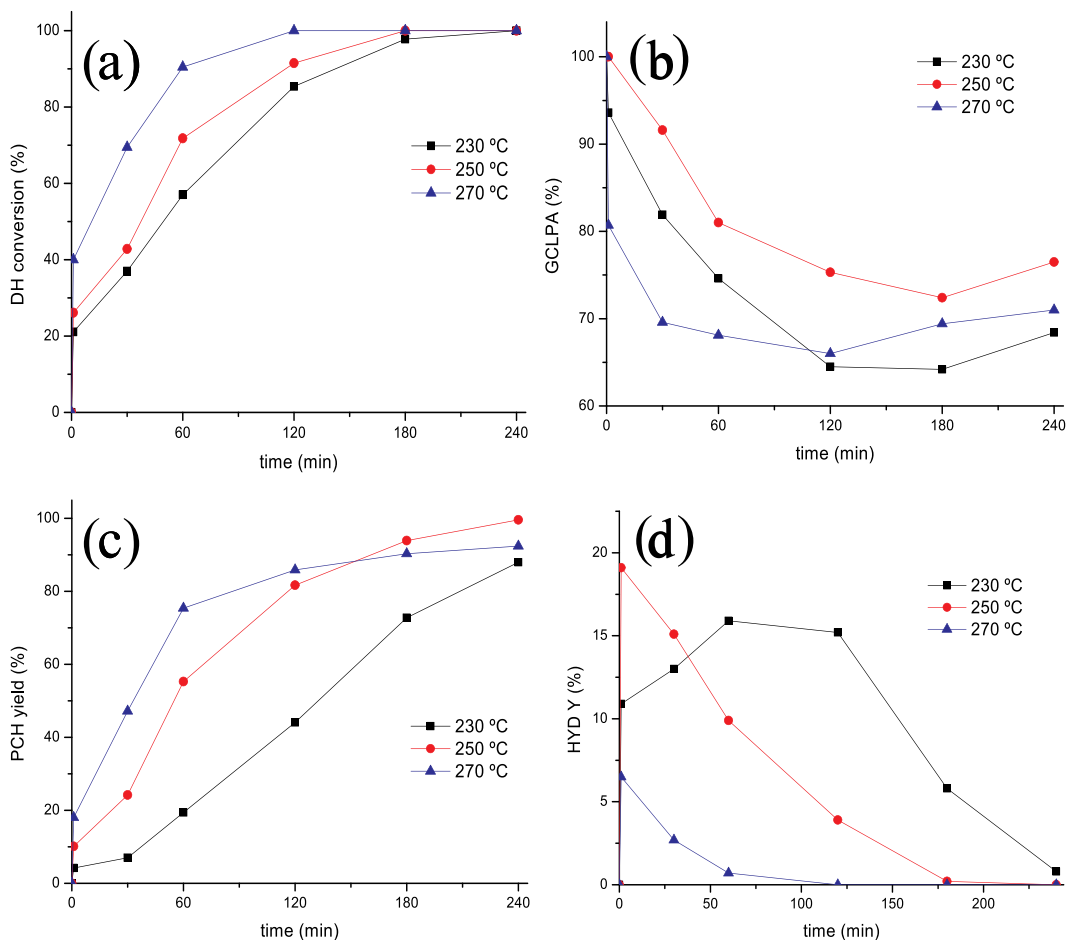


Figure 14. (a) Conversion of dihydroeugenol, (b) GCLPA, (c) PCH Y, and (d) HYD Y for PRC15 at 230, 250, and 270 °C.

For PRC15 and PRC12 catalysts, activity and selectivity toward the deoxygenated product increased, indicating that the deoxygenation route was promoted.

The results of XPS, EXAFS, and XANES reveal the presence of ReOx species when the loading of Re was higher and the particle size was smaller. This can explain the enhanced activity and selectivity toward the deoxygenated product for PRC12 and PRC15 catalysts. Metallic Pt and ReOx have a promotion effect when they are together, improving deoxygenation or breakage of the C–O bond. Similar findings have been reported in the literature, namely, oxophilic oxide in close proximity to a metal particle activates the C–O bond, promoting deoxygenation.⁶³

Activation energy was calculated for the HDO of isoeugenol with PRC15 from experiments conducted at 230–270 °C (Table 6 and Figure 14).

The liquid-phase mass balance (GCLPA, Figure 13b) was ca. 70% at 4 h for all temperatures, indicating that majority of the products remained in the liquid phase.

The PCH yield (Figure 14c) was the highest (ca. 99%) at 250 °C, even if the initial PCH yield values were higher at 270 °C. Simultaneously, the yield of HYD (Figure 14d) was the highest at 230 °C, which can be a consequence of stronger catalyst deactivation at a higher temperature. After 4 h only trace amounts of HYD were obtained (<1%). Overall, the highest PCH selectivity (at 80% conversion of DH) was obtained at 270 °C.

The apparent activation energy was calculated for the transformations of dihydroeugenol using experiments at 230, 250, and 270 °C. For this purpose, the reaction was considered as the first-order reaction for DH because of the constant pressure of H₂ also being in excess, the reaction order toward hydrogen is zero. Additionally, only the time between 1 and 120 min was considered. The values for the constant (*k*) were obtained for each temperature by linear regression and then plotted in the Arrhenius coordinates (Figure 15). The apparent activation energy obtained for HDO of IE using PRC15 was 43.7 kJ/mol.

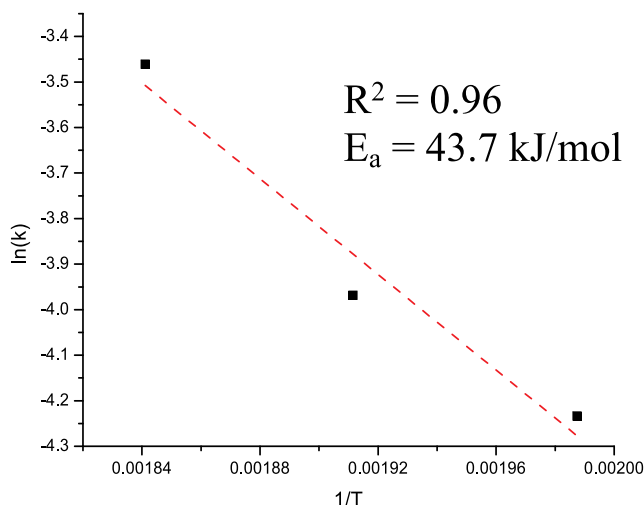


Figure 15. Arrhenius plot for the hydrodeoxygenation of isoeugenol on PRC15.

In our previous work, activation energy for HDO of isoeugenol (15 kJ/mol) was determined in a continuous reactor where mass-transfer limitations were present.¹⁷ The value obtained in this article is of the same magnitude as activation energies for HDO of other phenol-based model compounds reported in the literature.^{59,60} The apparent activation energy for ring saturation and hydrodeoxygenation of phenol was ca. 59 kJ/mol, using a Pt/Al₂O₃ catalyst in a batch reactor.⁶⁴ HDO of dihydroeugenol using a sulfided NiMo catalyst resulted in an activation energy of ca. 34 kJ/mol in a packed-bed microreactor.⁶⁵ DH conversion reached 100% at 4 h for all temperatures. As expected, the fastest DH was achieved at the highest temperature (Figure 14a).

CONCLUSIONS

Bimetallic Pt–Re catalysts supported on microporous activated carbon catalysts displayed high activity for the HDO of isoeugenol. A higher amount of Re resulted in smaller Pt particles, and therefore, higher dispersion. Characterization of the catalysts revealed that after reduction, Pt was present in the metallic state, while Re was predominantly present as ReOx. Regarding catalytic activity, a promotion effect was observed for bimetallic catalysts. Complete conversion of isoeugenol and dihydroeugenol were observed for all bimetallic catalysts, with the yields of the desired product, propylcyclohexane, increasing with the Re content. As such, the Pt–Re catalyst with a Pt/Re atomic ratio of 1/5 was the most active catalyst, achieving 99% propylcyclohexane yield at 4 h and 77% mass balance closure in the liquid phase. Selectivity at 60% of dihydroeugenol conversion was also the highest for the same catalyst (56%).

The most active catalyst exhibited the smallest particle sizes and more ReOx species, verified by XPS, EXAFS, and XANES, which could explain the catalytic performance, as they provide the oxygen vacancies required for the deoxygenation to take place.

The catalyst with a higher Pt/Re ratio (2:1) displayed a decrease in activity (34% propylcyclohexane yield, 21% propylcyclohexane selectivity). Also giving the highest yield

(ca. 25%) of the hydrogenated intermediate, 2-methoxy-4-propylcyclohexanol, among all bimetallic catalysts. For this bimetallic system, Pt performed the hydrogenation of double bonds while ReOx was needed to deoxygenate dihydroeugenol. A higher Re content and a lower Pt/Re ratio also had a positive effect on activity.

The apparent activation energy was determined for the first time for HDO of isoeugenol in a batch reactor in a temperature range of 230–270 °C, the value was 43.7 kJ/mol.

AUTHOR INFORMATION

Corresponding Author

Dmitry Yu. Murzin – Johan Gadolin Process Chemistry Centre, Åbo Akademi University, 20500 Turku/Åbo, Finland; orcid.org/0000-0003-0788-2643; Email: dmurzin@abo.fi

Authors

Mark Martinez-Klimov – Johan Gadolin Process Chemistry Centre, Åbo Akademi University, 20500 Turku/Åbo, Finland
Päivi Mäki-Arvela – Johan Gadolin Process Chemistry Centre, Åbo Akademi University, 20500 Turku/Åbo, Finland; orcid.org/0000-0002-7055-9358

Ayşegül Çiftçi – Laboratory of Inorganic Materials and Catalysis, Department of Chemical Engineering and Chemistry, Eindhoven University of Technology, 5600 MB Eindhoven, The Netherlands

Narendra Kumar – Johan Gadolin Process Chemistry Centre, Åbo Akademi University, 20500 Turku/Åbo, Finland

Kari Eränen – Johan Gadolin Process Chemistry Centre, Åbo Akademi University, 20500 Turku/Åbo, Finland

Markus Peurla – Institute of Biomedicine, University of Turku, 20520 Turku, Finland

Emiel J. M. Hensen – Laboratory of Inorganic Materials and Catalysis, Department of Chemical Engineering and Chemistry, Eindhoven University of Technology, 5600 MB Eindhoven, The Netherlands; orcid.org/0000-0002-9754-2417

Complete contact information is available at:
<https://pubs.acs.org/10.1021/acseengineeringau.2c00015>

Notes

The authors declare no competing financial interest.

■ ACKNOWLEDGMENTS

Electron microscopy samples were processed and analyzed in the Electron Microscopy Laboratory, Institute of Biomedicine, University of Turku, which receives financial support from Biocenter Finland. XPS samples were processed and analyzed in the Department of Physics and Astronomy, Quantum Building, University of Turku. The authors acknowledge Sari Granroth and Atte Aho for support in utilizing and analyzing XPS results. This work was supported by the Magnus Ehrnrooth Foundation.

■ REFERENCES

- (1) Markard, J. The Next Phase of the Energy Transition and its Implications for Research and Policy. *Nat. Energy* **2018**, *3*, 628–633.
- (2) Horn, R. A. *Morphology of Wood Pulp Fiber from Softwoods and Influence on Paper Strength*. Research Paper FPL-242; Department of Agriculture, Forest Service, Forest Products Laboratory: Madison, WI, USA, 1974.
- (3) Miura, M.; Shimotori, Y.; Nakatani, H.; Harada, A.; Aoyama, M. Bioconversion of Birch Wood Hemicellulose Hydrolyzate to Xylitol. *Appl. Biochem. Biotechnol.* **2015**, *176*, 947–955.
- (4) Delbecq, F.; Wang, Y.; Muralidhara, A.; El Ouardi, K.; Marlair, G.; Len, C. Hydrolysis of Hemicellulose and Derivatives—A Review of Recent Advances in the Production of Furfural. *Front. Chem.* **2018**, *6*, No. 146.
- (5) Abdullah, B.; Muhammad, S. A. F. A. S.; Mahmood, N. A. N. Production of Biofuel via Hydrogenation of Lignin from Biomass. In *New Advances in Hydrogenation Processes - Fundamentals and Applications*, IntechOpen, 2017; pp 289–305.
- (6) Schutysen, W.; Renders, T.; Van den Bosch, S.; Koelewijn, S.-F.; Beckham, G. T.; Sels, B. F. Chemicals from Lignin: An Interplay of Lignocellulose Fractionation, Depolymerisation, and Upgrading. *Chem. Soc. Rev.* **2018**, *47*, 852–908.
- (7) Sudarsanam, P.; Peeters, E.; Makshina, E. V.; Parvulescu, V. I.; Sels, B. F. Advances in Porous and Nanoscale Catalysts for Viable Biomass Conversion. *Chem. Soc. Rev.* **2019**, *48*, 2366–2421.
- (8) Haq, I.; Mazumder, M.; Kalamdhad, A. S. Recent Advances in Removal of Lignin from Paper Industry Wastewater and its Industrial Applications—A Review. *Bioresour. Technol.* **2020**, *312*, No. 123636.
- (9) Sun, Z.; Fridrich, B.; de Santi, A.; Elangovan, S.; Barta, K. Bright Side of Lignin Depolymerization: Toward New Platform Chemicals. *Chem. Rev.* **2018**, *118*, 614–678.
- (10) Meng, J.; Moore, A.; Tilotta, D.; Kelley, S.; Park, S. Toward Understanding of Bio-Oil Aging: Accelerated Aging of Bio-oil Fractions. *ACS Sustainable Chem. Eng.* **2014**, *2*, 2011–2018.
- (11) Mortensen, P. M.; Grunwaldt, J.-D.; Jensen, P. A.; Knudsen, K. G.; Jensen, A. D. A Review of Catalytic Upgrading of Bio-oil to Engine Fuels. *Appl. Catal., A* **2011**, *407*, 1–19.
- (12) Mäki-Arvela, P.; Murzin, D. Y. Hydrodeoxygenation of Lignin-Derived Phenols: from Fundamental Studies Towards Industrial Applications. *Catalysts* **2017**, *7*, No. 265.
- (13) Laurent, E.; Delmon, B. Study of the Hydrodeoxygenation of Carbonyl, Carboxylic and Guaiacyl Groups over Sulfided CoMo/ γ -Al₂O₃ and NiMo/ γ -Al₂O₃ Catalysts. *Appl. Catal., A* **1994**, *109*, 77–96.
- (14) Ohta, H.; Kobayashi, H.; Hara, K.; Fukuoka, A. Hydrodeoxygenation of Phenols as Lignin Models under Acid-Free Conditions with Carbon-Supported Platinum Catalysts. *Chem. Commun.* **2011**, *47*, 12209.
- (15) Vasilievich, A. V.; Baklanova, O. N.; Lavrenov, A. V. Hydrodeoxygenation of Guaiacol with Molybdenum-Carbide-Based Carbon Catalysts. *ChemistrySelect* **2020**, *5*, 4575–4579.
- (16) Jung, K. B.; Lee, J.; Ha, J.-M.; Lee, H.; Suh, D. J.; Jun, C.-J.; Jae, J. Effective Hydrodeoxygenation of Lignin-Derived Phenols using Bimetallic RuRe Catalysts: Effect of Carbon Supports. *Catal. Today* **2018**, *303*, 191–199.
- (17) Martínez-Klimov, M. E.; Mäki-Arvela, P.; Vajglova, Z.; Alda-Onggar, M.; Angervo, L.; Kumar, N.; Eränen, K.; Peurla, M.; Calimli, M. H.; Muller, J.; Shchukarev, A.; Simakova, I. L.; Murzin, D. Y. Hydrodeoxygenation of Isoleugenol over Carbon-Supported Pt and Pt-Re Catalysts for Production of Renewable Jet Fuel. *Energy Fuels* **2021**, *35*, 17755–17768.
- (18) Lu, M.; Du, H.; Wei, B.; Zhu, J.; Li, M.; Shan, Y.; Song, C. Catalytic Hydrodeoxygenation of Guaiacol over Palladium Catalyst on Different Titania Supports. *Energy Fuels* **2017**, *31*, 10858–10865.
- (19) Mäkelä, E.; González Escobedo, J. L.; Lindblad, M.; Käldestrom, M.; Meriö-Talvio, H.; Jiang, H.; Puurunen, R. L.; Karinen, R. Hydrodeoxygenation of Levulinic Acid Dimers on a Zirconia-Supported Ruthenium Catalyst. *Catalysts* **2020**, *10*, No. 200.
- (20) Afrin, S.; Bollini, P. Cerium Oxide Catalyzes the Selective Vapor Phase Hydrodeoxygenation of Anisole to Benzene at Ambient Pressures of Hydrogen. *Ind. Eng. Chem. Res.* **2019**, *58*, 14603–14607.
- (21) Chen, M.-Y.; Huang, Y.-B.; Pang, H.; Liu, X.-X.; Fu, Y. Hydrodeoxygenation of Lignin-Derived Phenols into Alkanes over carbon Nanotube Supported Ru Catalysts in Biphasic Systems. *Green Chem.* **2015**, *17*, 1710–1717.
- (22) Vargas-Villagrán, H.; Flores-Villeda, M. A.; Puente-Lee, I.; Solís-Casados, D. A.; Gómez-Cortés, A.; Díaz-Guerrero, G.; Klimova, T. E. Supported Nickel Catalysts for Anisole Hydrodeoxygenation: Increase in the Selectivity to Cyclohexane. *Catal. Today* **2018**, *341*, 26–41.
- (23) Guan, Q.; Wan, F.; Han, F.; Liu, Z.; Li, W. Hydrodeoxygenation of Methyl Palmitate over MCM-41 Supported Nickel Phosphide Catalysts. *Catal. Today* **2016**, *259*, 467–473.
- (24) Martínez-Klimov, M. E.; Mäki-Arvela, P.; Murzin, D. Y. Catalysis for Production of Jet Fuel from Renewable Sources by Hydrodeoxygenation and Hydrocracking. In *Catalysis*, RSC, 2021; Vol. 33, pp 181–213.
- (25) Burch, R. The Oxidation State of Rhenium and Its Role in Platinum-Rhenium Reforming Catalysts. *Platinum Met. Rev.* **1978**, *22*, 57–60.
- (26) Ciftci, A.; Ligthart, D. A. J. M.; Sen, A. O.; van Hoof, A. J. F.; Friedrich, H.; Hensen, E. J. M. Pt-Re Synergy in Aqueous-Phase Reforming of Glycerol and the Water-gas Shift Reaction. *J. Catal.* **2014**, *311*, 88–101.
- (27) Sakkas, P. M.; Argirusi, M.; Sourkouni, G.; Argirusis, C. Rhenium Oxide Nanoparticles – Sonochemical Synthesis and Integration on Anode Powders for Solid Oxide Fuel Cells. *Ultrason. Sonochem.* **2020**, *69*, No. 105250.
- (28) Jüntgen, H. Activated carbon as catalyst support. *Fuel* **1986**, *65*, 1436–1446.
- (29) Dowaidar, A. M.; El-Shahawi, M. S.; Ashour, I. Adsorption of Polycyclic Aromatic Hydrocarbons onto Activated Carbon from Non-Aqueous Media: 1. The Influence of the Organic Solvent Polarity. *Sep. Sci. Technol.* **2007**, *42*, 3609–3622.
- (30) Sarioğlu, Ş. Recovery of Palladium from Spent Activated Carbon-Supported Palladium Catalysts. *Platinum Met. Rev.* **2013**, *57*, 289–296.
- (31) Berenguer, A.; Sankaranarayanan, T. M.; Gómez, G.; Moreno, I.; Coronado, J. M.; Pizarro, P.; Serrano, D. P. Evaluation of Transition Metal Phosphides Supported on Ordered Mesoporous Materials as Catalysts for Phenol Hydrodeoxygenation. *Green Chem.* **2016**, *18*, 1938–1951.
- (32) Sulman, A.; Mäki-Arvela, P.; Bomont, L.; Alda-Onggar, M.; Fedorov, V.; Russo, V.; Eränen, K.; Peurla, M.; Akhmetzyanova, U.; Skuhrovcová, L.; Tišler, Z.; Grénman, H.; Wärnå, J.; Murzin, D. Y. Kinetic and Thermodynamic Analysis of Guaiacol Hydrodeoxygenation. *Catal. Lett.* **2019**, *149*, 2453–2467.
- (33) Gao, D.; Xiao, Y.; Varma, A. Guaiacol Hydrodeoxygenation over Platinum Catalyst: Reaction Pathways and Kinetics. *Ind. Eng. Chem. Res.* **2015**, *54*, 10638–10644.

- (34) Santos, J. L.; Alda-Onggar, M.; Fedorov, V.; Peurla, M.; Eränen, K.; Mäki-Arvela, P.; Centeno, M. A.; Murzin, D. Y. Hydrodeoxygenation of Vanillin Over Carbon Supported Metal Catalysts. *Appl. Catal., A* **2018**, *561*, 137–149.
- (35) Lyu, G.; Wu, S.; Zhang, H. Estimation and Comparison of Bio-Oil Components from Different Pyrolysis Conditions. *Front. Energy Res.* **2013**, *3*, No. 28.
- (36) Duval, A.; Lawoko, M. A. Review on Lignin-Based Polymeric, Micro- and Nano-structured Materials. *React. Funct. Polym.* **2014**, *85*, 78–96.
- (37) Hileman, J. I.; Stratton, R. W. Alternative Jet Fuel Feasibility. *Transp. Policy* **2014**, *34*, 52–62.
- (38) Kallio, P.; Pásztor, A.; Akhtar, M. K.; Jones, P. R. Renewable Jet Fuel. *Curr. Opin. Biotechnol.* **2014**, *26*, 50–55.
- (39) Markard, J. The Next Phase of the Energy Transition and its Implications for Research and Policy. *Nat. Energy* **2018**, *3*, 628–633.
- (40) Kammermann, J.; Bolvashenkov, I.; Tran, K.; Herzog, H. -G.; Frenkel, I. In *Feasibility Study for a Full-Electric Aircraft Considering Weight, Volume, and Reliability Requirements*, International Conference on Electrotechnical Complexes and Systems (ICOECS), 2020; pp 1–6.
- (41) Hu, X.; Gholizadeh, M. Progress of the Applications of Bio-Oil. *Renewable Sustainable Energy Rev.* **2020**, *134*, No. 110124.
- (42) Leofanti, G.; Padovan, M.; Tozzola, G.; Venturelly, B. Surface Area and Pore Texture of Catalysts. *Catal. Today* **1998**, *41*, 207–219.
- (43) Dexpert, H.; Lagarde, P.; Bournonville, J. P. EXAFS Studies of Bimetallic Pt-Re/Al₂O₃ Catalysts. *J. Mol. Catal.* **1984**, *25*, 347–355.
- (44) Yentekakis, I. V.; Goula, G.; Panagiotopoulou, P.; Kampouri, S.; Taylor, M. J.; Kyriakou, G.; Lambert, R. M. Stabilization of Catalyst Particles Against Sintering on Oxide Supports with High Oxygen Ion Lability Exemplified by Ir- Catalyzed Decomposition of N₂O. *Appl. Catal., B* **2016**, *192*, 357–364.
- (45) Chen, N.-Y.; Liu, M.-C.; Yang, S.-C.; Chang, J.-R. EXAFS Peaks and TPR Characterizing Bimetallic Interactions: Effects of Impregnation Methods on the Structure of Pt-Ru/C Catalysts. *J. Spectrosc.* **2014**, *34*, No. 347078.
- (46) Di, X.; Li, C.; Lafaye, G.; Especel, C.; Epron, F.; Liang, C. Influence of Re–M Interactions in Re–M/C Bimetallic Catalysts Prepared by a Microwave-Assisted Thermolytic Method on Aqueous-Phase Hydrogenation of Succinic Acid. *Catal. Sci. Technol.* **2017**, *7*, 5212–5223.
- (47) Iida, H.; Igarashi, A. Structure Characterization of Pr-Re/TiO₂ (Rutile) and Pt-Re/ZrO₂ Catalysts for Water gas Shift Reaction at Low-temperature. *Appl. Catal., A* **2006**, *303*, 192–198.
- (48) Iida, H.; Igarashi, A. Difference in the Reaction Behaviour Between Pt-Re/TiO₂ (Rutile) and Pt-Re/ZrO₂ Catalysts for Low-Temperature Water Gas Shift Reactions. *Appl. Catal., A* **2006**, *303*, 48–55.
- (49) Simonetti, D.; Kunkes, E.; Dumesic, J. Gas-Phase Conversion of Glycerol to Synthesis Gas over Carbon-Supported Platinum and Platinum–Rhenium Catalysts. *J. Catal.* **2007**, *247*, 298–306.
- (50) Azzam, K. G.; Babich, I. V.; Seshan, K.; Lefferts, L. A Bifunctional Catalyst for the Single-stage Water-gas Shift Reaction in Fuel Cell Applications. Part 2. Roles of the Support and Promoter on Catalyst Activity and Stability. *J. Catal.* **2007**, *251*, 163–171.
- (51) Conner, W. C.; Falconer, J. L. Spillover in Heterogeneous Catalysis. *Chem. Rev.* **1995**, *95*, 759–788.
- (52) Prins, R. Hydrogen Spillover. Facts and Fiction. *Chem. Rev.* **2012**, *112*, 2714–2738.
- (53) Nakagawa, Y.; Tazawa, S.; Wang, T.; Tamura, M.; Hiyoshi, N.; Okumura, K.; Tomishige, K. Mechanistic Study of Hydrogen-Driven Deoxydehydration over Ceria-Supported Rhenium Catalyst Promoted by Au Nanoparticles. *ACS Catal.* **2018**, *8*, 584–595.
- (54) Moulder, J. F.; Stickle, W. F.; Sobol, P. E.; Bomben, K. D. In *Handbook of X-ray Photoelectron Spectroscopy*, Chastain, J., Ed.; Perkin Elmer, 1992.
- (55) Takeda, Y.; Tamura, M.; Nakagawa, Y.; Okumura, K.; Tomishige, K. Characterization of Re-Pd/SiO₂ Catalysts for Hydrogenation of Stearic Acid. *ACS Catal.* **2015**, *5*, 7034–7047.
- (56) Sá, J.; Kartusch, C.; Makosch, M.; Paun, C.; van Bokhoven, J. A.; Kleymenov, E.; Szlachetko, J.; Nachtegaal, M.; Manyar, H. G.; Hardacre, C. Evaluation of Pt and Re Oxidation State in a Pressurized Reactor: Difference in Reduction Between Gas and Liquid Phase. *Chem. Commun.* **2011**, *47*, 6590–6592.
- (57) Tougeri, A.; Cristol, S.; Berrier, E.; Briois, V.; La Fontaine, C.; Villain, F.; Joly, Y. XANES Study of Rhenium Oxide Compounds at the L1 and L3 Absorption Edges. *Phys. Rev. B* **2012**, *85*, No. 125136.
- (58) Xiao, J. L.; Puddephatt, R. J. Pt-Re Clusters and Bimetallic Catalysts. *Coord. Chem. Rev.* **1995**, *143*, 457–500.
- (59) Ebashi, T.; Ishida, Y.; Nakagawa, Y.; Ito, S.; Kubota, T.; Tomishige, K. Preferential CO Oxidation in a H₂-Rich Stream on Pt-ReOx/SiO₂: Catalyst Structure and Reaction Mechanism. *J. Phys. Chem. C* **2010**, *114*, 6518–6526.
- (60) Ma, L.; He, D. H.; Li, Z. P. Promoting Effect of Rhenium on Catalytic Performance of Ru Catalysts in Hydrogenolysis of Glycerol to Propanediol. *Catal. Commun.* **2008**, *9*, 2489–2495.
- (61) Lindfors, C.; Mäki-Arvela, P.; Paturi, P.; Aho, A.; Eränen, K.; Hemming, J.; Peurla, M.; Kubicka, D.; Simakova, I. L.; Murzin, D. Y. Hydrodeoxygenation of Isoeugenol Over Ni- and Co-Supported Catalysts. *ACS Sustainable Chem. Eng.* **2019**, *7*, 14545–14560.
- (62) Teles, C. A.; Rabelo-Neto, R. C.; Duong, N.; Quiroz, J.; Camargo, P. H.; Jacobs, G.; Resasco, D. E.; Noronha, F. B. Role of the Metal-Support Interface in the Hydrodeoxygenation Reaction of Phenol. *Appl. Catal., B* **2020**, *277*, No. 119238.
- (63) Bomont, L.; Alda-Onggar, M.; Fedorov, V.; Aho, A.; Peltonen, J.; Eränen, K.; Peurla, M.; Kumar, N.; Wärnå, J.; Russo, V.; Mäki-Arvela, P.; Grénman, H.; Lindblad, M.; Murzin, D. Y. Production of Cycloalkanes in Hydrodeoxygenation of Isoeugenol over Pt- and Ir-Modified Bifunctional Catalysts. *Eur. J. Inorg. Chem.* **2018**, *2018*, 2841–2854.
- (64) Funkenbusch, L. T.; Mullins, M. E.; Salam, M. A.; Creaser, D.; Olsson, L. Catalytic Hydrotreatment of Pyrolysis Oil Phenolic Compounds over Pt/Al₂O₃ and Pd/C. *Fuel* **2019**, *243*, 441–448.
- (65) Joshi, N.; Lawal, A. Hydrodeoxygenation of 4-Propylguaicol (2-Methoxy-4-propylphenol) in a Microreactor: Performance and Kinetic Studies. *Ind. Eng. Chem. Res.* **2013**, *52*, 4049–4058.

M. E. Martínez-Klimov, P. Mäki-Arvela, Z. Vajglová, C. Schmidt, O. Yevdokimova, M. Peurla, N. Kumar, K. Eränen, D. Y. Murzin, D. Y. Bifunctional Pt catalysts supported on a zeolite-binder matrix for the hydrodeoxygenation of isoeugenol for renewable jet fuel production *Topics in Catalysis*, 66 (2023) 1296 – 1309.





Bifunctional Pt Catalysts Supported on a Zeolite-Binder Matrix for the Hydrodeoxygenation of Isoeugenol for Renewable Jet Fuel Production

Mark E. Martínez-Klimov¹ · Päivi Mäki-Arvela¹ · Zuzana Vajglová¹ · Christoph Schmidt¹ · Olha Yevdokimova¹ · Markus Peurla² · Narendra Kumar¹ · Kari Eränen¹ · Dmitry Yu. Murzin¹

Accepted: 6 June 2023 / Published online: 21 June 2023
© The Author(s) 2023

Abstract

Hydrodeoxygenation (HDO) of isoeugenol was carried out at 200 °C and 30 bar of H₂ in a batch reactor using a series of bifunctional catalysts consisting of platinum supported on zeolite H-Beta-25 or H-Beta-300 and Bindzil as a binder. The purpose of the matrix was to understand the effect of the binder on the reaction, emulating the components of industrial catalysts and therefore facilitating catalyst scale-up. The effect of the supports acid strength, the location of metal nanoparticles, and their proximity to acid sites was also studied. The catalysts were characterized by N₂ physisorption, inductively coupled plasma atomic emission spectrometry, Fourier transform infrared spectroscopy of adsorbed pyridine and scanning and transmission electron microscopy. It was found that platinum supported only on the zeolite was more active compared to platinum located on the binder. High levels of isoeugenol conversion (ca. 100%), propylcyclohexane yield (56%) and the liquid-phase mass balance (68%) were obtained for the catalyst consisting of Pt supported on both zeolite H-Beta-25 and Bindzil.

Keywords Hydrodeoxygenation · Bifunctional catalyst · Platinum · Zeolite · Bindzil · Binder · Isoeugenol

1 Introduction

An interest in developing alternative and renewable fuels has increased recently in a quest to reduce contaminant emissions and dependence on fossil fuels, as well as to meet climate regulations [1]. Currently, one of the main challenges for the energy transition of the aviation industry is that the fuels used in commercial planes cannot be replaced by batteries, mainly due to their low energy to weight ratio [2]. A viable alternative would be to obtain hydrocarbons from renewable sources, thus lowering their environmental impact [3, 4].

Among many renewable energy sources, lignocellulosic biomass is considered as an attractive source for biofuels, materials, and chemicals, due to its abundance and availability. Consisting of cellulose, hemicellulose, and lignin, it can be converted through thermochemical or chemical processes into highly desired compounds. While cellulose, hemicellulose and extractives are employed extensively within the pulp and papermaking industry and to produce fine chemicals [5, 6] respectively, lignin is yet to make a commercial breakthrough.

Recent research has focused on the valorization of lignin, a complex biopolymer rich in aromatics and oxygenated moieties. Pyrolysis of lignin results in a mixture of smaller oxygenated compounds commonly called lignin-derived bio-oil, which displays low heating value, high viscosity and corrosiveness caused by its oxygen content, thereby limiting its use as a fuel [7].

These oxygen moieties need to be removed to obtain hydrocarbons that can be utilized in modern combustion engines, which can be done through hydrodeoxygenation (HDO). Two types of active sites are required to carry out HDO: metal (to activate hydrogen) and acid sites or oxygen

✉ Mark E. Martínez-Klimov
mklimov@abo.fi

✉ Dmitry Yu. Murzin
dmurzin@abo.fi

¹ Johan Gadolin Process Chemistry Centre, Åbo Akademi University, Henriksgatan 2, 20500 Turku/Åbo, Finland

² Institute of Biomedicine, University of Turku, Kiinamylynkatu 10, 20520 Turku/Åbo, Finland

vacancies (to activate the oxygen moieties in biomass-derived compounds) [8].

HDO of model phenolic compounds is commonly studied instead of bio-oil per se due to the complexity of the latter. Among the most commonly used molecules are phenol [9], guaiacol [10, 11] anisole [27] and vanillin [12]. Isoeugenol is of particular interest as it resembles the phenylpropane units constituting lignin and the molecules obtained from its pyrolysis; its HDO product being propylcyclohexane [13], which is within the hydrocarbon range utilized in jet fuel.

Renewable jet fuel must exhibit similar properties as conventional jet fuel in order to be used within existing infrastructure. In general, fossil-derived jet fuel consists of hydrocarbons in the range of C_8 – C_{16} , with alkanes, alkenes, cycloalkanes, and aromatics being the main components [14, 15].

Recent development of HDO catalysts has shifted towards transition metals such as: Ni, Mo and Co [16, 17]. However, also noble metals such as Pt, Ru and Pd, deposited on a variety of supports including zeolites, metal oxides [18–20], different types of carbon [21–25], and nanostructured materials [26–28], have been investigated.

Zeolites are structured aluminosilicates of considerable interest, as they are one of the most extensively used supports and catalysts, mainly due to their inherent acidity (essential for HDO), large surface area and porosity [29]. Often used in petroleum refining and petrochemical industry (e.g., isomerization, alkylation, and cracking reactions [30]), they can be found either as naturally occurring minerals or synthesized ones, allowing to tune their acidity by varying their Si:Al ratio [31] depending on the desired use or target reaction. Research on the scaling-up of zeolite-based catalysts has recently become an attractive topic not only in industry, but also in academia [34, 36]. Catalysts used in industry need to be shaped to reduce pressure drops and resist the conditions used in continuous systems [32], which requires fundamental understanding of shaping processes such as extrusion, for example. Commercial catalyst extrudates are composed of a mixture of materials (a matrix), containing not only a metal and a support, but also a binder (10–35 wt%), as well as a number of other components [33]. Binders, usually alumino-silicate clays, are added to aid with the catalysts shaping and to provide mechanical strength. However, their effect on catalytic activity or other physical properties has been scarcely studied in academic research.

The importance of active site proximity for bifunctional catalysts containing a binder has been studied in several works in the literature, namely for hydroconversion reactions. It was found that close proximity between Pt and Beta zeolite resulted in higher conversion and C_6 selectivity for the hydroisomerization of n-hexane when using Pt supported on H-Beta-25 and Bentonite extrudates [34]. In contrast, close proximity between Pt and acid sites was detrimental

for selectivity in the hydroisomerization of n-heptane when using catalysts comprised of zeolite ZSM-22 and mordenite and γ -alumina binder, as it resulted in undesired cracking reactions [35]. These results highlight the necessity of studying the effects of the intimacy between the sites for particular systems.

Our previous studies on the HDO of lignin-derived model compounds have focused on metal-support systems without considering the addition of a binder [44]. In a recent work [44], bifunctional Pt- and Ir-modified Beta zeolites and mesoporous materials (SiO_2 , Al_2O_3 and MCM-41) were tested for the deoxygenation of isoeugenol in a batch reactor at 200 °C, 30 bar of total pressure and 4 h of the reaction time. While studying the effect of the support on the reaction, it was found that complete conversion of isoeugenol and up to 89% selectivity was achieved using Pt/H-Beta-300 in 240 min. The other supports tested displayed conversions of < 10%, highlighting the importance of support acidity. An additional benefit of the zeolite-supported catalysts over other supports, such as activated carbon, is that it can be regenerated through calcination, while retaining similar catalytic activity.

In the present work, hydrodeoxygenation of isoeugenol over a bifunctional matrix consisting of Pt supported on zeolite Beta and Bindzil as a binder was studied. The former (zeolite Beta) was chosen due to its commercial availability and relatively big pore size, while the latter (Bindzil), a type of colloidal silica without impurities, allows easy shaping of the zeolite-based catalysts [36].

Several catalyst parameters were modified to better understand their effect on the reaction. First, a binder (Bindzil) was used in the matrix to observe its effect on the reaction. Two types of zeolites (H-Beta-25 and H-Beta-300) were used to determine the effect of acidity. Similarly, the location of Pt was also varied to determine the importance of the proximity between the active sites. Pt was alternatively loaded on Bindzil or on zeolite or on both. The results show that Pt location and the selection of catalyst preparation method have a large impact on the catalyst performance.

2 Experimental

2.1 Reagents

Zeolites NH_4 -Beta-25 and H-Beta-300 were obtained from Zeolyst International ($SiO_2/Al_2O_3 = 25$ and $SiO_2/Al_2O_3 = 300$, respectively) while Binder Bindzil-50/80 (50% colloidal SiO_2 in H_2O) was obtained from AzkoNobel. Zeolite NH_4 -Beta-25 was transformed into the proton form by calcination at 400 °C [37]. The platinum precursor, $[Pt(NH_3)_4](NO_3)_2$, ($\geq 50.0\%$ Pt basis) was acquired from Sigma-Aldrich. For the reactions, n-dodecane (Acros

Organics, 99%) and isoeugenol (Sigma Aldrich, 98%, mixture of *cis* and *trans*) were used.

2.2 Catalyst Synthesis

The location of the metal deposition was varied for both series of catalysts in order to modify the proximity between the metal and acid sites. Platinum was deposited by the evaporation-impregnation method. The nominal metal loading for all catalysts was 2 wt%. All catalysts have the same ratio of the zeolite-to-Bindzil of 70:30. The catalysts were denoted as either PtB300ZX or PtB25ZX, depending on the zeolite used as a support. Z was used to denote the presence of Bindzil while X corresponds to the location of the metal; A was used for Pt supported on both zeolite and the binder, B for Pt supported only on the zeolite, and C for Pt supported only on the binder. The preparation method has been thoroughly described in previous publications [37, 38]. The following is a brief summary:

Type A—Pt located on both: A mixture of 70% zeolite and 30% Bindzil in water (80% water to 20% mixture) was stirred for 24 h, followed by evaporation of water and calcination at 500 °C. After deposition of platinum from $[\text{Pt}(\text{NH}_3)_4](\text{NO}_3)_2$, the catalyst was reduced under hydrogen flow (40 mL/min) at 350 °C for 3 h with a heating rate of 2 °C/min.

Type B—Pt located on zeolite: First, platinum was deposited on the zeolite by evaporation-impregnation from $[\text{Pt}(\text{NH}_3)_4](\text{NO}_3)_2$ followed by reduction under hydrogen flow (40 mL/min) at 350 °C for 3 h with a heating ramp of 2 °C/min. Pt/zeolite was mixed afterwards with Bindzil in water for 24 h. After water was evaporated, the catalyst was calcined at 500 °C.

Type C—Pt located on binder: Bindzil was dried and sieved to a size of 45–63 µm prior to deposition of Pt. After deposition of platinum, Pt/Bindzil was reduced under hydrogen flow (40 mL/min) at 350 °C for 3 h with a heating ramp of 2 °C/min. Thereafter, it was mixed in water with the corresponding amount of the zeolite, followed by calcination of the catalyst at 500 °C.

All catalysts were sieved to a particle size of 45–63 µm to avoid internal mass transfer limitations.

A summary of the catalysts used in the current work is presented in Table 1.

2.3 Catalytic Tests

The catalysts were reduced *ex-situ* under continuous hydrogen flow (40 mL/min, 350 °C for 180 min, 10 °C/min) in a glass reactor. The system was flushed with argon (50 mL/min, 10 min) prior and after the reduction procedure to remove air and hydrogen, respectively. Dodecane, the solvent used in the reaction, was added to avoid reoxidation of the catalyst.

HDO reactions were performed in a stainless-steel batch reactor (PARR, 300 mL) equipped with a heating jacket and mechanical stirring, as well as a sampling, gas inlet and outlet valves. The following quantities were used for the reaction: 0.1 g of isoeugenol, 0.05 g of the catalyst, and 50 mL of dodecane.

After the reactant, the catalyst and the solvent were loaded into the reactor, it was purged with 7 bar of argon first (AGA, 99.999%) for 10 min and afterwards with 10 bar of hydrogen (AGA, 99.999%) for 10 min. The reactor was pressurized to an initial pressure of 20 bar with hydrogen. The reactor was heated to 200 °C with a heating ramp of 10 °C/min without stirring. When the reaction temperature was reached, hydrogen was added to reach 30 bar of total pressure and stirring was started with a speed of 900 rpm to avoid external mass transfer limitations. Reaction conditions we chosen based on our previous work [44].

The time zero was set when the reaction temperature and stirring speed were reached. Samples taken at regular time intervals were analyzed by GC (Agilent Technologies 6890N, 7683 Series Injector) and GC/MS (Agilent Technologies 6890, 7683 Series Injector) both equipped with a DB-1 capillary column (Agilent 122-103e, 30 m length, 250 µm internal diameter and 0.5 µm film thickness) using the following temperature program: 60 °C (5 min), 3 °C/min to 135 °C, and 15 °C/min to 300 °C. Helium was employed as a carrier gas (flow rate of 1.7 mL/min).

Table 1 Denomination and characteristics of the catalysts used for HDO of isoeugenol

Catalyst denomination	Metal deposition location	Zeolite	Binder	Metal	Nominal Pt loading (wt%)
PtB25ZA	On both	H-Beta 25	Bindzil	Platinum	2
PtB25ZB	On zeolite	H-Beta 25	Bindzil	Platinum	2
PtB25ZC	On binder	H-Beta 25	Bindzil	Platinum	2
PtB300ZA	On both	H-Beta 300	Bindzil	Platinum	2
PtB300ZB	On zeolite	H-Beta 300	Bindzil	Platinum	2
PtB300ZC	On binder	H-Beta 300	Bindzil	Platinum	2

Conversion of dihydroeugenol (X) was calculated using Eq. (1), where C_0 is the initial concentration of dihydroeugenol and C_{DH} is the concentration of dihydroeugenol at a given time:

$$X = \frac{C_0 - C_{DH}}{C_0} * 100 \quad (1)$$

The yield of propylcyclohexane (Y_{PCH}) was determined using the concentration of propylcyclohexane at a certain time (C_{PCH}) and the initial concentration of dihydroeugenol (C_0) as shown below:

$$Y_{PCH} = \frac{C_{PCH}}{C_0} * 100 \quad (2)$$

Selectivity towards propylcyclohexane (S_{PCH}) was calculated using Eq. (3), where C_{PCH} is the concentration of propylcyclohexane at a certain time and Σ_{prod} is the sum of concentrations of all products at the corresponding time:

$$S_{PCH} = \frac{C_{PCH}}{\Sigma_{prod.}} * 100 \quad (3)$$

Gas chromatography liquid phase analysis (GCLPA) was used to determine the mass balance of products remaining in the liquid phase:

$$GCLPA = \frac{\Sigma_{all}}{C_0} * 100 \quad (4)$$

In Eq. (4) Σ_{all} is the sum of the concentrations of reactants and products at a specific time while C_0 is the initial concentration of dihydroeugenol.

Rate constants were determined using numerical data fitting of the dihydroeugenol concentrations throughout all the reaction duration, employing Eq. (5) for a zero-order reaction implemented in Origin 2019 software:

$$C_{DH} - C_0 = -k_0 t \quad (5)$$

The zero-order reaction kinetics was used as it most adequately described the experimental data. In Eq. (5) C_{DH} is the concentration of dihydroeugenol at a given time, C_0 is the initial concentration of dihydroeugenol, k_0 is the zero-order rate constant and t is time.

2.4 Materials Characterization

Determination of the catalyst metal loadings was performed by inductively coupled plasma atomic emission spectrometry (ICP-AES, Goffin Meyvis Spectro Ciruscdd).

Textural characteristics of the catalysts were determined by nitrogen physisorption (Micromeritics 3Flex-3500). For all catalysts containing zeolites, the Dubinin–Radushkevich method was used to determine the specific surface area while

the density functional theory (NL-DFT) method was used to determine pore size distributions. For pure Bindzil the surface area and pore volumes were determined, respectively, using the BET and the BJH method for the desorption branch. The samples underwent a two-stage pretreatment. *Ex-situ* outgassing was done in a Micromeritics VacPrep 061 Sample Degas System under vacuum at 200 °C for 20–24 h, followed by in-situ degassing for 5 h at 250 °C.

Metal particle sizes of the reduced catalysts were measured by transmission electron microscopy (JEM-1400Plus, JEOL, Japan). The samples were suspended in ethanol and mounted on a copper grid prior to the analysis. Determination of the average metal particle size was performed by measuring the diameter of over 200 particles using the ImageJ software. On average 8–10 images per sample have been evaluated.

Scanning electron microscopy (Zeiss Leo Gemini 1530) was utilized to observe the morphological differences between the supports.

Quantification of the Brønsted and Lewis acid sites of the catalysts was done by Fourier transform infrared spectroscopy of adsorbed pyridine (ATI Mattson FTIR Infinity Series) using molar extinction coefficients reported in the literature [39]. Desorption of pyridine at 250, 350, and 450 °C was done to determine the weak, medium, and strong acid sites, respectively; measurements were taken at 100 °C.

3 Results and Discussion

3.1 Catalyst Characterization

Morphological differences among the zeolites, Bindzil and the mixture of the zeolite and Bindzil can be observed using scanning electron microscopy (Fig. 1). H-Beta-25 particles are much smaller (ca. 20–250 nm, Fig. 1a) than those from H-Beta-300 (ca. 300–1000 nm, Fig. 1b). On the other hand, Bindzil displays mostly spherical particles (ca. 50–200 nm, Fig. 1c). For zeolite and Bindzil mixtures (Fig. 1d,e), it can be observed that the zeolitic particles are surrounded by the spherical Bindzil particles.

A summary of the metal loadings, metal particle sizes and textural properties of the catalysts and pure supports is presented in Table 2.

The catalyst metal loadings obtained by ICP were close to the nominal value of 2 wt%.

Transmission electron microscopy images (Fig. 2) were used to determine the metal particle sizes; a summary is presented in Table 2. All catalysts exhibited an average metal particle size in the range of 4–5 nm, indicating that the metal dispersion was 20–25%. Particle size histograms can be consulted in the supporting information, Fig. S1. Dispersion was calculated based on [40] using the formula

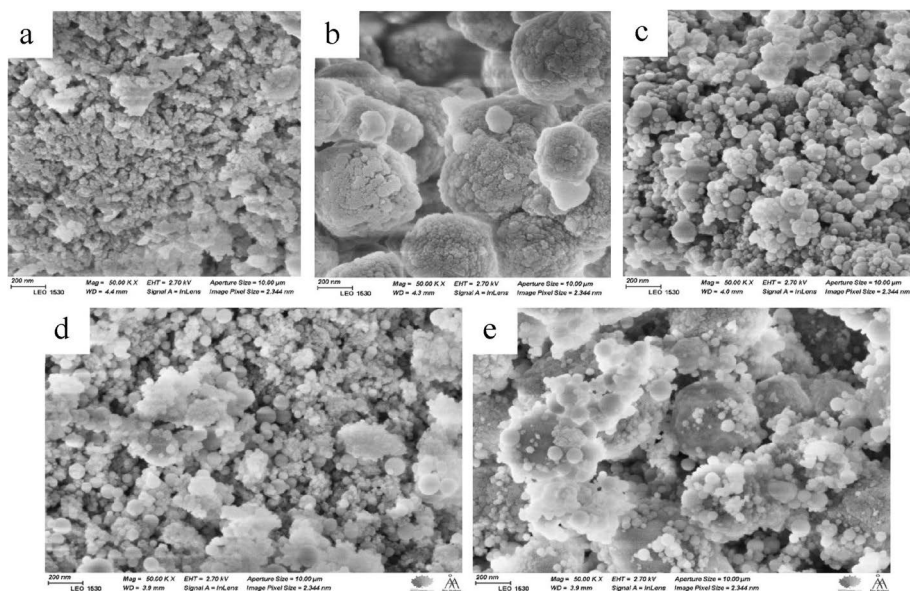


Fig. 1 SEM images of **a** H-Beta-25, **b** H-Beta-300, **c** Bindzil, **d** H-Beta-25 + Bindzil and **e** H-Beta-300 + Bindzil

Table 2 Metal loadings, metal particle sizes and textural properties of supports and catalysts

Catalyst	Pt loading (wt%)	Metal particle size (nm)	Textural characteristics		
			SSA (m ² /g)	V _Σ (cm ³ /g)	V _{MP} (cm ³ /g)
H-Beta-25	–	–	638	0.36	0.31
H-Beta-300	–	–	617	0.29	0.19
Bindzil	–	–	154	0.30	–
PtB25ZA	1.9	4.2	490	0.31	0.13
PtB25ZB	1.8	4.3	466	0.29	0.11
PtB25ZC	1.9	4.7	493	0.32	0.14
PtB300ZA	1.7	4.4	459	0.23	0.15
PtB300ZB	1.8	4.2	443	0.22	0.14
PtB300ZC	1.8	4.6	467	0.26	0.15
PtB300ZA (spent)	n.d	4.7	432	0.20	0.12
PtB300ZB (spent)	n.d	4.8	421	0.18	0.11
PtB300ZC (spent)	n.d	5.3	425	0.21	0.13

n.d. not determined

$d_{p1} = 108/D(\%)$. Dispersion values were similar between samples given their similar metal particle sizes. The presence of bigger particles (up to 50 nm) was observed in the case of both PtB300ZC and PtB25ZC, where Pt was deposited on Bindzil. This could be caused by the preparation of these materials; namely deposition of platinum only on a lower amount of the support (29 wt% corresponding to Bindzil) and different point zero charges (pzc) of zeolites and Bindzil. The latter difference implies also

differences between the zeta potential of these materials at the pH of deposition and pzc, resulting in different degree of Pt agglomeration on the zeolite and the binder.

TEM micrographs of spent PtB300ZX catalysts are shown in Fig. 3 and the corresponding average metal particle sizes are presented in Table 2. A slight increase in metal particle size was observed for spent catalysts, indicating that agglomeration occurred during the catalytic reactions.

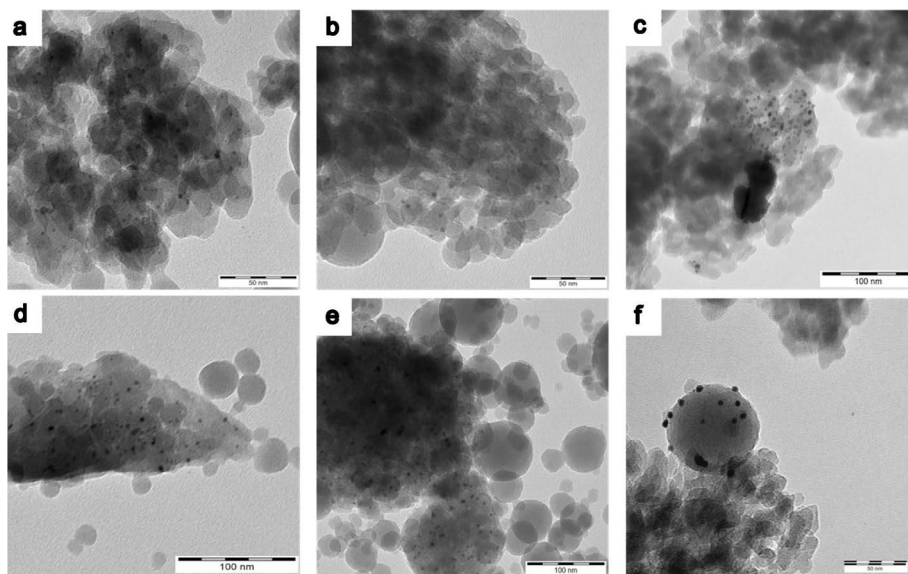


Fig. 2 TEM images of fresh **a** PtB25ZA, **b** PtB25ZB, **c** PtB25ZC and **d** PtB300ZA, **e** PtB300ZB, **f** PtB300ZC catalysts

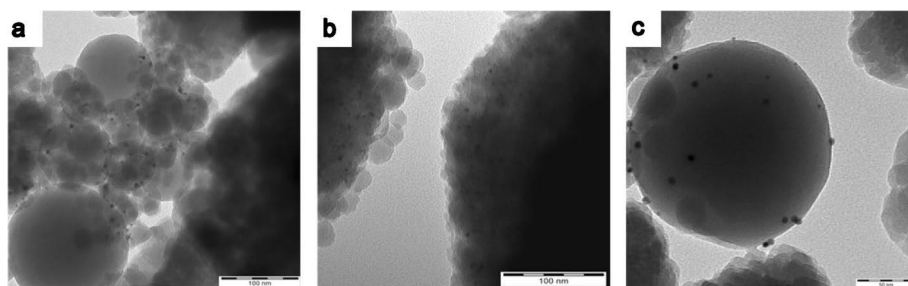


Fig. 3 TEM micrographs of spent **a** PtB300ZA, **b** PtB300ZB and **c** PtB300ZC

According to the nitrogen physisorption measurements, the catalysts exhibited high specific surface (SSA) areas (ca. 450 m²/g), as well as total pore volume (V_{Σ}) of 0.2–0.3 cm³/g and a pore diameter of 0.6 nm.

A decrease in the surface area and the micropore volume (V_{MP}) can be observed when comparing the catalysts to the corresponding pure zeolitic supports, which could be explained by the presence of Bindzil with a lower surface area (154 m²/g), in addition to the blockage of the micropores during metal deposition. Among the catalysts, those supported on H-Beta-25 displayed higher SSA and higher total pore volume (V_{Σ}) than those supported on H-Beta-300. The pore diameter for all zeolitic-based catalysts was ca. 0.6 nm,

indicating microporosity. On the other hand, neat Bindzil displayed a pore size of 12 nm due to its mesoporosity.

The textural properties of the spent H-Beta-300 catalysts were also measured after being washed with 100 mL of acetone. The same degassing procedure as for the fresh catalysts was followed. A slight decrease in the textural properties can be observed when comparing with the corresponding fresh catalysts; this could be caused by coke formation during the reaction.

Adsorption–desorption isotherms and the pore size distributions are presented in Fig. 4.

Figure 4a illustrates the difference in isotherm profiles between zeolites and the colloidal silica (Bindzil).

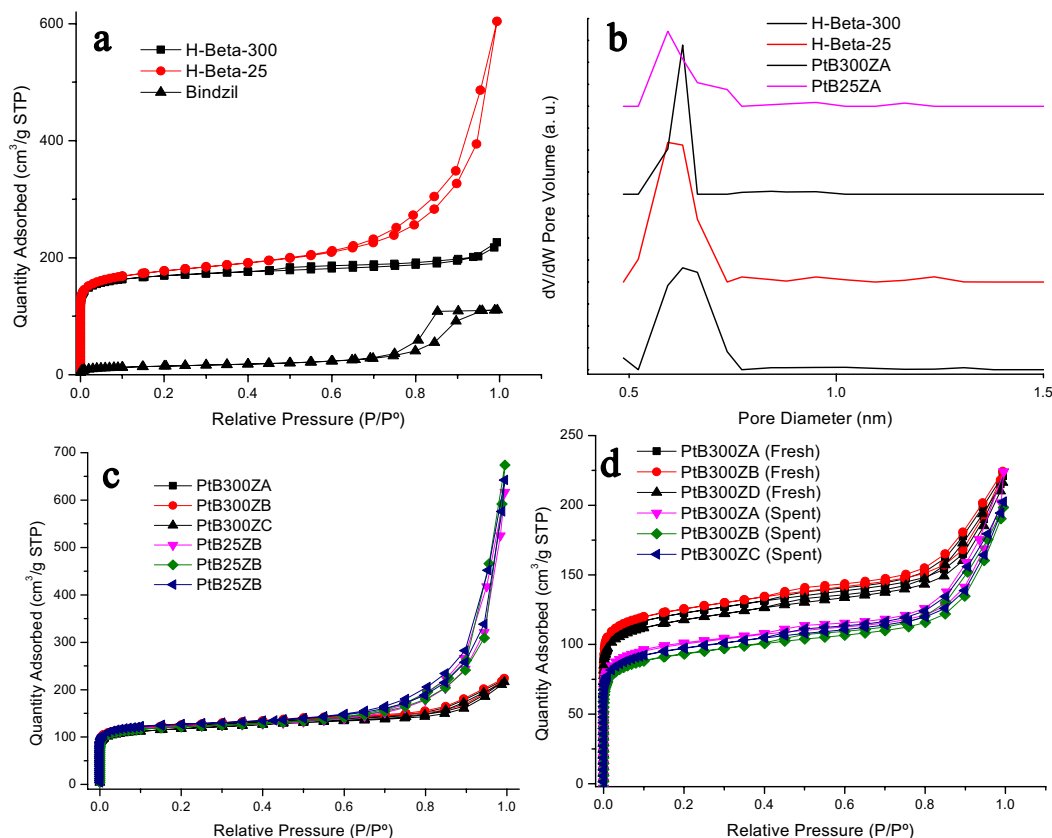


Fig. 4 **a** Adsorption–desorption isotherms of zeolites H-Beta-300, H-Beta-25 and Bindzil, **b** pore size distribution of zeolites H-Beta-25, H-Beta-300, and catalysts PtB300ZA and PtB25ZA, **c** adsorp-

tion–desorption isotherm comparison of both series of catalysts and **d** adsorption–desorption isotherm comparison of fresh and spent PtB300ZX catalysts

Both zeolites display type I isotherms, characteristic of microporous materials [41]. Zeolite H-Beta-25 exhibits an H3 hysteresis type, while Bindzil displays a type IV isotherm and hysteresis H2, due to mesoporosity. The main pore contribution obtained by NL-DFT (Fig. 4b) was ca. 0.6 nm for pure zeolites and all catalysts. The catalysts maintained similar adsorption–desorption isotherms to their corresponding zeolite support (Fig. 4c) and no changes in microporosity were observed after addition of the binder.

A noticeable difference in the adsorption isotherms could be observed in Fig. 4d between fresh and spent PtB300ZX catalysts, which also resulted in decreased textural properties of spent catalysts (Table 2). This could be due to the formation of carbon deposits during the reaction.

Pyridine FTIR was used to measure the acid site amount and strength of the catalysts and pure supports, results are presented in Table 3.

As expected, pure H-Beta-25 displayed the highest acidity, over 4 times higher than H-Beta-300. On the other hand, Bindzil contained the lowest amount of acid sites. Addition of Bindzil to the catalyst mixture resulted in a decrease in overall acidity, as expected, being also in line with changes in the textural properties obtained from nitrogen physisorption. The catalysts containing H-Beta-25 were more acidic than those with H-Beta-300. A trend was observed for both series of catalysts. The most acidic catalyst was type C, where Pt was located on the binder, indicating that deposition of the metal affected zeolite acidity, as previously reported in the literature [42]. The catalyst with the highest amount of acid sites was PtB25ZC. All catalysts from

Table 3 Support and catalyst acidity determined by Pyridine FTIR

Catalyst	Brønsted acid sites (μmol/g)*			Lewis acid sites (μmol/g)*			Total acid sites (μmol/g)		
	W	M	S	W	M	S	BAS	LAS	Total
H-Beta-25	67	33	129	26	5	6	229	37	266
H-Beta-300	7	29	19	4	1	1	55	6	61
Bindzil	12	0	0	3	0	0	12	3	15
PtB25ZA	44	10	4	12	4	2	58	18	76
PtB25ZB	51	4	8	7	2	4	63	13	76
PtB25ZC	61	4	28	8	1	11	93	20	113
PtB300ZA	9	2	0	5	3	0	11	8	19
PtB300ZB	6	2	0	6	0	0	8	6	14
PtB300ZC	10	8	0	13	2	0	18	15	33

*Desorption of pyridine at 250, 350, and 450 °C was done to determine the weak, medium, and strong acid sites, respectively; measurements were taken at 100 °C

the PtB300ZX series based on beta-300 with a high ratio of silica to alumina lacked strong acid sites.

3.2 Hydrodeoxygenation of Isoeugenol

Hydrodeoxygenation (HDO) of isoeugenol (IE) was performed in a batch reactor at 200 °C.

The transformation of isoeugenol into dihydroeugenol (DH) occurred almost instantaneously, reaching 100% conversion within 1 min of reaction time. Subsequently, conversion of dihydroeugenol was followed [43]. The steps comprising the reaction network (Scheme 1) that follow are hydrogenation of the aromatic ring, dehydration, and demethoxylation, resulting in formation of the propylcyclohexane (PCH) desired product. A comparison of the catalytic results for HDO of isoeugenol using Pt/zeolite without the binder and both series of catalysts with the binder, under the same conditions, is presented in Table 4. The corresponding graphs for the catalytic activity; dihydroeugenol (DH) conversion, propylcyclohexane (PCH) yield and gas chromatography liquid phase analysis (GCLPA) for both series of catalysts are displayed in Fig. 5.

Catalysts Pt/H-Beta-25 and Pt/H-Beta-300 without a binder (Pt/B25 and Pt/B300, respectively) were included in entries 1 and 2 as a comparison. These values were obtained from a previous publication [44]. Entries 3–5 correspond to the catalysts containing zeolite H-Beta-25, while entries 6–8 correspond to those containing H-Beta-300.

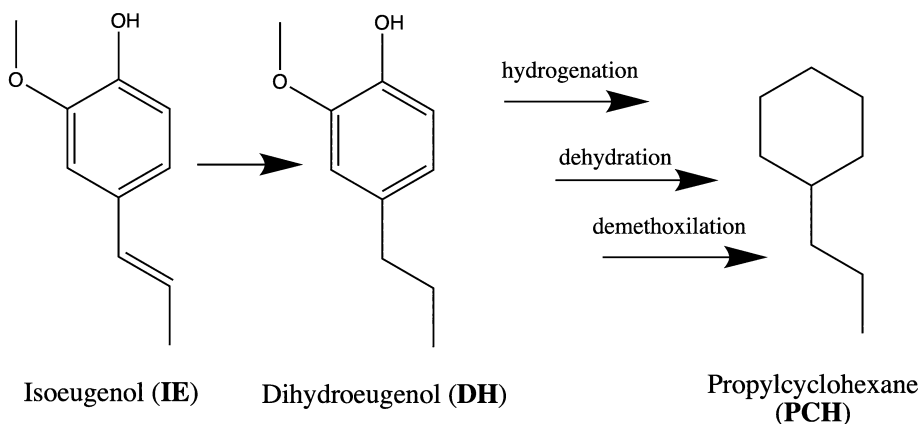
Overall, activity was higher for catalysts without a binder (entries 1 and 2). For the binder-containing catalysts, the rate constant (k) values were the highest for catalysts PtB25ZB and PtB300ZA in their corresponding series ($3.8 \cdot 10^{-2}$ and $1.6 \cdot 10^{-2} \text{ M h}^{-1} \text{ g}_{\text{cat}}^{-1}$, entries 4 and 6, respectively). Although these values are in the same order of magnitude as those obtained for Pt/B25 and Pt/B300 [44], they are 2–4 times lower, indicating that when using catalysts

containing a binder, activity is lower than when using only Pt on zeolite. Such differences in catalytic activity could be attributed to addition of the binder, which resulted in considerable changes in acidity and the surface area. This is especially noticeable when comparing acidity of Pt/B300 (TAS = 52 μmol/g, [44]) and Pt/B25 (TAS = 406 μmol/g, [44]) and the series of catalysts containing Bindzil. Acidity for Pt/B300 is more similar to acidity of PtB25ZX series (TAS = 76–113 μmol/g) than of PtB300ZX series in the current work. Additionally, the zeolite fraction for the binder-containing catalysts is lower due to the addition of Bindzil, which is not the case for Pt/B300 and Pt/B25 used in [44].

Activity of the different catalysts towards DH transformation varies very much, as can be seen in Fig. 5a and Table 4. Dihydroeugenol (DH) conversion was higher for catalysts without a binder (entries 1 and 2), reaching 100% for both at 4 h of the reaction time, thus highlighting the effect of Bindzil addition on the catalytic activity. For both series of catalysts containing Bindzil, it can be observed that DH conversion is higher for the PtB25ZX series (78–53%) than for PtB300ZX (61–25%). Deactivation could also be observed for PtB300ZC catalyst, as DH conversion did not increase considerably after the initial period, which was not the case for all other catalysts. While the results further indicate that acidity plays a crucial role, its impact is not straightforward.

The most active catalysts for both Bindzil-containing series were those of type A and B (DH conversion of about 80% for PtB25ZA and PtB25ZB, entries 3 and 4; and 61% for PtB300ZA, entry 6).

In contrast, catalysts of the type C displayed the lowest conversions, almost half of that of type B (DH conversion of 53% for PtB25ZC, entry 5; and 25% for PtB300ZC, entry 8). This indicates that proximity between the acid sites and the metal particles is beneficial for the reaction giving improved activity. In these catalysts, Pt is located on the non-acidic Bindzil; therefore, further from the acid sites of the zeolites.



Scheme 1 A general reaction network for hydrodeoxygenation of isoeugenol

Additionally, the metal particle sizes for catalysts of type C were larger than for other types, contributing to a decrease in activity. The catalysts of type A displayed a slightly lower DH conversion than the catalysts of type B, which can be explained by a lower amount of Pt located on zeolites, as platinum was deposited on both the zeolite and the binder.

Gas Chromatography Liquid Phase Analysis (GCLPA) is a mass balance approximation for the reactants and products remaining in the liquid phase, as gaseous and heavy products (dimers, trimers, etc....) have not been quantified. As presented in Table 4, GCLPA values decreased with the increase of DH conversion. This is generally due to the

formation of products in the gas phase, such as water or methanol, which were not analyzed. The differences that are observed when comparing the GCLPA of catalysts with similar DH conversion, such as PtB25ZC (DH conversion = 53%, GCLPA = 66 entry 5) and PtB300ZA (DH conversion = 61%, GCLPA = 78%, entry 6) can be caused by formation of the oligomerization products, such as dimers, or by cracking/isomerization of the reactant, both of which were not measured, but have been reported in the literature [44].

The yield of propylcyclohexane (75%) and the reaction rate constant ($8.0 \cdot 10^{-2} \text{ M h}^{-1} \text{ g}_{\text{cat}}^{-1}$) were the highest for Pt/

Table 4 Catalytic activity of PtB300ZX and PtB25ZX series of catalysts in hydrodeoxygenation of isoeugenol, performed in a batch reactor at 200 °C and 30 bar of H₂

Entry	Catalyst	IE conversion (%) ^a	DH conversion (%) ^a	$k \cdot 10^2 (\text{M h}^{-1} \text{ g}_{\text{cat}}^{-1})^b$	GCLPA (%) ^{a,c}	PCH yield (%) ^a	PCH selectivity (%) ^d
1	Pt/B25 ^e	100 ^e	100 ^e	6.4 ^e	45 ^e	55 ^e	93 ^e
2	Pt/B300 ^e	100 ^e	100 ^e	8.0 ^e	61 ^e	75 ^e	96 ^e
3	PtB25ZA	100	78	3.7	68	56	82
4	PtB25ZB	100	82	3.8	62	53	81
5	PtB25ZC	100	53	2.8	66	21	79
6	PtB300ZA	100	61	1.6	78	45	84
7	PtB300ZB	100	46	1.5	85	37	92
8	PtB300ZC	100	25	0.8	83	6	n.d

n.d. not determined

^aValues determined at 4 h of the reaction time

^bValues for the rate constant (k) have been determined using a curve fitting method, considering the time dependent dihydroeugenol concentration

^cGas chromatography liquid phase analysis (GCLPA) is a mass balance approximation for the liquid phase

^dSelectivity estimated at 40% DH conversion

^eValues obtained from Ref. [44]

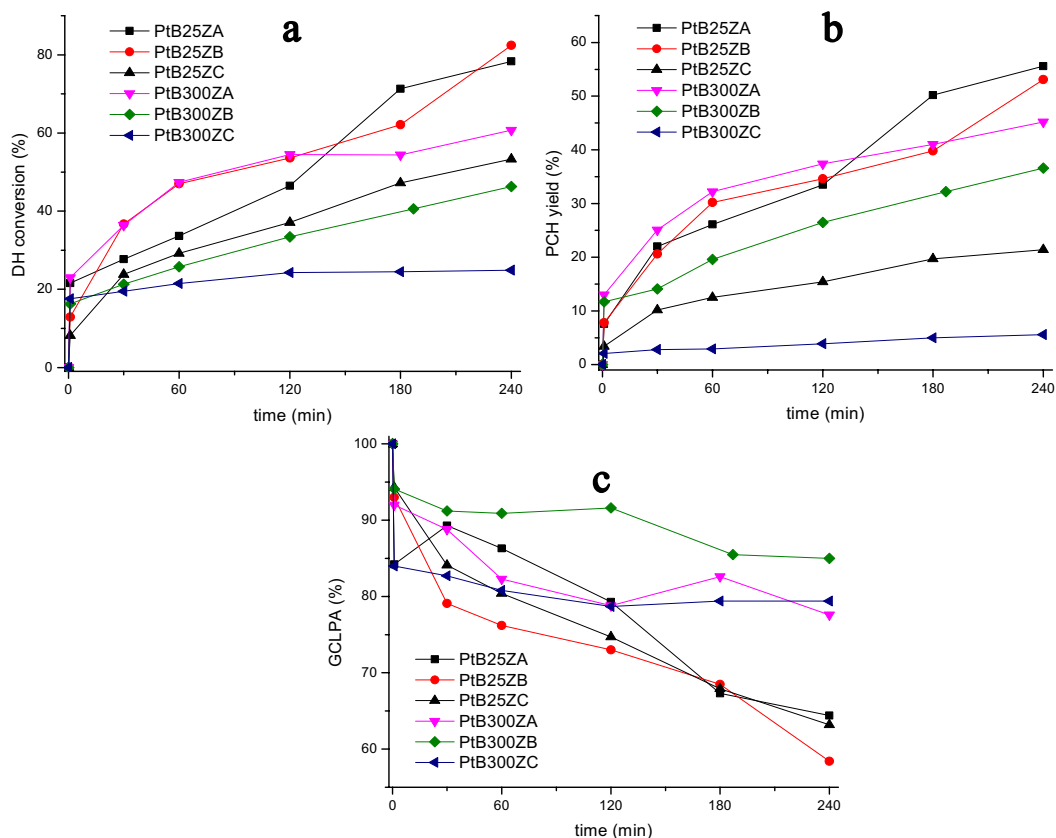


Fig. 5 Transformations of isoeugenol at 200 °C and 30 bar of H₂ **a** dihydroeugenol conversion, **b** propylcyclohexane yield and **c** GCLPA as a function of time

B300. It is important to note that in entries 1 and 2, the secondary products formed were 1-methyl-4-ethylcyclohexane and 1-methyl-2-propyl-cyclohexane, which are isomerization products. Zeolite H-Beta-25 has more total and strong acid sites than H-Beta-300, which could explain its lower selectivity to PCH due to secondary reactions.

On the other hand, the secondary product obtained when using the catalysts containing Bindzil was 2-methoxy-4-propylcyclohexanol, an oxygenated intermediate determined by GC–MS. This indicates that lower amounts of isomerization or cracking products for the Bindzil-containing catalysts could be due to their overall lower acidity. As observed from Pyridine FTIR results (Table 3), addition of the binder decreased the amount of total and strong acid sites. Such sites can lead to secondary reactions and

deactivation of the catalyst, resulting in lower activity and selectivity [44].

While the catalysts containing more acidic zeolite H-Beta-25 display higher activity and yield of propylcyclohexane, the catalysts with H-Beta-300 zeolite exhibited higher selectivity (> 84%). Additionally, the PtB300ZA catalyst afforded a relatively high PCH yield (45%, entry 6), comparable to that of catalysts containing H-Beta-25. These results are in accordance with our previous publication when Pt/B25 displayed lower selectivity towards propylcyclohexane [44].

Interestingly, propylcyclohexane (PCH) yields were higher in both series for catalysts of type A (PCH yield of 56% for PtB25ZA, entry 3; and 45% for PtB300ZA, entry 6), which could also be caused by a higher dispersion of the

metal particles, i.e. their smaller cluster size, as in this type of catalyst, Pt was located on both zeolite and Bindzil.

Selectivity towards PCH was estimated for 40% DH conversion to be able to compare the values for different catalysts. As mentioned previously, higher PCH selectivities were obtained for PtB300ZA and PtB300ZB catalysts (> 84%, entries 6 and 7) which follows the same trend as observed for catalysts without Bindzil (entries 1–2). Furthermore, PCH selectivity for PtB300ZB (92%, entry 7) is comparable to that displayed by Pt/B25 and Pt/B300 (ca. 95%, entries 1–2). In the PtB300ZX series of catalysts, the lowest PCH selectivity was obtained for the catalyst of type A (PCH selectivity of 84%, entry 6).

From Fig. 5 it can be inferred that proximity between Pt particles (metal sites) and acid sites of the zeolites is important for hydrodeoxygenation. Additionally, the PtB25ZX series displayed higher DH conversion and PCH

yield, indicating the effect of higher acidity on the catalytic activity. A clear difference in the GCLPA for both series of catalysts can also be observed in Fig. 5c, pointing out the formation of side products when using more acidic catalysts, as previously discussed. The effect of metal location and acidity on activity can be better observed in Fig. 6.

In Fig. 6a it can be observed that while dihydroeugenol conversion is higher for catalysts supported on H-Beta-25, the yield of propylcyclohexane for PtB300ZA catalyst is similar despite having almost four-fold fewer acid sites, which indicates that such high acidity is not necessary to obtain the same amount of the desired deoxygenation product. This conclusion is further illustrated in Fig. 6b,c. When comparing the rate constants to the total amount of acid sites (Fig. 6b) it can be observed that the PtB25ZX series (higher acidity) displays higher conversion. However, the PtB300ZX series displays similar yields of propylcyclohexane (Fig. 6c).

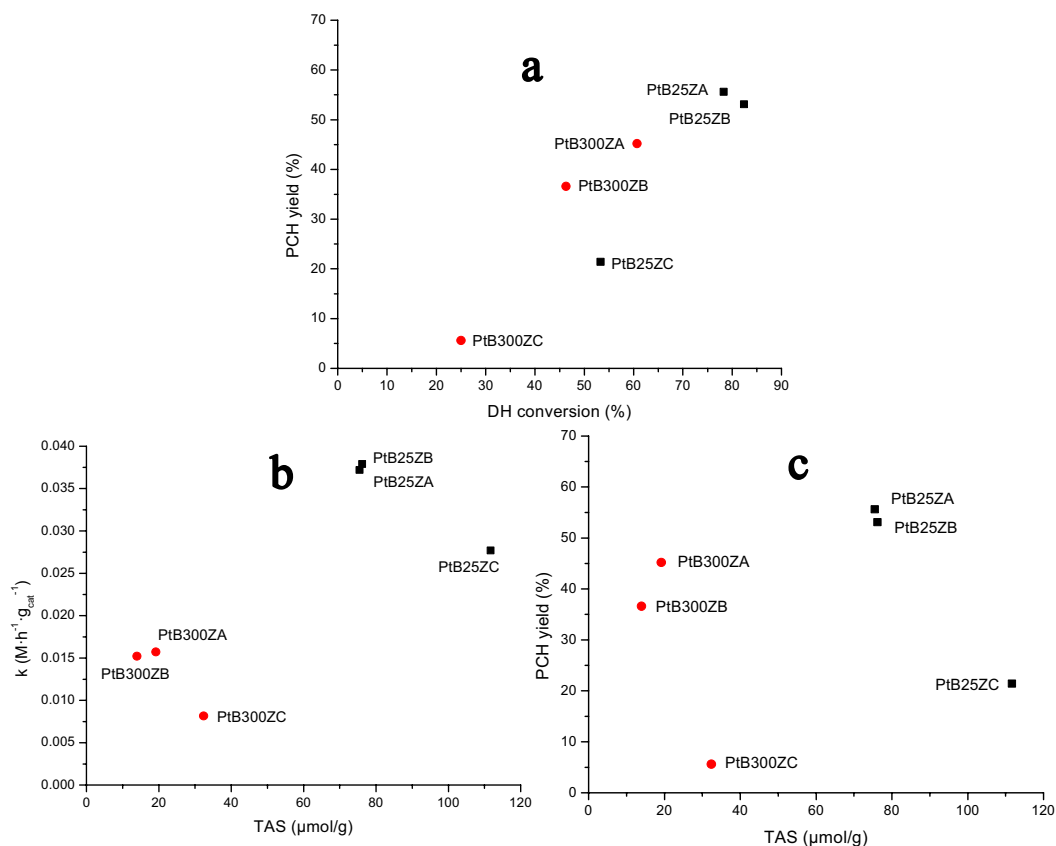


Fig. 6 Transformations of isoeugenol at 200 °C and 30 bar of H₂ **a** propylcyclohexane yield vs. dihydroeugenol conversion, **b** rate constant vs. total acid sites and **c** propylcyclohexane yield vs. total acid sites

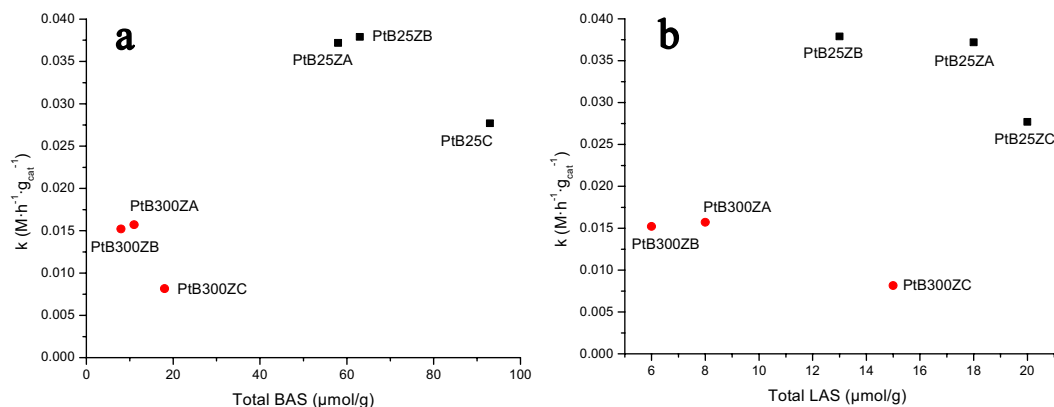


Fig. 7 Transformations of dihydroeugenol at 200 °C and 30 bar of H₂: **a** rate constants vs. total Brønsted acid sites and **b** rate constants vs. total Lewis acid sites

In Fig. 7 the relationship between the rate constants and the total amount of different acid sites (Brønsted and Lewis) is displayed.

Figure 7 seems to indicate that there is an optimum level of acidity for the hydrodeoxygenation of isoeugenol under the conditions and catalysts tested. In this case, the PtB25ZB catalyst displayed intermediate acidity among the tested catalysts and thus higher values for the rate constant.

Dispersion of Pt was similar for all catalysts (20–25%); therefore, we cannot attribute worse behavior of C catalysts to worse dispersion of Pt. In this case, acidity of the zeolites is necessary for HDO to activate the oxygen moieties on acid sites and carry out dehydration and demethoxylation reactions.

Our findings suggest that proximity between two types of active sites is necessary for catalytic performance. It has been documented in the literature [25] that acid sites or oxygen vacancies, provided by the support or oxophilic metals, are required to carry out the deoxygenation (hydrogenolysis of C–O bond) in HDO.

4 Conclusions

A catalytic matrix comprising 2 wt% of platinum supported on 69 wt% of zeolite H-Beta-300 or H-Beta25, and 29 wt% of Bindzil as a binder, displayed high activity for the hydrodeoxygenation of isoeugenol at 200 °C and 30 bar of hydrogen pressure. The effects of the binder addition, acidity of the zeolite and the metal location, were studied. Addition of Bindzil resulted in a decrease of the surface area and the total amount of acid sites when compared to the unmodified zeolite. The location of the

platinum was varied depending on its deposition, whether it was on the zeolite, the binder or both. The deposition of platinum on the zeolite also resulted in a decrease in acidity. These changes reflected considerably the catalytic activity. Overall, the catalysts where Pt was located closer to the acid sites (being deposited on only zeolite or both zeolite and the binder) displayed higher dihydroeugenol conversion and propylcyclohexane yield, while deposition of platinum on the binder gave the lowest activity. Furthermore, while catalysts containing a more acidic zeolite (H-Beta-25) displayed higher activity, catalysts with Pt on the binder and H-Beta-300 displayed a similar propylcyclohexane yield. Results suggest that an optimum acidity is required for complete deoxygenation of isoeugenol. The highest selectivity to propylcyclohexane of 92% with 85% mass balance closure in the liquid phase was achieved for the catalyst when platinum was located only on the H-Beta zeolite with silica to alumina ratio of 300, while the highest conversion of dihydroeugenol of 82% and the yield of propylcyclohexane of 53% was obtained for the catalyst where platinum was located on both zeolite H-Beta with a silica to aluminum ratio 25 and the binder.

Supplementary Information The online version contains supplementary material available at <https://doi.org/10.1007/s11244-023-01836-1>.

Acknowledgements The authors would like to acknowledge the Electron Microscopy Laboratory, Institute of Biomedicine, University of Turku, and Biocenter Finland for access to Transmission Electron Microscopy. This work was supported by the Magnus Ehrnrooth Foundation.

Funding Open access funding provided by Abo Akademi University (ABO).

Data availability Data will be available upon request.

Open Access This article is licensed under a Creative Commons Attribution 4.0 International License, which permits use, sharing, adaptation, distribution and reproduction in any medium or format, as long as you give appropriate credit to the original author(s) and the source, provide a link to the Creative Commons licence, and indicate if changes were made. The images or other third party material in this article are included in the article's Creative Commons licence, unless indicated otherwise in a credit line to the material. If material is not included in the article's Creative Commons licence and your intended use is not permitted by statutory regulation or exceeds the permitted use, you will need to obtain permission directly from the copyright holder. To view a copy of this licence, visit <http://creativecommons.org/licenses/by/4.0/>.

References

- Markard J (2018) The next phase of the energy transition and its implications for research and policy. *Nat Energy* 3(8):628–633. <https://doi.org/10.1038/s41560-018-0171-7>
- Kammermann J, Bolvashenkov I, Tran K, Herzog HG, Frenkel I (2020) Feasibility study for a full-electric aircraft considering weight, volume, and reliability requirements. In: International conference on electrotechnical complexes and systems (ICOECS) 1–6. <https://doi.org/10.1109/ICOECS50468.2020.9278461>
- Wei H, Liu W, Chen X, Yang Q, Li J, Chen H (2019) Renewable bio-jet fuel production for aviation: a review. *Fuel* 254:115599. <https://doi.org/10.1016/j.fuel.2019.06.007>
- Field CB, Campbell JE, Lobell DB (2008) Biomass energy: the scale of the potential resource. *Trends Ecol Evol* 23(2):65–72. <https://doi.org/10.1016/j.tree.2007.12.001>
- Miura M, Shimotori Y, Nakatani H, Harada A, Aoyama M (2015) Bioconversion of birch wood hemicellulose hydrolyzate to xylitol. *Appl Biochem Biotechnol* 176(3):947–955. <https://doi.org/10.1007/s12010-015-1604-4>
- Delbecq F, Wang Y, Muralidhara A, El Ouardi K, Marlaire G, Len C (2018) Hydrolysis of hemicellulose and derivatives—a review of recent advances in the production of furfural. *Front Chem*. 6. <https://doi.org/10.3389/fchem.2018.00146>
- Meng J, Moore A, Tilotta D, Kelley S, Park S (2014) Toward understanding of bio-oil aging: accelerated aging of bio-oil fractions. *ACS Sustain Chem Eng* 2(8):2011–2018. <https://doi.org/10.1021/sc500223e>
- Wang X, Arai M, Wu Q, Zhang C, Zhao F (2020) Hydrodeoxygenation of lignin-derived phenolics—a review on the active sites of supported metal catalysts. *Green Chem* 22(23):8140–8168. <https://doi.org/10.1039/D0GC02610G>
- Berenguer A, Sankaranarayanan TM, Gómez G, Moreno I, Coronado JM, Pizarro P, Serrano DP (2016) Evaluation of transition metal phosphides supported on ordered mesoporous materials as catalysts for phenol hydrodeoxygenation. *Green Chem* 18(7):1938–1951. <https://doi.org/10.1039/C5GC02188J>
- Sulman A, Mäki-Arvela P, Bomont L, Alda-Onggar M, Fedorov V, Russo V, Eränen K, Peurla M, Akhmetzyanova U, Skuhrovová L, Tišler Z, Grénman H, Wärnå J, Murzin DY (201) Kinetic and thermodynamic analysis of guaiacol hydrodeoxygenation. *Catal Lett* 149(9):2453–2467. <https://doi.org/10.1007/s10562-019-02856-x>
- Gao D, Xiao Y, Varma A (2015) Guaiacol hydrodeoxygenation over platinum catalyst: reaction pathways and kinetics. *Ind Eng Chem Res* 54(43):10638–10644. <https://doi.org/10.1021/acs.iecr.5b02940>
- Santos JL, Alda-Onggar M, Fedorov V, Peurla M, Eränen K, Mäki-Arvela P, Centeno MA, Murzin DY (2018) Hydrodeoxygenation of vanillin over carbon supported metal catalysts. *Appl Catal A* 561:137–149. <https://doi.org/10.1016/j.apcata.2018.05.010>
- Lyu G, Wu S, Zhang H (2013) Estimation and comparison of bio-oil components from different pyrolysis conditions. *Front Energy Res* 3(28):1–11. <https://doi.org/10.3389/fenrg.2015.00028>
- Hileman JJ, Stratton RW (2014) Alternative jet fuel feasibility. *Transp Policy* 34:52–62. <https://doi.org/10.1016/j.tranpol.2014.02.018>
- Kallio P, Pásztor A, Akhtar MK, Jones PR (2014) Renewable jet fuel. *Curr Opin Biotechnol* 26:50–55. <https://doi.org/10.1016/j.copbio.2013.09.006>
- Mortensen PM, Grunwaldt JD, Jensen PA, Jensen AD (2016) Influence on nickel particle size on the hydrodeoxygenation of phenol over Ni/SiO₂. *Catal Today* 259:277–284. <https://doi.org/10.1016/j.cattod.2015.08.022>
- Bakhtyari A, Rahimpour MR, Raeissi S (2020) Cobalt-molybdenum catalysts for the hydrodeoxygenation of cyclohexanone. *Renew Energy* 150:443–455. <https://doi.org/10.1016/j.renene.2019.12.119>
- Lu M, Du H, Wei B, Zhu J, Li M, Shan Y, Song C (2017) Catalytic hydrodeoxygenation of guaiacol over palladium catalyst on different titania supports. *Energy Fuels* 31(10):10858–10865. <https://doi.org/10.1021/acs.energyfuels.7b01498>
- Mäkelä E, González Escobedo JL, Lindblad M, Källdström M, Meriö-Talvio H, Jiang H, Puurunen RL, Karinen R (2020) Hydrodeoxygenation of levulinic acid dimers on a zirconia-supported ruthenium catalyst. *Catalysts* 10(2):200. <https://doi.org/10.3390/catal10020200>
- Afrin S, Bollini P (2019) Cerium oxide catalyzes the selective vapor phase hydrodeoxygenation of anisole to benzene at ambient pressures of hydrogen. *Ind Eng Chem Res* 58:14603–14607. <https://doi.org/10.1021/acs.iecr.9b01987>
- Ohta H, Kobayashi H, Hara K, Fukuoka A (2011) Hydrodeoxygenation of phenols as lignin models under acid-free conditions with carbon-supported platinum catalysts. *Chem Comm* 47(44):12209. <https://doi.org/10.1039/C1CC14859A>
- Vasilevich AV, Baklanova ON, Lavrenov AV (2020) Hydrodeoxygenation of guaiacol with molybdenum-carbide-based carbon catalysts. *Chem Select* 5(15):4575–4579. <https://doi.org/10.1002/slct.202000361>
- Jung KB, Lee J, Ha J-M, Lee H, Suh DJ, Jun C-J, Jae J (2018) Effective hydrodeoxygenation of lignin-derived phenols using bimetallic RuRe catalysts: effect of carbon supports. *Catal Today* 303:191–199. <https://doi.org/10.1016/j.cattod.2017.07.027>
- Martínez-Klimov M, Mäki-Arvela P, Vajglova Z, Alda-Onggar M, Angervo I, Kumar N, Eränen K, Peurla M, Calimli MH, Muller J, Shchukarev A, Simakova IL, Murzin DY (2021) Hydrodeoxygenation of isoeugenol over carbon-supported Pt and Pt-Re catalysts for production of renewable jet fuel. *Energy Fuels* 35:17755–17768. <https://doi.org/10.1021/acs.energyfuels.1c02656>
- Martínez-Klimov M, Mäki-Arvela P, Çiftçi A, Kumar N, Eränen K, Peurla M, Hensen EJM, Murzin DY (2022) Bifunctional Pt–Re catalysts in hydrodeoxygenation of isoeugenol as a model compound for renewable jet fuel production. *ACS Eng Au* 2(5):436–449. <https://doi.org/10.1021/acsengineeringau.2c00015>
- Chen M-Y, Huang Y-B, Pang H, Liu X-X, Fu Y (2015) Hydrodeoxygenation of lignin-derived phenols into alkanes over carbon nanotube supported Ru catalysts in biphasic systems. *Green Chem* 17(3):1710–1717. <https://doi.org/10.1039/C4GC01992J>
- Vargas-Villagrán H, Flores-Villeda MA, Puente-Lee I, Solís-Casados DA, Gómez-Cortés A, Díaz-Guerrero G, Klimova TE (2018) Supported nickel catalysts for anisole hydrodeoxygenation:

- increase in the selectivity to cyclohexane. *Catal Today* 341:26–41. <https://doi.org/10.1016/j.cattod.2018.07.057>
28. Guan Q, Wan F, Han F, Liu Z, Li W (2016) Hydrodeoxygenation of methyl palmitate over MCM-41 supported nickel phosphide catalysts. *Catal Today* 259:467–473. <https://doi.org/10.1016/j.cattod.2015.03.010>
 29. Fan X, Jiao Y (2020) Porous materials for catalysis: Toward sustainable synthesis and applications of zeolites. In: *Sustainable nanoscale engineering*, pp 115–137. Elsevier. <https://doi.org/10.1016/B978-0-12-814681-1.00005-9>
 30. Choudary NV, Newalkar BL (2011) Use of zeolites in petroleum refining and petrochemical processes: recent advances. *J Porous Mater* 18:685–692. <https://doi.org/10.1007/s10934-010-9427-8>
 31. Derouane EG, Vedrine JC, Pinto RR, Borges PM, Costa L, Lemos MA, Lemos F, Ribeiro F (2013) The acidity of zeolites: concepts, measurements and relation to catalysis: a review on experimental and theoretical methods for the study of zeolite acidity. *Catal Rev* 55(4):454–515. <https://doi.org/10.1080/01614940.2013.822266>
 32. Whiting GT, Chung S-H, Stosic D, Chowdhury AD, van der Wal LI, Fu D, Zecevic Z, Travert A, Houben K, Baldus M, Weckhuysen BM (2019) Multiscale mechanistic insights of shaped catalyst body formulations and their impact on catalytic properties. *ACS Catal* 9:4792–4803. <https://doi.org/10.1021/acscatal.9b00151>
 33. Murzin D (2020) *Engineering catalysis*. De Gruyter, Berlin, Boston. <https://doi.org/10.1515/9783110614435>
 34. Vajglová Z, Kumar N, Peurla M, Hupa L, Semikin K, Sladkovskiy DA, Murzin DY (2019) Effect of the preparation of Pt-modified zeolite beta-bentonite extrudates on their catalytic behavior in n-hexane hydroisomerization. *Ind Eng Chem Res* 58(25):10875–10885. <https://doi.org/10.1021/acs.iecr.9b01931>
 35. Cheng K, van der Wal LI, Yoshida H, Oenema J, Harmel J, Zhang Z, Sunley G, Zečević J, de Jong KP (2020) Impact of the spatial organization of bifunctional metal–zeolite catalysts on the hydroisomerization of light alkanes. *Angewandte Chemie* 132(9):3620–3628. <https://doi.org/10.1002/ange.201915080>
 36. Vajglová Z, Simakova IL, Eränen K, Mäki-Arvela P, Kumar N, Peurla M, Tolvanen S, Efimov A, Hupa L, Peltonen J, Murzin DY (2022) The physicochemical and catalytic properties of clay extrudates in cyclization of citronellal. *Appl Catal A* 629:118426. <https://doi.org/10.1016/j.apcata.2021.118426>
 37. Vajglová Z, Kumar N, Peurla M, Peltonen J, Heinmaa I, Murzin DY (2018) Synthesis and physicochemical characterization of beta zeolite-bentonite composite materials for shaped catalysts. *Catal Sci Technol* 8:6150–6162. <https://doi.org/10.1039/C8CY01951G>
 38. Vajglová Z, Kumar N, Mäki-Arvela P (2019) Synthesis and physico-chemical characterization of shaped catalysts of beta and Y zeolites for cyclization of citronellal. *Ind Eng Chem Res* 58:18084–18096. <https://doi.org/10.1021/acs.iecr.9b02829>
 39. Emeis CA (1993) Determination of integrated molar extinction coefficients for infrared-adsorption bands of pyridine adsorbed on solid acid catalysts. *J Catal* 141:347–354. <https://doi.org/10.1006/jcat.1993.1145>
 40. Murzin DY (2020) *Engineering catalysis*. In *Engineering catalysis*. de Gruyter. <https://doi.org/10.1515/9783110614435>
 41. Leofanti G, Padovan M, Tozzola G, Venturelly B (1998) Surface area and pore texture of catalysts. *Catal Today* 41(1–3):207–219. [https://doi.org/10.1016/S0920-5861\(98\)00050-9](https://doi.org/10.1016/S0920-5861(98)00050-9)
 42. Kubička D, Kumar N, Venäläinen T, Karhu H, Kubičková I, Österholm H, Murzin DY (2006) Metal-support interactions in zeolite-supported noble metals: influence of metal crystallites on the support acidity. *J Phys Chem* 110:4937–4946. <https://doi.org/10.1021/jp055754k>
 43. Alda-Onggar M, Mäki-Arvela P, Eränen K, Aho A, Hemming J, Paturi P, Peurla M, Lindblad M, Simakova IL, Murzin DY (2018) Hydrodeoxygenation of isoeugenol over alumina-supported Ir, Pt, and Re catalysts. *ACS Sustain Chem Eng* 6(12):16205–16218. <https://doi.org/10.1021/acssuschemeng.8b03035>
 44. Bomont L, Alda-Onggar M, Fedorov V, Aho A, Peltonen J, Eränen K, Peurla M, Kumar N, Wärnå J, Russo V, Mäki-Arvela P, Grénman H, Lindblad M, Murzin DY (2018) Production of cycloalkanes in hydrodeoxygenation of isoeugenol over Pt- and Ir-modified bifunctional catalysts. *Eur J Inorg Chem* 24:2841–2854. <https://doi.org/10.1002/ejic.201800391>

Publisher's Note Springer Nature remains neutral with regard to jurisdictional claims in published maps and institutional affiliations.

M. E. Martínez Klimov, O. Yevdokimova, P. Mäki-Arvela, J. Cueto, N. Shcherban, Z. Vajglová, K. Eränen, D. Y. Murzin, Hydrodeoxygenation of isoeugenol in continuous mode using bifunctional Pt-Beta 25-binder catalysts for renewable jet fuel production, *Sustainable Energy and Fuels*, 8 (2023) 90 – 102.



Cite this: *Sustainable Energy Fuels*,
2024, 8, 90

Hydrodeoxygenation of isoeugenol in continuous mode using bifunctional Pt-Beta 25-binder catalysts for renewable jet fuel production

Mark E. Martínez-Klimov,^{*a} Olha Yevdokimova,^a Päivi Mäki-Arvela,^{id a}
Jennifer Cueto,^{id b} Nataliya Shcherban,^{id c} Zuzana Vajglová,^a Kari Eränen^a
and Dmitry Yu. Murzin^{id *a}

A series of extrudates composed of platinum, zeolite H-Beta-25 and Bindzil as a binder were tested in the hydrodeoxygenation of isoeugenol in a continuous trickle-bed reactor to produce propylcyclohexane, a compound within the hydrocarbon range of jet fuel. All catalytic tests were performed at 30 bar of hydrogen, with a gas flow rate of 40 mL min⁻¹, and a liquid flowrate of 0.5 mL min⁻¹ of a mixture of isoeugenol in dodecane (0.012 M). Screening of the catalysts was performed at 150 °C to determine the effect of the metal location, catalyst acidity and the platinum particle size. A higher conversion (53%) and the propylcyclohexane yield (39%) were obtained when Pt was located on both zeolite and the binder, while platinum located on the binder resulted in a lower activity (49% dihydroeugenol conversion and 30% propylcyclohexane yield). The effect of temperature on activity and catalyst deactivation was determined using the catalyst with platinum supported on both the zeolite and the binder. A range of temperatures between 65 and 200 °C was used with a total time on stream of ca. 30 h showing ca. 10% of deactivation. High dihydroeugenol conversions (ca. 100%) and propylcyclohexane yields (>66%) were obtained at 150 °C.

Received 16th August 2023
Accepted 17th November 2023

DOI: 10.1039/d3se01061a

rsc.li/sustainable-energy

Introduction

Environmental regulations aimed at reducing pollutants emissions and decrease dependence on the fossil fuels have caused a recent surge in the development of alternative and renewable fuels.¹ The transition towards cleaner fuels or technologies is still a major challenge for the aviation industry as battery technologies cannot be implemented due to weight limitations.² An attainable solution is to derive hydrocarbons from renewable sources, such as biomass, thereby minimizing their environmental impact.^{3,4}

Lignocellulosic biomass is a promising option to obtain valuable compounds, such as biofuels, materials, and chemicals through thermochemical or chemical processes.⁵

Although an attractive, available, and abundant resource, lignocellulosic biomass has yet to make significant commercial progress as a source of chemicals and fuels.

In the recent studies, considerable attention has been given to the valorization of lignin, a complex biopolymer abundant in

aromatic and oxygenated moieties. Pyrolysis of lignin produces a mixture of oxygenated compounds known as lignin-derived bio-oil, which needs to be upgraded further as the oxygen moieties limit its use as a fuel directly.⁶

To overcome the low heating value, high viscosity, and corrosiveness of lignin-derived bio-oil, the oxygen groups must be removed through a process called hydrodeoxygenation (HDO). HDO requires two types of active sites: metal sites to activate hydrogen and acid sites or oxygen vacancies to activate the oxygen moieties found in the bio-oil compounds.⁷

Phenol, guaiacol, isoeugenol, and vanillin are among the most studied model molecules for HDO, as they can represent the phenolic compounds found in bio-oil.⁸ Isoeugenol is of particular interest as it has similar functional groups which resemble the phenylpropane units constituting lignin. An additional benefit is that the HDO product of isoeugenol is propylcyclohexane,⁹ which falls within the hydrocarbon range suitable for jet fuel.

The utilization of the existing infrastructure is key to make renewable jet fuel a viable alternative to fossil-derived fuels. For this reason, it needs to possess similar properties to conventional jet fuel. The main components of fossil-derived jet fuel consist primarily of diverse alkanes, alkenes, cycloalkanes, and aromatics hydrocarbons, ranging from C8 to C16.^{10,11}

Noble metals (Pt, Ru, and Pd) deposited on a variety of supports (zeolites, metal oxides, carbon) have shown to be

^aJohan Gadolin Process Chemistry Centre, Åbo Akademi University, Henriksgatan 2, Turku/Åbo, 20500, Finland. E-mail: dmurzin@abo.fi

^bThermochemical Processes Unit, IMDEA Energy Institute, Avda. Ramón de la Sagra, 3, Móstoles, 28935, Madrid, Spain

^cL.V. Pysarzhevsky Institute of Physical Chemistry, NAS of Ukraine, 31 pr. Nauky, Kyiv 03028, Ukraine

highly active in the HDO of organic molecules.¹² However, recent developments in HDO catalysts have also explored the utilization of more affordable transition metals such as Ni, Co, Mo and even Fe.^{13,14}

Zeolites have garnered significant attention as supports and catalysts for a wide range of applications, mainly due to their inherent acidity, high thermal stability and developed porosity.¹⁵ They are mainly employed in petroleum refining processes such as isomerization, alkylation, and cracking reactions.¹⁶ Zeolites can be found either in nature or synthesized, allowing for the adjustment of their acid characteristics mainly by varying Si:Al ratios thus enabling their use for specific applications.¹⁷

While catalyst forming operations are of immense importance for industry, interest in developing shaped catalysts (granules, extrudates) in academia was very limited. There has been, however, a recent surge also in academia to develop shaped catalysts with the intention of bridging the gap between laboratory-scale research and industrial applications.^{18,19} Continuous systems applied in industry demand the application of shaped catalysts to reduce the pressure drop.²⁰ For this reason, it is fundamental to understand shaping processes as well as the interactions between components of a catalyst matrix.

Extrudates are composed of a mixture of various materials that not only function as the catalytically active phase, but also facilitate catalyst shaping and provide the mechanical strength. This matrix of materials usually includes a metal, a support, and a binder.¹⁹ The latter, typically aluminosilicate clays, aid in catalyst shaping and mechanical strength, yet studies of their effect on catalytic activity or other physical properties remain largely unexplored in academic research as already mentioned.

Several studies focused on hydroconversion reactions have examined the significance of active site proximity in catalysts that incorporate a binder. Results from the previous research strongly indicate that a close proximity between Pt and Beta zeolite resulted in higher conversion and C₆ selectivity in hydroisomerization of *n*-hexane when using Pt supported on H-Beta-25 and bentonite extrudates.²¹ In contrast, in hydroisomerization of *n*-heptane using catalysts consisting of zeolite ZSM-22, mordenite, and γ -alumina binder, the proximity between active sites was unfavorable for selectivity, leading to the undesired cracking reactions.¹⁸ These findings emphasize the importance of investigating the effects of sites proximity.

A recent study from our group focused on the HDO of isoeugenol in a batch reactor using a catalyst matrix consisting of platinum, zeolites Beta-300 and Beta-25 and Bindzil as a binder was aimed at understanding the effect of acidity, binder addition, and the metal location. The results demonstrated that high isoeugenol conversions and propylcyclohexane yields were obtained for the catalyst where Pt was supported on a more acidic zeolite H-Beta-25 and Bindzil. However, higher selectivity to propylcyclohexane and mass balance in the liquid phase compared to H-Beta-25 were reached for the catalysts that included H-Beta-300.²²

In the current work, hydrodeoxygenation of isoeugenol was performed in a trickle-bed reactor over a series of shaped

bifunctional catalysts comprising platinum, zeolite H-Beta-25 and Bindzil. Zeolite H-Beta-25 was selected due to its high acidity, commercial availability, and a suitable pore size, while Bindzil was used as a binder to facilitate catalyst shaping.²³ The purpose of the current work is to determine the effect that the addition of the binder has on the mechanical and chemical properties of the extrudates. The effect of the proximity between metal and acid sites was conducted by changing the deposition location of platinum; Pt was loaded alternatively on H-Beta-25, on Bindzil or on both. In addition, the effect of temperature and catalyst stability were studied.

Experimental

Reagents

Zeolite NH₄-Beta-25 was obtained from Zeolyst International (SiO₂/Al₂O₃ = 25). Binder Bindzil-50/80 (50% colloidal SiO₂ in H₂O) was supplied by AzkoNobel. The organic binder was methylcellulose (viscosity: 4000 cP, Sigma-Aldrich). Tetraamine platinum nitrate ([Pt(NH₃)₄](NO₃)₂, Sigma-Aldrich, $\geq 50.0\%$ Pt basis) was applied as the platinum precursor. Isoeugenol (Sigma Aldrich, 98%, mixture of *cis* and *trans*) and *n*-dodecane (Acros Organics, 99%) were used for the catalytic reactions.

Catalyst preparation

Three types of extrudates were prepared, all containing 2 wt% of Pt, 69 wt% of zeolite H-Beta-25 and 29 wt% of Bindzil. These catalysts are differentiated by the platinum location. The catalyst notation was as follows; Pt/EZB when platinum (Pt) was deposited on both zeolite (Z) and the binder (B), Pt/EZ when platinum was located only on the zeolite, and Pt/EB when platinum was only on the binder. The E indicates that all catalysts were shaped as extrudates, therefore, Pt/E will be used when referring to all catalysts presented in the current work.

The general preparation procedure has been thoroughly described in the previous publications.^{21,22,24,25} First, the zeolite NH₄-Beta-25 was transformed into its proton form, H-Beta-25, by two-step calcination in air, heating first at 250 °C for 50 min followed by 400 °C for 4 h, using a heating ramp of 4 °C min⁻¹ for both steps. Deposition of platinum was done using the evaporation-impregnation method with [Pt(NH₃)₄](NO₃)₂ as a precursor, considering a nominal metal loading of 2 wt% for all catalysts.

General synthesis steps for the different catalysts before shaping are the following ones:

Pt/EZB – Pt deposited on both H-Beta-25 and Bindzil: a mixture of H-Beta 25 and Bindzil (70 : 30) was stirred in water (80% water to 20% mixture) at room temperature for 24 h, followed by evaporation of water under vacuum, drying at 100 °C for 7 h and calcination at 500 °C. Pt was deposited by evaporation-impregnation, followed by reduction in a U-shaped glass reactor under hydrogen flow (40 mL min⁻¹, Woikoski, 99.999%) at 350 °C for 3 h and a heating rate of 2 °C/min.

Pt/EZ – Pt deposited on H-Beta-25: platinum was first deposited on the zeolite followed by reduction (350 °C for 3 h, heating ramp of 2 °C/min.) under 40 mL min⁻¹ of hydrogen flow

(Woikoski, 99.999%). Pt/H-Beta-25 was mixed with Bindzil in water (80% water to 20% mixture) for 24 h. The water was evaporated, and the catalyst was first dried at 100 °C and then calcined at 500 °C.

Pt/EB – Pt deposited on Bindzil: Bindzil was dried prior to deposition of Pt, followed by its reduction under hydrogen flow (40 mL min⁻¹, Woikoski, 99.999%) at 350 °C for 3 h with a heating ramp of 2 °C min⁻¹. Thereafter, it was mixed in water H-Beta-25 (80% water to 20% mixture), followed by drying and calcination of the catalyst at 500 °C.

Shaping of the catalysts was performed in an extrusion device (TBL-2, Tianjin Tianda Beiyang Chemical Co. Ltd., China) after all the components were mixed and dried. For this, a suspension composed of the catalyst mixture, distilled water and methylcellulose was prepared with a wt. ratio of 44.5/54.5/1.0, respectively. The resulting extrudates exhibited a cylindrical shape with a diameter of 1.4 mm and *ca.* 1 cm of length. After shaping the extrudates were dried at 100 °C and calcined at 400 °C.

Physicochemical characterization

Transmission Electron Microscopy (TEM, JEM-1400Plus, JEOL, Japan) was used to determine the platinum particle sizes. Fresh catalysts were reduced *ex-situ* in a glass reactor under a hydrogen flow of 40 mL min⁻¹ and heating of 350 °C for 2 h. The spent catalysts were washed with acetone prior to their analysis. The extrudates were crushed, suspended in ethanol, and mounted on a copper grid. The average metal particle sizes were determined by measuring *ca.* 150 particles using the ImageJ software.

Brønsted and Lewis acid sites of the catalysts were quantified using Fourier transform infrared spectroscopy of adsorbed pyridine (Py-FTIR, ATI Mattson FTIR Infinity Series) using the molar extinction coefficients reported in the literature.²⁶ Determination of weak, medium, and strong acid sites was done by desorbing pyridine at 250, 350, and 450 °C, respectively. Measurements, however, were taken at 100 °C. Pellets of *ca.* 20 mg and 1 cm of diameter were prepared for each material analyzed.

The catalyst metal loading was determined by inductively coupled plasma atomic emission spectrometry (ICP-AES, Goffin Meyvis Spectro Ciruscdd) by dissolving *ca.* 100 mg of the catalysts in aqua regia (9 mL HCl 30% + 3 mL HNO₃ 65%) under microwave digestion for 1 hour.

Nitrogen physisorption (Micromeritics 3Flex-3500) was used to determine the textural properties of fresh and spent catalysts. The specific surface areas were determined by the BET and Dubinin–Radushkevich methods. Pore size distributions were determined using the non-local density functional theory method (NL-DFT). The samples were degassed twice prior to the analysis. *Ex situ* outgassing was done in a Micromeritics Vac-Prep 061 Sample Degas System under vacuum at 200 °C for 20–24 h, followed by *in situ* degassing for 5 h at 250 °C.

Crush tests (Crush tester SE 048, Lorentzen & Wettre) were performed to measure the mechanical strength of the extrudates in both vertical and horizontal positions. *Ca.* 10 extrudates were analyzed per position.

Temperature-programmed reduction (TPR, Microtrac Belcat II) was performed to determine the reduction temperature and

hydrogen consumption of the fresh catalysts. For each measurement, around 30 mg of the catalyst was loaded in a quartz reactor and pretreated *in situ* at 200 °C for 2 h under argon flow to remove excess moisture. The analysis was performed under a 5% H₂/Ar flow from 35 °C until 800 °C with a temperature ramp of 10 °C min⁻¹.

Temperature-programmed oxidation (TPO, Microtrac Belcat II) of the spent catalysts was used to determine the quantity of carbonaceous deposits. The spent catalysts (*ca.* 30 mg) were loaded in a quartz reactor and pretreated *in situ* at 200 °C for 2 h under argon flow. The analysis was performed under a 5% O₂/Ar flow from 35 °C until 865 °C with a temperature ramp of 10 °C min⁻¹.

Catalytic tests of hydrodeoxygenation of isoeugenol in trickle-bed reactor

Hydrodeoxygenation of isoeugenol was performed in a trickle-bed reactor equipped with a high-performance liquid chromatography (HPLC) pump (Knauer Smartline Pump 100).

The reactor was 12 cm in length with an inner diameter of 1.2 cm and a catalyst zone of 7 cm. The catalysts were mixed with 15 g of fine granular quartz (200–800 µm) to have a uniform distribution throughout the catalytic bed.

The catalysts were reduced *in situ* before the reaction. The system was flushed with an Ar flow (AGA, 99.999%) of 50 mL min⁻¹ prior to the reduction. The *in situ* reduction was carried out at 350 °C for 180 min, with a heating ramp of 10 °C min⁻¹, under a continuous hydrogen flow (AGA, 99.999%) of 40 mL min⁻¹.

A mixture of isoeugenol in dodecane (0.012 M) was used for the catalytic tests. Reaction conditions were chosen based on the previous work.^{22,27}

After the catalyst reduction, the system was pressurized to 30 bars with hydrogen and heated to reach the reaction temperature with a ramp of 10 °C min⁻¹.

For the catalyst screening, the reactions were performed at 150 °C, with a heating ramp of 10 °C min⁻¹. The system was pressurized to 30 bar of H₂ (AGA, 99.999%) and liquid and gas flow rates were of 0.5 mL min⁻¹ and 40 mL min⁻¹ were applied, respectively. The amount of catalyst for these tests was 0.4 g.

The effect of temperature was tested with catalyst Pt/EA, increasing the catalyst amount to 1 g. These reactions were performed in a temperature range between 65–200 °C while the other conditions were kept the same.

Downflow feeding of the reaction mixture started after the reaction temperature was reached. The samples were analyzed by GC (Agilent Technologies 6890N) and GC/MS (Agilent Technologies 6890) both equipped with a DB-1 capillary column (Agilent 122-103e, 30 m length, 250 µm internal diameter and 0.5 µm film thickness) using helium as a carrier gas. The temperature program employed for both chromatographs was: 60 °C (5 min), 3 °C min⁻¹ to 135 °C, and 15 °C min⁻¹ to 300 °C.

Results and discussion

Catalyst characterization

Results from ICP-AES, pyridine FTIR, nitrogen physisorption and crush tests have been reported in the previous publication²¹

and will be briefly mentioned here. ICP was also applied for determination of Pt content in the spent catalysts and the reaction samples.

A summary of the catalysts used in the current work, as well as the Pt loadings and metal particle sizes is presented in Table 1.

From Table 1, it can be observed that the real platinum loadings determined by ICP-AES were near the nominal value of 2% for all catalysts.

Pt content remained the same for the spent catalysts, moreover Pt content in the liquid samples of the reaction was below the detection limit. These results indicate that platinum was not leached from the catalyst into the reaction mixture.

Platinum particle sizes, determined by transmission electron microscopy (Fig. 1), varied in the range of 2.9–5.5 nm for the fresh catalysts. In accordance with the previous work,²² the metal particle sizes were larger (5.5 nm) for the catalyst where Pt was deposited only on Bindzil (Pt/EB), which could be due to weaker interactions between the non-acidic binder and the Pt particles, leading to agglomeration. Platinum particles were smaller for the catalyst Pt/EZB (2.9 nm), where Pt was deposited on both zeolite and binder, resulting in a better distribution of the metal.

Dispersion for the fresh catalysts was calculated using the formula $d_{\text{Pt}} = 108/D(\%)$,²⁸ where d_{Pt} is dispersion of platinum and D is the diameter of the metallic particles (nm).

Metal dispersion decreased in the following trend Pt/EZB > Pt/EZ > Pt/EB.

TEM micrographs of the spent catalysts are shown in Fig. 1 and the corresponding average metal particle sizes are also presented in Table 1. A slight increase in the metal particle size was observed for spent catalysts, indicating that agglomeration occurred during the catalytic reactions. TEM images could also help to distinguish the binder particles from those of H-Beta-25, as Bindzil displays a characteristic round shape with sizes ranging between 30 and 200 nm.

Specific surface area, the pore size distribution, and the pore volumes of the fresh and spent catalysts, as well as the pure zeolite and binder, were determined by nitrogen physisorption. The results are summarized in Table 2 while the adsorption-desorption isotherms and NL-DFT pore-size distributions for the fresh and spent catalysts are presented in Fig. 2.

The textural properties of neat H-Beta-25 and Bindzil were also measured to compare with the mixture that comprised the catalysts. The Dubinin–Radushkevich method was used for the comparison due to the microporosity of the zeolite-based materials which is not considered in the BET method.

It can be initially observed that neat H-Beta-25 has a higher specific surface area (SSA, 638 m² g^{−1}) compared to the Pt/E catalysts. However, the extrudates contained 69% of the zeolite and 29% Bindzil (SSA = 154 m² g^{−1}). A theoretical surface area of ca. 490 m² g^{−1} for the extrudates calculated as a weight average from the respective surface areas is in line with the values obtained for Pt/E catalysts. Additionally, deposition of Pt could also lead to a decrease in the textural properties by blocking the pores.

The fresh catalysts displayed specific surface areas in the range of 460–498 m² g^{−1}, as well as the total pore volume (V_{Σ}) of ca. 0.7 cm³ g^{−1} and a micropore volume (V_{MP}) of ca. 0.2 cm³ g^{−1}. The highest surface area was obtained for Pt/EB catalyst (498 m² g^{−1}), where Pt was deposited only on the binder while the lowest surface area was recorded for Pt/EZB catalyst (460 m² g^{−1}), indicating that the introduction of Pt in the zeolite blocks mainly micropores as can be seen from a slight shift in the pore size distribution maxima for catalysts Pt/EZB and Pt/EZ towards smaller pore sizes (Fig. 2b), additionally decreasing the specific surface area and pore volume.

The textural properties of the spent catalysts displayed a noticeable decrease when compared to the fresh catalysts, giving a two-fold decrease, with SSA values in the 228–323 m² g^{−1} range. The same trend was observed for the total pore volume (0.3–0.4 cm³ g^{−1}) and the micropore volume (ca. 0.1 cm³ g^{−1}). This could be caused by blocking of zeolite micropores by coke formed during the reaction, as spent Pt/EZ displayed the lowest surface area (228 m² g^{−1}) among the tested catalysts, correlating with the TPO results, as this catalyst also displayed the highest TPO area (Table 4, Fig. 4).

A comparison of the adsorption-desorption isotherms between the fresh and spent Pt/E catalysts is illustrated in Fig. 3a. All catalysts display type I isotherms which are characteristic of microporous materials and H3 hysteresis.²⁹ A noticeable difference in the isotherms between the fresh and spent catalysts could be observed, which resulted in the decrease of the nitrogen uptake of spent catalysts. This decrease attributed to the formation of carbonaceous deposits after the reaction.

NL-DFT pore size distributions (Fig. 2b) showed a main peak between 0.6 and 0.7 nm, for all catalysts, indicating microporosity. No significant changes were observed for the spent catalysts compared to the fresh ones in terms of the mean pore size.

The type, strength and concentration of acid sites of the catalysts, as well as of the starting H-Beta-25 and Bindzil were determined by pyridine FTIR (Table 3).

Table 1 Notation and characteristics of the shaped catalysts used for HDO of isoeugenol

Catalyst	Platinum deposition location	Nominal Pt loading (wt%)	Real Pt loading ^a (wt%)	Fresh catalyst metal particle size (nm)	Dispersion (%)	Spent catalyst metal particle size (nm)
Pt/EZB	On both	2	2.0	2.9	37	4.3
Pt/EZ	On zeolite	2	2.3	3.9	27	4.8
Pt/EB	On binder	2	1.7	5.5	20	9.3

^a Values take from ref. 21.

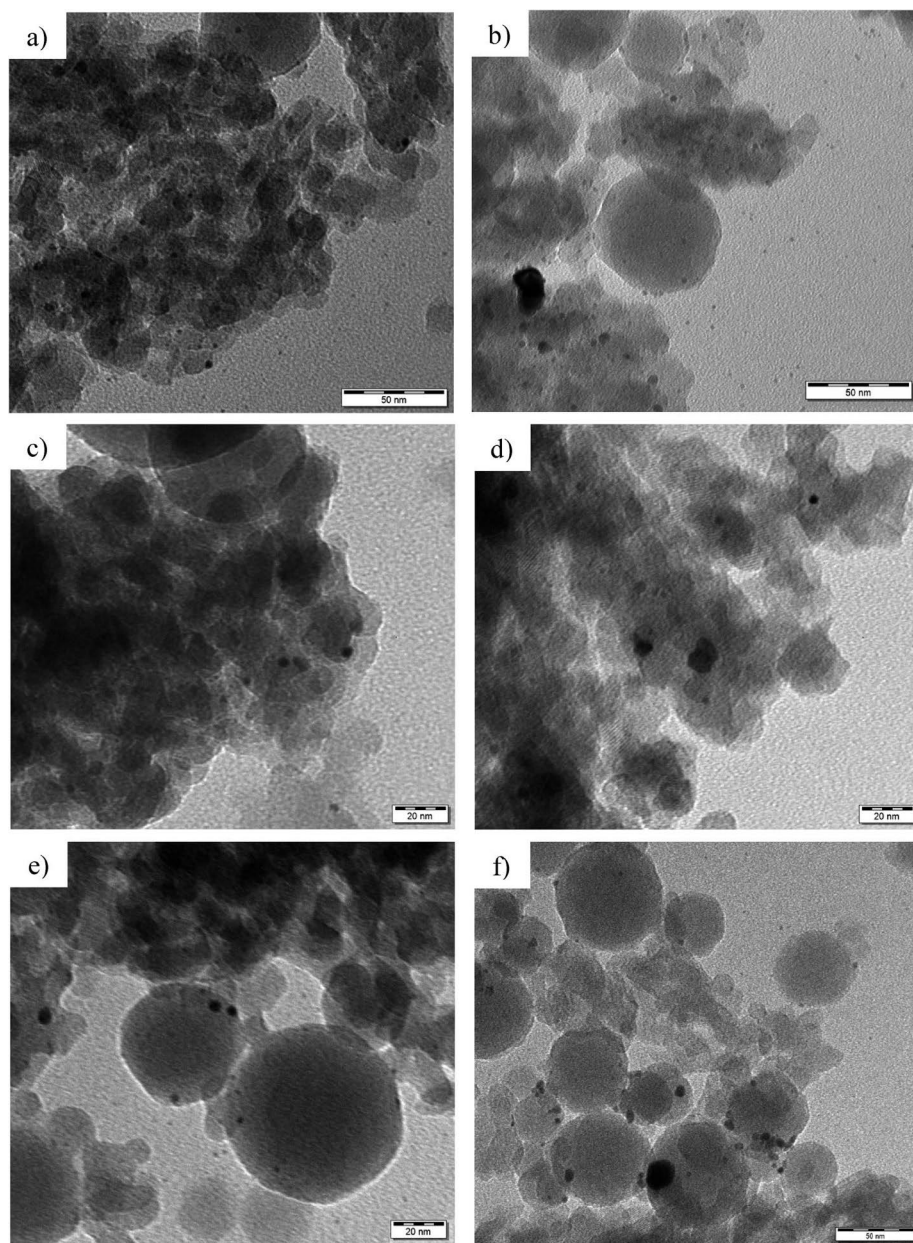


Fig. 1 TEM micrographs of (a) fresh and (b) spent Pt/EZB, (c) fresh and (d) spent Pt/EZ, and (e) fresh and (f) spent Pt/EB catalysts.

Neat H-Beta-25 displayed the highest acidity, while Bindzil contained the lowest amount of acid sites. A decrease in acidity for all catalysts was expected after deposition of Pt and addition

of Bindzil in the mixture. The catalyst Pt/EZB displayed the most acid sites, followed by Pt/EB. Pt/EZ catalyst where Pt was located only on the zeolite, exhibited the lowest acidity, which could

Table 2 Textural properties of supports and shaped catalysts

Material	BET SSA ($\text{m}^2 \text{g}^{-1}$)	Dubinin-Radushkevich SSA ($\text{m}^2 \text{g}^{-1}$)	V_{Σ} ($\text{cm}^3 \text{g}^{-1}$)	V_{MP} ($\text{cm}^3 \text{g}^{-1}$)
H-Beta-25 ^a	522	638	0.89	0.31
Bindzil ^a	154	—	0.30	—
Pt/EZB (fresh) ^b	372	460	0.64	0.19
Pt/EZ (fresh) ^b	397	488	0.67	0.19
Pt/EB (fresh) ^b	405	498	0.74	0.20
Pt/EZB (spent)	218	317	0.44	0.11
Pt/EZ (spent)	184	228	0.28	0.10
Pt/EB (spent)	257	323	0.38	0.13

^a values taken from ref. 22. ^b values taken from ref. 21.

suggest interactions between Pt and the acid sites of the zeolite, as previously reported.²² Additionally, all extrudate catalysts featured low amounts of Lewis acid sites when compared to the initial zeolite, as observed in the increase of the BAS/LAS ratios (Table 3).

Crush tests were performed to determine the mechanical strength of the extrudates. The mechanical strength results, as well as the peak areas for the TPR of the fresh catalysts and TPO of spent ones are given in Table 4.

As presented in Table 4, the catalysts displayed a vertical mechanical strength of 2.9–4.4 MPa and a horizontal mechanical strength of 0.7–1.2 MPa. The catalyst with the highest strength was Pt/EZB (4.4 and 1.2 MPa in the vertical and horizontal position, respectively), where Pt was located on both the zeolite and the binder. The catalyst with lowest mechanical strength was Pt/EB (2.9 MPa for vertical and 0.7 MPa for horizontal position), which as discussed in the previous work, could be caused by a larger intracrystalline void space between the particles.²¹

The mechanical strength obtained for Pt/E is within the range for similar types of catalysts reported in the literature; TS-1 zeolite and sepiolite extrudates displayed horizontal and vertical strengths of 1.78 and 2.44 MPa, respectively.³⁰ Beta-25

and bentonite extrudates showed slightly higher mechanical strengths, within 3.8–7.8 MPa.²⁵ Similarly, extrudates composed of X13 zeolite and various binders exhibited higher mechanical strengths (2.5 to 7.6 MPa).³¹ These tests reinforce the

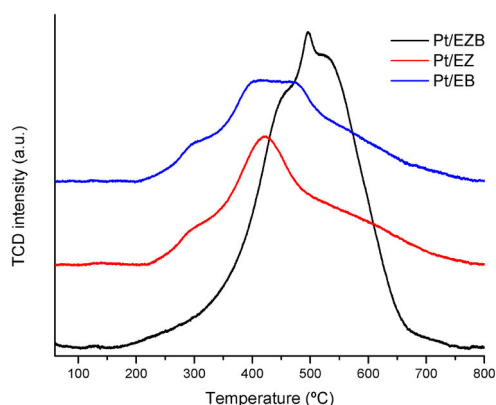


Fig. 3 Temperature programmed reduction of Pt/E catalysts.

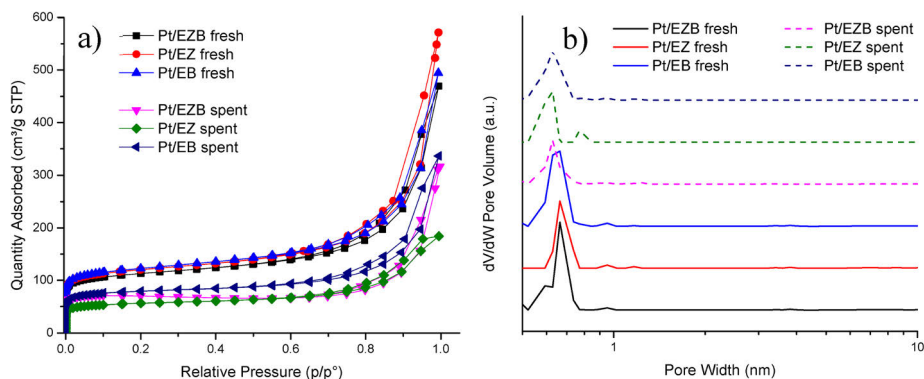


Fig. 2 (a) Adsorption–desorption isotherms and (b) pore size distribution of the fresh and spent Pt/E catalysts.

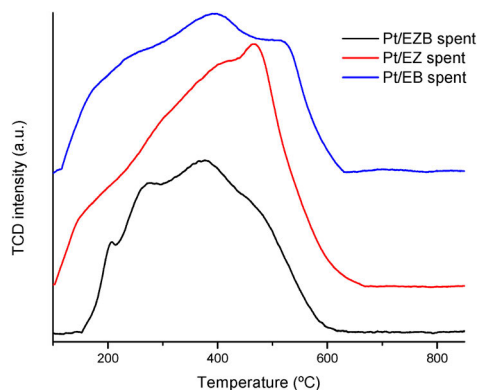


Fig. 4 Temperature programmed oxidation of Pt/E catalysts.

Table 3 Catalyst acidity determined by pyridine FTIR

Catalyst	Brønsted acid sites ^a (BAS, $\mu\text{mol g}^{-1}$)			Lewis acid sites ^a (LAS, $\mu\text{mol g}^{-1}$)			Total acid sites ($\mu\text{mol g}^{-1}$)			BAS/LAS
	W	M	S	W	M	S	BAS	LAS	Total	
H-beta-25 ^b	67	33	129	26	5	6	229	37	266	6.2
Bindzil ^b	12	0	0	3	0	0	12	3	15	4
Pt/EZB ^c	62	2	3	1	1	0	67	2	69	33.5
Pt/EZ ^c	42	0	1	3	0	0	43	3	46	14.3
Pt/EB ^c	49	5	7	1	1	0	61	2	63	30.5

^a Desorption of pyridine was performed at 250, 350, and 450 °C to determine the weak (W), medium (M), and strong (S) acid sites, respectively; measurements were done at 100 °C. ^b Values taken from ref. 22. ^c Values taken from ref. 21.

importance of the chemical interactions between the different components that constitute the extrudates.

Temperature programmed reduction of the fresh catalysts was performed to determine the effect of the platinum location on its reduction. The reduction profiles for the fresh catalysts are displayed in Fig. 3, while the corresponding integrated areas are presented in Table 4.

TPR reduction profiles for Pt/EZ and Pt/EB catalysts show a small shoulder at *ca.* 300 °C and main peak ranging from 350–

475 °C. The lack of the reduction peaks at low-temperatures (*ca.* 100 °C) indicate absence of the PtO species for all catalysts, while reduction peaks between 200–425 °C is usually attributed to PtO₂ species.³² Additionally, peaks at temperatures higher than 400 °C have been attributed to strong interactions caused by the formation of Pt-silanol species on zeolite-based catalysts. The results, therefore, indicate that most of Pt is present in the 4⁺ oxidation state after the catalyst calcination.³³

Pt/EZB catalyst exhibited a shift in the reduction temperature (towards 500 °C) indicating stronger interactions between the metal particles and the support. This effect has been attributed to a higher coordination between Pt and oxygen species of the zeolite, making the platinum more difficult to reduce.³⁴

A higher intensity peak for Pt/EBZ, resulting in more than double the consumption of hydrogen when compared to the other catalysts, could be due to a larger amount of Pt particles being available either in the surface or in the pores of the catalyst.

High reduction temperatures indicating strong interactions between Pt particles and the support was also observed by the reduction of strong acid sites after the deposition of Pt, as presented in pyridine FTIR acidity measurements (Table 3).

Temperature programmed oxidation was performed to gain an insight on the formation of carbonaceous deposits such as coke on the spent catalysts. The results are presented in Fig. 4 as well as in Table 4.

TPO peak areas presented in Table 4 indicate that Pt/EZB catalyst had the lowest formation of carbonaceous species after the reaction. On the other hand, Pt/EZ exhibited larger amounts of carbon deposits, which could negatively impact its catalytic activity, as seen in Fig. 5 and Table 5. Additionally, these results were also reflected in a noticeable decrease of the textural properties, as determined by nitrogen physisorption, between the fresh and spent Pt/EZ catalysts (Table 2, Fig. 2).

The TPO profiles display wide peaks, which indicate the presence of different types of carbonaceous deposits. As reported in the literature, a first peak at *ca.* 200 °C is ascribed to reaction intermediates. A second peak in the range of 350–400 °C can be associated to side polymeric compounds or active carbon species,³⁵ while a peak at higher temperatures, closer to 600 °C could be assigned to graphite and/or amorphous carbons.³⁶

Catalytic tests in a trickle-bed reactor

Testing of the catalysts in hydrodeoxygenation (HDO) of isoeugenol (IE) was performed in a trickle-bed reactor at 150 °C at

Table 4 Mechanical strength of extrudates, TPR areas for fresh catalysts and TPO areas of spent catalysts

Catalyst	Mechanical strength ^a (MPa)		TPR peak area for fresh catalyst ^b (a.u.)	TPO peak area for spent catalyst ^b (a.u.)
	Vertical	Horizontal		
Pt/EZB	4.4	1.2	753	106
Pt/EZ	3.8	1.2	324	157
Pt/EB	2.9	0.7	311	120

^a Values taken from ref. 21. ^b Values normalized by mass of catalyst.

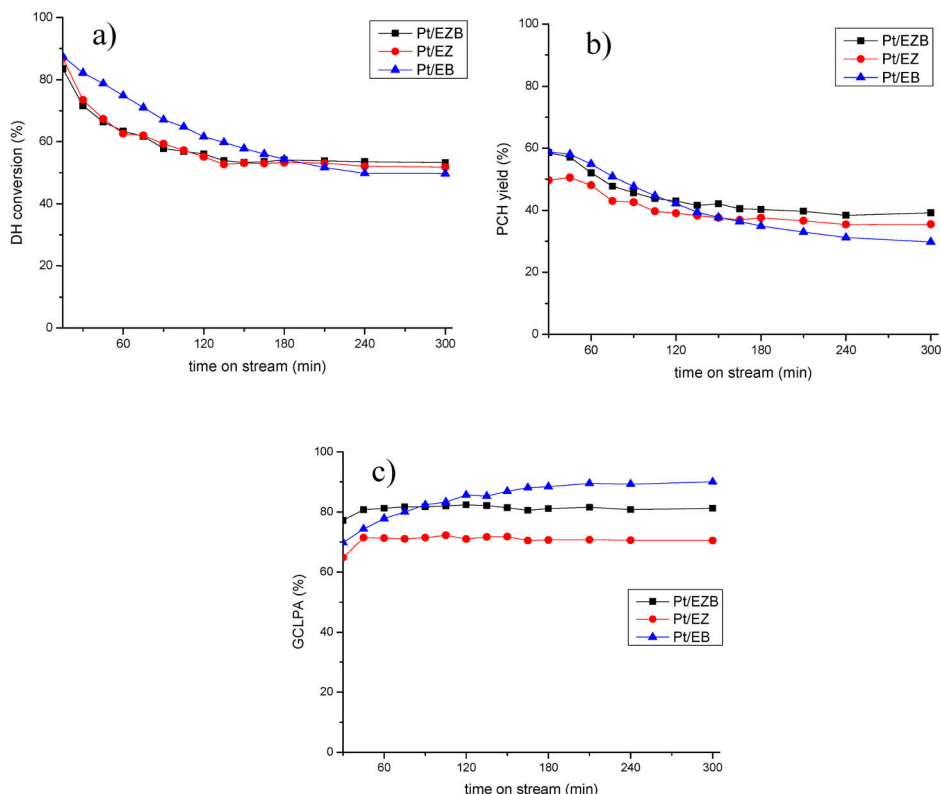


Fig. 5 Catalytic activity of Pt/H-Beta-25 and Bindzil extrudates in HDO of isoeugenol at 150 °C and 30 bar of H₂, liquid flow of 0.5 mL min⁻¹ and gas flow of 40 mL min⁻¹ (a) dihydroeugenol conversion, (b) propylcyclohexane yield and (c) GCLPA as a function of time on stream.

30 bar of H₂ with liquid flow of 0.5 mL min⁻¹ and the gas flow of 40 mL min⁻¹. The amount of catalyst for these tests was 0.4 g.

Scheme 1 shows an overall reaction network for this reaction as determined in this and previous studies. First isoeugenol (IE) is converted into dihydroeugenol (DH) through hydrogenation of the double bond of the propene group, which was reported as the fastest reaction. Followed by hydrogenation of the aromatic ring, resulting in 2-methoxy-4-propylcyclohexanol, a hydrogenated intermediate (HYD) with oxygen still in its structure. Subsequent dehydration and demethoxylation give the desired oxygen-free product, propylcyclohexane (PCH).³⁷

The catalytic results for Pt/E catalysts are presented in Table 5 and in Fig. 5.

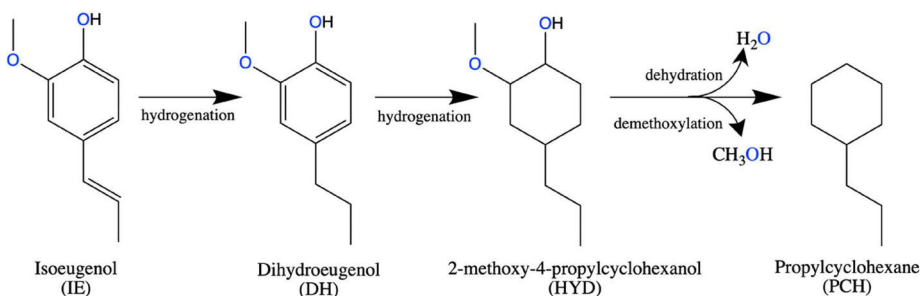
All catalysts exhibited 100% conversion of isoeugenol. As reported previously, this transformation occurs rapidly, hence the conversion of dihydroeugenol was monitored.²² Different catalysts displayed a similar behavior regarding DH conversion, *ca.* 50%. The catalyst with the highest conversion was Pt/EZB (53%), while somewhat lower was recorded for Pt/EB (49%).

GCLPA (Gas Chromatography Liquid Phase Analysis) is an approximation for the mass balance of the compounds in the liquid phase and is determined by adding all the compounds

Table 5 Catalyst screening in hydrodeoxygenation of isoeugenol at 150 °C, 30 bar of H₂, liquid flow of 0.5 mL min⁻¹ and gas flow of 40 mL min⁻¹

Catalyst	IE conversion ^a (%)	DH conversion ^a (%)	GCLPA ^{a,b} (%)	PCH yield ^a (%)	TOF (h ⁻¹)
Pt/EZB	100	53	81	39	12.6
Pt/EZ	100	51	70	35	16.8
Pt/EB	100	49	90	30	21.6

^a Values determined at steady state. ^b Gas Chromatography Liquid Phase Analysis (GCLPA) is the mass balance considering only the reactants and products in the liquid phase.



Scheme 1 A general reaction network for hydrodeoxygenation of isoeugenol.

obtained from the GC analysis, as gases and heavy products, such as dimers, trimers, *etc.* are not quantified. As expected, GCLPA values decrease with an increase in the conversion of dihydroeugenol, which is the result of the formation of products in the gas phase, such as water or methanol, or coke on the surface of the catalyst. The catalyst with the highest GCLPA was Pt/EB (90%), however, this catalyst also displayed the lowest DH conversion (49%). Interestingly, Pt/EZB and Pt/EZ catalysts exhibited different GCLPA values (81% and 70%, respectively) despite having similar DH conversion (*ca.* 50%). This difference could be attributed to the formation of oligomerization products, which is reflected in the TPO results of spent catalysts (Fig. 4, Table 4).

Additional differences between the catalysts can be seen in the formation of the desired product; namely, the propylcyclohexane yield was the highest for the Pt/EZB catalyst (39%) and the lowest for Pt/EB (30%). Hinting at the importance of the proximity between acid sites and the metal particles.

Time-on-stream behavior for dihydroeugenol (DH) conversion, propylcyclohexane (PCH) yield and GCLPA is displayed in Fig. 5. Less prominent decline in the catalytic performance for Pt/EZB probably connected with both more stable work of small Pt nanoparticles and their proximity with acid sites should be noted.

As reported in our previous publications,^{21,22} catalytic activity was improved when Pt was located on the zeolite, and not on the non-acidic Bindzil, in other words, closer proximity between the acid sites of the zeolite and the platinum particles was beneficial.

Minimal solvent cracking was observed under the reaction conditions used, as formation of the cracking-related products for *n*-dodecane was below 0.1%.

Catalyst acidity did not seem to directly influence the yield of propylcyclohexane, as the catalyst with the lowest acidity (Pt/EZ, total acid sites = 46 $\mu\text{mol g}^{-1}$, Table 3) displayed an intermediate PCH yield (35%), however, acidity influenced the side reactions, as the same spent catalyst (Pt/EZ spent) displayed a larger amount of carbonaceous deposits, as can be seen in TPO (Table 4).

TOF values were calculated considering conversion of dihydroeugenol (Table 5) and platinum dispersion as determined by

Pt particle sizes (Table 1). A high TOF obtained for Pt/EB catalyst (21.6 h^{-1}) could be explained by the structure-sensitive nature³⁸ of the hydrogenolysis reaction, where larger Pt clusters result in a higher activity.

This is further illustrated in Fig. 6, where a clear trend between TOF and platinum particle size can be observed. A potential explanation for this effect is related to a larger space available on larger cluster need for accommodation of a bulky reagent. Similar dependences have been reported in the literature for transformations of bulky organic compounds.^{39,40}

The effect of the reaction temperature on hydrodeoxygenation of isoeugenol was tested using Pt/EZB catalyst, which displayed higher catalytic activity, compared to other materials. The results are illustrated in Table 6 and Fig. 7. These reactions were performed in the same trickle-bed reactor, varying the temperature between 65 and 200 °C. The other conditions were maintained the same as in preliminary catalyst testing.

In a comparable manner as in the catalyst screening, 100% conversion of isoeugenol was achieved at all temperatures as double bond hydrogenation is a very fast reaction, while DH conversion decreased accordingly with the reaction temperature.

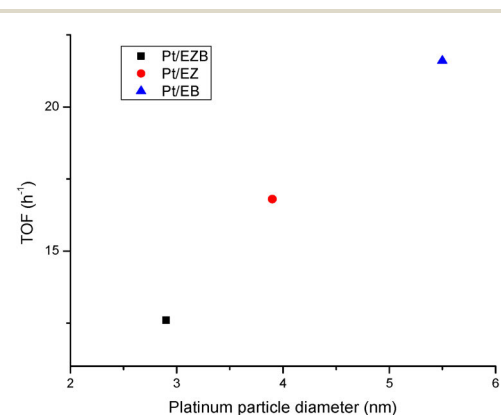


Fig. 6 Dependence of TOF on platinum particle size.

Table 6 Effect of temperature on the catalytic activity of Pt/EZB in hydrodeoxygenation of isoeugenol in a continuous trickle-bed reactor at 30 bar of H₂, liquid flow of 0.5 mL min⁻¹ and gas flow of 40 mL min⁻¹

Temperature (°C)	DH conversion ^a (%)	GCLPA ^{a,b} (%)	PCH yield ^a (%)	HYD yield ^a (%)
200	100	61	80	0
150	100	51	66	0
100	95	58	38	24
75	65	72	5	32
65	44	71	3	26
200	100	53	70	0

^a Values determined at steady state. ^b Gas Chromatography Liquid Phase Analysis (GCLPA) is the mass balance for reactants and products in the liquid phase.

GCLPA values decreased between 200 and 150 °C (from 61% to 51%), despite the same conversion, which could be a first indication of catalyst deactivation. GCLPA increased after lowering further the temperature from 100 °C (58%) to 75 and 65 °C (ca. 71%).

The yield of propylcyclohexane was the highest at 200 °C (80%) decreasing considerably at lower temperature, being at its lowest (5 and 3%) at 75 and 65 °C, indicating that

deoxygenation does not take place at such low temperatures. Instead, hydrogenation of the aromatic ring was predominant, as observed by the formation of 2-methoxy-4-propylcyclohexanol, the HYD product. These findings have also been reported in previous works.^{27,41}

HYD yield increased from 24% at 100 °C to 32% at 75 °C, however, it decreased again to 26% at 65 °C, due to low overall catalytic activity at this temperature (44% DH conversion).

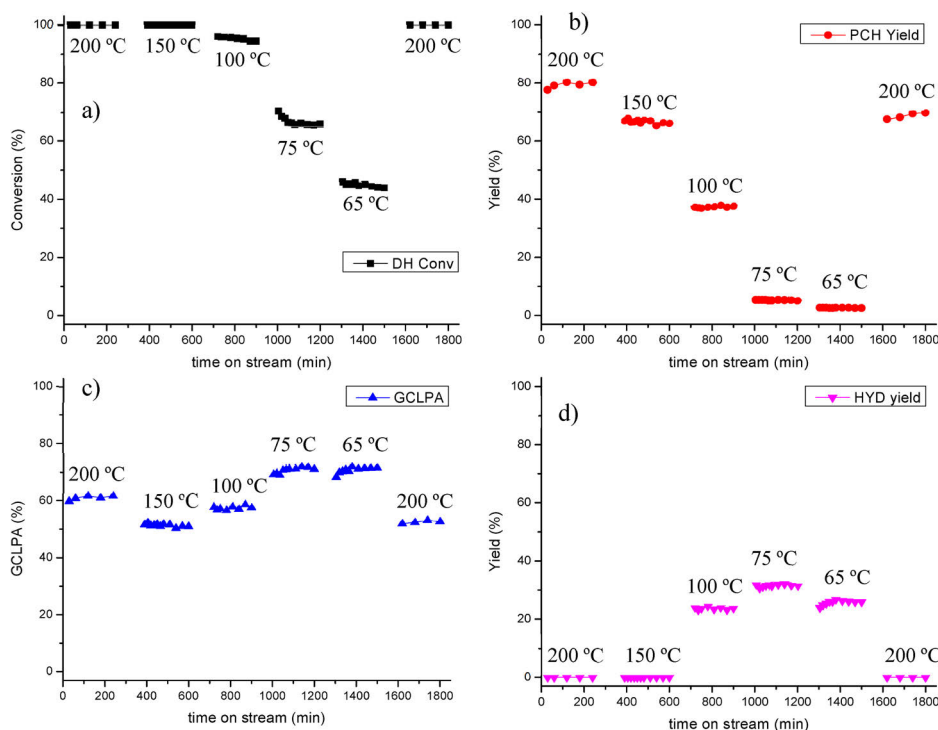


Fig. 7 Transformations of isoeugenol using Pt/EZB in a continuous reactor at different temperatures, 30 bar of H₂, liquid flow of 0.5 mL min⁻¹ and gas flow of 40 mL min⁻¹ (a) dihydroeugenol conversion, (b) propylcyclohexane yield, (c) GCLPA and (d) hydrogenated intermediate yield as a function of time on stream.

Table 7 Catalytic results²⁷ of the HDO of isoeugenol using PtRe/Sibunit (0.3 g) in a continuous reactor at different temperatures, 30 bar of H₂, gas flow of 40 mL min⁻¹ and liquid flow of 0.5 mL min⁻¹

Temperature (°C)	IE conversion ^a (%)	DH conversion ^a (%)	GCLPA ^{a,b} (%)	PCH yield ^a (%)	HYD yield ^a (%)
200	100	100	76	90	7
170	100	100	80	46	44
150	100	100	85	10	78
75	100	70	94	0	61

^a Values determined at steady state. ^b Gas Chromatography Liquid Phase Analysis (GCLPA) is the mass balance considering reactants and products in the liquid phase.

Returning to the initial temperature of 200 °C after testing catalytic activity at lower T (Fig. 7) confirms that deactivation of the catalyst took place during the testing, as both GCLPA and PCH yield decreased *ca.* 10% each GCLPA from 61 to 53% and PCH yield from 80% to 70%.

The catalyst effectiveness factor was calculated to determine the extent of mass transfer limitations when using extrudates, employing the following equation:²⁸

$$\eta_{\text{eff}} = \frac{r_{\text{extrudates}}}{r_{\text{powder}}} \quad (1)$$

where η_{eff} is the catalyst effectiveness factor, and $r_{\text{extrudates}}$ and r_{powder} are the rates of formation of propylcyclohexane in the continuous and batch reactors, respectively.

Eqn (1) implicitly assumes, that the batch reactor data were obtained in the kinetic regime, which is justified by efficient stirring and small catalyst particle sizes applied in that study.²² The rates were determined at 200 °C using Pt/EZB catalyst. The data in the batch reactor were reported previously.²² The catalyst effectiveness factor calculated from eqn (1) was $\eta_{\text{eff}} = 0.17$, indicating that there are significant mass transfer limitations, as expected for shaped catalysts in a trickle bed reactor.

In our previous work the HDO of isoeugenol was carried out using bimetallic platinum-rhenium catalysts supported on mesoporous carbon (1 mm granules, 0.3 g of catalyst, 4 wt% Pt and 4 wt% Re) under similar conditions using the same continuous reactor system.²⁷ The results are summarized in Table 7.

Comparing the results obtained with Pt/EA used in the current work and previous studies with PtRe/Sibunit it can be concluded that dihydroeugenol conversion is similar at the corresponding temperatures (*e.g.* 65% for Pt/EZB and 70% for PtRe/Sibunit at 75 °C). However, several differences are evident, especially in GCLPA values as well as PCH and HYD yields.

GCLPA values were higher when using the carbon-supported catalyst, which could be due to its low acidity, resulting in less prominent side by-product formation compared to zeolite-based catalysts. In addition, propylcyclohexane yield was higher for PtRe/Sibunit than for Pt/EZB at 200 °C (90% *vs.* 80%), however, at 150 °C, Pt/EZB exhibits over six times higher PCH yield (10% *vs.* 66%). Formation of the hydrogenated intermediate is also higher for the bimetallic PtRe catalyst throughout the whole temperature range (7–61%), indicating that deoxygenation was not as prevalent at temperatures lower than 200 °C.

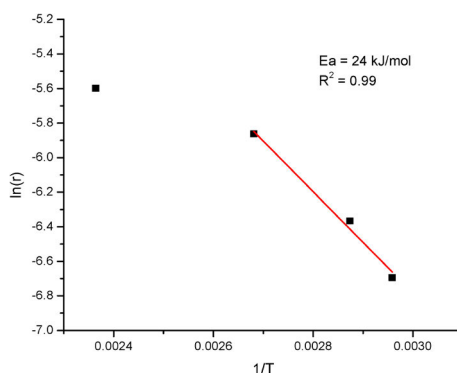


Fig. 8 Arrhenius plot for the hydrodeoxygenation of isoeugenol on extrudates comprised of platinum, zeolite H-Beta-25 and Bindzil as the binder.

C. Even though Pt/EZB displayed a similar propylcyclohexane yield at 100 °C (*ca.* 40%) as PtRe/Sibunit at 170 °C (46%), the bimetallic carbon-supported catalyst is three-fold more active at higher temperatures, which can be related to mass transfer limitations with extrudates applied in this work.

An apparent activation energy was calculated for hydrodeoxygenation of isoeugenol at 65–100 °C performed in the continuous reactor using Pt/EZB catalyst with the Arrhenius plot presented in Fig. 8. An apparent activation energy of 24 kJ mol⁻¹ along with visible changes in the slope upon the elevation of temperature indicate the presence of mass-transfer limitations when using extrudates, as confirmed by the catalyst effectiveness factor. This value was very close to the one reported for PtRe/Sibunit (15 kJ mol⁻¹).²⁷

Conclusions

Extrudates comprising of 69 wt% of zeolite H-Beta-25, 29 wt% of Bindzil as a binder and 2 wt% of platinum were tested in hydrodeoxygenation of isoeugenol in dodecane as a solvent to produce propylcyclohexane in a continuous trickle-bed reactor under 30 bar of hydrogen at 65–200 °C. A screening of catalysts at 150 °C was performed to determine the effect of the platinum location, which was deposited either on the zeolite, on the

binder or on both, resulting in changes in the catalytic activity. Although all catalysts displayed similar dihydroeugenol conversion (*ca.* 50%), a higher propylcyclohexane yield was obtained when Pt was located on both zeolite and binder (39%), while deposition of platinum on the non-acidic binder resulted in lower activity (30%). Furthermore, minimal solvent cracking was observed under these conditions, less than 0.1%.

The catalyst with a lower amount of acid sites, where platinum was located only on the zeolite, exhibited a lower mass balance in the liquid phase, which was attributed to a higher formation of carbonaceous species, as confirmed by temperature programmed oxidation of the spent catalysts.

Therefore, a close arrangement between metal and acid sites can be considered a key factor determining catalytic performance of zeolite-supported metal nanoparticles in the hydrodeoxygenation of isoeugenol.

The catalyst where platinum was located on both zeolite and binder was selected to determine the effect of temperature on the reaction in the range of 65–200 °C with the total time on stream of *ca.* 30 h. It was found that minor deactivation of *ca.* 10% was obtained when comparing with the initial reaction at 200 °C. At low temperatures (65 and 75 °C) the hydrogenation of the aromatic ring dominated over deoxygenation. However, complete dihydroeugenol conversions achieved at elevated temperatures resulted in high propylcyclohexane yields (80 and 66% at 200 and 150 °C, respectively). Determination of the catalyst effectiveness factor (0.17) and a low value of the apparent activation energy of 24 kJ mol⁻¹ demonstrated significant mass transfer limitations.

Conflicts of interest

There are no conflicts to declare.

Acknowledgements

The authors would like to acknowledge the Electron Microscopy Laboratory, Institute of Biomedicine, University of Turku, and Biocenter Finland for access to Transmission Electron Microscopy. This work was supported by the Magnus Ehrnrooth Foundation. N. S. acknowledges the support of the National Research Foundation of Ukraine to the project “New effective zeolite catalysts for environmentally friendly processes of the conversion of renewable raw materials into valuable organic compounds” (project number 2020.02/0335).

References

- 1 J. Markard, *Nat. Energy*, 2018, **3**, 628–633.
- 2 J. Kammernann, I. Bolvashenkov, K. Tran, H. G. Herzog and I. Frenkel, *Proceedings – ICOECS 2020: 2020 International Conference on Electrotechnical Complexes and Systems*, 2020, pp. 1–6.
- 3 C. B. Field, J. E. Campbell and D. B. Lobell, *Trends Ecol. Evol.*, 2008, **23**, 65–72.
- 4 H. Wei, W. Liu, X. Chen, Q. Yang, J. Li and H. Chen, *Fuel*, 2019, 254.
- 5 M. S. Singhvi and D. V. Gokhale, *Appl. Microbiol. Biotechnol.*, 2019, **103**, 9305–9320.
- 6 J. Meng, A. Moore, D. Tilotta, S. Kelley and S. Park, *ACS Sustain. Chem. Eng.*, 2014, **2**, 2011–2018.
- 7 X. Wang, M. Arai, Q. Wu, C. Zhang and F. Zhao, *Green Chem.*, 2020, **22**, 8140–8168.
- 8 M. Bertero, G. De La Puente and U. Sedran, *Fuel*, 2012, **95**, 263–271.
- 9 G. Lyu, S. Wu and H. Zhang, *Front. Energy Res.*, 2015, **3**, 1–11.
- 10 J. I. Hileman and R. W. Stratton, *Transport Policy*, 2014, **34**, 52–62.
- 11 P. Kallio, A. Pásztor, M. K. Akhtar and P. R. Jones, *Curr. Opin. Biotechnol.*, 2014, **26**, 50–55.
- 12 B. Güvenatam, O. Kurşun, E. H. J. Heeres, E. A. Pidko and E. J. M. Hensen, *Catal. Today*, 2014, **233**, 83–91.
- 13 L. Qu, X. Jiang, Z. Zhang, X. G. Zhang, G. Y. Song, H. L. Wang, Y. P. Yuan and Y. L. Chang, *Green Chem.*, 2021, **23**, 9348–9376.
- 14 A. Berenguer, T. M. Sankaranarayanan, G. Gómez, I. Moreno, J. M. Coronado, P. Pizarro and D. P. Serrano, *Green Chem.*, 2016, **18**, 1938–1951.
- 15 X. Fan and Y. Jiao, *Porous Materials for Catalysis: toward Sustainable Synthesis and Applications of Zeolites*, Elsevier Inc., 2019.
- 16 N. V. Choudary and B. L. Newalkar, *J. Porous Mater.*, 2011, **18**, 685–692.
- 17 E. G. Derouane, J. C. Védrine, R. Ramos Pinto, P. M. Borges, L. Costa, M. A. N. D. A. Lemos, F. Lemos and F. Ramôa Ribeiro, *Catal. Rev.: Sci. Eng.*, 2013, **55**, 454–515.
- 18 K. Cheng, L. I. Wal, H. Yoshida, J. Oenema, J. Harmel, Z. Zhang, G. Sunley, J. Zečević and K. P. Jong, *Angew. Chem.*, 2020, **132**, 3620–3628.
- 19 K. Yang, D. Zhang, M. Zou, L. Yu and S. Huang, *ChemCatChem*, 2021, **13**, 1414–1423.
- 20 G. T. Whiting, S. H. Chung, D. Stosic, A. D. Chowdhury, L. I. Van Der Wal, D. Fu, J. Zecevic, A. Travert, K. Houben, M. Baldus and B. M. Weckhuysen, *ACS Catal.*, 2019, **9**, 4792–4803.
- 21 Z. Vajgllová, N. Kumar, M. Peurla, L. Hupa, K. Semikin, D. A. Sladkovskiy and D. Y. Murzin, *J. Chem. Technol. Biotechnol.*, 2021, **96**, 1645–1655.
- 22 M. E. Martínez-Klimov, P. Mäki-Arvela, Z. Vajgllová, C. Schmidt, O. Yevdokimova, M. Peurla, N. Kumar, K. Eränen and D. Y. Murzin, *Top. Catal.*, 2023, **66**, 1296–1309.
- 23 Z. Vajgllová, I. L. Simakova, K. Eränen, P. Mäki-Arvela, N. Kumar, M. Peurla, S. Tolvanen, A. Efimov, L. Hupa, J. Peltonen and D. Y. Murzin, *Appl. Catal., A*, 2022, **629**, 1–11.
- 24 Z. Vajgllová, N. Kumar, M. Peurla, J. Peltonen, I. Heinmaa and D. Y. Murzin, *Catal. Sci. Technol.*, 2018, **8**, 6150–6162.
- 25 Z. Vajgllová, N. Kumar, P. Mäki-Arvela, K. Eränen, M. Peurla, L. Hupa, M. Nurmi, M. Toivakka and D. Y. Murzin, *Ind. Eng. Chem. Res.*, 2019, **58**, 18084–18096.
- 26 C. A. Emeis, *J. Catal.*, 1993, **141**, 347–354.
- 27 M. E. Martínez-Klimov, P. Mäki-Arvela, Z. Vajgllová, M. Alda-Onggar, I. Angervo, N. Kumar, K. Eränen, M. Peurla,

- M. H. Calimli, J. Muller, A. Shchukarev, I. L. Simakova and D. Y. Murzin, *Energy Fuels*, 2021, **35**, 17755–17768.
- 28 D. Yu. Murzin, *Engineering Catalysis*, De Gruyter, 2020.
- 29 G. Leofanti, M. Padovan, G. Tozzola and B. Venturelli, *Catal. Today*, 1998, **41**, 207–219.
- 30 D. P. Serrano, R. Sanz, P. Pizarro, I. Moreno, P. de Frutos and S. Blázquez, *Catal. Today*, 2009, **143**, 151–157.
- 31 A. M. Najafi, S. Soltanali, F. Khorashe and H. Ghassabzadeh, *Chemosphere*, 2023, **324**, 138275.
- 32 B. R. Vieira Dos Santos, M. Montoya Urbina, M. J. B. Souza, A. M. Garrido Pedrosa, A. O. S. Silva, E. V. Sobrinho and R. Velasco Castedo, *J. Therm. Anal. Calorim.*, 2015, **119**, 391–399.
- 33 L. W. Ho, C. P. Hwang, J. F. Lee, I. Wang and C. T. Yeh, *J. Mol. Catal. A: Chem.*, 1998, **136**, 293–299.
- 34 H. J. Jiang, M. S. Tzou and W. M. H. Sachtler, *Appl. Catal.*, 1988, **39**, 255–265.
- 35 Z. Alipour, M. Rezaei and F. Meshkani, *J. Ind. Eng. Chem.*, 2014, **20**, 2858–2863.
- 36 S. Wang and G. Q. Lu, *J. Chem. Technol. Biotechnol.*, 2000, **75**, 589–595.
- 37 M. Alda-Onggar, P. Mäki-Arvela, K. Eränen, A. Aho, J. Hemming, P. Paturi, M. Peurla, M. Lindblad, I. L. Simakova and D. Y. Murzin, *ACS Sustain. Chem. Eng.*, 2018, **6**, 16205–16218.
- 38 R. A. van Santen, *Acc. Chem. Res.*, 2009, **42**, 57–66.
- 39 U. Sanyal, Y. Song, N. Singh, J. L. Fulton, J. Herranz, A. Jentys, O. Y. Gutiérrez and J. A. Lercher, *ChemCatChem*, 2019, **11**, 575–582.
- 40 R. K. Herz, *J. Catal.*, 1981, **386**, 371–386.
- 41 M. Martinez-Klimov, P. Mäki-Arvela, A. Çiftçi, N. Kumar, K. Eränen, M. Peurla, E. J. M. Hensen and D. Yu. Murzin, *ACS Eng. Au*, 2022, **2**, 436–449.

ISBN: 978-952-12-4335-6 (printed version)
ISBN 978-952-12-4336-3 (electronic version)
ISSN 2669-8315 (*Acta technologiae chemicae Aboensia 2023 A/5*)

Painosalama Oy Turku/Åbo, Finland 2023